

# **Solar-Driven High-Temperature Electrolysis Reactor for Fuel Processing**

-

## **Modeling, Optimization, and Experimentation**

THÈSE N° 8465 (2018)

PRÉSENTÉE LE 16 AVRIL 2018

À LA FACULTÉ DES SCIENCES ET TECHNIQUES DE L'INGÉNIEUR  
LABORATOIRE DE LA SCIENCE ET DE L'INGÉNIERIE DE L'ÉNERGIE RENOUVELABLE  
PROGRAMME DOCTORAL EN ENERGIE

ÉCOLE POLYTECHNIQUE FÉDÉRALE DE LAUSANNE

POUR L'OBTENTION DU GRADE DE DOCTEUR ÈS SCIENCES

PAR

**Meng LIN**

acceptée sur proposition du jury:

Prof. F. Maréchal, président du jury  
Prof. S. Haussener, directrice de thèse  
Dr M. Roeb, rapporteur  
Prof. A. Ghoniem, rapporteur  
Prof. J. R. Thome, rapporteur



ÉCOLE POLYTECHNIQUE  
FÉDÉRALE DE LAUSANNE

Suisse  
2018





Truth is ever to be found in the simplicity,  
and not in the multiplicity and confusion of things.

— Isaac Newton

To my family...



# Acknowledgements

I would like to express my gratitude to Prof. Sophia Haussener for her constant support and guidance throughout my studies at the Laboratory of Renewable Energy Science and Engineering (LRESE), EPFL. I thank her for giving the opportunity to carry out research related to high temperature solar fuel generation. Her strong expertise and time dedication provided me with an excellent working environment which largely boosted my professional and personal development.

I thank various collaborators involved in the SOPHIA project. Special thanks go to Dr. Van Herle Jan, Stefan Diethelm, David Constantin, and Nicola Accardo for their strong support during the experimental campaigns at the group of energy materials (GEM), EPFL. I thank Nathalie Monnerie, Jan Reinhold, Moises Romero, and Hans-Peter Streber from Deutsche Zentrum für Luft- und Raumfahrt (DLR) for providing experimental data of tubular receiver for the receiver model validation.

I am grateful to Prof. John Thome, Navid Borhani, Houxue Huang at Heat and Mass Transfer Laboratory (LTCM) for fruitful discussions and suggestions on two-phase flow modeling and experimentation.

I thank Roman Bader of Solar Thermal Group at Australian National University for the discussions on thermochemical cycle and natural convection modeling.

I thank all my colleagues and friends of LRESE for providing a congenial and joyful working environment. Special thanks go to Saurabh Temburne for beneficial discussions in electrochemical device modeling and being a trusted friend, and to Clemens Suter for his support in design, fabrication, and experimentation of our solar reactor without whom the experimental part of this thesis will not be possible. I appreciate the passionate introduction of electrochemistry by Mikael Dumortier. I thank Lihao Han for sharing his expertise in photocatalytic water splitting and experimental skills. I thank Gutierrez Ronald for fruitful discussions in SOEC cell modeling. I thank Fouad Aabid, Yannick Gaudy, Nithin Mallya, Gaël Levêque, Xiaoyu Dai, Fredy Nandjou, Silvan Suter, and Selmar Binder for interesting scientific discussions. I appreciate the help offered by Dominique Espic and Géraldine Palaj which makes my life in Lausanne easier and more comfortable.

I would like to thank André Seuret, Sarah van Rooij, Sheng Jiang, and Etienne Droz for doing master semester projects under my supervision, and Rahul Udiaver for conducting his master

## Acknowledgements

---

thesis with me. In addition, I thank Julien Furrer, Yang Jiao, Matthieu Jonin, Sebastien Pozzo, and Gauvain Ramseier for performing their bachelor project under my supervision.

I am grateful to my close friends in EPFL for their encouragement and for the joyful time we spent together out of the lab. I particularly indebted to Wei Yan, Shenghan Zhang, Xiaoqin Zhong, Liang Zhang, Chunyu Zhang, Yang Sun, Shiwei Zhou, Liu Qiu, Cuiyun Shao, Shaoran Qiu, and Shaoqing Gou for sharing happy cooking, hiking, game playing, and badminton time with me. I thank Shuai Deng of Tian Jin University for his encouragement and suggestions.

European Union's Seventh Framework Programme (FP7/2007-2013) for the Fuel Cells and Hydrogen Joint Technology Initiative under grant agreement n° 621173 (project SOPHIA) and the Chinese Scholarship Council are acknowledged for supporting my doctoral studies and researches.

Finally, I thank my family for their unconditional support, encouragement, trust, and love. I thank my parents and grandparents for their unwavering support and trust ever since my infancy. My very special thanks to my beloved wife, Jiangman, for her understanding, patience, and accompany throughout my doctoral studies.

*Lausanne, 3 January 2018*

Meng Lin

# Abstract

Solar-driven high-temperature electrolysis (HTE) and thermochemical cycles (TCC) are two promising pathways for fuel processing and energy storage, which are considered in this thesis. The goals of this thesis are: *i*) offering engineering guidelines at system level via thermodynamic modeling frameworks for both technologies to evaluate and maximize their solar-to-fuel (STF) efficiencies and economic competitiveness, *ii*) the modeling, optimization, and experimental demonstration of a tubular solar reactor for efficient STF generation, and *iii*) investigation of a fully integrated solar reactor, which uses a tubular high-temperature electrolyzer as the solar absorber to reduce transmission heat losses and hence to improve the STF efficiency.

The techno-economic analysis of HTE systems is performed leading to the identification of the hybrid approach (utilizing concentrated solar heating and photovoltaics) as the optimal choice generating hydrogen at a high efficiency and low costs. This supports the competitiveness of the hybrid approach for scaled solar hydrogen generation.

A thermodynamic modeling framework for a two-step ceria-based TCC is developed analyzing different routes for oxygen partial pressure reduction. This allows for performance comparison between HTE and TCC. Compared with TCC systems, HTE systems work at significantly lower temperatures and the less stringent requirement for heat recovery and low oxygen partial pressure, while equivalent STF efficiency can be achieved indicating that HTE can be a more promising technology for scaled-up solar fuel plants.

The design and optimization of a tubular solar receiver, a key component in HTE system, are conducted based on an experimentally validated coupled heat and mass transfer model for the concurrent direct steam and CO<sub>2</sub> generation. This integrated numerical model is composed of a detailed 1D two-phase flow model in the receiver tubes, which is then incorporated into a coupled 3D heat transfer model for tubular reactor cavity. Based on the model, design and demonstration of a 1 kW<sub>th</sub> solar reactor are presented. The demonstrator employs a direct steam generation solar absorber (two parallel helical tubes) directly connected to a 250 W<sub>el</sub> solid oxide electrolyzer stack forming a compact design to reduce the transmission heat losses of high-temperature fluids. A solar-to-thermal efficiency of 77.8% (at a fluid temperature of 700 K) and STF efficiency of 5.3% (with a 15% solar-to-electricity efficiency) are achieved. The proof-of-concept demonstration leads to a promising pathway for highly efficient STF

## Abstract

---

generation.

Further, a fully integrated solar reactor where the tubular solid oxide electrolyzer cell acts as the absorber as well as the reactor is investigated based on a 2D multi-physics model to further reduce the transmission heat losses and hence improving the STF efficiency.

A comprehensive investigation of HTE for solar fuel processing is presented in this thesis. The hybrid coupling strategy between solar energy and HTE using concentrated solar heating and photovoltaics is proven to have a high techno-economic competitiveness. This thesis provides a detailed and powerful tool for analysis, optimization, design, and prototyping of solar driven HTE systems and reactors. This thesis opens a new pathway toward compact solar reactor design and engineering for highly efficient solar fuel generation.

**Keywords:** Solar fuel, High-temperature electrolysis, Thermochemical cycle, Techno-economic analysis, Two-phase flow, Concentrated solar energy, Tubular solid oxide electrolyzer, Integrated reactor, Concentrated photovoltaics.

# Zusammenfassung

In der vorliegenden Arbeit werden Hochtemperatur-Elektrolyse mittels Sonnenenergie sowie thermochemische Zyklen betrachtet, welche zwei vielversprechende Wege darstellen, um Brennstoffe zu verarbeiten oder Energie zu speichern. Die Ziele der Arbeit sind: *i)* konstruktive Vorgaben auf Systemebene mittels eines thermodynamischen Modells für beide Technologien, um den Solar-zu-Brennstoff-Wirkungsgrad und deren ökonomische Wettbewerbsfähigkeit zu bestimmen und maximieren, *ii)* die Modellierung, Optimierung und experimentelle Vorführung eines solaren Röhrenreaktors zur effizienten Solar-zu-Brennstoff-Erzeugung, und *iii)* Untersuchung eines vollstufigen Solarreaktors, welcher einen röhrenförmigen Hochtemperatur-Elektrolyseur als Absorber für Sonnenlicht verwendet, um Verluste bei der Wärmeübertragung zu reduzieren und folglich den Solar-zu-Brennstoff-Wirkungsgrad zu verbessern.

Eine technisch-ökonomische Analyse des Hochtemperatur-Elektrolyse-Systems wird durchgeführt, um einen Kompromiss zwischen thermischer und photovoltaischer Nutzung der konzentrierten Sonnenstrahlung zu finden, damit Wasserstoff mit einem hohen Wirkungsgrad und zu tiefen Kosten hergestellt werden kann. Dies unterstützt die Wettbewerbsfähigkeit des hybriden Ansatzes für die Wasserstoffherzeugung im industriellen Massstab.

Ein thermodynamisches Modell für einen zweistufigen thermochemischen Ceria-basierten Zyklus wird entwickelt, welcher verschiedene Wege für die Sauerstoff-Partialdruckreduktion analysiert. Dies ermöglicht den Leistungsvergleich zwischen Hochtemperatur-Elektrolyse und thermochemischen Zyklen. Im Vergleich mit letzteren funktioniert erstere bei viel niedrigeren Temperaturen und unter weniger hohen Anforderungen bezüglich Wärmerückgewinnung und tief zu haltendem Sauerstoff-Partialdruck. Dabei wird ein gleichhoher Solar-zu-Brennstoff-Wirkungsgrad erzielt, was aufzeigt, dass die Hochtemperatur-Elektrolyse die vielversprechendere Technologie für Anlagen im industriellen Massstab darstellt. Das Design und die Optimierung des röhrenförmigen Absorbers für Sonnenlicht, eine Schlüsselkomponente im Hochtemperatur-Elektrolyse-System, werden basierend auf einem experimentell validierten Computermodell durchgeführt, welches Wärme- und Massentransport koppelt und die gleichzeitige Simulation der Dampf- und CO<sub>2</sub>-Produktion ermöglicht. Das numerische Modell umfasst ein detailliertes 1D Zweiphasen-Strömungsmodell für die Absorberrohre, welches dann in ein 3D gekoppeltes Wärmeübertragungsmodell für die röhrenförmige Reaktorkavität eingegliedert wird. Basierend darauf werden das Design und die experimentelle Vorführung

eines Solarreaktors mit einer thermischen Leistung von  $1 \text{ kW}_{\text{th}}$  gezeigt. Das Vorführmodell verfügt über einen Dampferzeuger in Form zweier parallel angeordneter spiralförmiger Rohre als Absorber für Sonnenlicht und einen damit direkt verbundenen Festoxid-Elektrolyseur mit einer elektrischen Leistung von  $250 \text{ W}_{\text{el}}$ . Diese Konfiguration ermöglicht ein kompaktes Design, welches es erlaubt, die Verluste durch Wärmeübertragung zu reduzieren. Der Solar-zu-Wärme-Wirkungsgrad beträgt 77.8% bei einer Fluidtemperatur von 700 K und einem Solar-zu-Brennstoff-Wirkungsgrad von 5.3% (mit einem Solar-zu-Strom-Wirkungsgrad von 15%). Der Nachweis des Konzepts («proof-of-concept») zeigt einen aussichtsreichen Weg für die hocheffiziente Solar-zu-Brennstoff-Produktion auf.

Des Weiteren wird ein vollstufiger Solarreaktor untersucht, in welchem der Feststoff-Elektrolyseur sowohl als Absorber als auch als Reaktor fungiert, welcher auf einem 2D multiphysikalischen Modell basiert, um die Verluste durch Wärmeübertragung weiter zu verringern und folglich den Solar-zu-Brennstoff-Wirkungsgrad zu erhöhen.

Eine umfassende Untersuchung der Hochtemperatur-Elektrolyse für die Verarbeitung von solaren Brennstoffen wird in der vorliegenden Arbeit dargelegt. Hierbei wird gezeigt, dass die hybride Kopplungsstrategie zwischen Solarenergie und Hochtemperatur-Elektrolyse, wobei die konzentrierte Sonnenstrahlung sowohl thermisch als auch photovoltaisch genutzt wird, eine hohe technisch-ökonomische Wettbewerbsfähigkeit hat. Die Arbeit stellt ein detailliertes und solides Werkzeug für das Design, die Analyse, die Optimierung sowie die Entwicklung von Prototypen von Hochtemperatur-Elektrolyse-Systemen und -Reaktoren dar. Hierbei wird ein neuartiger Weg aufgezeigt, wie das Design und die Konstruktion kompakter Solarreaktoren für die hocheffiziente Brennstoff-Produktion aussehen.

**Stichwörter:** Solarer Brennstoff, Hochtemperatur-Elektrolyse, thermochemischer Zyklus, technisch-ökonomische Analyse, Zweiphasen-Strömung, konzentrierte Sonnenenergie, röhrenförmiger Feststoff-Elektrolyseur, vollstufiger Reaktor, konzentrierte Photovoltaik.



# Contents

<b>Acknowledgements</b>	<b>v</b>
<b>Abstract (English/Deutsch)</b>	<b>vii</b>
<b>List of figures</b>	<b>xxv</b>
<b>List of tables</b>	<b>xxviii</b>
<b>Nomenclature</b>	<b>xxxvi</b>
<b>Introduction</b>	<b>1</b>
<b>1 Techno-economic modeling of high-temperature electrolysis systems</b>	<b>7</b>
1.1 System description . . . . .	7
1.2 Governing equations and methodology . . . . .	10
1.2.1 Electrolyzer performance model . . . . .	10
1.2.2 CSP performance model . . . . .	14
1.2.3 Photovoltaic cell array performance model . . . . .	16
1.2.4 Auxiliary devices . . . . .	18
1.2.5 System efficiency definition . . . . .	19
1.2.6 Cost model of the systems . . . . .	19
1.3 Results and discussion . . . . .	21
1.3.1 Reference case comparison of the three systems . . . . .	21
1.3.2 Effect of the diffuse irradiation ratio . . . . .	23
1.3.3 Effects of electrolyzer operating temperature and pressure . . . . .	24
1.3.4 Performance and cost sensitivity of system 3 . . . . .	25
1.3.5 Synthesis gas production in system 3 . . . . .	31
1.4 Summary and conclusions . . . . .	33
<b>2 Thermodynamic analysis on ceria-based thermochemical cycles</b>	<b>37</b>
2.1 System description and model development . . . . .	37
2.1.1 System description . . . . .	38

## Contents

---

2.1.2	Model development . . . . .	41
2.1.3	Performance definition . . . . .	43
2.2	Results and discussion . . . . .	44
2.2.1	Operational feasibility for ceria-based fuel processing cycles . . . . .	44
2.2.2	Effects of temperature swing and oxygen partial pressure . . . . .	45
2.2.3	Hydrogen productivity . . . . .	49
2.2.4	Water utilization factor . . . . .	50
2.2.5	Pump efficiency . . . . .	51
2.2.6	Heat recovery effectiveness . . . . .	52
2.2.7	Concentration ratio . . . . .	55
2.2.8	Combined mechanical and mechanical-chemical approaches . . . . .	56
2.2.9	Counterflow versus ideal mixing reactor configurations . . . . .	58
2.3	High temperature electrolysis vs. thermochemical cycles . . . . .	59
2.4	Summary and conclusions . . . . .	60
<b>3</b>	<b>Tubular solar receiver for direct steam generation</b>	<b>63</b>
3.1	Receiver model development . . . . .	64
3.1.1	Cavity model . . . . .	66
3.1.2	Tube model . . . . .	69
3.1.3	Model coupling . . . . .	75
3.1.4	Numerical solution . . . . .	76
3.2	Results and discussion . . . . .	77
3.2.1	Model validation . . . . .	77
3.2.2	Reference cases results . . . . .	80
3.2.3	Flow rates . . . . .	84
3.2.4	Pressure . . . . .	85
3.2.5	Surface emissivity . . . . .	86
3.2.6	Effect of fluid inlet position . . . . .	87
3.2.7	Tube diameter . . . . .	89
3.2.8	Shape of the helical tube . . . . .	91
3.2.9	Cooled receiver front . . . . .	92
3.2.10	Double helical tube receiver . . . . .	93
3.3	Summary and conclusions . . . . .	94
<b>4</b>	<b>A compact solar reactor design and experimentation</b>	<b>97</b>
4.1	Reactor design . . . . .	97
4.2	Performance definitions . . . . .	99
4.3	Experimentation . . . . .	100
4.3.1	Characterization of the SOEC stack (campaign 1) . . . . .	100

4.3.2	Thermal performance of the receiver (campaign 2) . . . . .	103
4.3.3	Compact solar reactor testing (campaign 3) . . . . .	108
4.4	Summary and conclusions . . . . .	111
<b>5</b>	<b>An integrated concentrated solar fuel generator concept</b>	<b>113</b>
5.1	Reactor description . . . . .	115
5.2	Model development . . . . .	116
5.3	Cavity model . . . . .	116
5.4	SOEC models . . . . .	117
5.4.1	Fluid flow and species transport . . . . .	117
5.4.2	Charge conservation . . . . .	118
5.4.3	Electrochemical reactions . . . . .	118
5.4.4	Thermochemical reactions . . . . .	120
5.4.5	Heat transfer in SOEC . . . . .	120
5.4.6	Carbon deposition boundaries in C-H-O ternary diagram . . . . .	122
5.4.7	Microstructure properties for the porous electrodes . . . . .	122
5.5	PV cell model . . . . .	124
5.6	Performance definitions . . . . .	126
5.7	Numerical solutions . . . . .	126
5.8	Results and discussion . . . . .	127
5.8.1	Model validations . . . . .	127
5.8.2	Reference case . . . . .	128
5.8.3	Effect of inlet flow velocity . . . . .	136
5.8.4	Flow arrangement . . . . .	139
5.8.5	Molar reactant composition at inlets . . . . .	141
5.8.6	Reactor with multiple in-series SOEC stacks . . . . .	144
5.8.7	Effect of $\eta_{STF}$ definitions . . . . .	146
5.9	Summary and conclusions . . . . .	147
<b>6</b>	<b>Summary and outlook</b>	<b>149</b>
<b>A</b>	<b>Definition of energy fractions high-temperature electrolysis systems</b>	<b>155</b>
<b>B</b>	<b>Supplementary data for two-step thermochemical cycles</b>	<b>157</b>
B.1	Efficiency curves for carbon dioxide splitting . . . . .	157
B.2	System performance behavior using ideal mixing model . . . . .	157
<b>C</b>	<b>Supplementary data for tubular receiver modeling</b>	<b>163</b>
C.1	Effect of flux distribution at aperture . . . . .	163
C.2	Effect of the thin wall thickness . . . . .	164

## Contents

---

<b>D</b>	<b>Supplementary data for the compact solar reactor experimentation</b>	<b>165</b>
D.1	Technical drawing for the reactor frame . . . . .	166
D.2	Technical drawing for the bipolar plate . . . . .	167
<b>E</b>	<b>Supplementary data for a novel integrated solar reactor concept model</b>	<b>169</b>
E.1	Thermal conductivities . . . . .	169
E.2	Heat capacities . . . . .	170
E.3	Fluid and solid densities . . . . .	170
E.4	Intrinsic electrical conductivities . . . . .	170
E.5	Model parameters for the III-V PV cell . . . . .	171
E.6	SOEC model validations . . . . .	172
E.7	2D CFD simulation for an insulated pipe . . . . .	174
E.8	Cell voltage partitioning with different flow arrangements . . . . .	175
E.9	Cathode inlet gas compositions . . . . .	175
E.10	WGSR vs. eletrochemical reactions . . . . .	176
E.11	SOEC temperature . . . . .	177
	<b>Bibliography</b>	<b>196</b>
	<b>Curriculum Vitae</b>	<b>197</b>

# List of Figures

1	General non-biological solar-to-fuel conversion pathways. . . . .	1
1.1	Flowchart of the three systems, constructed with five different sub-components: electrolyzer and auxiliaries (red block), concentrated solar heating system (purple block), fluid connection system (green block), concentrated solar power system (black block), and PV system (blue block). System 1 represents the thermal-only system using concentrated solar technology to provide both heat and electricity. System 2 represents the electricity-only system using PV technology as the only source for both heat and electricity. System 3 represents the hybrid heat-electricity system using concentrated solar technologies and PV providing solar heat and electricity, respectively. The black arrows indicate mass flow and energy streams, the blue lines indicate electricity streams, and the blue colored components are electricity consuming devices connected to the CSP or PV systems. . . . .	10
1.2	Schematic of a planar SOEC for the synthesis gas production. The reactant mixture ( $H_2$ , CO, $H_2O$ , and $CO_2$ ) passes through the cathode channel and diffuses into the cathode towards the TPB. At the anodic channel, air removes the generated $O_2$ . The x-direction is the direction of gas diffusion in the porous electrodes, and the y-direction is the direction of flow in the channels. The required power is provided either by CSP (system 1) or PV (systems 2 and 3). . . . .	11
1.3	Model validation for the electrolyzer model with experimental data: (a) electrolyzer operation potential as a function current density under three different temperatures (solid lines are for simulated data and the symbols are for experimented data) for hydrogen production [2] and (b) electrolyzer operation potential as a function of current density at 1073 K with inlet gas composition of 25% $H_2$ , 25% $CO_2$ , and 50% $H_2O$ [1]. . . . .	15
1.4	Comparison of the simulated current and voltage characteristics (black solid line) for a single-crystalline solar cell (Sunpower SPR-210-BLK-U) with the data provided by the manufactory (red dashed line) under nominal conditions. . . .	18
1.5	Hydrogen price plotted as a function of the electrolyzer cost with the reference value marked in red. . . . .	21

## List of Figures

---

- 1.6 (a) Energy fraction (equivalent solar field fraction) for power and heat driving of the components (left axis),  $\eta_{STF}$  (right axis), and total solar field area (top axis), for the three systems at the reference condition, and (b) fractional cost of system components (left axis), hydrogen cost (right axis), and  $C_{annual,totla}$  (top axis) for the three systems at the reference condition. . . . . 23
- 1.7  $\eta_{STF}$  and  $C_{fuel}$  as a function of electrolyzer pressure,  $p_{el}$ , and electrolyzer working temperature,  $T_{el}$ , for (a) system 1, (b) system 2, and (c) system 3. (d) The  $C_{fuel}$  difference between system 1 and system 2 under various  $p_{el}$  and  $T_{el}$ . The dashed line in (d) represent the cases when the fuel price difference is zero. Other operational parameters are at the reference state (tables 1.1 and 1.3). . . . . 25
- 1.8 For system 3, (a)  $\eta_{STF}$  and  $C_{fuel}$  as a function of  $J_{el}$  and  $T_{el}$  with  $p_{el} = 10$  atm, (b)  $T_{el} = 1000$  K. Symbol colors indicate the current density, and (c) Thermoneutral operational conditions for various  $T_{el}$ ,  $p_{el}$ , and  $J_{el}$  for system 3 with other parameters held at the reference values. In (a) and (b), the solid lines with symbols represent  $T_{el}$  for a) and  $p_{el}$  for (b). Dashed lines are for the reference case with changing  $J_{el}$ . Black symbols represent thermoneutral conditions. In (c), the dashed line represents the reference  $p_{el}$  with changing  $J_{el}$ . . . . . 27
- 1.9 For system 3,  $\eta_{STF}$  and  $C_{fuel}$  as a function of  $\epsilon_{HE}$  and (a)  $T_{el}$  with  $p_{el} = 10$  atm, and (b)  $p_{el}$  with  $T_{el} = 1000$  K. Symbol colors indicate  $\epsilon_{HE}$ . The solid lines with symbols represent  $T_{el}$  for (a), and  $p_{el}$  for (b). Dashed lines are for the reference case with changing  $\epsilon_{HE}$ . . . . . 28
- 1.10 For system 3,  $\eta_{STF}$  and  $C_{fuel}$  as a function of DNI and (a)  $T_{el}$  for  $p_{el} = 10$  atm, or (b)  $p_{el}$  and  $T_{el} = 1000$  K. (c)  $\eta_{STF}$  and  $C_{fuel}$  as a function of  $CR$  and  $DNI$  for  $p_{el} = 10$  atm and  $T_{el} = 1000$  K. In (a) and (b), symbol colors indicate the  $DNI$ . The solid lines with symbols represent  $T_{el}$  for (a) and  $p_{el}$  for (b). Dashed lines are for the reference case with varying  $DNI$ . In (c), symbols represent varying  $CR$ , and hollow symbols are for reference cases with changing  $DNI$ . . . . . 29
- 1.11 For system 3,  $\eta_{STF}$  and  $C_{fuel}$  as a function of  $W_{CE}$  and (a)  $T_{el}$  for  $p_{el} = 10$  atm, or (b)  $p_{el}$  for  $T_{el} = 1000$  K. Symbol colors indicate  $W_{CE}$ . The solid lines with symbols represent  $T_{el}$  for (a) and  $p_{el}$  for (b). Dashed lines are for the reference case with changing  $W_{CE}$ . . . . . 31
- 1.12 (a)  $H_2$  to  $CO$  molar ratio of synthesis gas as a function of cathode inlet molar ratio of  $CO_2$  to  $H_2O$  for varying  $T_{el}$  and  $p_{el}$  (solid lines for 1 atm and dashed lines for 10 atm), and (b)  $\eta_{STF}$  as a function of cathode inlet molar ratio of  $CO_2$  to  $H_2O$  for various  $T_{el}$  and  $p_{el}$ . Symbols in (b) represent cases that result in a molar ratio of  $H_2$  to  $CO$  equal to 2, with the number indicating the corresponding fuel cost. 31

1.13 (a) the effect of $T_{el}$ and $p_{el}$ on the reaction rate of the reversible water-gas shift reaction with molar ratio of $CO_2$ to $H_2O$ equals to 1 and other parameters kept at reference values, and (b) the reversible water-gas shift reaction rate as a function of $T_{el}$ and molar ratio of $CO_2$ to $H_2O$ at the cathode inlet with $p_{el} = 10$ atm and other parameters at reference value. . . . .	33
1.14 Equilibrium potential as a function of $T_{el}$ for both $CO_2$ and $H_2/CO$ splitting . .	33
2.1 Schematic of the five ceria-based thermochemical cycling schemes modeled (a to e), which are combinations of four different sub-components: oxidation chamber and auxiliaries (blue), reduction chamber and sweep gas connections (purple), chemical scavenger (red), and reduction chamber and vacuum pump (green). The five schemes differ in the methods used for the oxygen partial pressure reduction in the reduction chamber, namely: using inert sweep gas, a vacuum pump, a chemical scavenger, or combinations thereof. . . . .	40
2.2 Feasibility of ceria-based thermochemical cycling under various operation conditions: (a) the non-stoichiometric coefficient of ceria at various temperatures and $p_{O_2,4}$ , and (b) $p_{O_2,4}$ as a function of $\Delta T$ for various $T_{red}$ . . . . .	44
2.3 Optimal $\eta_{STF}$ (dotted lines) and corresponding $\Delta T$ for various $T_{red}$ and $p_{O_2,1}$ combinations for (a) scheme (a), and (b) scheme (b). The solid lines indicate the efficiency at corresponding $T_{red}$ and $p_{O_2,1}$ for isothermal operation ( $\Delta T = 0$ ). . .	46
2.4 Energy balance for scheme (a) at 1 kW solar power input under various working conditions: a) isothermal cases at $p_{O_2,1} = 1$ Pa for varying $T_{red}$ , (b) optimal cases at $T_{red} = 1800$ K for varying $p_{O_2,1}$ , (c) cases at $p_{O_2,1} = 1$ Pa and $T_{red} = 1800$ K for varying $\Delta T$ , and (d) optimal cases at $p_{O_2,1} = 1$ Pa for varying $T_{red}$ . . . . .	47
2.5 Energy balance for scheme (b) at 1kW solar power input under various working conditions: (a) $p_{O_2,1} = 1$ Pa for varying $T_{red}$ , (b) optimal cases at $T_{red} = 1800$ K for varying $p_{O_2,1}$ , (c) $p_{O_2,1} = 1$ Pa and $T_{red} = 1800$ K for varying $\Delta T$ , and (d) optimal cases at $p_{O_2,1} = 1$ Pa for varying $T_{red}$ . . . . .	49
2.6 $H_2$ productivity as a function of $\Delta T$ for different $p_{O_2,1}$ at $T_{red} = 1800$ K for scheme (a) (Zone 1) and scheme (b) (Zones 1 and 2). Dots indicate the optimal efficiency at the corresponding conditions ( $\Delta T$ and $p_{O_2,1}$ ) for scheme (a) (hollow dots) and scheme (b) (filled dots). . . . .	50
2.7 $f_w$ as a function of $\Delta T$ for different $p_{O_2,1}$ at $T_{red} = 1800$ K for scheme (a) (Zone 1) and scheme (b) (Zones 1 and 2). Dots indicate the optimal efficiency at the corresponding conditions ( $p_{O_2,1}$ and $\Delta T$ ) for scheme (a) (hollow dots) and scheme (b) (filled dots). . . . .	51
2.8 (a) Optimal $\eta_{STF}$ for various $T_{red}$ and for scheme (b) with changing $\eta_{pump}$ according to eq. 2.15, and (b) optimal $\eta_{STF}$ as a function of $\eta_{pump}$ for three different $p_{O_2,1}$ (1Pa, 10Pa, and 100Pa). . . . .	52

## List of Figures

---

2.9	STF efficiency at isothermal conditions for $p_{O_2,1} = 1$ Pa and varying $T_{red}$ and $\varepsilon_g$ , for (a) scheme (a), and (c) scheme (b); and non-isothermal conditions at $p_{O_2,1} = 1$ Pa and $T_{red} = 1800$ K for varying $\Delta T$ and $\varepsilon_g$ , for (b) scheme (a), and (d) scheme (b). The maximal efficiencies for each $\varepsilon_g$ are marked by the dots. . . . .	53
2.10	STF efficiency as a function of $\Delta T$ for varying $\varepsilon_s$ at $p_{O_2,1} = 1$ Pa and $T_{red} = 1800$ K for (a) scheme (a), and (b) scheme (b). The maximal efficiencies for each $\varepsilon_s$ are marked by the dots. . . . .	54
2.11	$\eta_{STF}$ as a function of $T_{red}$ for various $C$ at $p_{O_2,1} = 1$ Pa at isothermal operation for (a) scheme (a), and (c) scheme (b). $\eta_{STF}$ as a function of $\Delta T$ for various $C$ at $p_{O_2,1} = 1$ Pa and $T_{red} = 1800$ K for (b) scheme (a), and (d) scheme (b). The maximal efficiencies for each $C$ are marked by the dots. . . . .	55
2.12	(a) $\eta_{STF}$ as a function of $T_{red}$ at various $p_{O_2,1}$ for $\dot{Q}_{Mg,pr} = 3600$ kJ/mol for optimal and isothermal cases. (b) $\eta_{STF}$ as a function of $\dot{Q}_{Mg,pr}$ for various of $p_{O_2,1}$ at $T_{red} = 1800$ K for optimal and isothermal cases. . . . .	57
2.13	$\eta_{STF}$ as a function of $p_{system}$ for various $T_{red}$ at $\dot{Q}_{Mg,pr} = 3600$ kJ/mol for both optimal and isothermal cases for scheme (c). . . . .	57
2.14	$\eta_{STF}$ as a function of $T$ for high temperature electrolysis systems (solid lines, system 1,2, and 3 with ambient pressure), and thermochemical cycles (dashed lines, scheme a, b, and c with selected $p_{O_2,1}$ ). The arrow indicates the STF efficiency drop for schema a when $\varepsilon_g$ decreased from 0.955 to 0.8. . . . .	59
3.1	Schematic of the two investigated types of cavity receivers with tubular absorber tubes, receiver 1 utilizing a helical absorber tube: (a) and (b), and receiver 2 utilizing multiple connected straight absorber tubes: (c) and (d). . . . .	66
3.2	Schematic of the coupling between the 1D tube model and the 3D - receiver cavity heat transfer model. . . . .	76
3.3	(a) Experimentally measured fluid temperature and pressure profiles along the absorber tube given for case 1 in [2] compared with our numerical model results, and (b) the calculated flow pattern evolution for case 1 at $q_w = 12.3$ kW/m <sup>2</sup> (calculated peak flux was up to 25.7 kW/m <sup>2</sup> ). . . . .	77



3.4	(a) Schematics and main components of the experimental receiver setup at DLR's high-flux solar simulator (HFSS), and (b) comparison of the simulated temperatures and the measured values along the helical tube (at positions indicated in figure 3.5a). The positions 1 and 16 stand for the inlet and outlet fluid temperatures, respectively. Other positions represent surface temperatures of the absorber tube. Red symbols indicate experimental data and the black symbols indicate the simulated data. Error bars for the simulated data indicate the position uncertainties of thermocouples ( $\pm 1$ mm) and errors bars for experiment data result from the standard deviation over the steady state testing time of 2 hours . . . . .	79
3.5	(a) Side view of the helical tube indicating the locations of the thermocouples used for the temperature measurements, and (b) recorded temperature measurements during the experimental run at DLR. The time (12:15 to 14:00) was selected as steady state period for the model validation. This steady state was defined by ensuring that the standard deviation of the measured temperatures (T1 - T16) was within 0.5 K during the selected period. . . . .	80
3.6	(a) Computed fluid temperature (solid lines) and fluid pressure (dashed lines) along the absorber tube, (b) the fractions of energy losses due to convection, conduction, and re-radiation from the receiver, (c) tube surface temperature for receiver 1 at reference conditions with solar energy input of 1.5 kW, and (d) tube surface temperature for receiver 2 at reference conditions with solar energy input of 1.5 kW. In (a), the thick lines represent the reference case with input solar energy of 1.5 kW and water flow rate of 0.0003 kg/s, and the thin lines stand for the reference case with input solar energy of 10 kW and flow rate of 0.0021kg/s. Inlet and outlet positions and directions for receiver 1 and receiver 2 are indicated with arrows. Tube connection sequence for receiver 2 is indicated by tube numbers (from 1 - 38). . . . .	83
3.7	Heat losses (bar), solar-to-thermal efficiency (solid line, decreasing), and fluid outlet temperature (dashed line, increasing) as a function of molar fraction of CO <sub>2</sub> at the inlet. The three bar types represent convection, conduction, and re-radiation losses. . . . .	84
3.8	(a) Fluid outlet temperature, solar-to-thermal efficiency, and vapor quality as a function of the flow rate for both receiver types, and (b) composition of the different heat loss terms as a function of the flow rate for receiver 1 (black frame) and receiver 2 (red frame). . . . .	85
3.9	(a) Fluid outlet temperatures (black lines) and solar-to-thermal efficiencies (red lines) as a function of inlet fluid pressure, and (b) composition of heat losses, both for receiver 1 (solid lines) and receiver 2 (dotted lines). . . . .	86

## List of Figures

---

3.10 (a) Fluid outlet temperatures (black lines) and solar-to-thermal efficiencies (red lines) as a function of tube surface emissivity, and (b) composition of the heat losses, both for receiver 1 (solid lines) and receiver 2 (dotted lines). . . . .	87
3.11 (a) Fluid temperature along the tube for receiver 1 with inlet position at front (solid lines) and rear (dashed lines) and for input solar energy input of 1.5 kW (red lines) and 10 kW (blue lines), (b) composition of heat losses for receiver 1 with front and rear inlet positions and for solar energy input of 1.5 kW (red frame) and 10 kW (blue frame), and (c) averaged inner tube wall temperature along the tube (from inlet to outlet) for inlet at rear (blue line) and front (black line) for receiver 1 and for receiver 2 (red line). The dashed line boxes are for the indication of dryout point. . . . .	88
3.12 Averaged inner tube wall net heat flux along the tube (from inlet to outlet) for inlet at rear (blue line) and front (black line) for receiver 1, and for receiver 2 (red line). . . . .	89
3.13 (a) Fluid outlet temperatures (left y-axis in black) and solar-to-thermal efficiencies (right y-axis in red) plotted as a function of tube inner diameter at reference conditions, and (b) composition of the heat losses plotted as a function of tube inner diameter at reference conditions. The solid lines are for receiver 1 and dotted lines are for receiver 2. . . . .	90
3.14 Heat losses, STT efficiency, and fluid outlet temperature for the three difference shapes of helical tubes (shape 1, shape 2, and reference case) and two different solar irradiation energies at the aperture (1.5 kW and 10 kW). The different shapes are illustrated in the top left corner. The solid lines with square symbols indicate the solar-to-thermal efficiency. The fluid outlet temperatures are shown on top of each bar. . . . .	91
3.15 Heat losses, STT efficiency, and fluid outlet temperature for receivers with and without a water-cooled front and for two different solar irradiation magnitudes (1.5 kW and 10 kW). (a) shows the results for receiver 1, and (b) for receiver 2. The solid lines with square symbols indicate solar-to-thermal efficiency. The fluid outlet temperatures are shown on top of each bar. . . . .	92
3.16 (a) Fluids' temperature as a function of tube length. (b) Temperature profiles for the outer surfaces of two helical tubes. . . . .	93
4.1 Schematic of the novel compact solar reactor with a double helical tubes solar absorber and a 16-cell SOEC stack directly connected on the back of the solar absorber. . . . .	98
4.2 Schematic of the test setup for the SOEC stack under controlled condition at EPFL Sion (campaign 1). The MFC represents mass flow controller and the GC represents gas chromatography. . . . .	100

4.3	Schematic and photography of the SOEC stack tested in this study: (a) The photography of the 16-cell SOEC stack, (b) the lateral view schematic for the stack, and (c) the top view of the stack showing four holes for install thermocouples. Two filled dots were inserted with thermocouples during our tests, while two unfilled dots were left unused. . . . .	102
4.4	$J$ - $V$ characterization curves of the SOEC stack at 600 °C, 650 °C, and 700 °C with gas flows: (a) 4 Nml/min/cm <sup>2</sup> , (b) 8 Nml/min/cm <sup>2</sup> , and (c) 12 Nml/min/cm <sup>2</sup> . The colored dots are the current-voltage data. The solid lines are the average temperature at the stack center ( $y$ -axis). The stack voltage and the average cell potential (over 16 cells) are shown in left $y$ -axis. The bottom $x$ -axis is the stack operation current and the top $x$ -axis is the cell current density correspondingly. The dashed lines represent the cell potential of 1.3 V (20.8 V for the stack). . . .	103
4.5	(a) Photograph of the solar reactor operating at the HFSS of EPFL, (b) incident power at the reactor aperture under lamps 1, 3, and 5 and lamps 2, 4, and 6 with various current supplies, and (c) the flux map at the reactor aperture with lamps 1, 3, and 5 at 85 A current for each lamp. The red circle in (c) is the reactor aperture. . . . .	105
4.6	Thermal couple positions on the double helical tube solar absorber. . . . .	105
4.7	Test setup for campaign 2 and campaign 3 performed under HFSS, LRESE. Campaign 2 is the receiver thermal test without integrating the SOEC stack. Campaign 3 is the compact reactor test with the SOEC stack and the tubular receiver compact. . . . .	107
4.8	(a) Measured temperature evolution vs. time for all 6 runs under various flow rates. (b) Solar thermal efficiency and fluid outlet temperatures for 6 runs of campaign 2 with changing flow rates under lamps 1, 3, and 5 at 85 A (power at aperture 0.91 kW). The flow rates for water and N <sub>2</sub> are shown in top $x$ -axis. Run 4 (green) represent the typical run showed in figure 4.9 with the minimal outlet temperature difference between water and N <sub>2</sub> (11 K). Black squares are the solar thermal efficiencies, black circles for N <sub>2</sub> outlet temperatures, and white filled circles for water outlet temperature. . . . .	107
4.9	Temperatures for a typical run of campaign 2. The dashed vertical line indicates the start of steady state. . . . .	108
4.10	Temperature evolution over the testing time for the thermocouples on the solar absorber ( $T_1$ to $T_6$ ) and the SOEC stack ( $T_{\text{stack,top}}$ , $T_{\text{stack,bottom}}$ , $T_{\text{stack,center1}}$ , and $T_{\text{stack,center2}}$ ). $J$ - $V$ curves were measured at 3 selected flow and irradiation conditions (run 1 to run 3). Blue block covered region is one of a thermal behavior testing regions. . . . .	109

## List of Figures

---

- 4.11 *J-V* curves for the selected 3 runs with 3 different averaged stack temperatures. The thermoneutral operations (cell voltage equal to 1.3V) of the stack are indicated by the filled black dots. Filled red dots are the data measured under stable conditions for the same flow (identical flow rate in cathode, while air instead of  $N_2$  was used for anode sweeping) and temperature conditions (figure 4.4b for 8 Nml/min/cm<sup>2</sup> and 700 °C) . . . . . 110
- 5.1 Schematic of the axisymmetric calculation domain for the proposed integrated solar reactor (not to scale). The dashed red box is the SOEC cell domain. The white thick arrows stand for species transport and the dashed black lines stand for current flows. The coordinate 0 point (black dot) is on the aperture (black dot at the aperture domain). The DC-DC converter only appears in the indirect connected cases. . . . . 115
- 5.2 Schematic of the SOEC and the random packing of binary spheres for electrodes. The definition of the contact angle,  $\theta$ , is schematically shown on the right side. Example electron, ion, and species transport at one triple phase boundary (TPB) well as the transport pathways are shown, for both cathode and anode. The solid-line paths are for ions and the dash-line paths are for electrons. . . . . 122
- 5.3 Equivalent circuit model for the III-V triple junction PV cell. . . . . 125
- 5.4 Simulated *J-V* results (lines) and the experimental (dots) [3, 4, 5] for (a)  $H_2$  production at three different temperatures (1173 K, 1223 K, and 1273 K), (b) CO production for two inlet different  $CO_2/CO$  compositions (0.5/0.5 and 0.7/0.3) at 1173 K [4], and (c) syngas production for a cathode inlet gas composition of  $H_2/CO_2/H_2O$  : 0.25/0.25/0.5 at 1083 K [44]. (d) Simulated (lines) and experimentally obtained (dots) [6] PV open circuit voltage (left *y*-axis) and efficiency (right *y*-axis) as a function of the cell temperature. . . . . 128
- 5.5 SOEC performance at reference conditions. (a) The surface-averaged potential (left *y*-axis) and volume-averaged cell and surface-averaged cathode outlet temperatures (right *y*-axis) as a function of the current density. (b) The breakdown of the surface-averaged cell potential into the various overpotentials for varying current densities. (c) The molar fraction of cathode outlet species for varying current densities. (d) The contributions of electro- and thermochemistry to the syngas production for varying current densities. . . . . 131
- 5.6 The carbon deposition boundaries for 5 selected temperatures at 1 atm and their intersections (red dots) with the cathode outlet C-H-O curves for the reference case for various operation current densities. The SOEC surface-averaged temperature and operation current densities at intersections are indicated in red. 132

5.7	(a) J-V curves for SOEC and PV for varying concentrations and corresponding STF efficiency for directly (grey dots) and indirectly (colored dots) coupled PV and SOEC. Energy breakdown for the solar reactor for (b) direct coupling and (c) indirect coupling cases. For (b) and (c), top $x$ axis shows the total solar energy input to the system with $\dot{Q}_{\text{solar,ap}} = 100 \text{ W}$ . . . . .	133
5.8	Three sub-models are considered (dashed black boxes): <i>i</i> ) Receiver model which uses the SOEC cell only as the solar absorber, <i>ii</i> ) the insulated connection pipe with a temperature drop of 300 K, and <i>iii</i> ) tubular SOEC cell model. . . . .	134
5.9	(a) Fluid outlet temperatures under various $\dot{Q}_{\text{solar,ap}}$ , and (b) the STF efficiency for the reference case, case 1, and case 2 with $C_{\text{PV}} = 100$ for both direct and indirect PV - SOEC connections. Fill cycle dots are for direct connection cases, and the filled square dots are for indirect connection cases. . . . .	135
5.10	Temperature profiles for five inlet flow velocities at their maximum achievable current densities for the reference arrangement. The 0 m position on the $z$ -axis represents the fluid inlet position. The SOEC volume-averaged temperature are indicated on the right side of the figure. . . . .	137
5.11	(a) Operation cell potential (thick solid lines) and volume-averaged SOEC temperature (thick dashed lines) as a function of operation current density for various inlet flow velocities (differentiated by the colors), and the $J$ - $V$ curves of the PV cell (thin solid black lines) for selected $C_{\text{PV}}$ . (b) The $\text{H}_2\text{O}$ molar fraction along the cathode-side triple phase boundaries at the cathode-electrolyte interface (solid lines) and channel-cathode interface (dashed lines) for various cathode inlet velocities at their limiting current density with the cathode outlet averaged $\text{H}_2\text{O}$ molar fraction indicated on the bottom left. (c) STF efficiency for the direct (dashed lines) and indirect (solid lines) connections cases for varying flow rates and $C_{\text{PV}}$ . . . . .	138
5.12	(a) $J$ - $V$ curves of the SOEC for the four flow arrangements at reference conditions and $J$ - $V$ curves of the PV for varying $C_{\text{PV}}$ . (b) STF efficiency for the four flow arrangements for varying solar concentrations for the indirect (thick lines) and direct (thin lines) cases. (c) $\text{H}_2/\text{CO}$ molar ration of the product gas at the SOEC cathode outlet for current densities between $300 \text{ A/m}^2$ and $10000 \text{ A/m}^2$ . (d) Temperature profiles along the cathode-side triple phase boundaries at the cathode-electrolyte interface and temperature distribution in the SOEC for the four flow arrangements at $5000 \text{ A/m}^2$ . . . . .	140

## List of Figures

---

- 5.13 (a) STF efficiency as a function of the PV solar concentration for direct (solid lines) and indirect (dashed lines) connection cases under varying current densities, (b) contour plot of the  $R_{\text{HC}}$  at the cathode outlet as a function of various inlet gas compositions ( $\text{H}_2\text{O}/\text{CO}_2$ ) and current densities, and (c) the C-H-O ternary diagram for various cathode inlet composition cases ( $0.125 < \text{H}_2\text{O}/\text{CO}_2 < 8$ ) with changing current densities and for five selected carbon deposition boundaries (for 890 K, 950 K, 1000 K, 1050 K and 1100 K at 1 atm). . . . . 142
- 5.14 Schematic of a possible design of an integrated reactor with two in-series connected SOEC cells (inner cell in dashed red box and outer cell in dashed black box). The two tubular SOEC cells are concentrically arranged. . . . . 144
- 5.15 (a)  $J$ - $V$  curves for the two-cell SOEC stacks and the PVs for three different solar energy inputs ( $\dot{Q}_{\text{solar,ap}} = 125 \text{ W}$ ,  $150 \text{ W}$ , and  $175 \text{ W}$ ) for direct connection cases, and (b) STF efficiencies (solid lines, left  $y$ -axis) and the average stack temperatures (dashed lines, right  $y$ -axis) as a function of the concentration for three different  $\dot{Q}_{\text{solar,ap}}$ . . . . . 145
- 5.16  $\eta_{\text{STF}}$  as a function of solar concentration at PV cell under reference conditions for both direct (black lines) and indirect (red lines) connections for efficiency definition 1 (solid lines) and definition 2 (dashed lines) . . . . . 146
- B.1 Optimal  $\eta_{\text{STF}}$  and corresponding  $\Delta T$  for various  $T_{\text{red}}$  and  $p_{\text{O}_2,1}$  combinations for (a) sweep gassing (scheme (a)), and (b) vacuum pumping (scheme (b)). The solid lines indicate the efficiency at corresponding  $T_{\text{red}}$  and  $p_{\text{O}_2,1}$  for isothermal operation ( $\Delta T=0$ ). The red lines show exemplary performance for a water splitting system at  $p_{\text{O}_2,1} = 1 \text{ Pa}$ . . . . . 158
- B.2 Optimal  $\eta_{\text{STF}}$  and corresponding  $\Delta T$  for various  $T_{\text{red}}$  and  $p_{\text{O}_2,1}$  combinations for (a) scheme (a), and (b) scheme (b) using an ideal mixing arrangement. The solid lines indicate the efficiency at corresponding  $T_{\text{red}}$  and  $p_{\text{O}_2,1}$  for isothermal operation ( $\Delta T=0$ ). . . . . 159
- B.3 Energy balance for scheme (a) at 1 kW solar power input under various working conditions: (a) isothermal cases at  $p_{\text{O}_2,1} = 1 \text{ Pa}$  for varying  $T_{\text{red}}$ , (b) optimal cases at  $T_{\text{red}} = 1800 \text{ K}$  for varying  $p_{\text{O}_2,1}$ , (c) cases at  $p_{\text{O}_2,1} = 1 \text{ Pa}$  and  $T_{\text{red}} = 1800 \text{ K}$  for varying  $\Delta T$ , and (d) optimal cases at  $p_{\text{O}_2,1} = 1 \text{ Pa}$  for varying  $T_{\text{red}}$ . . . . . 160
- B.4 Energy balance for scheme (b) at 1 kW solar power input under various working conditions: (a) isothermal cases at  $p_{\text{O}_2,1} = 1 \text{ Pa}$  for varying  $T_{\text{red}}$ , (b) optimal cases at  $T_{\text{red}} = 1800 \text{ K}$  for varying  $p_{\text{O}_2,1}$ , (c) cases at  $p_{\text{O}_2,1} = 1 \text{ Pa}$  and  $T_{\text{red}} = 1800 \text{ K}$  for varying  $\Delta T$ , and (d) optimal cases at  $p_{\text{O}_2,1} = 1 \text{ Pa}$  for varying  $T_{\text{red}}$ . . . . . 160

B.5	Solar-to-fuel efficiency for isothermal conditions at $p_{\text{O}_2,1} = 10$ Pa and varying $T_{\text{red}}$ and $\varepsilon_g$ , for (a) scheme (a), and (c) scheme (b); and non-isothermal conditions at $p_{\text{O}_2,1} = 10$ Pa and $T_{\text{red}} = 1800$ K for varying $\Delta T$ and $\varepsilon_g$ . The maximal efficiencies for each $\varepsilon_g$ are marked by the dots. . . . .	161
B.6	Solar-to-fuel efficiency as a function of $\Delta T$ for various $\varepsilon_s$ at $p_{\text{O}_2,1} = 10$ Pa and $T_{\text{red}} = 1800$ K for (a) scheme (a), and (b) scheme (b). The optimal cases are indicated by the dots. . . . .	161
C.1	(a) Fluid outlet temperature (black lines) and solar-to-thermal efficiency (red lines) as a function of $\delta_x$ , and (b) composition of heat losses for receiver 1 (solid lines) and receiver 2 (dotted lines). . . . .	163
C.2	(a) Fluid outlet temperature (black lines) and solar-to-thermal efficiency (red lines) as a function of $\delta_x$ , and (b) composition of heat losses for receiver 1 (solid lines) and receiver 2 (dotted lines). . . . .	164
D.1	Technical drawings for the reactor steel frame: (a) the front view showing the water-cooled front and reactor aperture, (b) side view for A-A, and (c) back view of the reactor. . . . .	166
D.2	Bipolar plate design for both cathode and anode side with the channel width of 1.5 mm and the rib width of 0.5 mm (Almus AG). . . . .	167
E.1	Modeling domain and temperature distribution (in K) for an insulated pipe (4 mm in diameter, 5 cm in length). . . . .	174
E.2	The cell voltage breakdown for the reference case and flow 2 with reference case in thin lines and the flow 2 in thick lines. . . . .	175
E.3	Operation current density of the SOEC under various PV solar concentrations and molar ratios of $\text{H}_2\text{O}/\text{CO}_2$ at the cathode inlet for indirect connection cases. . . . .	175
E.4	Contour plots for (a) the WGSR contributions, (b) electrochemical hydrogen generation, (c) electrochemical CO generation, and (d) the $\text{H}_2$ and CO production difference due to electrochemical reactions under various molar ratios of $\text{H}_2\text{O}/\text{CO}_2$ at the cathode inlet and current densities. The $R_{\text{HC}} = 2$ is indicated in solid black line and the dashed line is for the cases when the electrochemical generation of $\text{H}_2$ and CO are equal. . . . .	176
E.5	SOEC average temperature as a function of current density under various inlet ratios of $\text{H}_2\text{O}/\text{CO}_2$ (differentiated by colors). . . . .	177





# List of Tables

1.1	Model parameters and dimensions used in the SOEC model. . . . .	14
1.2	Values for a monocrystalline PV module (Sunpower SPR-210-BLK-U) [7]. . . . .	17
1.3	Parameters and parameter ranges considered in the techno-economic model for the three systems. . . . .	22
2.1	Reference case parameters used for the comparison of the five different models of the ceria cycling. . . . .	45
3.1	Summary of $\theta_{\text{dry}}$ and $\delta_{\text{lf}}$ for different flow patterns in horizontal tube [8] . . . . .	73
3.2	Parameters and conditions used in Lobon et al. [2] case 1 . . . . .	78
3.3	Locations of the thermocouples for the solar receiver tested at DLR. . . . .	80
3.4	Reference case parameters used for the comparison of the five different models of the ceria cycling. . . . .	82
3.5	Tube configurations for changing tube diameters, for receiver 1 and receiver 2 .	90
3.6	Parameters used for the double helical tube receiver modeling . . . . .	94
5.1	Modeling parameters for electrochemical reactions [9]. . . . .	119
5.2	Reference geometrical and microstructure parameters for the SOEC membrane- electrolyte assembly. . . . .	124
5.3	Reactor geometry, anode and cathode inlet conditions, and irradiation concen- tration for the reference conditions. . . . .	130
5.4	The intersection points for 7 selected inlet $\text{H}_2\text{O}/\text{CO}_2$ ratios and 4 carbon deposi- tion boundaries. . . . .	143
A.1	Definition of energy fractions for all three systems. . . . .	156
E.1	Thermal conductivities. . . . .	169
E.2	Heat capacities. . . . .	170
E.3	Densities . . . . .	170
E.4	Intrinsic electrical conductivities. . . . .	170
E.5	Parameters for the PV cell model [10] . . . . .	171
E.6	SOEC model validation for hydrogen production [3, 11]. . . . .	172

## List of Tables

---

E.7 SOEC model validation for CO production [4]. . . . .	173
E.8 SOEC model validation for syngas production [5]. . . . .	173

# Nomenclature

## Latin symbols

$a$	modified ideality factor
$a_{td}$	thermal diffusivity, $m^2/s$
$A$	area, $m^2$
$B$	permeability, $m^2$
$c_p$	specific heat capacity, $J/mol/K$
$C$	cost, \$
$CR$	solar concentration for receiver
$C_{ap}$	solar concentration at the aperture
$C_{PV}$	solar concentration for PV
$d$	diameter, $m$
$D_{ij}$	binary diffusivity, $m^2/s$
$D_k$	Knudsen diffusivity, $m^2/s$
$D^{mk}$	mixture-averaged binary diffusivity, $m^2/s$
$DHI$	diffuse horizontal irradiance, $W/m^2$
$DNI$	direct normal irradiance, $W/m^2$
$E$	Nernst potential, $V$
$E_{act}$	activation energy, $kJ/mol$
$E_g$	bandgap energy, $eV$
$E_{tcm}$	two-phase convection multiplier
$F$	Faraday constant, $96485.3 C/mol$
$F_{ij}$	view factor between surface $i$ and $j$
$Fr$	Froude number

## Nomenclature

---

$f$	fraction
$f_w$	water utilization factor
$g$	acceleration of gravity, $\text{m/s}^2$
$HHV$	higher heating value, $\text{J/mol}$
$h$	molar enthalpy, $\text{J/mol}$
	heat transfer coefficient, $\text{W/m}^2/\text{K}$
$H$	height, $\text{m}$
$h_{lg}$	latent heat, $\text{kJ/kg}$
$i$	interest rate
$I$	current, $\text{A}$
$I_0$	diode reverse saturation current, $\text{A}$
$I_d$	identity matrix
$j_m$	mass flux, $\text{kg/m}^2/\text{s}$
$J$	current density, $\text{A/m}^2$
	radiosity, $\text{W}$
$J_0$	exchange current density, $\text{A/m}^2$
$k$	Boltzmann's constant, $1.38 \cdot 10^{-23} \text{ J/K}$
	thermal conductivity, $\text{W/m/K}$
$K_{eq}$	reaction equilibrium constant
$n_{tot}$	total number of particles per volume
$L$	length, $\text{m}$
$\dot{m}$	mass flow rate, $\text{kg/day}$
$\dot{m}''$	mass flux, $\text{kg/m}^2/\text{s}$
$M$	molar mass, $\text{g/mol}$
MPPT	maximum power point tracker
$\dot{n}$	molar flow rate, $\text{mol/s}$
$n_1$	ideality factor
$n_{tot}$	total number of particles per volume
$N$	molar flux, $\text{mol/m}^2/\text{s}$
Nu	Nusselt number

$N_s$	number of cells in series
OCV	open circuit voltage, V
$p$	pressure, Pa, bar
$p_r$	reduced pressure
$P$	power, J
	tube perimeter, m
	probability
Pr	Prandtl number
$q$	electron charge ( $1.6 \cdot 10^{-19}$ C)
$q'''$	heat sink, W/m <sup>3</sup>
$q_w$	heat flux, W/m <sup>2</sup>
$Q$	heat, J
$\dot{Q}$	heat rate, W
$Q_M$	mass source, kg/m <sup>3</sup> /s
$r$	radius, m
$r_{ij}$	distance, m
$R$	universal gas constant, 8.3145 J/mol/K
	reaction rate (mol/m <sup>3</sup> /s)
Ra	Rayleigh number
$R_{HC}$	ratio of produced molar ratio of H <sub>2</sub> /CO
$R_{HN}$	ratio of $DHI$ to $(DNI + DHI)$
$R_s$	series resistance, $\Omega$
$R_{sh}$	shunt resistance, $\Omega$
$R_{SRR}$	reaction rate of steam reforming reaction, mol/m <sup>3</sup> /s
$R_{WGSR}$	reaction rate of water-gas shift reaction, mol/m <sup>3</sup> /s
$s$	entropy, W/m <sup>2</sup> /K
$S$	current source, A/m
$S_{bsf}$	boiling suppression factor
$t$	thickness, $\mu$ m, mm
$t_{lt}$	life time, year

## Nomenclature

---

$T$	temperature, K
$u$	fluid velocity, m/s
$v$	speed, m/s
$V$	potential, V
$W$	work rate, W
	width, m
$W_{CE}$	water conversion extent
$We$	Weber number
$x, y$	coordinate direction, m
$x_{H_2}$	hydrogen productivity
$x_g$	vapor quality
$y_i$	molar fraction of species $i$
$Z$	coordinate number

## Greek symbols

$\alpha_{Isc}$	temperature coefficient for short circuit current, A/K
$\beta$	thermal expansion coefficient, 1/K
$\beta_{Voc}$	temperature coefficient for open circuit voltage, V/K
$\gamma$	pre-exponential factor, A/m <sup>2</sup>
$\delta$	standard deviation, m
	visibility
$\delta_{lf}$	liquid film thickness, m
$\Delta g$	Gibbs free energy of formation, J/mol
$\Delta h$	enthalpy of formation, J/mol
$\Delta s$	entropy of reaction, J/mol/K
$\Delta\delta$	non-stoichiometric coefficient difference
$\Delta$	non-stoichiometric coefficient
$\varepsilon$	emissivity
	heat recovery effectiveness
	porosity
$\varepsilon_g$	void fraction

$\nu$	kinematic viscosity, $\text{m}^2/\text{s}$
$\xi$	tortuosity
$\xi_{\text{ph}}$	liquid-vapor interfacial friction factor
$\zeta$	phase number fraction
$\rho$	density, $\text{kg}/\text{m}^3$
$\sigma$	Stefan-Boltzmann constant, $(5.67 \cdot 10^{-8} \text{ W}/\text{m}^2/\text{K})$
$\sigma_{\text{t}}$	surface tension, $\text{N}/\text{m}$
$\eta$	efficiency
	overpotential, $\text{V}$
$\theta$	tube inclination angle, $\text{rad}$
$\theta_{\text{dry}}$	dry angle, $\text{rad}$
$\theta_{\text{strat}}$	stratified angle, $\text{rad}$
$\mu$	dynamic viscosity, $\text{kg}/\text{m}/\text{s}$
$\tau_{\text{w}}$	shear stress, $\text{Pa}$
$\omega$	mass fraction

### Subscripts/Superscripts

0	reference condition
a	anode
act	activation
amb	ambient
anode	anode
ap	aperture
av	average
ca	cathode
cav	cavity
cb	convective boiling
ce	conversion extend
conc	concentration
cond	conduction
cool	cooling

## Nomenclature

---

conv	convection
crit	critical value
CSP	concentrated solar power
CEI	channel-electrode interface
d	direct
dry	dry-out
DC-DC	DC-DC converter
DNB	departure from nucleate boiling
e	electrolyte
eff	effective value
el	electrolyzer
elec	electrical conducting phase
electric	electricity
g	gas
HE	heat exchanger
$i,j$	species index
in	inlet
	inner
ind	indirect
insu	insulation material
invest	investment
ion	ionic conducting phase
IA	intermittent flow to annular flow
$k$	Knudsen diffusion
l	liquid
L	light
max	maximum value
Mg	magnesium
mp	maximum power
min	minimum value



mist	mist flow
nb	nucleate boiling
nc	natural convection
noct	nominal cell temperature value
oc	open circuit
op	operation
ox	oxidation
pump	pumping
pr	production
PV	photovoltaics
rerad	reradiation
rad	radiation
react	reaction
red	reduction
re	receiver
rev	reversible
R	reaction
sc	short circuit
scavenger	chemical scavenger
strat	stratified flow
SC	short circuit
SRR	steam reforming reaction
STE	solar-to-electricity
STF	solar-to-fuel
STT	solar-to-thermal
tn	thermoneutral
TTE	thermal-to-electricity
TPB	triple-phase boundary
wavy	stratified-wavy flow
WGSR	water-gas shift reaction



# Introduction

The global energy consumption is largely met by fossil fuels, accounting for more than 80% of total primary energy demand [12]. The dominance of fossil energy carriers in our current energy economy is associated with at least three pressing challenges: *i*) limited and non-renewable reserves, *ii*) increase in emission and environmental pollution (CO<sub>2</sub> from fossil-fuel accounts for 90% of energy-related emissions), and *iii*) supply insecurity and geopolitical tensions. These problems can be alleviated by increasing the price-competitive renewable energy share in the current energy market. Due to its abundant, renewable, and clean features, solar energy is one of the top candidates to tackle energy issues related to fossil fuels (e.g. limited reserves, pollution, and CO<sub>2</sub> emissions). In one single day, the earth receives enough solar energy to full fill the world's energy requirements for twenty years (based on global energy consumption on 2008) [12]. The processing of fuels by utilizing solar energy is one promising pathway to compete with conventional fossil fuels. One chemical route is to electrochemically/thermochemically split H<sub>2</sub>O and CO<sub>2</sub> into H<sub>2</sub> and CO, a mixture called syngas, by using concentrated solar energy. The syngas can then be converted into liquid fuels through a conventional Fischer-Tropsch process. Solar fuel technologies can not only produce renewable fuels, which are environmentally uncritical but also compatible with the existing energy infrastructure.

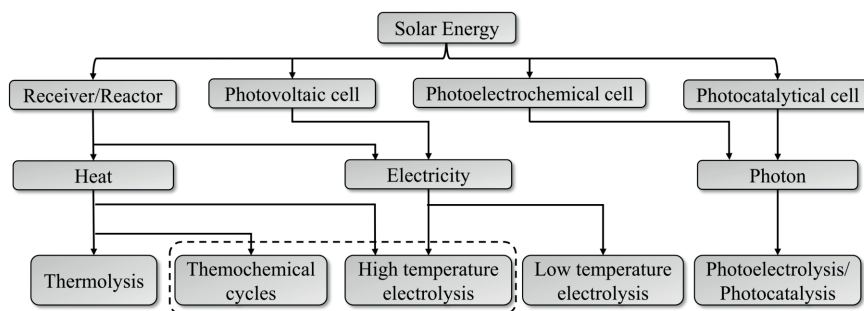


Figure 1 – General non-biological solar-to-fuel conversion pathways.

General non-biological routes of converting solar energy into fuels are shown in figure 1.

## Introduction

---

High-temperature routes includes direct thermolysis of water [13], thermochemical cycles (TCC) [14] and high-temperature electrolysis (HTE) [15] (dashed line box in figure 1 for the latter two routes). Direct thermolysis utilizes solar energy for the direct dissociation of H<sub>2</sub>O and CO<sub>2</sub> (eqs.1 and 2). This is challenging since it needs temperatures above 3000K [13] for H<sub>2</sub>O splitting and above 2700K [16] for CO<sub>2</sub> splitting to ensure a reasonable dissociation convergence. In addition, direct thermolysis faces the difficulty in high-temperature products separation of a possible explosive mixture.



To circumvent these drawbacks, TCC have been proposed [17, 18, 19]. Particularly two-step, non-volatile metal oxide-based cycles show promise in avoiding gas separation issues, working at lower temperatures compared to direct thermolysis, enabling relatively simple design and operation, and theoretically achieving high solar-to-fuel efficiencies [20, 21, 22, 23]. Ceria non-stoichiometric redox cycling has attracted interest due to its non-volatile characteristics even at high operating temperature, fast kinetics causing high hydrogen generation rates, theoretically high solar-to-fuel efficiencies [22, 23, 24], and practical demonstration of reasonable efficiencies (up to 5.25%) in working prototypes [25, 26, 27, 28]. The reduction step (eq. 3) of the ceria-based two-step thermochemical cycle requires high temperature (1400 K to 2100 K) and low partial pressure of oxygen (< 10 Pa) environment to ensure a reasonable conversion. The reduced ceria is then oxidized exothermically (eqs. 4 and 5) with H<sub>2</sub>O and CO<sub>2</sub> for H<sub>2</sub> and CO generation at typical temperature range of 700 K - 1100 K. The low partial pressure of oxygen for the reduction step is usually achieved by inert gas sweeping which requires intensive energy input for bringing the sweep gas temperature up to the reduction temperature. Heat recovery effectiveness of 0.955 is required to achieve a solar-to-fuel efficiency of 10%. Another widely proposed route is the use of vacuum pump to reduce the partial pressure of oxygen in the reactor [29]. The solar-to-fuel efficiency is largely dependent on the pump electrical efficiency (pump efficiency of 40% at 100 kPa and 5% at 1 Pa [30]). Hence, the identification of optimal oxygen partial pressure reduction methods is important for the engineering of the reactor for solar fuel processing.



Apart from thermochemical methods, HTE can also produce H<sub>2</sub> and CO at high efficiency

[31, 32, 33] while operating at significantly reduced temperature (800 K - 1100 K) and less stringent oxygen partial pressure requirement (air can be used in the anode). Compared to low-temperature electrolysis (e.g. proton exchange membrane electrolyzer), HTE has the advantage of operating at reduced electrical potentials and, consequently, enhanced efficiency. This potential reduction results from elevated temperatures which reduce the equilibrium potential, reaction overpotential, and ohmic losses in the solid electrolyte [34]. In HTE systems, H<sub>2</sub>O and CO<sub>2</sub> molecules are split into H<sub>2</sub>, CO, and oxygen ions in the porous cathode (eqs. 6 and 7), oxygen ions are transported through the electrolyte to the anode and further oxidized into O<sub>2</sub> and electrons (eq. 8).



Solar receiver is one of the key components in HTE systems significantly influencing the overall system efficiency. In this thesis, special attention is paid to the model, design, and optimization of solar receivers for the direct generation of high-temperature steam for solar-driven HTE systems. Tubular cavity receivers are the most commonly used indirectly irradiated receivers which can withstand high pressure and can be employed with gas/liquid working fluid [35, 36, 37, 38]. Compared to the indirectly irradiated receivers with a separate chamber for fluids heating, tubular receivers have better heat transfer, more uniform temperature distribution, as well as being more flexible in design. Numerical models offer an effective pathway for the characterization and quantification of the optical, thermal, and fluid flow behavior of receivers [37, 39, 40, 41, 42, 43]. When steam is used as the working fluid (concentrated solar power systems) or as the reactant in high-temperature systems (for example, TCC and HTE systems), the understanding of the complex two-phase flow boiling process inside the absorber tubes of the direct steam generation receiver is important for identifying local hot spots, and designing and predicting receiver performance.

This thesis is performed in the framework of the project SOPHIA (solar integrated pressurized high-temperature electrolysis). SOPHIA project is a collaborative project involving partners from HyGear B.V. (HYG, Netherland), HTceramix SA (HTc, Switzerland), Commissariat à l'Energie Atomique et aux Energies Alternatives (CEA, France), Deutsches Zentrum für Luft- und Raumfahrt (DLR, Germany), VTT Technical Research Centre of Finland (VTT, finland), ENGIE (ENGIE, France), and SOLIDpower S.P.A. (SP, Italy).

In this thesis, thermodynamic modeling frameworks are developed for two high-temperature solar fuel processing routes (HTE and TCC) allowing for the quantification of systems' perfor-

mance under various operation conditions and system integrations as well as for the comparison between these two high-temperature routes. In particular, the HTE route is investigated for its economic competitiveness considering and integrating various solar technologies for heat and electricity supply. The solar receiver for direct steam generation for HTE systems is modeled and optimized under various geometrical designs and operational conditions. Based on the modeling results, a compact solar reactor is designed, fabricated, and experimentally demonstrated which couples a double-helical tube solar absorber and a 16-cell SOEC stack in one single reactor for the reduction of heat losses related to high-temperature reactants transport between the solar absorber and the stack. To further reduce the transmission losses, a novel integrated solar reactor concept by using a tubular SOEC cell, at the same time, as the solar absorber is proposed and optimized based on an in-house multi-physics model.

In chapter 1, different strategies for the incorporation of solar energy are considered, distinguished by the use of different technologies to provide solar power and heat: *i*) thermal approaches (system 1) using concentrated solar technologies to provide heat and to generate electricity through thermodynamic cycles, *ii*) electrical approaches (system 2) using photovoltaic technologies to provide electricity and to generate heat through electrical heaters, and *iii*) hybrid approaches (system 3) utilizing concentrated solar technologies and photovoltaics to provide heat and electricity. Based on an in-house techno-economic model, the impact of operating temperature, pressure, current density, heat recovery effectiveness, direct normal irradiance, conversion extent, and concentration ratio were investigated and discussed. The model can be used for qualitative techno-economic performance prediction for different solar integration schemes under various operation conditions. Material from this chapter has been published in [44].

In chapter 2, a thermodynamic model is developed for five thermochemical redox cycle designs to investigate the effects of working conditions on the fuel production. The focus is paid on the influence of approaches to reduce the partial pressure of oxygen in the reduction step, namely by mechanical approaches (sweep gassing or vacuum pumping), chemical approaches (chemical scavenger), and combinations thereof. The results indicated that the sweep gas schemes work more efficient at non-isothermal than isothermal conditions, and efficient gas phase heat recovery and sweep gas recycling was important to ensure efficient fuel processing. The vacuum pump scheme achieved best efficiencies at isothermal conditions, and heat recovery was less essential at non-isothermal conditions. The use of oxygen scavengers combined with sweep gas and vacuum pump schemes further increased the system efficiency. The comparison between two high-temperature solar fuel production routes (i.e. high-temperature electrolysis vs. thermochemical redox cycle) is discussed at the end of the chapter. This study can be used to predict the performance of solar-driven non-stoichiometric redox cycles and further offers quantifiable guidelines for system design and operation. A

quantified comparison between TCC and HTE technologies is presented showing that HTE can achieve solar-to-fuel efficiency identical to TCC while operating at a reduced temperature and less stringent oxygen partial pressure environment. Material from this chapter has been published in [45].

In chapter 3, a coupled heat and mass transfer model of cavity receivers with tubular absorbers to guide the design of solar-driven direct steam generation is presented. The numerical model consists of a detailed 1D two-phase flow model of the absorber tubes coupled to a 3D heat transfer model of the cavity receiver. The absorber tube model simulates the flow boiling phenomena inside the tubes by solving 1D continuity, momentum, and energy conservation equations based on a control volume formulation. The Thome-El Hajal flow pattern maps are used to predict liquid-gas distributions in the tubular cross-sections, and heat transfer coefficients and pressure drop along the tubes. The heat transfer coefficient and fluid temperature of the absorber tubes' inner surfaces are then extrapolated to the circumference of the tube and used in the 3D cavity receiver model. The 3D steady-state model of the cavity receiver coupled radiative, convective, and conductive heat transfer. The complete model is validated with experimental data and used to analyze different receiver types and designs made of different materials and exposed to various operational conditions. The proposed numerical model and the obtained results provide an engineering design tool for cavity receivers with tubular absorbers (in terms of tube shapes, tube diameter, water-cooled front), support the choice of best-performant operation (in terms of radiative flux, mass flow rate, pressure), and aid in the choice of the component materials. Based on this study, a double-helical tube reactor for HTE is designed and its thermal behavior is studied. Material from this chapter has been published in [46].

In chapter 4, the design of a 1 kW<sub>th</sub> compact solar reactor which couples a double helical tube solar absorber and a 16-cell SOEC stack in one single reactor is presented. The two major components, i.e., the double helical receiver (solar absorber together with steel frame supported insulation) and the SOEC stack are designed, fabricated, and experimentally characterized separately (campaign 1 and 2). The two components are then coupled to form the compact reactor (campaign 3). The test for the compact reactor is performed under the high flux solar simulator (HFSS) at EPFL. Experimental setups for the three campaigns are introduced in detail. The experimental results are reported. The solar thermal efficiency of the solar absorber, the electrical efficiency of the stack, and the final solar-to-fuel efficiency are quantified based on the experimental data which shows a successful demonstration for the proof-of-concept of the compact solar reactor.

In chapter 5, an integrated solar reactor concept is presented. In this design, a tubular SOEC is utilized as the solar absorber to further minimize transmission losses and to reduce the system complexity. In addition, a III-V based PV cell is placed on the water-cooled reactor front

## Introduction

---

under concentrated solar irradiation as the electricity source for the SOEC. The performance of the proposed solar reactor is investigated based on an in-house 2D numerical model accounting for charge transfer in the membrane-electrolyte assembly, electrochemical and thermochemical reactions at the electrodes' reaction sites, species and fluid flow in the fluid channels and electrodes, and heat transfer for all reactor components. The solar-to-fuel efficiency, carbon deposition conditions, and two PV-EC electrical coupling strategies are discussed under various operation conditions and designs. In addition, the integrated solar reactor shows improved performance compared to non-integrated HTE system. Material from this chapter is in preparation for a journal publication in [47].



# 1 Techno-economic modeling of high-temperature electrolysis systems<sup>1</sup>

In this chapter, a techno-economic analysis of solar-driven high-temperature electrolysis systems used for the production of hydrogen and synthesis gas is presented. We consider different strategies for the incorporation of solar energy, distinguished by the use of differing technologies to provide solar power and heat: *i*) thermal approaches (system 1) using concentrated solar technologies to provide heat and to generate electricity through thermodynamic cycles, *ii*) electrical approaches (system 2) using photovoltaic technologies to provide electricity and to generate heat through electrical heaters, and *iii*) hybrid approaches (system 3) utilizing concentrated solar technologies and photovoltaics to provide heat and electricity.

## 1.1 System description

Design guidelines for optimized concentrated solar-driven HTE systems have been proposed based on a system process model [48, 49]. These systems suffer from a high hydrogen production price because of the high capital cost of solar concentrating systems [50]. Techno-economic models of HTE systems coupled with concentrated solar technologies using various coupling strategies are required to provide performance and cost estimates as well as to provide guidance for the design and optimization of cost-competitive systems. PV power generation is less costly and simpler (due to the absence of a solar tower and power block) than CSP generation. The introduction of PV into HTE systems shows the potential to reduce fuel production costs. Commercial polycrystalline Si-based PV shows solar-to-electricity efficiencies above 15%, and advanced PV technologies (multi-junction, III-V materials) can attain up to 42% [51]. A techno-economic analysis has shown that a hybrid HTE system (using parabolic trough concentrators for reactant heating and monocrystalline PV panels for electricity), with an optimized heat recovery system, leads to cheaper hydrogen production costs compared

---

<sup>1</sup>Material from this chapter has been published in: M. Lin and S. Haussener, “Techno-economic modeling and optimization of solar-driven hightemperature electrolysis systems,” *Sol. Energy*, vol. 155, pp. 1389–1402, 2017. [44]

to a concentrated solar technology driven HTE system [32]. This analysis used an outlet steam temperature for the parabolic trough concentrator of 593 K, and further heating to the operation temperature by the electrolyzer exhaust was needed requiring exothermic operation of the electrolyzer, increasing electricity demand. No details on tradeoffs between the benefits of electrolyzer performance and enhanced re-radiation losses in the solar receiver at higher operating temperature were given. More sophisticated HTE system analysis is required in order to quantify the performance and cost response of the system in varying operating conditions and for alternative solar coupling approaches.

Two relatively mature technologies are used for the design of HTE systems: *i*) concentrated solar technologies, and *ii*) photovoltaic technologies. Based on these technologies, three solar-driven HTE systems are sketched, illustrated in figure 1. System 1 is based on solar thermal input only, system 2 is based on solar electricity input only, and system 3 is based on a hybrid of solar heat and solar electricity inputs. In system 1, concentrated solar radiation is the source which heats and superheats the reactants, as well as heating a heat transfer fluid to drive a thermodynamic cycle for electricity generation. Two independent receivers are considered, differentiated by the working pressure: receiver 1 for the reactant heating (steam generation, and steam and CO<sub>2</sub> (super-) heating) works at low pressure (1 - 25 atm), and receiver 2 for pressurized steam generation works at a high pressure (50 - 70 atm). Receiver 1 feeds the electrolyzer, while receiver 2 feeds a Rankine cycle with two-stage regeneration. The feed water for receiver 1 is combined with recycled water from the cathode exhaust and pumped into mixer 1, where it is mixed with feed CO<sub>2</sub>/H<sub>2</sub>/CO gases and recycled CO<sub>2</sub> from compressor 2. The mixture (H<sub>2</sub>, CO, H<sub>2</sub>O, and CO<sub>2</sub>) is preheated in heat exchanger 1 using the recovered heat from the cathode exhaust before it enters receiver 1, where it is heated to 5 K below the targeted operating temperature of the electrolyzer,  $T_{el}$ . The electrical heater 1 is used to adjust and stabilize the fluid temperature to  $T_{el}$ . The reactant mixture is fed to the electrolyzer's cathode, where steam/CO<sub>2</sub> is split into H<sub>2</sub>/CO with conversion extent,  $W_{re}$ . The high-temperature exhaust (a mixture of H<sub>2</sub>, CO, H<sub>2</sub>O, and CO<sub>2</sub>) is recovered in heat exchanger 1, condensed in the condenser (splitting liquid water from the gases), and separated into pure CO<sub>2</sub> (piped into mixer 2 for recycling) and H<sub>2</sub>/CO streams. The H<sub>2</sub>/CO is further separated into two parts: *i*) a small fraction of hydrogen/CO (5%/5%) is injected into mixer 1 to prevent oxidation at the cathode electrode and to maintain an effective electrolysis reaction [52], and *ii*) the remaining fraction is compressed by a two-stage compressor (storage pressure 30 atm) before being stored in a hydrogen/synthesis gas storage tank. For the anode, a sweep gas (air) is used to evacuate the produced oxygen. An air compressor pumps the air into heat exchanger 2 for preheating by recovering heat from the anode exhaust (air with produced oxygen). The preheated air is heated up in receiver 1 to 5 K below  $T_{el}$  and then stabilized at  $T_{el}$  by electrical heater 2. A Rankine cycle with two-stage regeneration is considered, driven by a direct steam generation solar receiver (receiver 2). The Rankine cycle incorporates a boiler and superheater

and provides the electricity to drive the electrolyzer, pumps, and compressors. The electricity demand for the mixers and splitters is neglected.

System 2 is similar to system 1 with regards to the cathode and anode fluid preheating, product condensation, separation, storage, and electrolyzer operation. However, the reactant heating is solely accomplished by electrical heaters driven by the electricity generated by the PV panels. The electricity demand of the electrolyzer, pumps, and compressors is also met by PV electricity. System 3 is also similar to system 1 with regards to the cathode and anode fluid preheating, product condensation, separation, storage, and electrolyzer operation. However, the reactant heating is achieved by concentrated solar heat absorbed in a receiver (similar to system 1) and the electricity demand is met by PV panels (similar to system 2).

The scheme for the production of hydrogen only, or just CO, is obtained by removing CO<sub>2</sub>/CO or H<sub>2</sub>O/H<sub>2</sub> (together with the removal of the pump and mixer 1), respectively (figure 1.1).

Heat storage or electricity storage components were not considered in any of the systems. The continuous production of fuel can be obtained with the current system designs without any need for additional heat or electricity storage components. Namely, the produced fuels – inherently stored energy – can be continuously released from the compressed fuel storage tank independent of the transient and cyclical solar irradiation. Our solar HTE system stores solar energy directly in the chemical bonds of the products, making additional storage not compulsory for continuous fuel delivery. The use of additional storage technologies (such as heat storage for systems 1 or 3, or electricity storage for systems 2 and 3) could result in additional equipment investment cost. However, it is worth to mention that the thermal storage system will become important when studying the dynamic behavior of the system. The capacity factor can be designed at a higher value when a TES considered which could lead to the reduced size of equipment (e.g. electrolyzer stack). Moreover, the TES can ensure a smaller shut-down/start-up frequency of the system leading to the more reliable operation and smaller equipment degradation rates (especially for electrolyzer stack).

For simplicity, degradation of the components were not accounted, including heliostats and receiver(s) for system 1 and system 3, PV panels for system 2 and system 3, and electrolyzer for all three systems. The electrolyzer will most likely suffer from the most severe degradation, however, it will similarly affect all three systems and therefore not affect the trends and conclusions of the study. In addition, our model only predicted the yearly-averaged system performance in which the impact of daily irradiation variation was not discussed. These two assumptions lead to underestimation of the hydrogen price and to loss of the dynamic plant operational information. With all the assumptions made in this study, the use of this model for absolute quantitative prediction and design must be carefully considered. The trend of the system behaviors as well as the qualitative comparison among various solar energy integration

strategies can be well captured which is one of the major focus of this study.

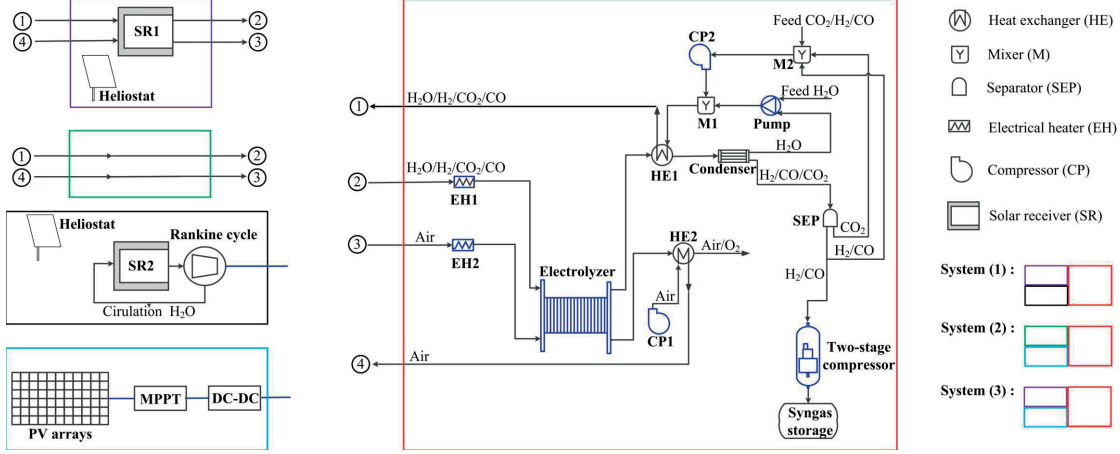


Figure 1.1 – Flowchart of the three systems, constructed with five different sub-components: electrolyzer and auxiliaries (red block), concentrated solar heating system (purple block), fluid connection system (green block), concentrated solar power system (black block), and PV system (blue block). System 1 represents the thermal-only system using concentrated solar technology to provide both heat and electricity. System 2 represents the electricity-only system using PV technology as the only source for both heat and electricity. System 3 represents the hybrid heat-electricity system using concentrated solar technologies and PV providing solar heat and electricity, respectively. The black arrows indicate mass flow and energy streams, the blue lines indicate electricity streams, and the blue colored components are electricity consuming devices connected to the CSP or PV systems.

## 1.2 Governing equations and methodology

### 1.2.1 Electrolyzer performance model

The electrolyzer stack considered in this study is composed of planar solid oxide electrolysis cells (SOECs) connected in parallel. A representative SOEC model is illustrated in figure 2 and includes a cathode, an anode, an electrolyte, and gas channels. In the SOEC, the gas mixture ( $\text{H}_2\text{O}$ ,  $\text{CO}_2$ ,  $\text{H}_2$ , and  $\text{CO}$ ) flows into the cathode channel, while the sweep gas (air) passes through the anode channel to remove the generated  $\text{O}_2$ . In the porous cathode,  $\text{H}_2\text{O}$  and  $\text{CO}_2$  diffuse through the porous electrode toward the catalysts at the cathode-electrolyte interface (considered the triple-phase-boundary (TPB)), where  $\text{H}_2\text{O}$  and  $\text{CO}_2$  molecules are split into  $\text{H}_2$ ,  $\text{CO}$ , and oxygen ions according to eqs. 6 and 7.

The produced  $\text{H}_2$  and  $\text{CO}$  are collected at the cathode gas channel outlet. The generated oxygen ions are transported through the electrolyte to the anode for the oxidation and the production of oxygen according to eq. 8:

The produced oxygen is swept away by air. For the synthesis gas production, the competing thermochemical water-gas shift reaction (WGSR) at the porous cathode is considered:

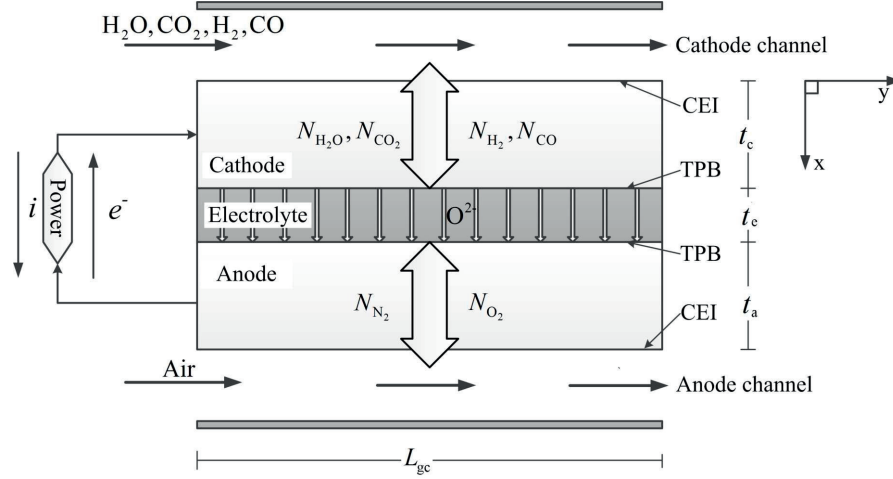


Figure 1.2 – Schematic of a planar SOEC for the synthesis gas production. The reactant mixture ( $\text{H}_2$ ,  $\text{CO}$ ,  $\text{H}_2\text{O}$ , and  $\text{CO}_2$ ) passes through the cathode channel and diffuses into the cathode towards the TPB. At the anodic channel, air removes the generated  $\text{O}_2$ . The x-direction is the direction of gas diffusion in the porous electrodes, and the y-direction is the direction of flow in the channels. The required power is provided either by CSP (system 1) or PV (systems 2 and 3).

A quasi 2-dimensional model of the species transport and mass conservation in the electrolyzer cell was developed. The model solves species transport in 1D in the gas channels (along the flow direction,  $y$ ) and in the porous electrodes (transverse to the flow direction,  $x$ ). The isothermal 1D channel model for the cathode and anode sides assumes plug flow, only considering convective transport in the flow direction, while neglecting species transport in the axial direction and pressure drops in the channel. The continuity equation,

$$\frac{d\dot{n}_i}{dy} = W_{gc} N_{i,CEI}, \quad i = 1 - n_{\text{species}}, \quad (1.2)$$

is solved along the anodic and cathodic flow channels, with representing the molar flow rate of species  $i$  ( $n_{\text{species}} = 2$  for the anode,  $n_{\text{species}} = 4$  for the cathode),  $W_{gc}$  the width of the gas channel, and the flux of species  $i$  at the gas channel-electrode interface (CEI) as calculated by the isothermal 1D porous electrode model. This model uses the dusty-gas model (DGM) for the species transport [53, 54], and the mass conservation equation accounting for WGSR:

$$\frac{dN_i}{dx} = R_{\text{WGSR}}, \quad i = 1 - n_{\text{species}}, \quad (1.3)$$

$$\frac{\dot{N}_i}{D_{i,k}^{\text{eff}}} + \sum_{j \neq i}^n \frac{y_j \dot{N}_i - y_i \dot{N}_j}{D_{ij}^{\text{eff}}} = -\frac{p}{RT} \frac{dy_i}{dx} - \frac{y_i}{RT_{\text{el}}} \left( 1 + \frac{Bp}{\mu D_{i,k}^{\text{eff}}} \right) \frac{dp}{dx}, \quad i = 1 - n_{\text{species}}, \quad (1.4)$$

where  $y_i$  is the molar fraction of species  $i$ ,  $\varepsilon$  the porosity of the electrode,  $R_{\text{WGSR}}$  the reaction rate of WGSR predicted by [55, 56, 57],  $D_{ij}^{\text{eff}}$  the effective binary diffusion coefficient of species  $i$  and  $j$ ,  $D_{i,k}^{\text{eff}}$  the effective Knudsen diffusion coefficient of species  $i$ ,  $\dot{N}_i$  the species flux, and  $B$  the electrode permeability. The binary diffusion coefficients are calculated based on Chapman-Enskog theory, the Knudsen diffusion coefficients based on the Knudsen theory, and the diffusivities corrected by porosity-tortuosity terms to account for the porous media (effective diffusivities). The two 1D models (channel model and electrode model) are coupled through the CEI boundary. At the cathodic TPB, the molar fluxes of the species are calculated according to the current densities applied at this boundary:

$$\begin{aligned} \dot{N}_{\text{H}_2}|_{x=d_c} &= -\frac{J_{\text{H}_2}}{2F}, \quad \dot{N}_{\text{H}_2\text{O}}|_{x=d_c} = \frac{J_{\text{H}_2\text{O}}}{2F}, \\ \dot{N}_{\text{CO}}|_{x=d_c} &= -\frac{J_{\text{CO}}}{2F}, \quad \dot{N}_{\text{CO}_2}|_{x=d_c} = \frac{J_{\text{CO}_2}}{2F}. \end{aligned} \quad (1.5)$$

The anodic TPB provides the boundary condition for the  $\text{O}_2$  flux as:

$$\dot{N}_{\text{O}_2}|_{x=d_c+d_e} = -\frac{J_{\text{CO}} + J_{\text{H}_2}}{4F}. \quad (1.6)$$

The current densities in eqs. 1.5 – 1.6 are calculated based on the developed isothermal, quasi 1-dimensional electrochemistry model of the SOEC. This model predicts the applied potential,  $V_{\text{el}}$ , under various working conditions for a given electrode current density,  $J_{\text{el}}$ . This model was locally solved along the channel ( $y$ -direction) using the species concentrations calculated by the quasi 2D species transport models, eqs. 1.2 – 1.4. In this model, the equilibrium voltage was considered,  $E$ , and the activation and ohmic overpotentials,  $\eta_i$ , resulting in the required SOEC voltage:

$$V_{\text{el}} = E + \eta_{\text{act,c}} + \eta_{\text{act,a}} + \eta_{\text{ohmic}}. \quad (1.7)$$

$E$  was predicted using Nernst's equation, considering concentration overpotentials [58]:

$$\begin{aligned} E_{\text{H}_2} &= E_{0,\text{H}_2} + \frac{RT_{\text{el}}}{2F} \ln \frac{p_{\text{H}_2}^{\text{TPB}} (p_{\text{O}_2}^{\text{TPB}})^{1/2}}{p_{\text{H}_2\text{O}}^{\text{TPB}}}, \\ E_{\text{CO}} &= E_{0,\text{CO}} + \frac{RT_{\text{el}}}{2F} \ln \frac{p_{\text{CO}}^{\text{TPB}} (p_{\text{O}_2}^{\text{TPB}})^{1/2}}{p_{\text{CO}_2}^{\text{TPB}}}. \end{aligned} \quad (1.8)$$

where  $E_0$  are the standard potentials ( $E_{0,\text{H}_2} = 1.253 - 2.452 \cdot 10^{-4} T_{\text{el}}$ ,  $E_{0,\text{CO}} = 1.46713 - 4.527 \cdot 10^{-4} T_{\text{el}}$ ), and  $p_i^{\text{TPB}}$  the partial pressures of  $\text{H}_2$ ,  $\text{O}_2$ ,  $\text{H}_2\text{O}$ ,  $\text{CO}$ , and  $\text{CO}_2$  at TPB.  $p_i^{\text{TPB}}$  were

obtained by solving the coupled quasi 2D species transport models.

$$\eta_{\text{act},i,j} = \frac{RT_{\text{el}}}{F} \sinh^{-1} \frac{J_{\text{el}}}{2J_{0,i,j}}, \quad (1.9)$$

$$J_{0,i} = \gamma_{i,j} \exp\left(-\frac{E_{\text{act},i,j}}{RT_{\text{el}}}\right), \quad (1.10)$$

$$J_{0,i} = \gamma_{i,j} \exp\left(-\frac{E_{\text{act},i,j}}{RT_{\text{el}}}\right), \quad (1.11)$$

where  $i = a$  or  $c$ , and  $j = \text{H}_2$ ,  $\text{CO}$ , or  $\text{O}_2$ .  $J_{0,i,j}$  is the exchange current density,  $E_{\text{act},i,j}$  the activation energy, and  $\gamma_{i,j}$  the pre-exponential factor. The exchange current density at the cathode for  $\text{CO}_2$  splitting was taken as 40% of that of  $\text{H}_2\text{O}$  splitting ( $J_{0,c,\text{CO}} = 0.4J_{0,c,\text{H}_2}$ ), and the pre-exponential factors were assumed to be equal ( $\gamma_{c,\text{CO}} = \gamma_{c,\text{H}_2}$ ) [55]. The parameter values used are listed in table 1.1. The ohmic overpotential was only considered for the electrolyte since electrodes generally have much higher electrical conductivity. The ohmic overpotential is [59]:

$$\eta_{\text{ohmic}} = 2.99 \cdot 10^{-5} J_{\text{el}} t_{\text{e}} \exp\left(\frac{10300}{T_{\text{el}}}\right), \quad (1.12)$$

where  $t_{\text{e}}$  is the thickness of the electrolyte.

For synthesis gas production, the two electrochemical reactions take place in parallel and, consequently, the potential of one SOEC element under a given total current density ( $J_{\text{el}} = J_{\text{el},\text{CO}} + J_{\text{el},\text{H}_2}$ ) is determined by ensuring that the sum of  $E_j + \eta_{\text{act},c,j}$  of the  $\text{H}_2$  and  $\text{CO}$  evolution reactions are equal.

The operational potential of the SOE stack is the electrode area-averaged potential,  $V_{\text{el}}$ . The required power,  $\dot{P}_{\text{el}}$ , of the SOE stack is:

$$\dot{P}_{\text{el}} = A_{\text{el}} J_{\text{el}} V_{\text{el}}, \quad (1.13)$$

where  $A_{\text{el}}$  is the area of all cells (the single cell area is the product of  $L_{\text{gc}}$  and  $W_{\text{gc}}$ ). The heating demand of the stack was evaluated as:

$$\dot{Q}_{\text{el}} = A_{\text{el}} J_{\text{el}} (V_{\text{tn}} - V_{\text{el}}), \quad (1.14)$$

where  $V_{\text{tn}}$  is the thermoneutral voltage for a given  $T_{\text{el}}$ . For  $V_{\text{tn}} < V_{\text{el}}$ ,  $\dot{Q}_{\text{el}} = 0$ , assuming effective electrolyzer cooling. This heat is either provided by the electrical heaters (system 2) or by the solar receiver (systems 1 and 3).

Both the quasi 2D species transport and conservation model and the quasi 1D electrolyzer model were solved in Matlab. The DGM equations were solved by a Matlab boundary value



Table 1.1 – Model parameters and dimensions used in the SOEC model.

Parameters	Vaule
Pre-exponential factor for anode ( $\gamma_{a,O_2}$ )	$2.051 \cdot 10^9 \text{ A/m}^2$ [11]
Pre-exponential factor for cathode ( $\gamma_{c,H_2}$ )	$1.344 \cdot 10^{10} \text{ A/m}^2$ [11]
Activation energy for anode ( $E_{act,a,O_2}$ )	$1.2 \cdot 10^5 \text{ J/mol}$ [11]
Activation energy for cathode ( $E_{act,c,H_2}$ )	$1.0 \cdot 10^5 \text{ J/mol}$ [11]
Average pore radius ( $r_p$ )	5.4 [11]
Electrode tortuosity ( $\xi$ )	$1.07 \mu\text{m}$ [11]
Electrode porosity ( $\epsilon$ )	0.48 [11]
Electrolyte thickness ( $t_e$ )	$50 \mu\text{m}$ [3]
Cathode thickness ( $t_c$ )	$100 \mu\text{m}$ [3]
Anode thickness ( $t_a$ )	$50 \mu\text{m}$ [3]
Gas channel length ( $L_{gc}$ )	0.05 m [60]
Gas channel width ( $W_{gc}$ )	0.001 m [60]

solver (bp4c), based on a collocation numerical method [61]. Following a mesh independent study with a relative error tolerance of  $10^{-3}$  for species flux, molar fractions, and pressure, Ten uniform mesh elements along the  $x$ -axis for each electrode, and ten uniform elements along the  $y$ -axis for both fluid channels and electrodes were used. The electrolyzer model was validated with experimental data in the literature and the details are in the supporting information for hydrogen generation (figure 1.3a) and syngas production (figure 1.3b). All reference cell parameters and properties used in the model are listed in table 1.1.

### 1.2.2 CSP performance model

For the CSP model, a point-concentrating solar tower system for the production of high-temperature heat was utilized. The heliostat field's annual optical efficiency was assumed to be 64% based on data from the 11 MW<sub>el</sub> power tower PS10 located in Andalusia, Spain [62]. Here two sub-models are introduced: *i*) a solar receiver model, and *ii*) a Rankine cycle model. We consider two types of receivers: *i*) a receiver for the high-temperature reactant and sweep gas heating, and *ii*) a receiver for high-temperature and high-pressure steam generation for the power cycle. The receiver is a cylindrical cavity receiver with a circular aperture area through which the concentrated solar radiation enters. The energy transferred to the fluid (H<sub>2</sub>, CO, H<sub>2</sub>O, CO<sub>2</sub>, and air) is calculated by considering the energy balance of the receiver. The working fluid in the power unit (H<sub>2</sub>O) and the electrolyzer (H<sub>2</sub>, CO, H<sub>2</sub>O, CO<sub>2</sub>, and air) were directly heated by the solar receiver without considering an intermediate heat transfer fluid (such as synthetic oil or molten salts) and a subsequent heat exchanger. This choice was made in order to increase the efficiency and keeping system complexity low. We only considered radiative and convective heat losses. Conductive heat losses were neglected. The



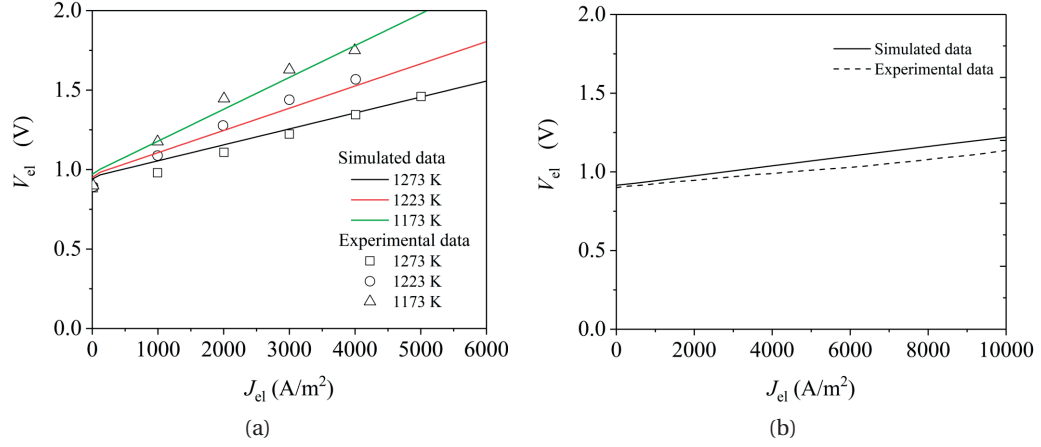


Figure 1.3 – Model validation for the electrolyzer model with experimental data: (a) electrolyzer operation potential as a function current density under three different temperatures (solid lines are for simulated data and the symbols are for experimented data) for hydrogen production [2] and (b) electrolyzer operation potential as a function of current density at 1073 K with inlet gas composition of 25% H<sub>2</sub>, 25% CO<sub>2</sub>, and 50% H<sub>2</sub>O [1].

energy balance of the receiver is given by:

$$\dot{Q}_{\text{fluid}} = \dot{Q}_{\text{aperture}} - \dot{Q}_{\text{rad}} - \dot{Q}_{\text{conv}} \quad (1.15)$$

where  $\dot{Q}_{\text{fluid}}$  represents the sensible and latent energy transferred to the working fluid,  $\dot{Q}_{\text{aperture}}$  the energy arriving at the receiver aperture,  $\dot{Q}_{\text{rad}}$  the radiative heat loss form the aperture,

$$\dot{Q}_{\text{rad}} = \varepsilon_{\text{apparent}} \sigma \pi r_{\text{ap}}^2 (T_{\text{re,av}}^4 - T_0^4), \quad (1.16)$$

and  $\dot{Q}_{\text{conv}}$  the combined natural and forced convection heat losses,

$$\dot{Q}_{\text{conv}} = (\pi r_{\text{ap}}^2 + 2\pi r_{\text{ap}} L_{\text{re}}) h_{\text{conv}} (T_{\text{re,av}} - T_0). \quad (1.17)$$

The heat transfer coefficient,  $h_{\text{conv}}$ , was evaluated from empirical correlations considering natural and forced convection [63, 64],. The cavity length was  $L_{\text{re}} = 3r_{\text{ap}}$ . The power from the heliostat field was given as a function of the aperture radius,  $r_{\text{ap}}$ :

$$\dot{Q}_{\text{aperture}} = \pi r_{\text{ap}}^2 \cdot DNI \cdot C, \quad (1.18)$$

$$C = \frac{A_{\text{heliostat}}}{\pi r_{\text{ap}}^2 \eta_{\text{optical}}},$$

where C is the effective concentration.  $\dot{Q}_{\text{rad}}$  was calculated by:

$$\dot{Q}_{\text{rad}} = \varepsilon_{\text{apparent}} \pi r_{\text{ap}}^2 (T_{\text{re,av}}^4 - T_0^4), \quad (1.19)$$

using an apparent emissivity,  $\varepsilon_{\text{apparent}}$  (a constant determined by the  $L_{\text{re}}/r_{\text{ap}}$  ratio and the material emissivity) [65], and the averaged fluid temperature,  $T_{\text{re,av}} = 0.5(T_{f,\text{in}} + T_{f,\text{out}})$ . The receiver's thermal efficiency is defined as the ratio of  $\dot{Q}_{\text{fluid}}$  to  $\dot{Q}_{\text{rad}}$ . We validated our receiver model with literature data [66]. The solar receiver thermal efficiency for our reference case for system 1 with a mean temperature of 727 K was 82% (see section 4.2) which agreed with the efficiency of 81.7% reported in [66] for their superheating receiver with a mean temperature of 736 K.

A Rankine cycle with two-stage regeneration was used [67]. The inlet temperature and pressure of the turbine was 823 K and 70 atm, and the back pressure was 1 atm. The two steam extraction pressures were 30 atm and 5 atm. A separate solar receiver was used for power generation. Solar receiver size and the additional size of the solar field were calculated according to the aforementioned receiver model with the exception that the fluid properties were different at the different operational pressures. The total electricity demand provided by the CSP sub-system of systems 1,  $\dot{P}_{\text{total,CSP}}$ , was the sum of the demands of the electrolyzer, pumps, compressors, and electrical heaters.

### 1.2.3 Photovoltaic cell array performance model

An equivalent circuit model for the individual PV modules was used to predict module current-voltage ( $I$ - $V$ ) characteristics based on the data provided by the manufacturer: the open circuit voltage,  $V_{\text{oc}}$ , the short circuit current,  $I_{\text{sc}}$ , the maximum power current and voltage,  $I_{\text{mp}}$  and  $V_{\text{mp}}$ , and the temperature coefficients of the open circuit voltage and short circuit current,  $\beta_{V_{\text{oc}}}$  and  $\alpha_{I_{\text{sc}}}$ . The circuit accounted for series and shunt resistances,  $R_s$  and  $R_{\text{sh}}$  [68]:

$$I_{\text{PV}} = I_L - I_0 \left( e^{\frac{V + I R_s}{a}} - 1 \right) - \frac{V_{\text{PV}} + I_{\text{PV}} R_s}{R_{\text{sh}}}, \quad (1.20)$$

$$a = \frac{N_s n_i k T_{\text{PV}}}{q}, \quad (1.21)$$

$$T_{\text{PV}} = T_0 + \frac{(DNI + DHI)(T_{\text{noct}} - T_0)}{(DNI_0 + DHI_0) + 6.62(\nu - \nu_0)(T_{\text{noct}} - T_0)}, \quad (1.22)$$

where  $I_L$  is the light current,  $I_0$  the diode reverse saturation current,  $a$  the modified ideality factor,  $N_s$  the number of cells in series in each PV module,  $T_{\text{PV}}$  the cell temperature, and  $n_i$  the ideality factor. In eq. 1.22,  $T_{\text{PV}}$  is given as a function of the nominal cell temperature,  $T_{\text{noct}} = 317$  K, nominal direct normal irradiance,  $DNI_0$ , nominal diffuse horizontal irradiance,  $DHI_0$ , nominal wind speed,  $\nu_0$ , ambient temperature,  $T_0$ , operating DNI and  $DHI$  ( $DHI = 0.165 \cdot DNI / (1 - 0.165)$  [69]), and operating wind speed,  $\nu$  [70]. The detailed calculation procedures for the parameters are detailed in [68]. A monocrystalline Si PV module (Sunpower SPR-210-BLK-U) for our investigation with module characteristics from Gilman et al was

## 1.2. Governing equations and methodology

used. [7], tabulated in table 1.2 The validation of the PV model was conducted under nominal conditions and the comparison between the simulated data and the reference curve of the provider shows good agreement (figure 1.4).  $v = 3$  m/s was assumed. Two-axis tracking was considered for the PV panels, maximizing the optical efficiency of the PV system. The total electricity demand of the PV array,  $\dot{P}_{total,PV}$ , for both systems 2 and 3, was the sum of the demands of the electrolyzer, pumps, compressors, and electrical heaters (heaters for system 2 and temperature stabilizer for system 3). Hence, the total PV panel area is given by:

$$A_{PV,array} = \frac{A_{PV}\dot{P}_{total,PV}}{I_{PV}V_{PV}}, \quad (1.23)$$

where  $A_{PV}$  is the PV module area. To make use of the maximum but varying power generated by the PV module arrays, the PV system used a maximum power point tracker (MPPT) with a full sun tracking system. Additionally, a DC-DC converter was used. The efficiency of the MPPT and the DC-DC converter were each assumed to be 95% [71].

Table 1.2 – Values for a monocrystalline PV module (Sunpower SPR-210-BLK-U) [7].

Parameters	Vaule
Type of cell	Monocrystalline silicon
Maximum power at SRC ( $P_{mp,ref}$ )	215.25 W
Short circuit current at SRC ( $I_{sc,ref}$ )	5.8 A
Open circuit voltage at SRC ( $V_{oc,ref}$ )	47.7 V
Current at maximum power point at SRC ( $I_{mp,ref}$ )	5.3 A
Voltage at maximum power point at SRC ( $V_{mp,ref}$ )	41.0 V
Temperature coefficient for short circuit current ( $\alpha_{Isc}$ )	0.003 A/K
Open voltage temperature coefficient ( $\beta_{Voc}$ )	-0.142 V/K
Number of cells connected in series ( $N_s$ )	72
Energy bandgap ( $E_g$ )	1.12 eV at 25 °C
Area of the module ( $A_{PV}$ )	1.2446 m <sup>2</sup>
Nominal wind speed ( $v_0$ )	1 m/s
Nominal direct normal irradiance ( $DNI_0$ )	800 W/m <sup>2</sup>
Nominal diffuse horizontal irradiance ( $DHI_0$ )	200 W/m <sup>2</sup>
Ambient temperature ( $T_0$ )	298.15 K
Shunt resistance ( $R_{sh}$ )	160.48 $\Omega$
Series resistance ( $R_s$ )	0.105 $\Omega$

Note: SRC=standard rating condition

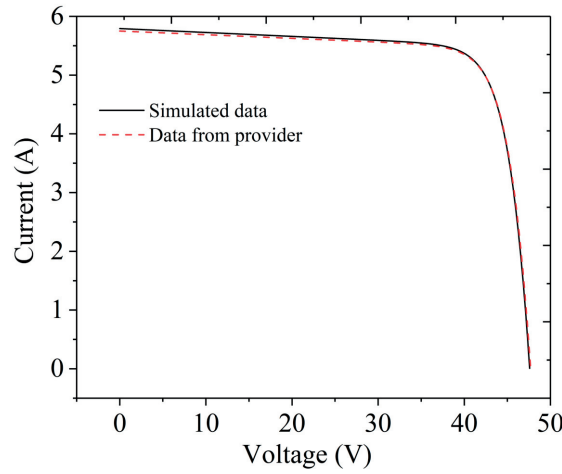


Figure 1.4 – Comparison of the simulated current and voltage characteristics (black solid line) for a single-crystalline solar cell (Sunpower SPR-210-BLK-U) with the data provided by the manufactory (red dashed line) under nominal conditions.

#### 1.2.4 Auxiliary devices

Heat exchangers were modeled in a counter flow manner with the temperature of the hot and cold streams predicted by the energy balance equation assuming a range of heat recovery effectiveness,  $\varepsilon_{HE}$ . For heat exchanger 1 (HE1), only the sensible heat of the exhaust stream could be recovered. In order to calculate log mean temperature differences and required heat exchanger surface areas of the cold stream undergoing phase change, heat transfer was divided into subcooled, two-phase, and superheating regions. The overall heat transfer coefficient,  $U$ , for each region was assumed to be constant ( $U = 500 \text{ W/m}^2/\text{K}$  for liquid-liquid heat exchange,  $U = 200 \text{ W/m}^2/\text{K}$  for gas-gas heat exchange, and  $U = 2000 \text{ W/m}^2/\text{K}$  for the two-phase region [72]). The electricity demand of pumps and compressors was estimated assuming isentropic compression with isentropic efficiencies of 0.8 and mechanical efficiencies of 0.9. The cost of separating  $\text{CO}_2$  from the produced gases was assumed to be  $10.28 \text{ \$/kg}_{\text{CO}_2}$  [73] based on a cheap cryogenic and distillation process which was added into  $C_{\text{feed}}$ . The energy consumption of the separation of  $1 \text{ kg}_{\text{CO}_2}$  by such process was  $0.45 \text{ MJ}$  [73]. For a reference case with inlet molar ratio of  $\text{H}_2\text{O}/\text{CO}_2$  equals to 1, working temperature of  $1000 \text{ K}$ , and pressure of  $1 \text{ atm}$ , the required energy power was  $235 \text{ kW}$  which is  $19.7\%$  of the required power for pumps and compressors ( $1133 \text{ kW}$ ) and hence was not considered in our study. The separation of  $\text{CO}_2$  from gaseous products may lead to cost differences depending on different gas separation techniques [40,41]. The cost of  $\text{CO}_2$  capture for PSA process was about  $57 \text{ \$/t}_{\text{CO}_2}$  ( $0.057 \text{ \$/kg}_{\text{CO}_2}$ ) [74]. This cost is  $31.7\%$  of the  $\text{CO}_2$  feedstock cost ( $0.18 \text{ \$/kg}_{\text{CO}_2}$ ) which is used in this study. The  $\text{CO}_2$  separation cost can be furthered reduced to  $10.28 \text{ \$/t}_{\text{CO}_2}$  by using an improved cryogenic separation and distillation processes [73]. The additional cost due to  $\text{CO}_2$  separation cost can be reasonably neglected due to our overestimation of the  $\text{CO}_2$  feedstock cost.

### 1.2.5 System efficiency definition

The overall solar-to-fuel efficiency of the system is defined as the ratio of the energy content of the products to the overall incident solar radiation and the energy content of the feed feedstock:

$$\eta_{\text{STF}} = \frac{\dot{n}_{\text{H}_2} HHV_{\text{H}_2} + \dot{n}_{\text{CO}} HHV_{\text{CO}}}{(DNI + DHI)(A_{\text{PV,array}} + A_{\text{heliostat}}) + \dot{n}_{\text{H}_2,\text{feed}} HHV_{\text{H}_2} + \dot{n}_{\text{CO,feed}} HHV_{\text{CO}}}. \quad (1.24)$$

The high heating value (*HHV*) of each of the products and feed streams was used.

### 1.2.6 Cost model of the systems

The cost model considers investment and operating cost for the major components of the three systems. The cost of the photovoltaic system depends on the unit cost of the module, which itself depends on the choice of module material. The price for monocrystalline Si-based modules is \$1.24/W [7]. The tracking and other auxiliary equipment cost was considered to be 40% of the total PV system cost [75], resulting in total PV cost of

$$C_{\text{PV}} = \frac{C_{\text{module}}^* \dot{P}_{\text{total,PV}}}{0.6}. \quad (1.25)$$

The cost of the electrolyzer unit per unit area was \$1695/m<sup>2</sup> [76] and a similar cost value (\$1555/m<sup>2</sup>) was reported by [77]. In addition, a recent paper by [78] showed that the SOFC stack cost is expected to drop 10 times by 2030 compared with 2013. Here, \$1695/m<sup>2</sup> was taken as the reference case value. The effect of the SOEC stack cost on the hydrogen production price was investigated with a sensitivity study and the results are shown in figure 1.5. This total electrolyzer unit cost consisted of the stack (46%), the balance of plant (21%), and the power electronics and gas conditioning (33%) [79],

$$C_{\text{el}} = \frac{C_{\text{unit}}'' A_{\text{el}}}{0.46}. \quad (1.26)$$

The cost of the concentrated solar power system consisted of four major parts: solar tower, heliostat field, receiver, and power unit, with the heliostat field the major fraction of the cost [80]:

$$C_{\text{heliostat}} = 3951.8 A_{\text{heliostat}}^{0.7}, \quad (1.27)$$

$$C_{\text{tower}} = 4785 H_{\text{tower}} - 10.51 A_{\text{heliostat}} + 0.608 H_{\text{tower}} A_{\text{heliostat}} - 82740, \quad (1.28)$$

$$C_{\text{reciever}} = 0.5224 \dot{Q}_{\text{fluid}}^{0.93}, \quad (1.29)$$

## Chapter 1. Techno-economic modeling of high-temperature electrolysis systems

$$C_{\text{powerunit}} = 2.7164 \dot{P}_{\text{csp}}^{0.93}. \quad (1.30)$$

For the hybrid system (system 3), the power unit is not present and is therefore not included. For the thermal only system (system 1), the receiver cost is counted twice and the cost of each receiver is calculated according to the energy delivered ( $\dot{Q}_{\text{fluid}}$ ). The land cost of the required PV plant and/or CSP plant areas is calculated by considering a land use factor of 0.35 and land unit cost of \$ 2/m<sup>2</sup> [81],

$$C_{\text{land}} = \frac{2(A_{\text{PV,array}} + A_{\text{heliostat}})}{0.35}. \quad (1.31)$$

Costs of the heat exchangers were derived from the total area of the heat exchanger [82],

$$C_{\text{HE}} = 2.78 \times 10^{3.6788+0.4412 \log A_{\text{HE}}}. \quad (1.32)$$

The costs of auxiliary devices such as pumps, compressors, and mixers were calculated based on available references [81, 83]. The costs of auxiliary devices and the heat exchangers were lumped into one term,  $C_{\text{other}}$ . The direct investment cost is the sum of the equipment,

$$C_{\text{d,total}} = (C_{\text{PV}} + C_{\text{el}} + C_{\text{heliostat}} + C_{\text{tower}} + C_{\text{receiver}} + C_{\text{powerunit}} + C_{\text{land}} + C_{\text{other}}). \quad (1.33)$$

The indirect investment cost,  $C_{\text{ind,total}}$ , for engineering, procurement, commissioning, and management were considered to be 20% of the initial direct capital cost, except for the heliostat costs, for which only 10% indirect investment costs were assumed [81]. Additionally, a 15% contingency cost,  $C_{\text{contingency}}$ , was added to the total investment cost. The maintenance cost,  $C_{\text{m}}$ , was included, assumed as equal to 4% of the total investment cost. The feedstock costs (feed H<sub>2</sub>O and CO<sub>2</sub>),  $C_{\text{feed}}$ , were based on a specific cost for CO<sub>2</sub> of \$0.1808/kg and for H<sub>2</sub>O of \$0.001/kg [76], multiplied by the quantity required over the lifetime. The total plant cost,  $C_{\text{total}}$ , is the sum of all the costs: investment, indirect, contingency, maintenance, and feed. The interest rate,  $i$ , was assumed to be 6% and a life time,  $t_{\text{lt}}$ , of 25 years was chosen. The total annual cost including interest is

$$C_{\text{annual,total}} = \frac{i(1+i)^{t_{\text{lt}}} C_{\text{total}}}{(1+i)^{t_{\text{lt}}} - 1}. \quad (1.34)$$

The levelized cost of fuel was calculated considering a target daily hydrogen production,

$$C_{\text{fuel}} = \frac{C_{\text{annual,total}}}{365 \dot{m}_{\text{fuel}}}. \quad (1.35)$$

The plant was assumed to continuously operate for 8 hours a day, producing 400 kg H<sub>2</sub> per day. For synthesis gas production, a production of 400 kg H<sub>2</sub> plus 4400 kg CO, equivalent to a molar ratio of H<sub>2</sub>/CO = 2 was assumed. The economic model can be used for qualitative

comparison for different systems while special attention is required for the simplifications and assumptions made in this study when the model is used for realistic plant designs and performance predictions.

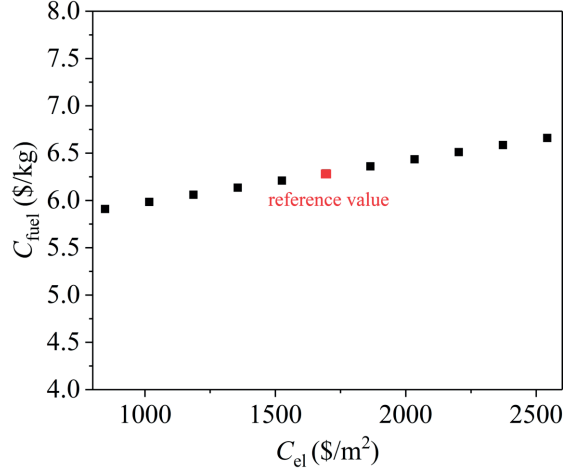


Figure 1.5 – Hydrogen price plotted as a function of the electrolyzer cost with the reference value marked in red.

## 1.3 Results and discussion

### 1.3.1 Reference case comparison of the three systems

A detailed performance and cost analysis for the three proposed systems under various design and operational conditions were conducted. The simulated reference parameters and parameter ranges for the sensitivity analysis are listed in the table 1.3. The reference case here is for water electrolysis and the production of hydrogen only. The operation temperature was chosen based on experimental data [3, 84, 85] and was pushed to values above the typically used 1273 K (all the way up to 1500 K), in order to explore high-temperature benefits which can be potentially used to guide future electrolyzer development. The current density range was chosen based on experimental data [86, 87, 88]. The reference irradiation magnitude chosen corresponds to the yearly averaged *DNI* (over 8 operational hours a day) of potential plant locations already used for commercial solar electricity production. For example, Sevilla, Southern Spain (636 W/m<sup>2</sup>, from Helioclim-3 database) or Barstow, CA, USA (932 W/m<sup>2</sup>, from NREL's TMY3 datasets). As a steady-state yearly averaged performance model was utilized in this study, the dynamic information for plants were not captured. In addition, the absence of thermal storage system (TSE) leads to underestimation of the fuel prices predicted due to more stringent requirement for electrolyzer under unsteady operation, larger degradation of equipment, more frequent shut-down and start-up of the plant, and small capacity factors.

## Chapter 1. Techno-economic modeling of high-temperature electrolysis systems

Table 1.3 – Parameters and parameter ranges considered in the techno-economic model for the three systems.

Parameters	Vaule	Reference case
Operation temperature for electrolyzer, $T_{el}$	800 - 1'500 K	1'000 K
Operation pressure for electrolyzer, $p_{el}$	1 - 25 atm	10 atm
Operation current density, $J_{el}$	1'000 - 10'000 A/m <sup>2</sup>	5'000 A/m <sup>2</sup>
Diffuse solar irradiation ratio, $RHN$	0.165 - 0.483	0.165
Direct normal insolation, $DNI$	100 - 1'000 W/m <sup>2</sup>	800 W/m <sup>2</sup>
Heat exchanger effectiveness, $\varepsilon_{HE}$	0.1 - 0.98	0.8
Water conversion extent, $W_{ce}$	0.1 - 1	0.2

To predict more realistic techno-economic performance, the importance TSE and dynamic behavior of the system cannot be neglected and are interesting to investigate for a better understanding of the system design and operation.

Figure 1.6 compares the three proposed systems at the reference state in terms of energy conversion efficiency,  $\eta_{STF}$ , and cost,  $C_{fuel}$ .  $f_{el,power}$  represents the fraction of the power of the system used to drive the electrolyzer,  $f_{pump\&comp,power}$  is the fraction of power to drive the pumps and compressors,  $f_{el,heat}$  is the heating demand of the electrolyzer (under endothermal operation), and  $f_{fluid,heat}$  is the heating power for reactants and sweep gas. The detailed definition of  $f_i$  is given in table A.1. System 1 showed the largest efficiency (10.6%), but at the highest hydrogen cost (\$8.19/kg). This is explained by the concentrated solar power sub-system, which is more expensive than the PV sub-system, leading to much higher annual costs (\$1'195'212 for system 1) compared to system 2 (\$1'171'393) and system 3 (\$917'506). System 2 showed the lowest efficiency (6.3%), but with a lower fuel cost (\$8.02/kg) compared to system 1. The low efficiency results from the low efficiency of heat produced by PV-electricity and subsequent electrical heaters (together 13.6%) compared to the high efficiency of concentrated solar heating (52.6% solar-to-heat efficiency in the receiver). Employing PV for heating led to a 48.5% occupation of the solar field for heating purposes, represented by  $f_{fluid,heat}$ . System 3, the hybrid system, exhibited both advantages: the high heating efficiency (52.6%) of system 1, resulting in  $\eta_{STF} = 9.9\%$ , and the low cost of system 2, resulting in  $C_{fuel} = \$6.28/\text{kg}$ . System 3 is less expensive than system 2, resulting from a dramatically reduced energy fraction needed for heating,  $f_{fluid,heat} + f_{el,heat}$ , (48.5% for system 2 and 19.2% for system 3). This is due to the higher heating efficiency of the concentrated solar technology compared to PV technology even with a higher cost for concentrated solar.  $f_{el,heat}$  is zero for the reference cases, as the operation is exothermic.  $V_{el}$  is 1.31 V for all systems, which is 0.03 V larger than the thermoneutral voltage (equals 1.28 V). The reference case results predicted competitive hydrogen prices (especially for system 3) compared with other solar hydrogen and fuel processing technologies such as PV and PEM electrolyzers (\$9.1/kg to \$12.1/kg), photoelectrochemical (PEC) cells (\$11.4/kg),



or solar thermochemical redox cycles (\$8.3/kg). Note that these prices were taken from the base case data discussed in [89] and [90].

A comparatively high STF efficiency and low levelized fuel cost provides the main rational for utilization of the hybrid PV-CSP approach (system 3), providing a promising pathway for scaled solar fuel processing by HTE. In order for system 1 to be competitive with system 2, the concentrated solar power sub-component cost would need to be reduced by 2.3%.

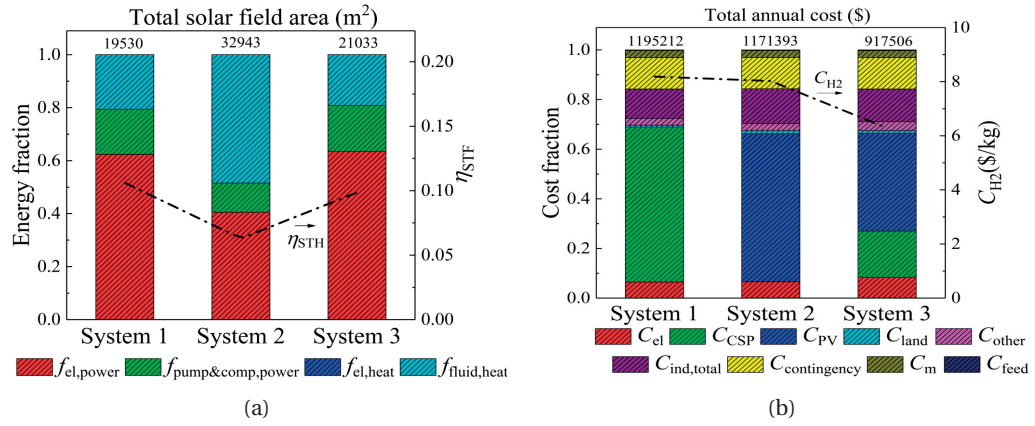


Figure 1.6 – (a) Energy fraction (equivalent solar field fraction) for power and heat driving of the components (left axis),  $\eta_{STF}$  (right axis), and total solar field area (top axis), for the three systems at the reference condition, and (b) fractional cost of system components (left axis), hydrogen cost (right axis), and  $C_{annual,totla}$  (top axis) for the three systems at the reference condition.

### 1.3.2 Effect of the diffuse irradiation ratio

Since the composition of solar irradiation (ratio  $R_{HN} = DHI/(DNI+DHI)$ ) varies according to time, weather, and plant location, the impact on the  $\eta_{STF}$  and  $C_{fuel}$  for different systems is different depending on whether the system utilizes the  $DHI$  part of solar irradiation. A study of the impact of  $R_{HN}$  on system performance was carried out at the reference case condition for each of the three proposed systems. The total solar irradiation ( $DNI+DHI$ ) was held at 958 W/m<sup>2</sup> (at the reference case) and only  $R_{HN}$  was varied. For system 1,  $\eta_{STF}$  reduced from 10.6%, at the reference condition, to 6.3% (equivalent to the efficiency for system 2 at the reference condition) as  $R_{HN}$  increased from 0.165 (reference value) to 0.499.  $C_{fuel}$  increased from \$8.19/kg to \$9.75/kg accordingly (\$5.31/kg for system 2 at reference conditions). This illustrates that system 1 is superior to system 2 in terms of  $\eta_{STF}$  only when  $R_{HN}$  is smaller than 0.499, while  $C_{fuel}$  is always inferior for system 1. System 3 shows the same  $\eta_{STF}$  as system 2 ( $\eta_{STF} = 6.3\%$ ) when  $R_{HN} = 0.783$  at  $C_{fuel} = \$8.09/kg$ . System 3 shows equivalent  $C_{fuel}$  with system 2 ( $C_{fuel} = \$8.02/kg$ ) when  $R_{HN} = 0.777$  at  $\eta_{STF} = 6.39\%$ . As long as  $R_{HN} < 0.777$ , system 3

is superior to system 2 in terms of  $\eta_{STF}$  and  $C_{fuel}$ .

### 1.3.3 Effects of electrolyzer operating temperature and pressure

The operating temperature of the electrolyzer is one of the key factors in determining the operating voltage of the electrolyzer, which in turn determines electrolyzer heating and power demands. Figure 1.7 shows  $\eta_{STF}$  and  $C_{fuel}$  for various operating  $T_{el}$  and  $p_{el}$  combinations for the three different systems with other parameters held at reference values (table 1 and 2).

For system 1, higher  $T_{el}$  always leads to larger  $\eta_{STF}$  for all studied pressures. The increase in  $\eta_{STF}$  with increasing  $T_{el}$  results from reduced  $V_{el}$  at high temperatures, while this increase in  $\eta_{STF}$  with increasing  $T_{el}$  is reduced as a result of increased heating demand ( $\dot{Q}_{fluid}$ ) and solar receiver heat losses ( $\dot{Q}_{rad}$  and  $\dot{Q}_{conv}$ ). Higher  $p_{el}$  always caused a drop in  $\eta_{STF}$  due to a significant increase in pumping power for the reactants and sweep gas. Similar trends were found for  $C_{fuel}$  with respect to  $T_{el}$  and  $p_{el}$ , where higher  $\eta_{STF}$  led to smaller-sized CSP sub-systems which, in turn, lowered the  $C_{fuel}$ .

For system 2, the optimal  $T_{el}$  for various  $p_{el}$  was 1300 K. The increase in  $\eta_{STF}$  with increasing  $T_{el}$  results from the domination of reduced  $V_{el}$  at high temperatures. While this increase in  $\eta_{STF}$  is counteracted with further increase in  $T_{el}$  resulting from an increasing heat demand at increased  $T_{el}$ , which counteracts the benefits given by reduced  $V_{el}$ . The penalty of increased heat demand induced by increasing  $T_{el}$  is more significant for system 2 than for system 1 at the same temperature, as the former has a lower heating efficiency. For system 2 at the same conditions, the  $\eta_{STF}$  is significantly reduced compared to system 1. Due to this low heat efficiency, system 2 could result in even larger  $C_{fuel}$  compare to system 1 (figure 4d) at larger  $T_{el}$ . For example, system 2 shows slightly smaller fuel cost than system 1 at reference conditions (in section I), while this advantage in fuel cost is counteracted when  $T_{el}$  is larger than 1050K (in section II) with other parameters kept at reference conditions. In addition, the transition  $T_{el}$  between section I and section II increases with increasing  $p_{el}$  due to increase electricity demand with increasing  $p_{el}$  which alleviates the effect of lower heating efficiency. System 2 showed similar trends as system 1 in terms of cost and efficiency variations with increasing pressure.

The  $\eta_{STF}$  of the hybrid system (system 3) showed the same variations with changing  $T_{el}$  and  $p_{el}$ , but at slightly lower values than system 1, due to the slightly lower solar-to-electricity efficiency of system 3 (15.2%) compared to system 1 (15.8%) at the reference condition. For system 3, the solar-to-electricity efficiency is 15.2% for the reference case, as a result of the monocrystalline silicon PV cell used in this study. For system 1, the solar-to-electricity efficiency (15.8% for the reference case) is a product of the solar-to-thermal efficiency (52.6% for the reference case)

and the power unit efficiency (30%, Rankine cycle including the generator).

The trend in the  $C_{\text{fuel}}$  of system 3 with changing  $T_{\text{el}}$  and  $p_{\text{el}}$  showed much lower values than system 2. This is due to the dominant benefits of the significantly enhanced solar-to-thermal efficiency of a concentrated solar thermal system, leading to a smaller heliostat field area for heating, and compensating the cost drawback of the CSP sub-system.

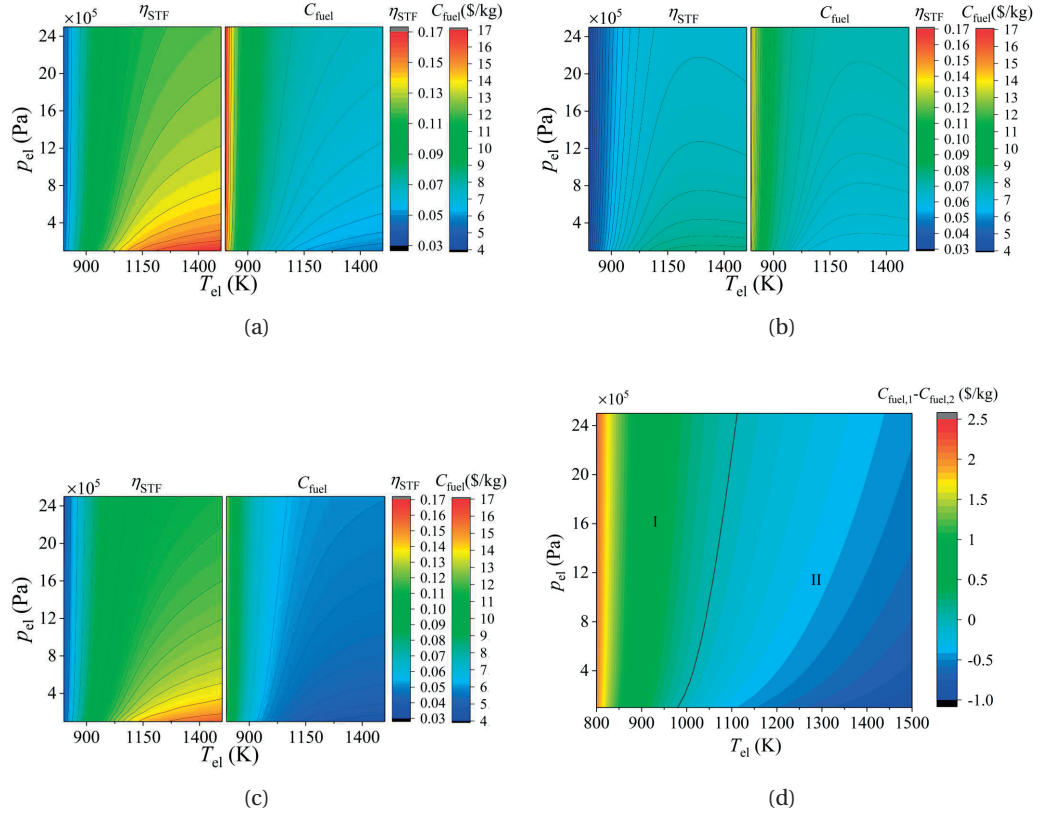


Figure 1.7 –  $\eta_{\text{STF}}$  and  $C_{\text{fuel}}$  as a function of electrolyzer pressure,  $p_{\text{el}}$ , and electrolyzer working temperature,  $T_{\text{el}}$ , for (a) system 1, (b) system 2, and (c) system 3. (d) The  $C_{\text{fuel}}$  difference between system 1 and system 2 under various  $p_{\text{el}}$  and  $T_{\text{el}}$ . The dashed line in (d) represent the cases when the fuel price difference is zero. Other operational parameters are at the reference state (tables 1.1 and 1.3).

### 1.3.4 Performance and cost sensitivity of system 3

#### Effect of current density

For system 3, the impact of the electrolyzer operational current density,  $J_{\text{el}}$ , on  $\eta_{\text{STF}}$  and  $C_{\text{fuel}}$ , for changing  $T_{\text{el}}$  and  $p_{\text{el}}$ , is shown in figure 1.8a and 1.8b. Generally, larger  $J_{\text{el}}$  causes a decrease in  $\eta_{\text{STF}}$  due to increased operating cell potential (eqs. 1.9 and 1.12), which in turn

increases power demand. At a low temperature range (800 K - 1100 K),  $C_{\text{fuel}}$  first decreased to a minimum value with increasing  $J_{\text{el}}$ , which resulted from the reduced electrolyzer area demand for a given plant size (400 kg<sub>H<sub>2</sub></sub>/day), and then increased when further increasing  $J_{\text{el}}$ , resulting from the dominant influence of ohmic losses. For example, at  $T_{\text{el}} = 800$  K, the  $C_{\text{fuel}}$  decreased from \$10.35/kg to \$9.85/kg when  $J_{\text{el}}$  increased from 1'000 A/m<sup>2</sup> to 2'000 A/m<sup>2</sup>, while the other parameters were held at the reference values. However,  $C_{\text{fuel}}$  increased from \$9.85/kg to \$10.56/kg as  $J_{\text{el}}$  further increased from 2'000 A/m<sup>2</sup> to 3'000 A/m<sup>2</sup> as a result of increasing ohmic overpotential. As  $T_{\text{el}}$  increased, the minimum  $C_{\text{fuel}}$  moved to larger  $J_{\text{el}}$  due to the exponential reduction of ohmic overpotential (eq. 1.12) at elevated temperatures. The minimum  $C_{\text{fuel}}$  was obtained at  $J_{\text{el}} > 10'000$  A/m<sup>2</sup> (the upper limit of  $J_{\text{el}}$  investigated in this study) when  $T_{\text{el}} > 1100$  K. The decrease in  $\eta_{\text{STF}}$  with increasing  $J_{\text{el}}$  was affected by  $T_{\text{el}}$  and  $p_{\text{el}}$ : the magnitude of the drop in  $\eta_{\text{STF}}$  with increasing  $J_{\text{el}}$  decreased with increasing  $T_{\text{el}}$  (figure 1.8a) and increasing  $p_{\text{el}}$  (figure 1.8b). For example, the absolute reduction of  $\eta_{\text{STF}}$  was 5.38 percentage points at 800K, and 0.81 percentage points at 1200 K, when  $J_{\text{el}}$  was increased from 1000 A/m<sup>2</sup> to 10'000 A/m<sup>2</sup>. The  $\eta_{\text{STF}}$  was relatively insensitive to changes in  $J_{\text{el}}$  at higher  $p_{\text{el}}$ . For example, the absolute reduction in  $\eta_{\text{STF}}$  was 2.75 percentage points at 10 atm, and 3.96 percentage points at 1 atm.

Isothermal operation was assumed in the current study, which assumes that the electrolyzer and inlet and outlet gas temperatures are at a constant temperature. This requires additional heating or cooling equipment for the electrolyzer depending on the difference between operation voltage,  $V_{\text{el}}$ , and thermoneutral voltage,  $V_{\text{tn}}$ . If  $V_{\text{el}} > V_{\text{tn}}$ , the electrolyzer works at an exothermic voltage, requiring a cooling device to maintain the temperature. If  $V_{\text{el}} < V_{\text{tn}}$ , additional heating is required. Operation at thermoneutral voltage simplifies the system design and avoids the need for additional heating or cooling components. The combinations of  $T_{\text{el}}$ ,  $p_{\text{el}}$ , and  $J_{\text{el}}$  resulting in thermoneutral voltage operation are shown in figure 1.8c. Thermoneutral operation is achieved when simultaneously increasing  $J_{\text{el}}$  and  $T_{\text{el}}$  at  $p_{\text{el}} = 10$  atm, suggesting that high efficiency and low cost can be achieved under thermoneutral electrolyzer conditions (figure 1.8a). For example: under thermoneutral operation,  $\eta_{\text{STF}} = 9.95\%$  and  $C_{\text{fuel}} = \$6.29/\text{kg}$  for  $T_{\text{el}} = 1000$  K,  $p_{\text{el}} = 10$  atm, and  $J_{\text{el}} = 4'642$  A/m<sup>2</sup>, while for the same  $T_{\text{el}}$  and  $p_{\text{el}}$ , either *i*) the maximal  $\eta_{\text{STF}}$  (11.4%) was achieved at  $J_{\text{el}} = 1000$  A/m<sup>2</sup>, and at a potential lower than  $V_{\text{tn}}$  (0.258 V lower), or *ii*) the minimum  $C_{\text{fuel}}$  (\$6.28/kg) was achieved at  $J_{\text{el}} = 6000$  A/m<sup>2</sup>, and at a potential slightly larger than  $V_{\text{tn}}$  (0.022 V higher). For a fixed  $T_{\text{el}}$ , a decrease in  $p_{\text{el}}$  resulted in larger  $J_{\text{el}}$  at thermoneutral conditions, resulting from the reduced Nernst potential, which in turn further reduced  $C_{\text{fuel}}$ . Additionally, the larger  $J_{\text{el}}$  reduces the electrolyzer cost, further reducing  $C_{\text{fuel}}$ .

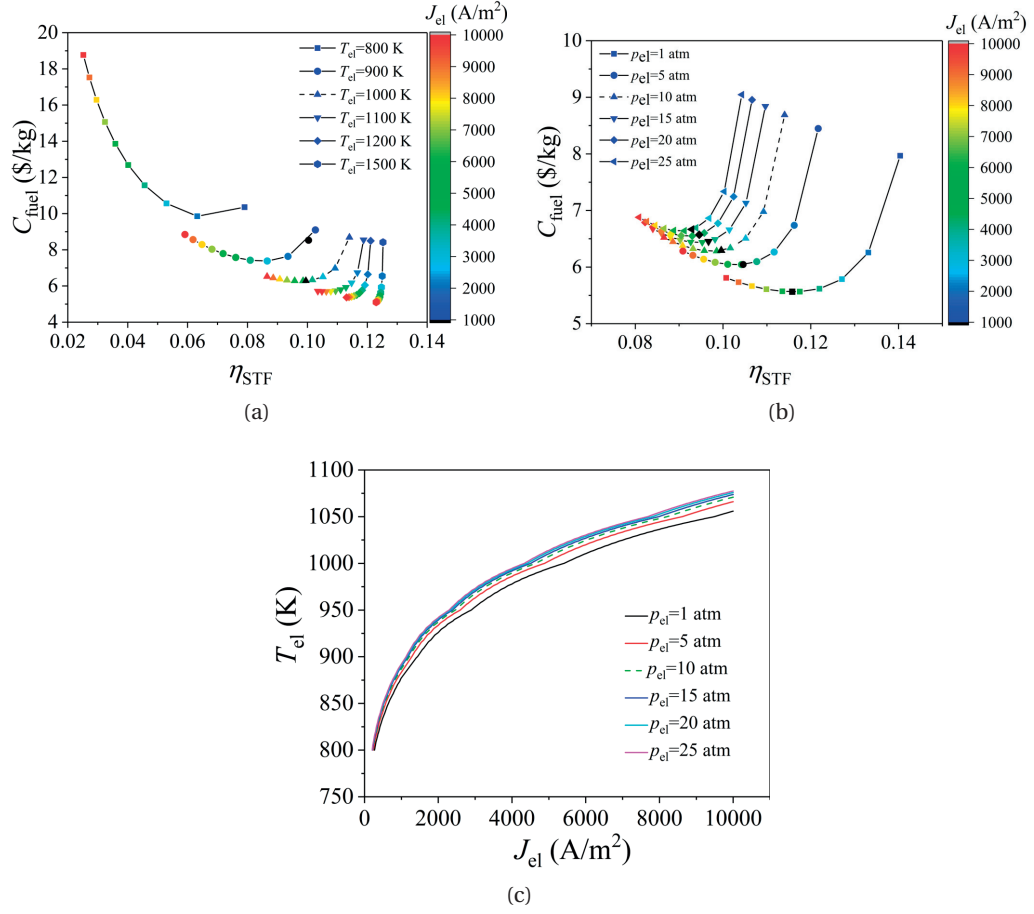


Figure 1.8 – For system 3, (a)  $\eta_{\text{STF}}$  and  $C_{\text{fuel}}$  as a function of  $J_{\text{el}}$  and  $T_{\text{el}}$  with  $p_{\text{el}} = 10$  atm, (b)  $T_{\text{el}} = 1000$  K. Symbol colors indicate the current density, and (c) Thermoneutral operational conditions for various  $T_{\text{el}}$ ,  $p_{\text{el}}$ , and  $J_{\text{el}}$  for system 3 with other parameters held at the reference values. In (a) and (b), the solid lines with symbols represent  $T_{\text{el}}$  for a) and  $p_{\text{el}}$  for (b). Dashed lines are for the reference case with changing  $J_{\text{el}}$ . Black symbols represent thermoneutral conditions. In (c), the dashed line represents the reference  $p_{\text{el}}$  with changing  $J_{\text{el}}$ .

### Effect of heat exchange effectiveness

Since the electrolyzer working temperature is in the range of 800 K to 1500 K, large amounts of heat are required for heating the reactants and the sweep gas, leading to a significant influence of heat exchange effectiveness on system efficiency. The cost of the heat exchanger is exponentially dependent on the heat exchanger area (eq. 1.32), which also depends on the heat transfer coefficient (depending on the phase of the streams). As depicted in figure 1.9,  $C_{\text{fuel}}$  first decreases with increasing  $\varepsilon_{\text{HE}}$  due to increasing system efficiency, and then increases due to the dominance of the heat exchanger costs. For the selected cases shown in figure 1.9, the minimal  $C_{\text{fuel}}$  at  $T_{\text{el}} = 800$  K was obtained at  $\varepsilon_{\text{HE}} = 0.9$ , and  $\varepsilon_{\text{HE}}$  increased to 0.94 as  $T_{\text{el}}$  increased to 1200 K. Increasing  $\varepsilon_{\text{HE}}$  beyond the minimum  $C_{\text{fuel}}$  point led to a sharper increase

in  $C_{\text{fuel}}$  at lower  $T_{\text{el}}$ . The  $\eta_{\text{STF}}$  always increased with increasing  $\varepsilon_{\text{HE}}$  due to increased heat recovery and, consequently, reduced requirement for energy input. Increasing  $\varepsilon_{\text{HE}}$  beyond the minimum  $C_{\text{fuel}}$  point led to a less steep increase in  $\eta_{\text{STF}}$  at lower  $T_{\text{el}}$ . This comes from the increased heat exchanger area required at elevated temperatures, which in turn exponentially increases the heat exchanger cost. Efficiency increases at higher temperatures due to reduced electrolyzer cell potential. The minimum  $C_{\text{fuel}}$  at  $T_{\text{el}} = 1000$  K was obtained at a constant  $\varepsilon_{\text{HE}} = 0.93$  for different  $p_{\text{el}}$  since the increase in the heat exchanger cost starts to dominate the cost reduction due to decreasing  $A_{\text{heliostat}}$ .

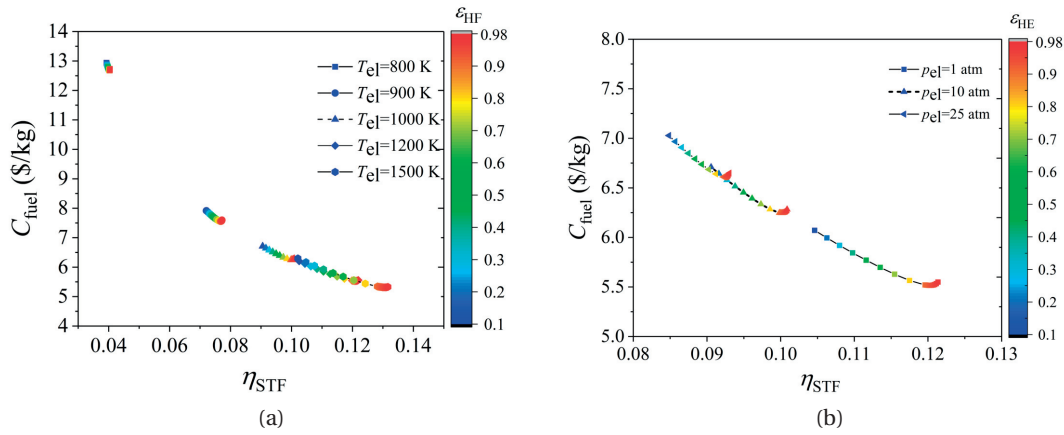


Figure 1.9 – For system 3,  $\eta_{\text{STF}}$  and  $C_{\text{fuel}}$  as a function of  $\varepsilon_{\text{HE}}$  and (a)  $T_{\text{el}}$  with  $p_{\text{el}} = 10$  atm, and (b)  $p_{\text{el}}$  with  $T_{\text{el}} = 1000$  K. Symbol colors indicate  $\varepsilon_{\text{HE}}$ . The solid lines with symbols represent  $T_{\text{el}}$  for (a), and  $p_{\text{el}}$  for (b). Dashed lines are for the reference case with changing  $\varepsilon_{\text{HE}}$ .

### Effect of solar irradiation

The impact of direct normal irradiance,  $DNI$ , on  $\eta_{\text{STF}}$  and  $C_{\text{fuel}}$  for system 3 under various  $T_{\text{el}}$  and  $p_{\text{el}}$  is shown in figure 1.10a and 1.10b. Changes in  $DNI$  result from variation in location, and seasonal and daily changes. For the concentrated solar system, only the direct part of the solar irradiation can be utilized, while both the direct and diffuse parts can be harvested by the photovoltaic system. For comparison reasons, both  $DHI$  and  $DNI$  were considered in solar irradiation, assuming  $DHI$  only depends on  $DNI$ , calculated with the equation introduced in section 1.2.3. Generally,  $\eta_{\text{STF}}$  increases and  $C_{\text{fuel}}$  decreases with increasing  $DNI$  due to increasing solar receiver efficiency and PV system efficiency. The increasing temperature of the PV reduces the efficiency (eqs. 1.21 and 1.22), and this effect starts to be dominant at  $DNI > 700$  W/m<sup>2</sup> at the reference condition. The optimal  $DNI$  in terms of  $\eta_{\text{STF}}$  is always 700 W/m<sup>2</sup> for various  $T_{\text{el}}$  and  $p_{\text{el}}$  with other parameters at reference conditions. However, the increased  $DNI$  always leads to reduced solar field areas, which in turn leads to lower investment cost.



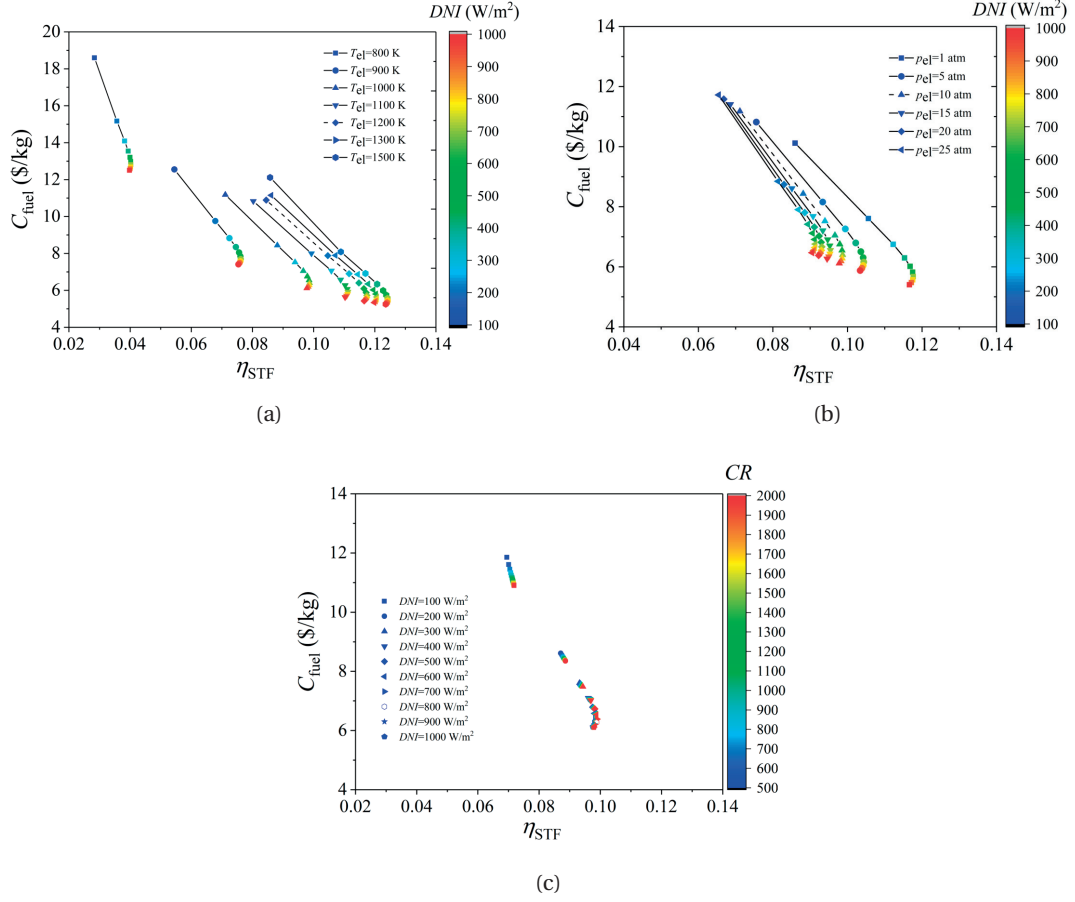


Figure 1.10 – For system 3,  $\eta_{\text{STF}}$  and  $C_{\text{fuel}}$  as a function of DNI and (a)  $T_{\text{el}}$  for  $p_{\text{el}} = 10$  atm, or (b)  $p_{\text{el}}$  and  $T_{\text{el}} = 1000$  K. (c)  $\eta_{\text{STF}}$  and  $C_{\text{fuel}}$  as a function of CR and DNI for  $p_{\text{el}} = 10$  atm and  $T_{\text{el}} = 1000$  K. In (a) and (b), symbol colors indicate the DNI. The solid lines with symbols represent  $T_{\text{el}}$  for (a) and  $p_{\text{el}}$  for (b). Dashed lines are for the reference case with varying DNI. In (c), symbols represent varying CR, and hollow symbols are for reference cases with changing DNI.

### Effect of concentration ratio

The concentration ratio,  $CR$ , is defined as the ratio between the solar power intensity at the cavity receiver aperture and the DNI. Variation in  $CR$  affects the aperture size of the receiver at a constant input power, resulting in changing the thermal performance of the cavity receiver. The ratio of cavity length to aperture radius was held constant at 3, and the surface emissivity at 0.88. For system 3, the effect of  $CR$  on  $\eta_{\text{STF}}$  and  $C_{\text{fuel}}$  for various DNI is shown in figure 1.10c. A range of  $CR$  between 500 and 2000 was chosen, representing typical values for solar tower concentrating technologies. For system 3, the larger the  $CR$ , the larger the  $\eta_{\text{STF}}$  and the lower the  $C_{\text{fuel}}$  reference conditions for all DNI. The increase of  $\eta_{\text{STF}}$  and decrease of  $C_{\text{fuel}}$  is more pronounced at lower DNI. The increase of  $CR$ , effectively reducing the aperture radius, leads

to decreased re-radiation losses. This effect was less pronounced at elevated  $DNI$ , which can be explained by the already reduced re-radiation losses for increasing  $DNI$ , diluting the effect of  $CR$ . This suggests that  $CR$  is not the limiting factor for high  $\eta_{STF}$  and low  $C_{fuel}$  when the  $DNI$  of the chosen location is larger than  $300 \text{ W/m}^2$ .

### Effect of water conversion extent

For system 3, the effect of water conversion extent,  $W_{CE}$ , on  $\eta_{STF}$  and  $C_{fuel}$  for varying  $T_{el}$  and  $p_{el}$  is shown in figure 1.11. The increase of  $W_{CE}$  can lead to three contradictory effects: *i*) a reduced energy need for heating the water to the required operational temperature (i.e. the total fluid heating demand was 1974.1 kW at the reference conditions, and decreased to 514.9 kW for  $W_{CE} = 1$ ), *ii*) mass transport limitations in the porous cathode increasing the Nernst potential (i.e. 0.954 V at the reference conditions, increased to 1.037 V for  $W_{CE} = 1$ ), which in turn leads to an increased electrolyzer electricity demand (i.e. total electricity demand for the electrolyzer was 1750 kW at the reference conditions, increased to 1861 kW for  $W_{CE} = 1$ ), and *iii*) reduced requirements for pumping of the fluid (i.e. total pumping power demand was 374.4 kW at the reference conditions, decreased to 74.9 kW for  $W_{CE} = 1$ ). As shown in figure 1.11, the increase of  $W_{CE}$  always benefits  $\eta_{STF}$  and  $C_{fuel}$ , dominantly coming from the effects of reduced heating and pumping demands compared to the increased electricity demand of the electrolyzer (due to increasing Nernst potential). Generally, an increase in  $W_{CE}$  leads to increasing  $\eta_{STF}$  and decreasing  $C_{fuel}$ . However, lower  $p_{el}$  may result in mass transport limitations of the water in the cathode. For example at  $p_{el} = 1 \text{ atm}$ , an increase of  $W_{CE}$  above 0.85 reduced  $\eta_{STF}$ , which results primarily from the potential increase effects over the benefit of pumping and heating demand reduction. At a constant  $W_{CE}$ , a reduction in pressure reduces  $C_{fuel}$  because of reduced compression demand.



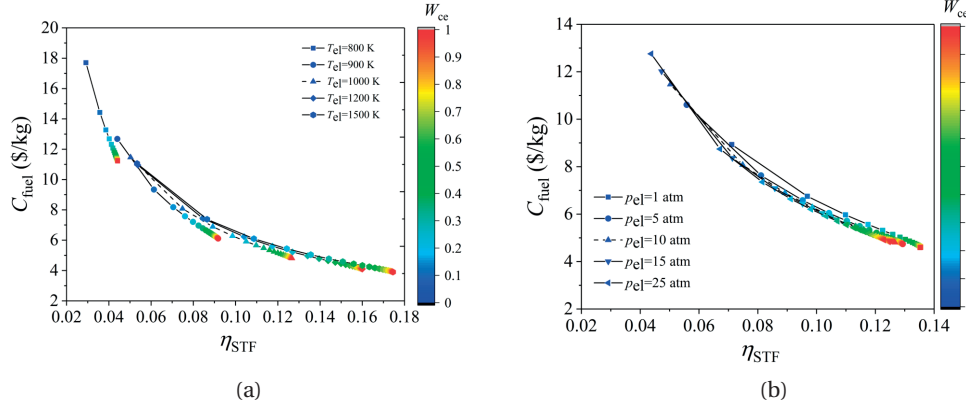


Figure 1.11 – For system 3,  $\eta_{STF}$  and  $C_{fuel}$  as a function of  $W_{CE}$  and (a)  $T_{el}$  for  $p_{el} = 10$  atm, or (b)  $p_{el}$  for  $T_{el} = 1000$  K. Symbol colors indicate  $W_{CE}$ . The solid lines with symbols represent  $T_{el}$  for (a) and  $p_{el}$  for (b). Dashed lines are for the reference case with changing  $W_{CE}$ .

### 1.3.5 Synthesis gas production in system 3

In the context of synthesis gas production, the desired molar ratio of  $H_2$  and CO in synthesis gas varies according to the targeted liquid fuel. For example, a  $H_2/CO$  ratio of 2:1 is required for the synthesis of methanol [91]. In this study, focus was paid on a particular  $H_2$  production ratio, as an example, of 2, and the effects of the working conditions on  $\eta_{STF}$  and  $C_{fuel}$ , and the required cathode inlet gas composition at the reference conditions were investigated.

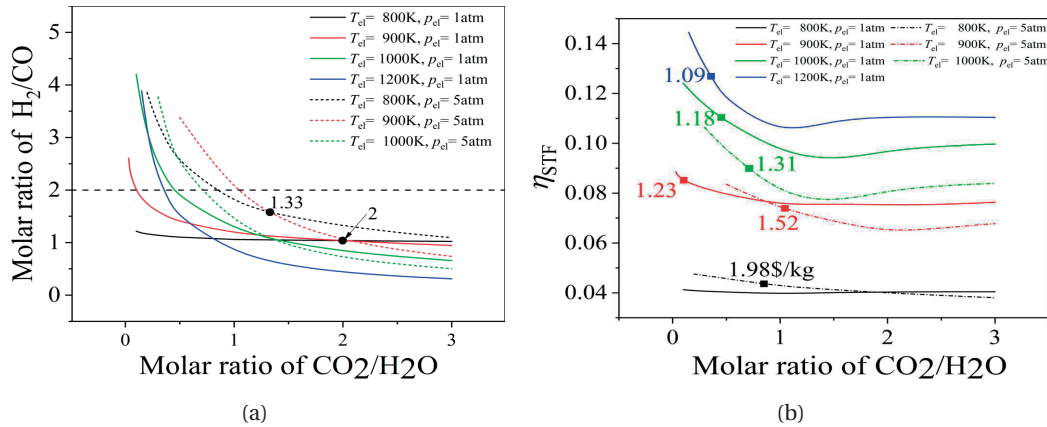


Figure 1.12 – (a)  $H_2$  to CO molar ratio of synthesis gas as a function of cathode inlet molar ratio of  $CO_2$  to  $H_2O$  for varying  $T_{el}$  and  $p_{el}$  (solid lines for 1 atm and dashed lines for 10 atm), and (b)  $\eta_{STF}$  as a function of cathode inlet molar ratio of  $CO_2$  to  $H_2O$  for various  $T_{el}$  and  $p_{el}$ . Symbols in (b) represent cases that result in a molar ratio of  $H_2$  to CO equal to 2, with the number indicating the corresponding fuel cost.

Figure 1.12 reveals the impact of  $T_{el}$ ,  $p_{el}$ , and cathode  $\text{CO}_2/\text{H}_2\text{O}$  inlet ratios on the product molar ratio of  $\text{H}_2$  to  $\text{CO}$ . In general, the molar  $\text{H}_2/\text{CO}$  ratio decreases with increasing  $\text{CO}_2/\text{H}_2\text{O}$  inlet molar ratio for a given  $T_{el}$ . This is due to the reduction in  $R_{\text{WGSR}}$  (figure 1.13b) and the reduction in the concentration overpotential for  $\text{CO}_2$  splitting, leading to increased current occupation for  $\text{CO}_2$  splitting and consequently to larger  $\text{CO}$  generation.

A higher  $T_{el}$  resulted in lower  $\text{H}_2/\text{CO}$  molar ratios for  $\text{CO}_2/\text{H}_2\text{O}$  inlet ratios larger than 2 ( $p_{el} = 1$  atm with other parameters held at reference values), primarily due to the reverse WGSR. This reverse WGSR rate ( $-R_{\text{WGSR}}$ ) was drastically increased with increasing  $T_{el}$ , leading to decreases in  $\text{H}_2/\text{CO}$  molar ratios. At smaller  $\text{CO}_2/\text{H}_2\text{O}$  molar inlet ratios ( $< 2$ ), the resulting  $\text{H}_2/\text{CO}$  molar ratios are mostly driven by the following effects: *i*) the decreasing difference between the equilibrium potential of  $\text{H}_2\text{O}$  and  $\text{CO}_2$  with increasing  $T_{el}$  (figure 1.14), which leads to an increase in  $J_{\text{CO}}$ , *ii*) the increase of  $R_{\text{WGSR}}$  with initial increase in  $T_{el}$  ( $T_{el} < 1009$  K) and the sharp decrease of  $R_{\text{WGSR}}$  with further increase in  $T_{el}$  ( $T_{el} > 1009$  K) (figure 1.13a), and *iii*) the steeper decrease of  $R_{\text{WGSR}}$  with  $\text{CO}_2/\text{H}_2\text{O}$  molar inlet ratios at increasing  $T_{el}$  (figure 1.13b). The aforementioned factors lead to complex behavior of the  $\text{H}_2/\text{CO}$  molar ratios. As  $T_{el}$  increases from 800 K to 1000 K, the increase in  $R_{\text{WGSR}}$  dominated, which provoked an increase in the  $\text{H}_2/\text{CO}$  molar ratio. Accordingly, the required  $\text{CO}_2/\text{H}_2\text{O}$  molar inlet ratios for a  $\text{H}_2/\text{CO}$  molar ratio of 2 increased from 0.104 to 0.454 as  $T_{el}$  increased from 900 K to 1000 K, both at  $p_{el} = 1$  atm. As  $T_{el}$  further increased from 1000 K to 1200 K, the equilibrium potential of  $\text{CO}_2$  became smaller than that of  $\text{H}_2\text{O}$  (figure 1.14) leading to a significant increase in  $J_{\text{CO}}$ . Furthermore, the sharp decrease in  $R_{\text{WGSR}}$  at high  $T_{el}$  ( $> 1009$  K) further reduced the production of  $\text{H}_2$ . These two effects lead to a decrease in the  $\text{H}_2/\text{CO}$  molar ratios. To maintain a  $\text{H}_2/\text{CO}$  product ratio of 2 at  $T_{el} = 1200$  K, a reduction in the  $\text{H}_2\text{O}$  and  $\text{CO}_2$  molar inlet ratio was required (0.357 at  $T_{el} = 1200$  K).

The influence of  $p_{el}$  on the product ratio ( $\text{H}_2$  to  $\text{CO}$ ) is shown in figure 1.12a. To produce synthesis gas at a  $\text{H}_2/\text{CO}$  product ratio of 2, the required  $\text{CO}_2/\text{H}_2\text{O}$  molar inlet ratio must be increased, compared to the  $p_{el} = 1$  atm case, in order to counteract the increase of  $R_{\text{WGSR}}$  with increasing  $p_{el}$ . For example, the corresponding  $\text{CO}_2/\text{H}_2\text{O}$  molar inlet ratio at 1000 K was 0.104 at  $p_{el} = 1$  atm and increased to 1.046 at  $p_{el} = 5$  atm.

Figure 1.12b shows  $\eta_{\text{STF}}$  as a function of  $\text{CO}_2/\text{H}_2\text{O}$  molar inlet ratio for varying  $T_{el}$  and  $p_{el}$ . Generally, working at lower  $p_{el}$  and higher  $T_{el}$  leads to higher  $\eta_{\text{STF}}$ . For cases with a  $\text{H}_2/\text{CO}$  molar product ratio of 2, high  $\eta_{\text{STF}}$  (12.7%) and low  $C_{\text{fuel}}$  (\$1.09/kg) were achieved at elevated  $T_{el}$  (1200 K) and low  $p_{el}$  (1 atm).

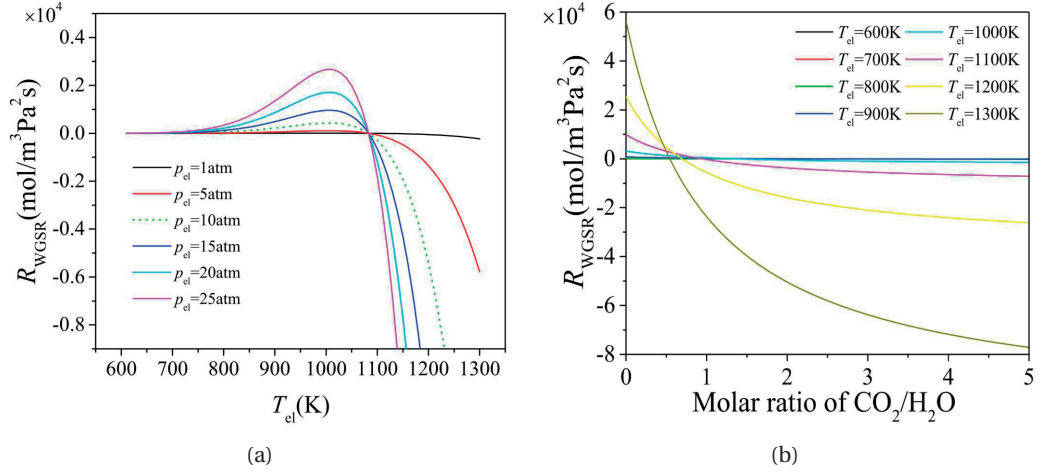


Figure 1.13 – (a) the effect of  $T_{\text{el}}$  and  $p_{\text{el}}$  on the reaction rate of the reversible water-gas shift reaction with molar ratio of  $\text{CO}_2$  to  $\text{H}_2\text{O}$  equals to 1 and other parameters kept at reference values, and (b) the reversible water-gas shift reaction rate as a function of  $T_{\text{el}}$  and molar ration of  $\text{CO}_2$  to  $\text{H}_2\text{O}$  at the cathode inlet with  $p_{\text{el}} = 10$  atm and other parameters at reference value.

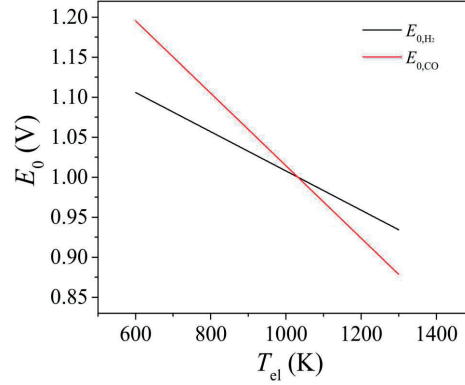


Figure 1.14 – Equilibrium potential as a function of  $T_{\text{el}}$  for both  $\text{CO}_2$  and  $\text{H}_2/\text{CO}$  splitting

## 1.4 Summary and conclusions

A methodology for the techno-economic assessment of solar-driven HTE of water and  $\text{CO}_2$  to hydrogen and CO was developed in order to compare the performance and cost of three different solar integration schemes at various working conditions. The three solar integration schemes incorporated concentrated solar technology (system 1), photovoltaic technology (system 2), and the combination thereof (system 3) for the production of power and heat

## Chapter 1. Techno-economic modeling of high-temperature electrolysis systems

---

needed in the process. The impact of operating temperature, pressure, current density, heat recovery effectiveness, direct normal irradiance, conversion extent, and concentration ratio were investigated and discussed. The model can be used for qualitative techno-economic performance evaluation prediction for different solar integration schemes under various operation conditions.

System 1, utilizing only concentrated solar technology for the production of heat and electricity, is able to work at high efficiency, but exhibits large fuel costs resulting from the expensive concentrated solar heat and power technologies. System 2, utilizing only PV technology, allowed for the production of hydrogen at a reduced levelized cost of \$8.02/kg at the reference condition. This resulted from the smaller costs of PV technologies compared to concentrated solar power (CSP) technologies. System 3 provides a superior and more competitive techno-economic performance compared to systems 1 and 2 individually. The predicted hydrogen price (especially for system 3) is competitive with other solar hydrogen and fuel processing technologies.

Higher operating temperature is always favorable for solar-to-fuel efficiency in system 1 and 3. There exists an optimal electrolyzer operating temperature for system 2 (1300 K) which allows to achieve the highest solar-to-fuel efficiency. Further increase in temperature leads to larger heating demand, resulting in reduced efficiency. The system 2 shows higher fuel cost at high temperature ( $>1050$  K at 10 atm) and this transition temperature increases with increasing pressure. Working at ambient pressure shows the best performance in terms of efficiency and fuel price.

The system can be optimized by tuning the operational temperature and pressure in order to achieve a current density which results in minimum efficiency drop and maximized cost reduction. Operation at thermoneutral voltage is suggested to simplify the heat management of the electrolyzer and shows to be close to the cost and efficiency-optimum case for large temperatures and small pressures. Optimized temperature and current density combinations for thermoneutral operation were predicted, resulting in high efficiency and low fuel cost.

A high heat exchanger effectiveness leads to higher efficiency due to increased heat recovery. However, large heat exchanger effectiveness requires a larger heat exchanger area, leading to exponentially increased heat exchanger cost. Consequently, an optimal effectiveness for minimized fuel price is observed (around 90 %). This optimal effectiveness value needs to be chosen for each system design and operating condition.

Larger *DNI* results in lower fuel cost due to reduced needed solar field area in the concentrated solar system (the dominating cost of systems 1 and 3) and due to reduced receiver heat losses owing to decreased receiver aperture. For system 2, initially PV efficiency increases with

increasing *DNI*. However, the solar-to-fuel efficiency was affected at high *DNI* ( $>700 \text{ W/m}^2$ ) due to increased PV cell temperature, reducing solar-to-electricity efficiency. Consequently, plant location and local irradiation conditions need to be carefully considered for system 2, while systems 1 and 3 should be built at locations with largest possible *DNI*.

Generally, larger water conversion results in larger efficiency and lower fuel cost. However, at large conversion rates, mass transport limits increased the Nernst potential which, in turn, counteracts the benefit of the reduced heating and pumping energy. Consequently, water conversion needs to be carefully tailored to the system and operating conditions for optimal system techno-economic performance.

In the context of synthesis gas production, the effects of temperature and pressure on fuel price and efficiency are similar to the hydrogen production cases. Due to the concurrent electrolysis and water-gas shift reactions, a smart combination of inlet  $\text{CO}_2/\text{H}_2\text{O}$  molar fraction,  $T_{\text{el}}$  and  $p_{\text{el}}$  is required to produce a syngas product with a desired molar ratio of  $\text{H}_2$  to  $\text{CO}$  (here illustrated with a  $\text{H}_2/\text{CO}$  ratio of 2). Lower  $p_{\text{el}}$  and higher  $T_{\text{el}}$  favors high efficiency and low cost syngas production with a  $\text{H}_2/\text{CO}$  ratio of 2. The system proposed allows to flexibly adjust the product composition by adjusting the inlet reactants compositions, or the operational temperature or pressure. Consequently, such a plant can be combined with a variety of downstream processes, which may require different product composition as an input.

In sum, a complete, detailed, and flexible simulation framework for the evaluation of the performance and cost of three conceptually different solar-driven high-temperature electrolysis systems is presented in this chapter. Three systems are differentiated by the utilization of different solar technologies for solar integration (concentrated solar or photovoltaics). The sensitivity of the performance and cost metrics towards operational conditions (temperature, pressure, current density, heat exchanger effectiveness, irradiation, concentration ratio) was quantified and provide guidance for operational conditions which maximize efficiency and minimize cost. Our assessment and comparison of these three competing solar integration approaches predict that the hybrid system proposed in this chapter exhibits an efficiency and cost advantage compared to the others and should be considered a promising scalable approach to large-scale solar fuel processing.



## 2 Thermodynamic analysis on ceria-based thermochemical cycles<sup>1</sup>

In this chapter, a competing high-temperature route, ceria-based two-step thermochemical cycles, for solar fuel processing is introduced and analysis with a detailed thermodynamic model. The evaluations for optimal operating conditions (system pressure, oxygen partial pressure, reduction temperature, oxidation temperature, heat recovery, and irradiation concentration ratio) for various system configurations of non-stoichiometric cycling of ceria using concentrated solar irradiation are presented in detail. Particularly, this study focuses on the reduction step and on the incorporation of alternative methods – mechanical and chemical – for reducing the oxygen partial pressure. The understanding of the influence of working conditions, component choices, and system configurations on system performance is required for the determination of the optimal operation conditions and design of practical system configurations for increased solar fuels processing efficiencies. A comparison between solar-driven high-temperature electrolysis and the two-step thermochemical cycles is presented at the end of this chapter based on the results obtained from chapter 1 and chapter 2.

### 2.1 System description and model development

Thermodynamic evaluations of the performance of ceria redox cycling has been reported in [92, 29, 23, 24, 93]. Panlener et al. studied the reaction enthalpy of non-stoichiometric ceria in a large range of temperatures and pressures by thermo gravimetric measurements [94]. Riess et al. [95] investigated the specific heat of ceria by an adiabatic temperature scanning calorimeter. Lapp et al. [23] performed a parametric thermodynamic analysis of a ceria-based cycling scheme using an ideal mixing model and sweep gassing to maintain a low oxygen

---

<sup>1</sup>Material from this chapter has been published in: M. Lin and S. Haussener, “Solar fuel processing efficiency for ceria redox cycling using alternative oxygen partial pressure reduction methods,” *Energy*, vol. 88, pp. 667–679, 2015. [45]

concentration atmosphere for the reduction step. They found that effective solid phase heat recovery was crucial in achieving STF efficiencies above 10%. Bader et al. [29] demonstrated numerically that isothermal cycling of ceria was possible at the expense of reduced system performance. Sweep gas was used to reduce the oxygen partial pressure in the reduction chamber, gas phase heat recovery was assumed, and plug flow reactor models in counter flow arrangements were employed in both chambers. Gas phase heat recovery with effectiveness above 95.5% was required for STF efficiencies above 10%. The energy penalty introduced through the use of immense amounts of sweep gas pointed to the need for alternative methods to reduce the oxygen partial pressure during the reduction reaction. Ermanoski et al. [24] showed for the non-isothermal cycling of ceria using ideal mixing in both reaction chambers that the efficiency of the process could be increased by using vacuum pumping schemes for the reduction of the oxygen partial pressure. It is unclear whether this conclusion applies to isothermal operation and whether a further decrease of the oxygen partial pressure in the reduction chamber through non-mechanical methods is required for competitive STF efficiencies provided the use of solid-solid and gas-gas heat recovery components with realistic heat exchange effectiveness.

### 2.1.1 System description

The five thermochemical fuel production systems investigated are depicted in figure B.1. They differed in their approach to reduce the oxygen partial pressure in the reduction chamber, namely: three mechanical schemes using *i*) sweep gas (scheme a) [23, 96], *ii*) vacuum pump (scheme b) [25], and *iii*) the combination thereof (scheme d); and two combined mechanical-chemical schemes using *i*) sweep gas and a chemical scavenger (scheme c), and *ii*) using the combination of sweep gas, vacuum pump, and a chemical scavenger (scheme e). All five systems used two continuously and simultaneously operating reaction chambers for the separated reduction and oxidation reactions. The systems incorporated two heat exchanges to recover the heat from the exhaust (sweep gas and products). Solid phase heat recovery was incorporated between the reduced and oxidized ceria streams.

In scheme (a) inert gas was used to sweep away the produced oxygen during the reduction and correspondingly maintaining a desired oxygen partial pressure at the entrance (process 3-4). The sweep gas flow and the ceria flow was considered in a counterflow arrangement [29], i.e. the pressure and temperature will stay constant while the concentration of oxygen and the  $\delta$  of ceria vary only in axial direction. Compared to the ideal mixing flow design used in [96, 25], the counterflow arrangement maximized the  $p_{O_2}$  in the sweep gas at the outlet of the reduction chamber and minimized the  $p_{O_2}$  at the outlet of the oxidation chamber, resulting in a reduced sweep gas demand and reactant input. The inert gas was preheated in a heat exchanger and further heated by concentrated solar energy to the reduction temperature,  $T_{red}$ ,



## 2.1. System description and model development

---

before entering the reduction chamber. The states 5 to 8 described a full, closed ceria cycle. The ceria was cooled to the oxidation temperature,  $T_{\text{ox}}$ , in the process 5-6 while rejecting  $\dot{Q}_{\text{ceria}}$  (not needed for isothermal operation), and isothermally reacted with the oxidizing agents ( $\text{H}_2\text{O}$ ,  $\text{CO}_2$ ) in the oxidation chamber during the process 6-7. Finally, the ceria temperature was heated to  $T_{\text{red}}$  (process 7-8) and then isothermally reduced in the reduction chamber (process 8-5). The oxidizer was preheated in the heat exchanger by effluent and further heated to  $T_{\text{red}}$  by concentrated solar energy (process 10-11). Since the oxidation reaction was an exothermic process, the energy needed to heat the oxidizer from  $T_{10}$  to  $T_{11}$  may be less than the heat released by the reaction and hence a heat changer was used for further exhaust cooling after heat recovery (process 13-14).

The processes of scheme (b) was similar to the processes in scheme (a) concerning the oxidation process and the ceria cycling process. However, the oxygen generated in the reduction chamber was not swept away by inert gas. Instead a vacuum pump was employed continuously removing the produced oxygen during the reduction and maintaining a desired oxygen partial pressure in the chamber.

In scheme (c), sweep gassing was combined with a chemical oxygen scavenger (process 1'-2') in which the oxygen in the sweep gas is reacted with an active metal (e.g. magnesium) to further reduce the oxygen partial pressure. Magnesium has been reported to be an alloying element in metals industries acting an important chemical oxygen scavenger which is widely used in large scale metal alloy production [97, 98]. Magnesium oxide can be recycled through various thermochemical and electrochemical processes which are commonly used for industrial magnesium production [99] .

Scheme (d) was a combination of both mechanical approaches, namely sweep gassing and vacuum pump. Scheme (e) combined scheme (d) with the chemical scavenger.

Additional assumptions used in the model were: *i*) the system was evaluated at steady state, *ii.a*) for scheme (a), counterflow arrangement was assumed for both reduction and oxidation chamber, *ii.b*) for scheme (b), counterflow arrangement was assumed in the oxidation chamber and the oxygen was uniformly distributed in the reduction chamber, *iii*) gases were modeled as ideal gases, and *iv*) temperatures of the reactants in the reduction and oxidation chambers were considered constant and uniform.

Additionally, ideal mixing models were used for the reduction and oxidation chambers to account for a less favorable reaction chamber design configuration. The ideal mixing model considered the equilibrium that was created by the water at  $T_{\text{ox}}$ , influencing the non-stoichiometry at oxidation. In this case, the in the oxidation chamber was determined by optimizing it for largest cycle efficiency while ensuring it was smaller than of water dissociation at  $T_{\text{ox}}$ .

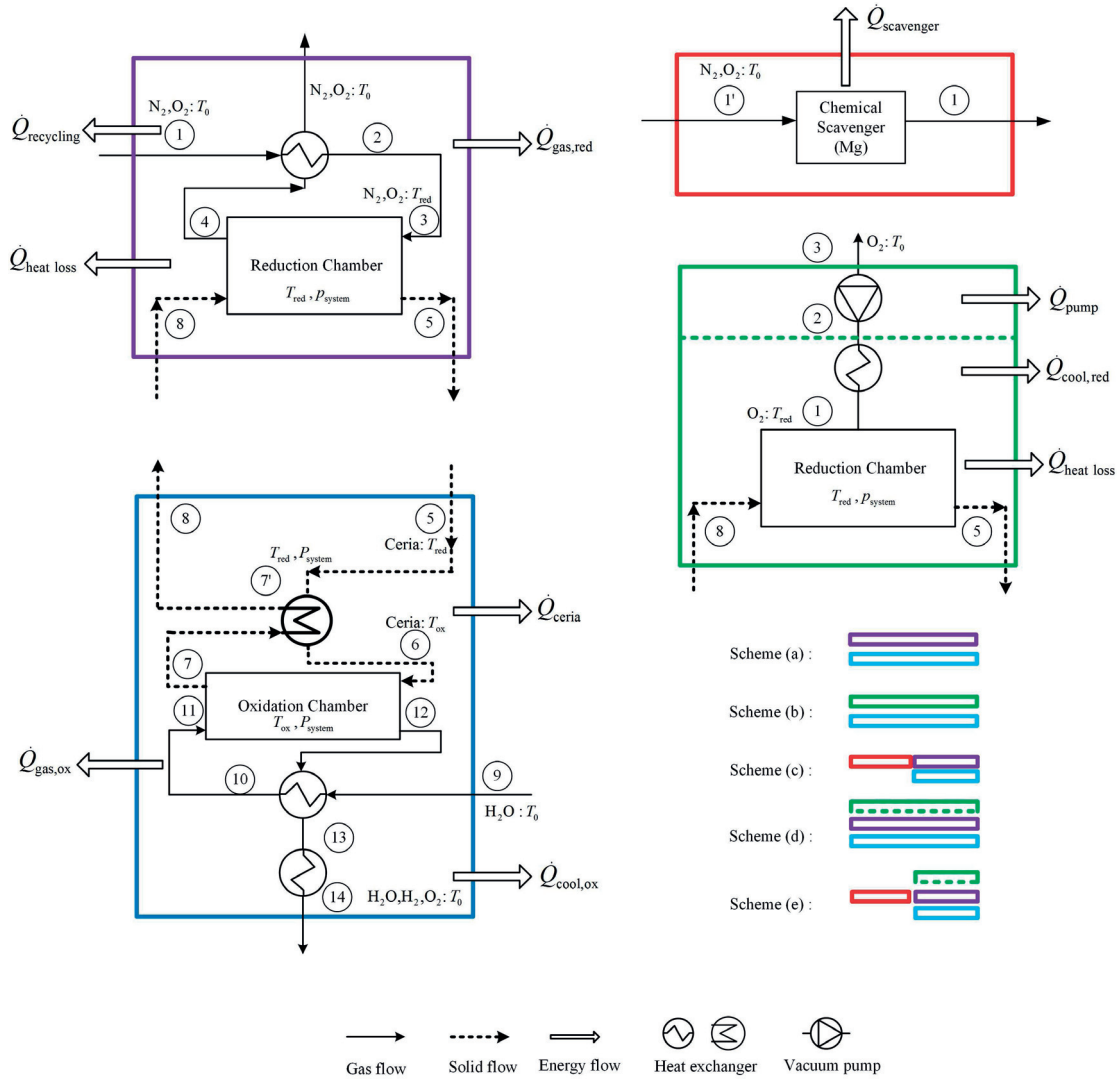


Figure 2.1 – Schematic of the five ceria-based thermochemical cycling schemes modeled (a to e), which are combinations of four different sub-components: oxidation chamber and auxiliaries (blue), reduction chamber and sweep gas connections (purple), chemical scavenger (red), and reduction chamber and vacuum pump (green). The five schemes differ in the methods used for the oxygen partial pressure reduction in the reduction chamber, namely: using inert sweep gas, a vacuum pump, a chemical scavenger, or combinations thereof.

### 2.1.2 Model development

The steady state energy balance for the modeled system was given by

$$\begin{aligned}\dot{Q}_{\text{solar}} = & \dot{Q}_{\text{heat loss}} + \dot{Q}_{\text{react}} + \dot{Q}_{\text{gas,red}} + \dot{Q}_{\text{gas,ox}} \\ & + \dot{Q}_{\text{cool,ox}} + \dot{Q}_{\text{cool,red}} + \dot{Q}_{\text{ceria}} + \dot{Q}_{\text{pump}} + \dot{Q}_{\text{recycling}} + \dot{Q}_{\text{scavenger}}.\end{aligned}\quad (2.1)$$

$\dot{Q}_{\text{solar}}$  was the solar energy incident on a blackbody receiver with a certain aperture area for concentrated solar irradiation ( $A_{\text{ap}} \cdot CR \cdot DNI$ ). Note that the last three terms on the right hand side ( $\dot{Q}_{\text{pump}}$ ,  $\dot{Q}_{\text{recycling}}$ , and  $\dot{Q}_{\text{scavenger}}$ ) are not all concurrently required for all schemes, as detailed below. The heat losses accounted for the radiation heat loss from the aperture, and conduction and convection losses through the cavity walls. The latter were assumed to be a constant fraction,  $f$ , of the total solar energy captured by the cavity and assumed 20% according to experimental observations [30]. Hence, the heat losses were given by

$$\dot{Q}_{\text{heat loss}} = \dot{Q}_{\text{rad}} + f(\dot{Q}_{\text{solar}} - \dot{Q}_{\text{rad}}) = (1 - f)A_{\text{ap}}\sigma T_{\text{red}}^4 + f\dot{Q}_{\text{solar}}.\quad (2.2)$$

The power utilized for the chemical reaction was the sum of the chemical reactions in the reduction and oxidation chambers,

$$\dot{Q}_{\text{react}} = \dot{Q}_{\text{react,ox}} + \dot{Q}_{\text{react,red}} = \dot{n}_{\text{H}_2} \Delta h_{\text{H}_2\text{O,react}}(T_{\text{ox}}),\quad (2.3)$$

where  $\dot{Q}_{\text{react,red}} = -\dot{Q}_{\text{react,ox}} = \frac{\dot{n}_{\text{ceria}}}{2} \int_{\delta_{\text{ox}}}^{\delta_{\text{red}}} \Delta h_{\text{O}_2}(\delta) d\delta$ . The investigations in this chapter focused on the splitting of water. Nevertheless, the splitting of  $\text{CO}_2$  or a combination of water and  $\text{CO}_2$  can be studied analogously and selected results are presented in the supporting information.

In scheme (a), the sweep gas was preheated in a heat exchanger (with recovery effectiveness,  $\varepsilon_g$ ) by heat of the effluent,

$$\dot{Q}_{\text{gas,red}} = (1 - \varepsilon_g) \dot{n}_{\text{N}_2,1} [h_{\text{N}_2}(T_{\text{red}}) - h_{\text{N}_2}(T_0)] + (1 - \varepsilon_g) \dot{n}_{\text{O}_2,1} [h_{\text{O}_2}(T_{\text{red}}) - h_{\text{O}_2}(T_0)],\quad (2.4)$$

before entering the reduction chamber where the final  $T_{\text{red}}$  was achieved through part of the solar irradiation.  $\dot{n}_{\text{O}_2,1}$  was the molar flow of oxygen in the inert gas before entering the reduction chamber.  $\dot{Q}_{\text{gas,red}} = 0$  in scheme (b) since no sweep gas was introduced. However, the oxygen produced in the ceria reduction process was continuously pumped out by a vacuum pump and, for practical reasons, has to be cooled before entering the pump. The energy loss due to cooling is calculated as

$$\dot{Q}_{\text{cool,red}} = (\dot{n}_{\text{O}_2,4} - \dot{n}_{\text{O}_2,1}) [h_{\text{O}_2}(T_{\text{red}}) - h_{\text{O}_2}(T_0)].\quad (2.5)$$

Similarly, the energy required for the heating of the oxidizer was given as

$$\begin{aligned} \dot{Q}_{\text{gas,ox}} = & (\dot{n}_{\text{H}_2\text{O},9} - \varepsilon_g \dot{n}_{\text{H}_2\text{O},12}) [h_{\text{H}_2\text{O}}(T_{\text{ox}}) - h_{\text{H}_2\text{O}}(T_0)] - \\ & \varepsilon_g \dot{n}_{\text{H}_2,12} [h_{\text{H}_2}(T_{\text{ox}}) - h_{\text{H}_2}(T_0)] - \varepsilon_g \dot{n}_{\text{O}_2,12} [h_{\text{O}_2}(T_{\text{ox}}) - h_{\text{O}_2}(T_0)]. \end{aligned} \quad (2.6)$$

The oxidation reaction was slightly endothermic which can lead to excessive heat in the oxidation chamber. In this case cooling was considered in the energy balance by

$$\dot{Q}_{\text{cool,ox}} = \dot{Q}_{\text{react,ox}} - \dot{Q}_{\text{gas,ox}}. \quad (2.7)$$

For non-isothermal operation, ceria needed to be heated from the oxidation to the reduction temperature,

$$\dot{Q}_{\text{ceria}} = \dot{n}_{\text{ceria}} \int_{T_{\text{ox}}}^{T_{\text{red}}} c_{p,\text{ceria}} dT. \quad (2.8)$$

Similarly, the ceria needed to be cooled from the reduction to the oxidation temperature when exiting the reduction chamber. Potentially, the rejected heat during this cooling step can be partially recovered in a solid-solid heat exchanger (with a effectiveness,  $\varepsilon_s$ ) in order to minimize the required for the solid heating step (eq. 2.8).

The pumping work for the cycling of the gas and solid reactants and products in both reaction chambers and through the piping was neglected in all schemes. The pumping work required in scheme (b) to remove the generated oxygen in the reduction process was calculated by

$$\dot{Q}_{\text{pump}} = \frac{W_{\text{pump}}}{\eta_{\text{TTE}} \eta_{\text{pump}}} = \frac{\dot{n}_{\text{O}_2,1} R T_0}{\eta_t \eta_{\text{pump}}} \ln \frac{p_0}{p_{\text{O}_2,1}}, \quad (2.9)$$

where  $W_{\text{pump}}$  was the pumping work for moving the oxygen stream out of reduction chamber,  $\eta_{\text{TTE}}$  was the heat-to-electricity efficiency,  $\eta_{\text{pump}}$  was the electricity-to-pumping work efficiency,  $p_0$  was the ambient pressure, and  $p_{\text{O}_2}$  was the partial pressure of oxygen in the reduction chamber.

The energy for recycling the sweep gas,  $\dot{Q}_{\text{recycling}}$ , occupied less than 1% of the total solar energy input [29] and was neglected in the current study. The recycling energy of the chemical scavenger is given by

$$\dot{Q}_{\text{scavenger}} = \frac{\dot{n}_{\text{N}_2,1'} (p_{\text{O}_2,2'} - p_{\text{O}_2,1'})}{p_0} \dot{Q}_{\text{Mg,pr}} \quad (2.10)$$

where the  $\dot{Q}_{\text{Mg,pr}}$  was the total energy need to produce one mole of magnesium, which was obtained from industrial databases [100].

The molar flow rates of all streams at each state were obtained by solving the mass balance in both chambers considering chemical equilibrium, counterflow or ideal mixing arrangement,

## 2.1. System description and model development

respectively, and a two-step oxidation reaction including the water thermolysis and oxidation of reduced ceria by oxygen [29].  $\delta_{\text{red}}$  was determined by the  $p_{\text{O}_2}$  and  $T_{\text{red}}$  at the inlet of the reduction chamber, and  $\delta_{\text{red}}$  was obtained according to the  $p_{\text{O}_2}$  and  $T_{\text{ox}}$  at the inlet of the oxidation chamber.  $p_{\text{O}_2}$  at the inlet of the oxidation chamber only depended on  $T_{\text{ox}}$  and hence also  $\delta_{\text{ox}}$  was only a function of  $T_{\text{ox}}$ .

The non-stoichiometry coefficient,  $\delta$ , for the undoped ceria reduction and oxidation reaction under various conditions was determined using the experimental data of Panlener et al. [94], in which experiments for oxygen partial pressures and temperatures ranging from  $10^{-22}$  atm to  $10^{-2}$  atm and 1023 K to 1774 K, respectively, with  $\delta$  varying from 0.00107 to 0.27 were performed. The values of  $\delta$  were calculated for given temperatures and  $p_{\text{O}_2}$  by,

$$\Delta g_{\text{O}_2}(\delta, T) = \Delta h_{\text{O}_2}(\delta) - T \Delta s_{\text{O}_2}(\delta) = RT \ln \frac{p_{\text{O}_2}}{p_0}. \quad (2.11)$$

The specific heat of nonstoichiometric ceria was estimated by the specific heat of cerium dioxide without considering the impact of phase transformations [95].

### 2.1.3 Performance definition

Three performance indicators were used in this study: *i*) the solar-to-fuel (STF) efficiency, *ii*) water utilization factor, and *iii*) hydrogen productivity. The STF efficiency,  $\eta_{\text{STF}}$ , was defined as

$$\eta_{\text{STF}} = \frac{\dot{n}_{\text{H}_2,12} \text{HHV}_{\text{H}_2}}{\dot{Q}_{\text{solar}}}. \quad (2.12)$$

The water utilization factor,  $f_w$ , was the ratio between the amount of hydrogen produced and the total water input into the oxidation chamber,

$$f_w = \frac{\dot{n}_{\text{H}_2,12}}{\dot{n}_{\text{H}_2\text{O},9}}. \quad (2.13)$$

$f_w$  indicated the efficiency of input water usage which can be maximized when the water input needs to be minimized (e.g. when water resources are scarce). Note that  $\dot{n}_{\text{H}_2\text{O},9}$  was determined by the reaction's thermodynamic equilibrium at state points 11 and 12, which was not randomly chosen but requires the oxygen partial pressure at the outlet to match  $p_{\text{O}_2,12}$ .

The hydrogen productivity,  $\chi_{\text{H}_2}$ , was the ratio between the production rate of hydrogen at 1kW solar power input and the solid metal oxide rate required for the cycling,

$$\chi_{\text{H}_2} = \frac{\dot{n}_{\text{H}_2,12}}{\dot{n}_{\text{ceria},5}}. \quad (2.14)$$

It quantified the efficiency of metal oxide utilization and indicated the amount of ceria which has to be moved in such a system.

All the aforementioned definitions are analogous when evaluating the  $\text{CO}_2$  dissociation for the CO production.

## 2.2 Results and discussion

### 2.2.1 Operational feasibility for ceria-based fuel processing cycles

The operational feasibility and limitation of the proposed ceria based thermochemical cycle schemes were given by two conditions: *i)*  $\delta_{\text{red}} > \delta_{\text{ox}}$  to ensure a net fuel production, and *ii)* for scheme (a) only,  $p_{\text{O}_{2,1}} \leq p_{\text{O}_{2,4}} \leq p_{\text{system}}$ . The combinations of  $T_{\text{red}}$ ,  $\Delta T = T_{\text{red}} - T_{\text{ox}}$ , and  $p_{\text{O}_{2,4}}$  for which condition *i)* is met are depicted in figure 2.2a. The combinations for which condition *ii)* is met (only required for scheme (a)) are depicted in figure 2.2b.

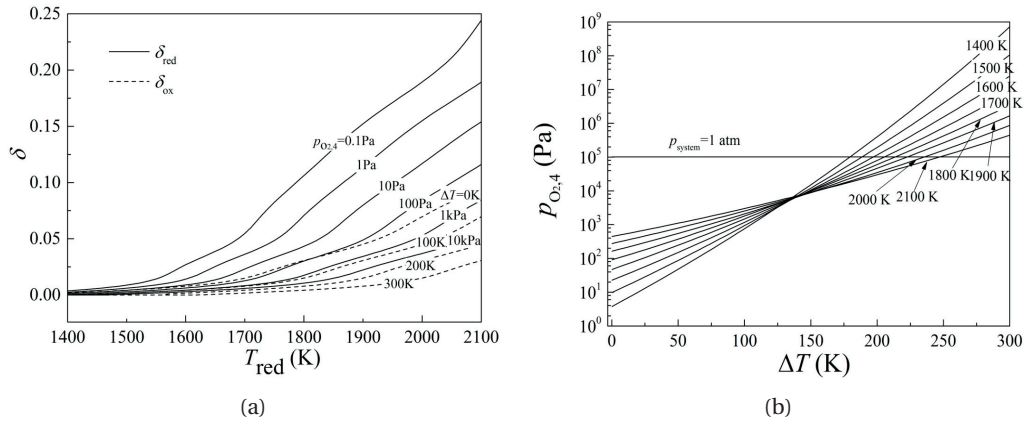


Figure 2.2 – Feasibility of ceria-based thermochemical cycling under various operation conditions: (a) the non-stoichiometric coefficient of ceria at various temperatures and  $p_{\text{O}_{2,4}}$ , and (b)  $p_{\text{O}_{2,4}}$  as a function of  $\Delta T$  for various  $T_{\text{red}}$ .

For isothermal operation ( $\Delta T = 0$  and  $p_{\text{O}_{2,4}} = p_{\text{O}_{2,11}}$ ), condition *ii)* was fulfilled for all  $T_{\text{red}}$  investigated ( $1400 \text{ K} < T_{\text{red}} < 2100 \text{ K}$ ) at a system pressures of 1 atm. A system pressure as low as 6 mbar could be tolerated. At  $p_{\text{system}} = 1 \text{ atm}$ , isothermal operation was feasible once the condition  $\delta_{\text{red}} > \delta_{\text{ox}}$  is met, which required for  $T_{\text{red}} > 1800 \text{ K}$  (see figure 2.2a). The higher  $p_{\text{O}_{2,4}}$  the higher  $T_{\text{red}}$  required for a positive net fuel production. The maximum  $p_{\text{O}_{2,4}}$  that was possible for isothermal operation was about 460 Pa for  $T_{\text{red}} > 1400 \text{ K}$ . For non-isothermal operation ( $\Delta T \neq 0$ ), the largest possible  $\Delta T$  was about 250 K for  $p_{\text{system}} = 1 \text{ atm}$  and  $T_{\text{red}} = 2100 \text{ K}$ . The increase in  $\Delta T$  from 0 K (isothermal) to 300 K enlarged the range of feasible operational

conditions that still ensured  $T_{\text{red}}$  (see figure 2.2a), but also increased  $\delta_{\text{red}}$ , eventually requiring an increased system pressure for feasibility. An increase in  $p_{\text{system}}$  increased the range of possible operational conditions, i.e. allows for larger  $\Delta T$ .

### 2.2.2 Effects of temperature swing and oxygen partial pressure

The  $T_{\text{red}}$ ,  $T_{\text{ox}}$  (or  $\Delta T$ ), and  $p_{\text{system}}$  were the most significant operational parameters. Large  $T_{\text{red}}$  led to increased heat losses (see eq. 2.2), but increased  $\delta_{\text{red}}$ , which increased the potential to produce hydrogen. Large  $\Delta T$  resulted in increased hydrogen production due to the decreased  $\delta_{\text{ox}}$ , while introducing an increased solid phase heat loss (see eq. 2.8) if solid heat recovery was not practical or efficient. A smaller  $p_{\text{O}_2,1}$  required higher flow rates of sweep gas and correspondingly more energy to heat up the sweep gas, or more pumping work for the vacuum pump. Nevertheless, small  $p_{\text{O}_2,1}$  increased  $\delta_{\text{red}}$  and provided a larger hydrogen production potential. A reference case was defined (see table 2.1) for the subsequent optimization. Particularly,  $\Delta T$  was optimized for maximum STF efficiency at a particular combination of  $T_{\text{red}}$  and  $p_{\text{O}_2,1}$ .

Table 2.1 – Reference case parameters used for the comparison of the five different models of the ceria cycling.

Parameters	Vaule
Direct normal irradiance, $I$	1000 W/m <sup>2</sup>
Solar concentration ratio, $CR$	3000
System pressure, $p_{\text{system}}$	1 atm
Heat loss factor, $f$	0.2 [100]
Heat-to-electricity efficiency, $\eta_t$	0.4
Electricity-to-pumping efficiency, $\eta_{\text{pump}}$	0.4 [101]
Reduction temperature, $T_{\text{red}}$	1400 K to 2100 K
Temperature swing, $\Delta T$	0 K to 300 K
Oxygen partial pressure in the sweep gas for scheme (a), $p_{\text{O}_2,1}$	0.1 Pa to 20000 Pa
Oxygen partial pressure in the sweep gas for scheme (b), $p_{\text{O}_2,1}$	0.1 Pa to 20000 Pa
Ambient temperature, $T_0$	298 K
Heat recovery effectiveness for gases, $\varepsilon_g$	0.955 [102]
Heat recovery effectiveness for solid, $\varepsilon_s$	0

Figure 2.3 shows the calculated largest possible efficiencies for various combinations of  $T_{\text{red}}$  and  $p_{\text{O}_2,1}$ , indicating the corresponding optimized  $\Delta T$ , for scheme (a) and (b). This efficiency is called optimal efficiency. Additionally, the efficiency for the same  $T_{\text{red}}$  and  $p_{\text{O}_2,1}$  combina-

tions at isothermal operation ( $\Delta T = 0$ ) are shown. The corresponding energy distribution is depicted in figures 2.4 and 2.5 for scheme (a) and (b), respectively.

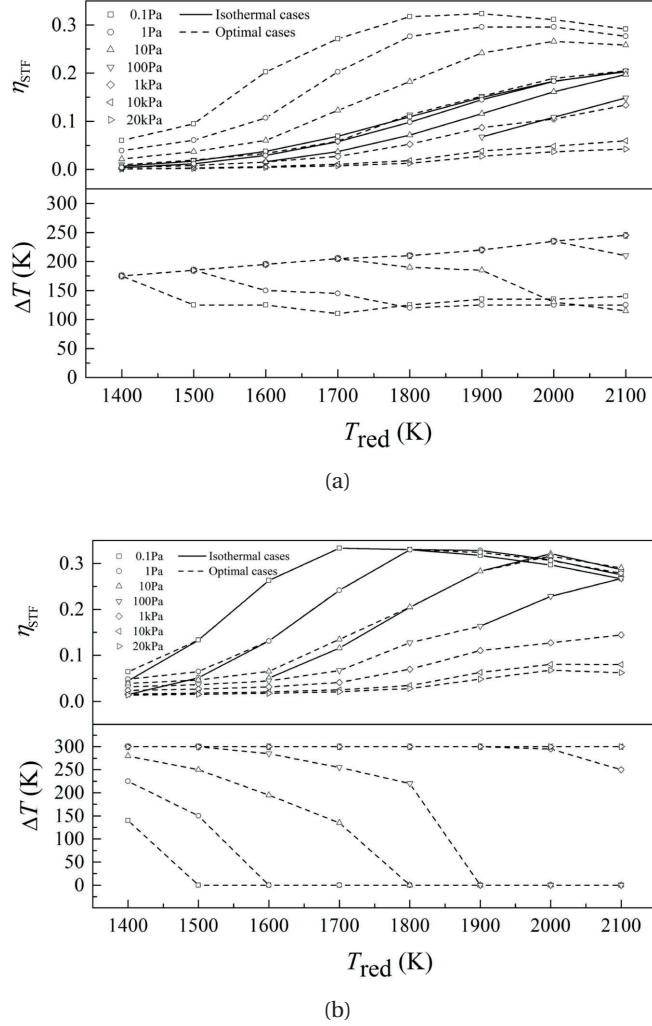


Figure 2.3 – Optimal  $\eta_{STF}$  (dotted lines) and corresponding  $\Delta T$  for various  $T_{red}$  and  $p_{O_2,1}$  combinations for (a) scheme (a), and (b) scheme (b). The solid lines indicate the efficiency at corresponding  $T_{red}$  and  $p_{O_2,1}$  for isothermal operation ( $\Delta T = 0$ ).

For scheme (a), the best performing cases for all combinations of  $T_{red}$  and  $p_{O_2,1}$  operated non-isothermally ( $\Delta T > 0$ ). The optimal  $\eta_{STF}$  increased with increasing  $T_{red}$  due to decreasing  $\dot{Q}_{gas,ox}$ , and increasing  $\Delta\delta$ , until  $\dot{Q}_{heat loss}$  started to dominate the energy balance resulting in a decreasing  $\eta_{STF}$  (see figure 2.4d). The impact of  $T_{red}$  on  $\eta_{STF}$  at isothermal operation is illustrated in figures 2.4a and revealed that initially  $\dot{Q}_{gas,red}$ ,  $\dot{Q}_{gas,ox}$ , and  $\dot{Q}_{heat loss}$  were dominating. The latter was continuously increasing with increasing  $T_{red}$ , while the former two were monotonically decreasing at a faster rate.



Compared to the isothermal operation, a small  $\Delta T$  led to a significantly higher  $\eta_{\text{STF}}$ , i.e. the STF efficiency for  $p_{\text{O}_2,1} = 0.1$  Pa,  $T_{\text{red}} = 1800$  K was 11% for isothermal operation and 31% at  $\Delta T = 135$  K. The increase of  $\Delta T$ , while increasing  $\dot{Q}_{\text{solid}}$ , resulted in a significant drop of  $\delta_{\text{ox}}$  which results in an increase in the hydrogen production due to the increasing (see figure 2.4c). The amount of inert sweep gas required decreased with increasing  $\Delta T$  due to significantly increasing  $p_{\text{O}_2,4}$  and consequently reduced sweep gas amount hence reduced  $\dot{Q}_{\text{gas,red}}$ . At  $\Delta T > 150$  K, appeared and increased with  $\dot{Q}_{\text{cool,ox}}$  reducing the efficiency gain brought by the decrease of  $\dot{Q}_{\text{gas,red}}$  (figure 2.4c). This indicates that a temperature swing will largely increase the system performance compared to isothermal operation and there exist an optimal  $\Delta T$  for the best performance which is in the range of 125 K.

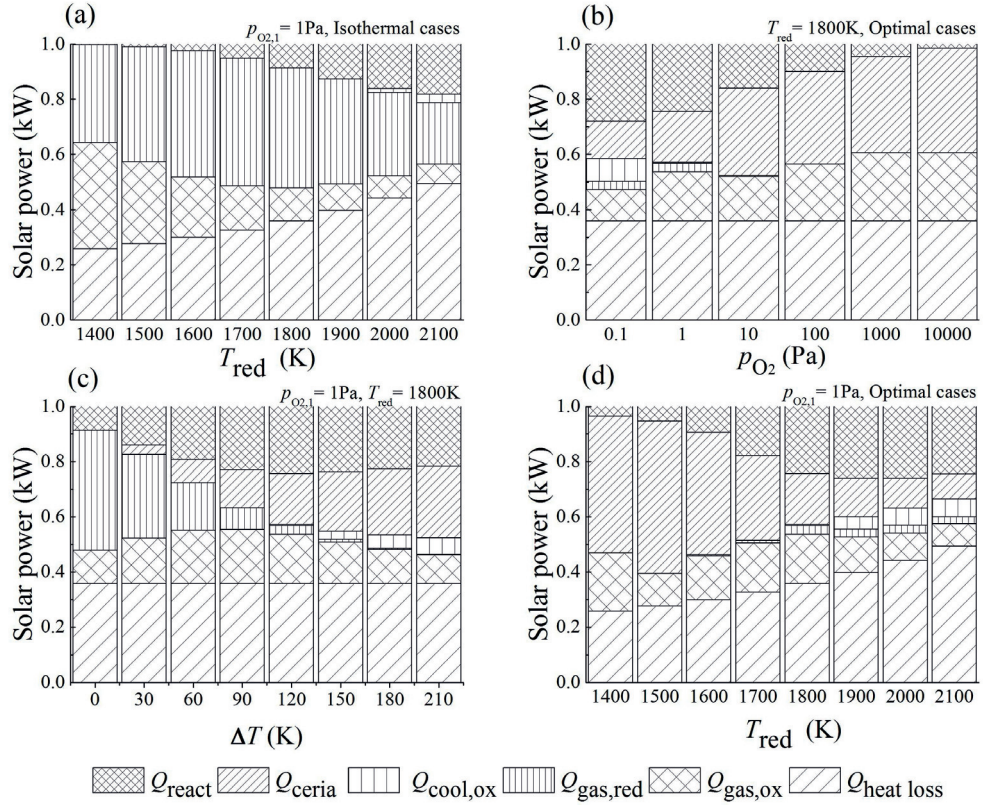


Figure 2.4 – Energy balance for scheme (a) at 1 kW solar power input under various working conditions: a) isothermal cases at  $p_{\text{O}_2,1} = 1$  Pa for varying  $T_{\text{red}}$ , (b) optimal cases at  $T_{\text{red}} = 1800$  K for varying  $p_{\text{O}_2,1}$ , (c) cases at  $p_{\text{O}_2,1} = 1$  Pa and  $T_{\text{red}} = 1800$  K for varying  $\Delta T$ , and (d) optimal cases at  $p_{\text{O}_2,1} = 1$  Pa for varying  $T_{\text{red}}$

Lowering  $p_{\text{O}_2,1}$  always causes an increase in  $\eta_{\text{STF}}$  for a given  $T_{\text{red}}$  due to the significant increase in  $\delta_{\text{red}}$ . The  $T_{\text{red}}$  for optimal  $\eta_{\text{STF}}$  moved to higher values as  $p_{\text{O}_2,1}$  increased while requiring larger  $\Delta T$  (see figure 2.3a). For very large  $p_{\text{O}_2,1}$ , the low  $\Delta \delta$  is the reason for low efficiencies.

This can be alleviated by operating at larger  $\Delta T$ .

Small  $\delta_{\text{red}}$  resulted at low  $T_{\text{red}}$  and large  $p_{\text{O}_2,1}$ . These combinations required a large  $\Delta T$  (often unfeasible, see figure 2.2b) for reasonable efficiencies and comparatively higher  $\Delta\delta$ . As  $T_{\text{red}}$  increased,  $\delta_{\text{red}}$  increased gradually leading to a dominating and corresponding required a decrease in  $\Delta T$ , for optimal  $\eta_{\text{STF}}$  (see figure 2.3a). For  $p_{\text{O}_2,1} > 100$  Pa,  $\Delta T$  was always restricted by the feasibility conditions and consequently the activity of the reduction of ceria is hindered at large  $p_{\text{O}_2,1}$ . A slight increase in  $\Delta T$  was detected for  $p_{\text{O}_2,1} = 0.1$  Pa and 1 Pa at 1700 K and 1800 K, respectively. This is due to the appearance of  $\dot{Q}_{\text{cool,ox}}$  at high temperatures which can partly be compensated by a larger  $\Delta T$ .

The results for scheme (b) revealed that the optimal  $\eta_{\text{STF}}$  under various given  $T_{\text{red}}$  and  $p_{\text{O}_2,1}$  tend to work at lower  $\Delta T$  which favored isothermal operation compared to scheme (a). This trend was especially pronounced at higher temperatures ( $T_{\text{red}} \geq 1800$  K). This was caused by the increase in  $\Delta\delta$  and decrease in  $\dot{Q}_{\text{pump}}$  and  $\dot{Q}_{\text{gas,ox}}$  with increasing  $\Delta T$  and  $T_{\text{red}}$ , which was overcompensated by the increasing  $\dot{Q}_{\text{cool,ox}}$  and  $\dot{Q}_{\text{ceria}}$  (see figure 2.5c and 2.5d).

Similar trends in the optimal  $\eta_{\text{STF}}$  (i.e. at non-isothermal conditions,  $\Delta T \neq 0$ ) were observed for scheme (b) and scheme (a). Increasing  $p_{\text{O}_2,1}$  led to a significant reduction in  $p_{\text{O}_2,1}$  for the whole range of  $p_{\text{O}_2,1}$  studied (0.1 Pa to 20000 Pa) for  $T_{\text{red}} < 1700$  K. For  $T_{\text{red}} > 1700$  K,  $p_{\text{O}_2,1} > 0.1$  Pa showed larger optimal  $\eta_{\text{STF}}$  than ( $\eta_{\text{STF}} = 30\%$  for  $p_{\text{O}_2,1} = 0.1$  Pa, and  $\eta_{\text{STF}} = 31\%$  for  $p_{\text{O}_2,1} = 1$  Pa at  $T_{\text{red}} = 2000$  K) due to the decrease in  $\dot{Q}_{\text{pump}}$ ,  $\dot{Q}_{\text{cool,ox}}$ , and  $\dot{Q}_{\text{cool,red}}$  at high  $T_{\text{red}}$  (figure 2.5b and 2.5d) which overruled the decrease of  $\Delta\delta$ .

The efficiencies of the system for  $\text{CO}_2$  splitting (eqs. 3 and 5) showed similar trends as the ones described for water splitting in schemes (a) and (b) with generally higher efficiencies due to larger equilibrium constants for the oxidation reaction in the  $\text{CO}_2$  splitting system. The efficiency variations for solar thermochemical ceria-based  $\text{CO}_2$  splitting for varying  $T_{\text{red}}$ ,  $p_{\text{O}_2,1}$ , and  $\Delta T$  are shown in figures B.1.

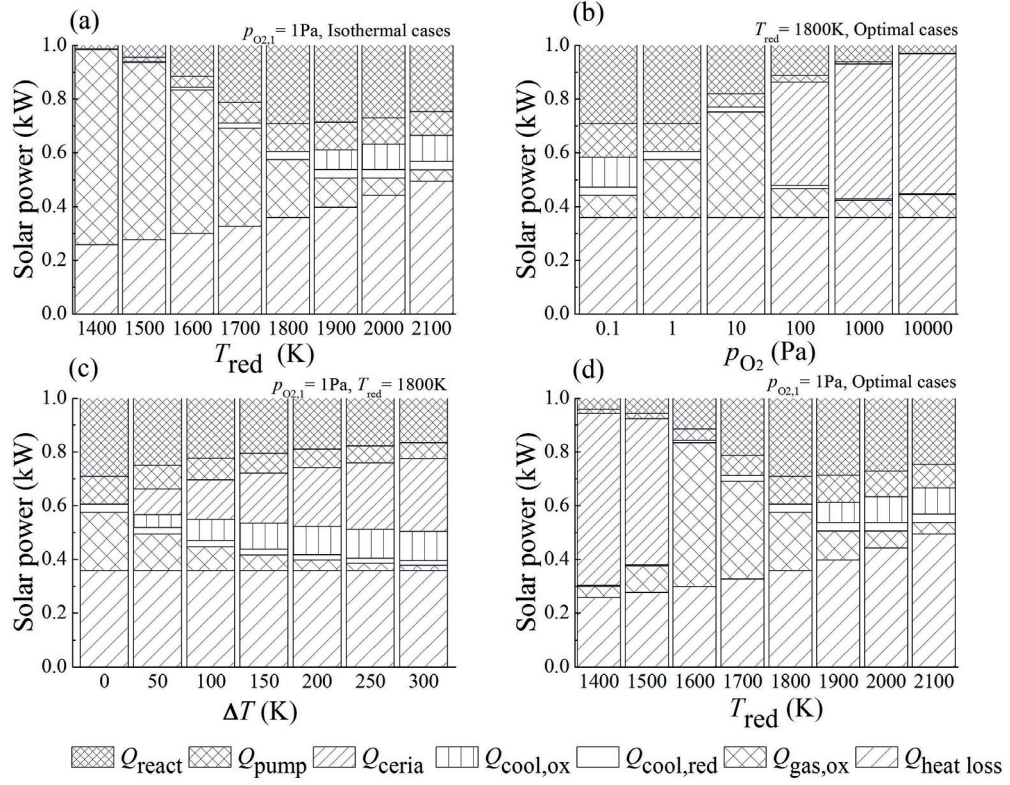


Figure 2.5 – Energy balance for scheme (b) at 1kW solar power input under various working conditions: (a)  $p_{O_2,1} = 1$  Pa for varying  $T_{red}$ , (b) optimal cases at  $T_{red} = 1800$  K for varying  $p_{O_2,1}$ , (c)  $p_{O_2,1} = 1$  Pa and  $T_{red} = 1800$  K for varying  $\Delta T$ , and (d) optimal cases at  $p_{O_2,1} = 1$  Pa for varying  $T_{red}$ .

### 2.2.3 Hydrogen productivity

In addition to an optimized STF efficiency, the hydrogen productivity should be maximized in order to minimize the amount of metal oxide which needs to be cycled (pumping requirements), bought and refilled (economic investment), and mined and recycled (sustainability issue).

$\chi_{H_2}$  is shown in figure 2.6 exemplary for a practical  $T_{red}$  of 1800 K.  $\chi_{H_2}$  increased with increasing  $\Delta T$  and decreasing  $p_{O_2,1}$ . The two zones shown in figure 2.6 distinguished the accessibility of  $\Delta T$  for scheme (a) and scheme (b) as discussed in section 2.2.1. For scheme (a), the  $\Delta T$  was limited by  $p_{O_2,4}$  and the operation is only possible in zone 1. For scheme (b), the operation was not confined by  $p_{O_2,4}$  and hence zone 1 and zone 2 were accessible. The increase in  $\Delta T$  effected a lower  $\delta_{ox}$  resulting in a larger  $\Delta\delta$  and correspondingly larger  $\chi_{H_2}$ . Generally, the optimal efficiencies of scheme (a) were situated at  $\Delta T > 0$  and correspondingly higher hydrogen productivities were achieved (indicated by the hollow dots in figure 2.6) compared

to the optimal efficiencies of scheme (b), which usually were isothermal or at low  $\Delta T$  (for  $p_{O_2,1} < 100$  Pa). For  $p_{O_2,1} \geq 100$  Pa, large  $\chi_{H_2}$  were achieved in scheme (b), however,  $\eta_{STF}$  was significantly limited by low  $\Delta\delta$ . Generally, operating at optimal efficiencies and low required more ceria per produced hydrogen for vacuum pumping approach (scheme (b)) compared to sweep gassing (scheme (a)). Since the sensitivity of the efficiency with the variation of  $\Delta\delta$  for scheme (b) at 1800 K is small (see figure 2.5c), it is possible to optimize the operational conditions for scheme (b) by operating at a small  $\Delta T$  (within 150 K) to achieve both high STF efficiency (28% at  $T_{red} = 1800$  K,  $p_{O_2,1} = 1$  Pa, and  $\Delta T = 120$  K) and comparatively larger hydrogen productivity.

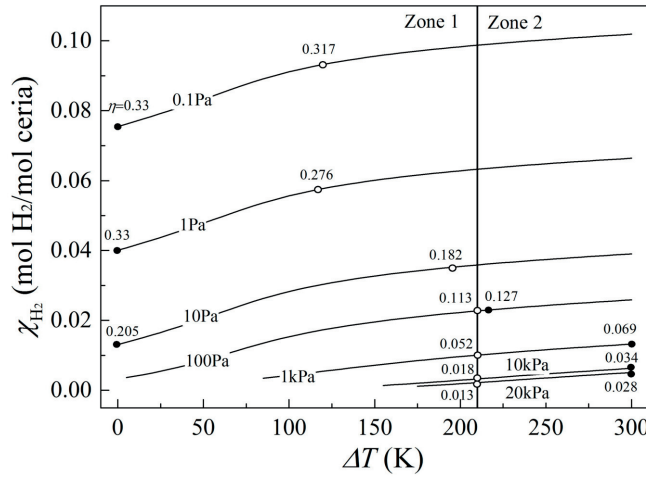


Figure 2.6 –  $H_2$  productivity as a function of  $\Delta T$  for different  $p_{O_2,1}$  at  $T_{red} = 1800$  K for scheme (a) (Zone 1) and scheme (b) (Zones 1 and 2). Dots indicate the optimal efficiency at the corresponding conditions ( $\Delta T$  and  $p_{O_2,1}$ ) for scheme (a) (hollow dots) and scheme (b) (filled dots).

#### 2.2.4 Water utilization factor

Figure 2.7 exemplary shows  $f_w$  for schemes (a) and (b) at  $T_{red} = 1800$  K for varying  $p_{O_2,1}$  and  $\Delta T$ . Generally, lower  $p_{O_2,1}$  and higher  $\Delta T$  led to larger  $f_w$ .  $\delta_{red}$  increases and correspondingly  $p_{O_2,12}$  decreased with decreasing  $p_{O_2,1}$  hence requiring a smaller water input. The enhancement in  $f_w$  with increasing  $\Delta T$  was more pronounced at lower  $p_{O_2,1}$  in accordance with a larger  $\Delta\delta$  at these conditions and more efficient water use. The increase in  $f_w$  with increasing  $\Delta T$  resulted from the lower  $p_{O_2,1}$  at higher  $\Delta T$ .

Similar as for  $\chi_{H_2}$ , scheme (a) worked at higher efficiency when  $\Delta T \neq 0$ , which in turn resulted in larger  $f_w$ . For scheme (b), isothermal operation led to higher  $\eta_{STF}$  while unfavorably reducing the hydrogen productivity and  $f_w$ , which increased the consumption of input materials (water and ceria).



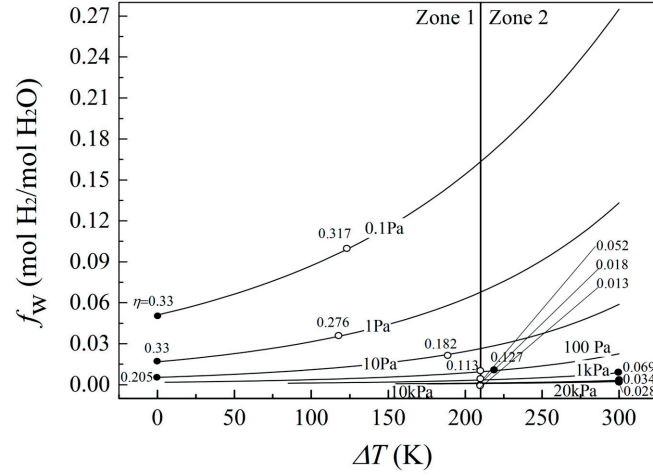


Figure 2.7 –  $f_w$  as a function of  $\Delta T$  for different  $p_{O_2,1}$  at  $T_{red} = 1800$  K for scheme (a) (Zone 1) and scheme (b) (Zones 1 and 2). Dots indicate the optimal efficiency at the corresponding conditions ( $p_{O_2,1}$  and  $\Delta T$ ) for scheme (a) (hollow dots) and scheme (b) (filled dots).

### 2.2.5 Pump efficiency

The electricity-to-pump efficiency,  $\eta_{pump}$ , for scheme (b) was assumed constant (40%) but practical vacuum pumps (rotary vane, piston, scroll, or roots pumps) show non-constant efficiencies changing with working conditions (pressure and flow rate). The effect of the decreasing pump efficiency with decreasing  $p_{O_2,1}$  is depicted in figure 2.8a for a turbo molecular vacuum pump system of Pfeiffer Vacuum with a pump efficiency estimated as [30],

$$\eta_{pump} = 0.4 + 0.07 \log \frac{p_{O_2,1}}{p_0}. \quad (2.15)$$

The optimal  $\eta$  was significant affected by  $\eta_{pump}$  at low  $p_{O_2,1}$  due to the decrease in  $\eta_{pump}$  with decreasing  $p_{O_2,1}$ . The increased power required for reducing the oxygen partial pressure is offset through an increase in  $T_{red}$ .

The optimal  $\eta_{STF}$  was achieved at isothermal operation at low  $p_{O_2,1}$ , supporting the previous conclusion that vacuum pumping is the method of choice to lower the at isothermal conditions. The effect of  $\eta_{pump}$  on the optimal  $\eta_{STF}$  under different  $p_{O_2,1}$  is depicted in figure 8.b and exhibits that  $\eta_{pump}$  of 40% is required to overcome the limitations posed by the pumping work. Further increase in  $\eta_{pump}$  showed no significant increase in the STF efficiency. These investigations provide guidelines for the choice of the vacuum pump technology and quality.

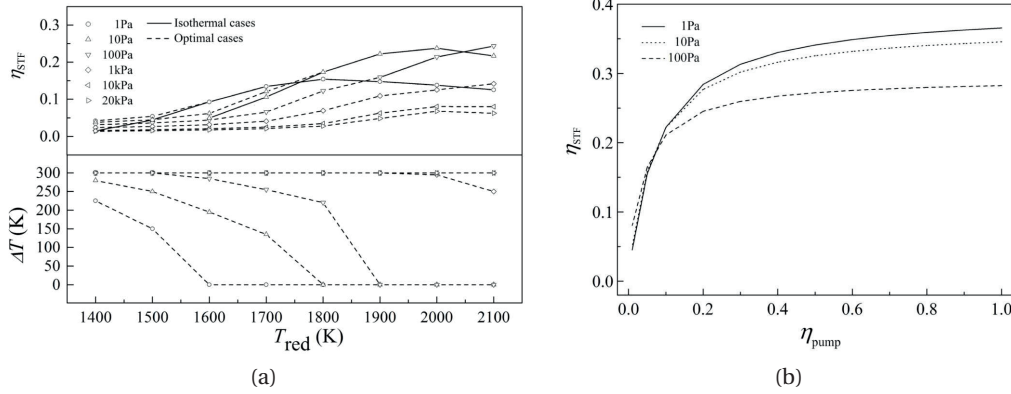


Figure 2.8 – (a) Optimal  $\eta_{STF}$  for various  $T_{red}$  and for scheme (b) with changing  $\eta_{pump}$  according to eq. 2.15, and (b) optimal  $\eta_{STF}$  as a function of  $\eta_{pump}$  for three different  $p_{O_{2,1}}$  (1Pa, 10Pa, and 100Pa).

## 2.2.6 Heat recovery effectiveness

### Gas phase heat recovery effectiveness

Gas phase heat recovery is crucial in dictating a large  $\eta_{STF}$  [29]. As depicted in figure 2.9a, the larger  $\varepsilon_g$  the larger  $\eta_{STF}$  at isothermal condition for scheme (a).  $\varepsilon_g$  as high as 0.975 was required for  $\eta_{STF} > 10\%$  at  $T_{red} = 1700$  K. The increase in  $\eta_{STF}$  was more pronounced at larger  $\varepsilon_g$  and with increasing  $T_{red}$ , further suggesting that the requirements on the high-temperature heat exchanger manufacturing and maintenance were stringent when considering isothermal operation. The requirements on the heat exchanger can be relaxed through the use of a temperature swing as depicted in figure 2.9b. At  $\varepsilon_g < 0.9$ , the maximum  $\eta_{STF}$  appeared at the largest possible  $\Delta T$ , where  $\Delta T$  was limited by the operational feasibility (see section 2.2.1). For  $\eta_{STF} > 0.9$ , the highest STF efficiency was observed at an optimized  $\Delta T$  which maximized the  $\Delta\delta$  while limiting  $\dot{Q}_{ceria}$ .

For scheme (b), increasing  $\varepsilon_g$  at isothermal operation led to a significant increase in  $\eta_{STF}$  at lower  $T_{red}$  ( $T_{red} < 1800$  K), while a less pronounced effect was exhibited at high  $T_{red}$  (see figure 2.9c) due to the exhibited dominance of  $\dot{Q}_{heat\ loss}$  (see figure 2.5). Compared to scheme (a), the requirements on the heat exchanger were less stringent and already a  $\varepsilon_g$  of 0.85 was sufficient to reach  $\eta_{STF} > 10\%$  at  $T_{red} = 1700$  K. The requirements on the heat exchanger can be further relaxed when operating non-isothermally, as depicted in figure 2.9d. At  $\Delta T = 300$  K,  $\eta_{STF}$  was equal for  $\varepsilon_g = 0.5$  and 0.975. An optimal  $\Delta T$  for maximized optimal efficiency was observed for  $\varepsilon_g < 0.9$ . This results from a tradeoff between decreasing  $\dot{Q}_{gas,ox}$  and increasing  $\dot{Q}_{ceria}$  and  $\dot{Q}_{cool,ox}$  as  $\Delta T$  increases. For  $\varepsilon_g > 0.9$ , the decrease in with increasing  $\Delta T$  was not observable as  $\dot{Q}_{ceria}$  and  $\dot{Q}_{cool,ox}$  dominate the losses already  $\Delta T = 0$  and further increase

with increasing  $\Delta T$ . Consequently, for  $\varepsilon_g > 0.9$ , isothermal operation results in the best performing STF efficiency. This feature of the scheme (b) indicates that  $\varepsilon_g \geq 0.9$  is required to ensure that isothermal operation results in the highest STF efficiency for a certain  $T_{\text{red}}$  and  $p_{\text{O}_{2,1}}$  combination. Nevertheless, the introduction of a small  $\Delta T$  can significantly reduce the requirements on the heat exchanger at a reasonable penalty in STF efficiency, i.e. introducing a  $\Delta T$  of 50 K reduced the STF efficiency by 5.2% at  $\varepsilon_g = 0.975$ .

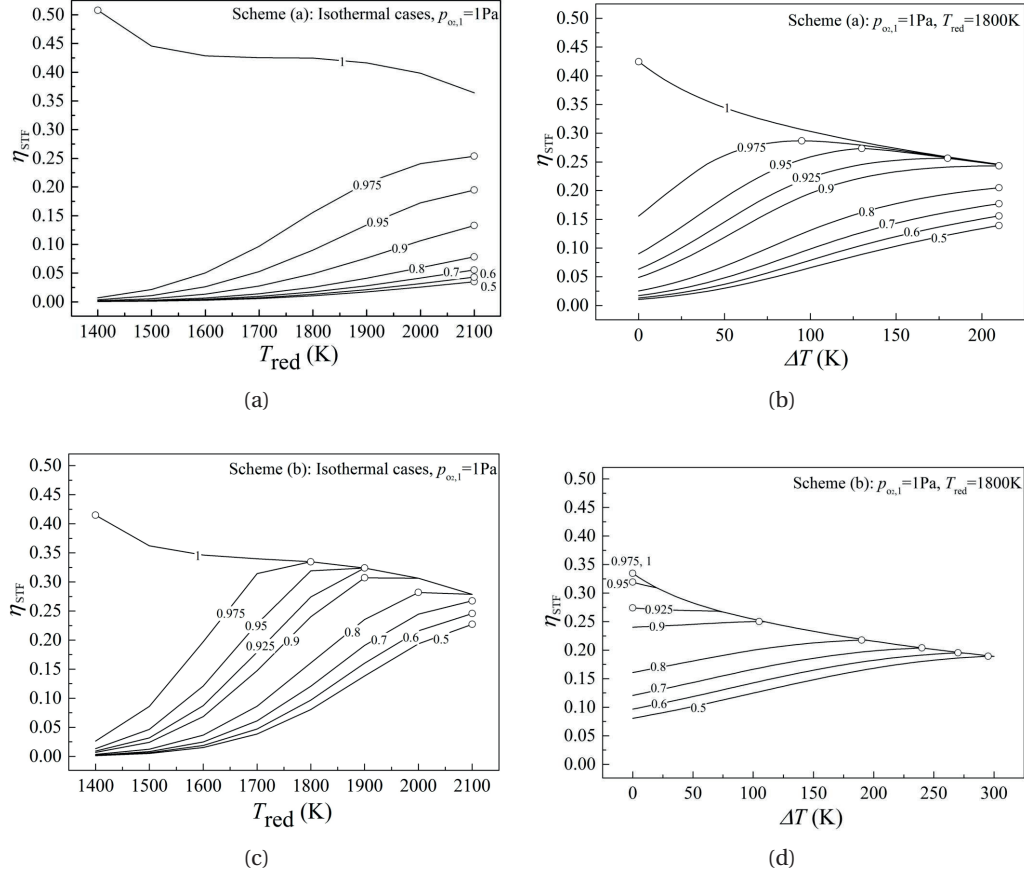


Figure 2.9 – STF efficiency at isothermal conditions for  $p_{\text{O}_{2,1}} = 1 \text{ Pa}$  and varying  $T_{\text{red}}$  and  $\varepsilon_g$ , for (a) scheme (a), and (c) scheme (b); and non-isothermal conditions at  $p_{\text{O}_{2,1}} = 1 \text{ Pa}$  and  $T_{\text{red}} = 1800 \text{ K}$  for varying  $\Delta T$  and  $\varepsilon_g$ , for (b) scheme (a), and (d) scheme (b). The maximal efficiencies for each  $\varepsilon_g$  are marked by the dots.

For  $\varepsilon_g = 1$ , the STF efficiency solely decreased with increasing  $T_{\text{red}}$  for isothermal operation of schemes (a) and (b), e.g. the efficiency of scheme (a) decreased from 50.8% to 36.4% as  $T_{\text{red}}$  increased from 1400 K to 2100 K. This was explained by the fact that the usually dominating  $\dot{Q}_{\text{gas,red}}$  and  $\dot{Q}_{\text{gas,ox}}$  (see figures 2.4 and 2.5) were significantly reduced and the energy balance was then dominated by the monotonically increasing  $\dot{Q}_{\text{heat loss}}$ . The STF efficiency was significantly increased at perfect gas heat recovery: the STF efficiency increased

up to 50% at  $T_{\text{red}} = 1400$  K when  $\varepsilon_g$  increases from 0.975 to 1 for scheme (a). Similar behavior was observed for the non-isothermal operation of scheme (a) at  $\varepsilon_g = 1$ , namely solely a decrease in STF efficiency with increasing  $\Delta T$ , which could again be explained by the reduction of the otherwise dominating  $\dot{Q}_{\text{gas,red}}$  and  $\dot{Q}_{\text{gas,ox}}$ .

### Solid phase heat recovery effectiveness

Effects of  $\varepsilon_s$  on  $\eta_{\text{STF}}$  for varying  $\Delta T$  are exemplary depicted in figure 2.10 at  $T_{\text{red}} = 1800$  K and  $p_{\text{O}_2,\text{red}} = 1$  Pa. Generally,  $\eta_{\text{STF}}$  increased with increasing  $\varepsilon_s$ . This enhancement was more pronounced for larger  $\Delta T$  due to the increased recuperation of  $\dot{Q}_{\text{solid}}$ . For scheme (a), a significant raise in the maximal optimal  $\eta_{\text{STF}}$  of absolute 5% was observed when raising  $\varepsilon_s$  from 0 to 0.5. The optimal  $\Delta T$  increased for maximal optimal  $\eta_{\text{STF}}$  with increasing  $\varepsilon_s$  due to reduction in  $\dot{Q}_{\text{solid}}$ .  $\dot{Q}_{\text{solid}}$  became less significant when  $\varepsilon_s$  increased above 0.5 and therefore the benefit of an increasing  $\Delta\delta$  at higher  $\Delta T$  dominated over the increased  $\dot{Q}_{\text{solid}}$  and  $\dot{Q}_{\text{cool,ox}}$ .

As shown in figure 2.10b, scheme (b) displayed the maximal  $\eta_{\text{STF}}$  at isothermal operation.  $\eta_{\text{STF}}$  decreased with increasing  $\Delta T$  at  $\varepsilon_s < 0.9$  due to increase in  $\dot{Q}_{\text{solid}}$  and  $\dot{Q}_{\text{cool,ox}}$ , which counteracted the decrease in  $\dot{Q}_{\text{pump}}$  and increase in  $\Delta\delta$ . At  $\varepsilon_s \geq 0.9$ , a small  $\Delta T$  of about 10 K led to increased  $\eta_{\text{STF}}$  due to the increase of  $\Delta\delta$  while the increase in  $\dot{Q}_{\text{solid}}$  and  $\dot{Q}_{\text{cool,ox}}$  were insignificant. As  $\Delta T$  increased further, the benefit of increased  $\Delta\delta$  became insignificant compared to the increasing losses.

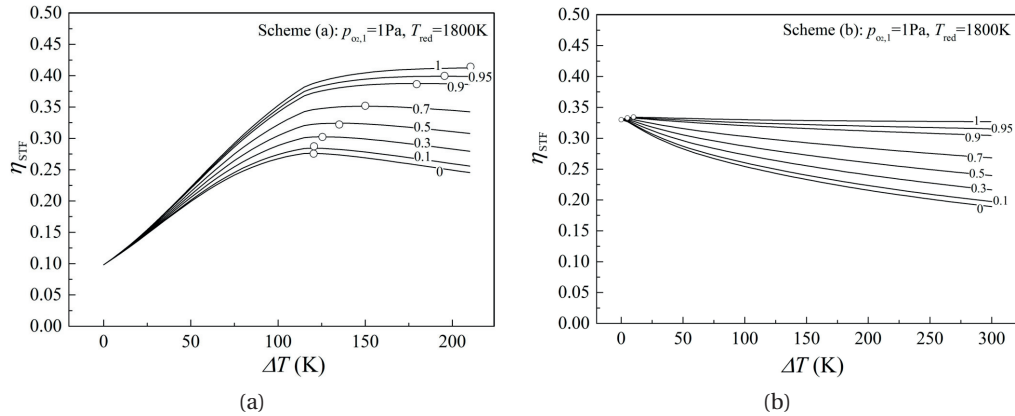


Figure 2.10 – STF efficiency as a function of  $\Delta T$  for varying  $\varepsilon_s$  at  $p_{\text{O}_2,1} = 1$  Pa and  $T_{\text{red}} = 1800$  K for (a) scheme (a), and (b) scheme (b). The maximal efficiencies for each  $\varepsilon_s$  are marked by the dots.



### 2.2.7 Concentration ratio

The impact of concentration ratio,  $CR$ , on  $\eta_{STF}$  for schemes (a) and (b) is shown in figure 2.11. The  $CR$  of a solar concentration system was determined by the type of the concentrator used and chosen from 1000 to 10000 according to the feasibility of solar tower and dish systems [103].

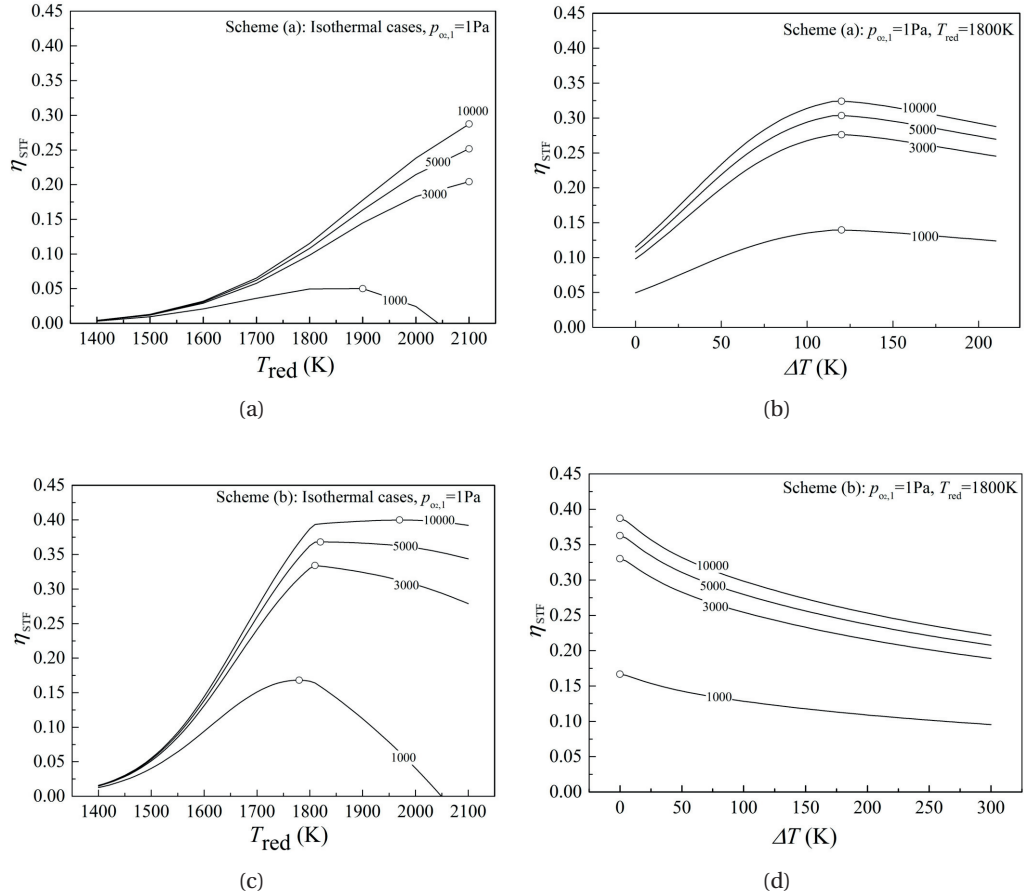


Figure 2.11 –  $\eta_{STF}$  as a function of  $T_{red}$  for various  $C$  at  $p_{O_2,1} = 1$  Pa at isothermal operation for (a) scheme (a), and (c) scheme (b).  $\eta_{STF}$  as a function of  $\Delta T$  for various  $C$  at  $p_{O_2,1} = 1$  Pa and  $T_{red} = 1800$  K for (b) scheme (a), and (d) scheme (b). The maximal efficiencies for each  $C$  are marked by the dots.

Generally, higher  $CR$  led to higher  $\eta_{STF}$ , although the increase in  $\eta_{STF}$  became small for  $CR > 5000$ . For isothermal operation,  $\eta_{STF}$  increased with  $T_{red}$  due to increasing  $\Delta\delta$  and decreased due to the dominance of  $\dot{Q}_{heat\ loss}$  at high  $T_{red}$ . The decrease in  $\eta_{STF}$  was reduced at increased  $CR$  as the aperture was reduced and correspondingly the losses were relatively reduced (see eq. 2.2). The optimal  $T_{red}$  for maximal  $\eta_{STF}$  increased for the isothermal cases in schemes (a) and (b) due to the beneficial higher  $\Delta\delta$ . For the selected cases at  $T_{red} = 1800$  K, the optimal  $\Delta T$  for

maximal optimal  $\eta_{\text{STF}}$  was always at 120 K for scheme (a) and 0 K for scheme (b), respectively.

### 2.2.8 Combined mechanical and mechanical-chemical approaches

Reduction in  $p_{\text{O}_2,1}$  significantly increased the STF efficiency. In order to further decrease the oxygen partial pressure while circumventing low pumping efficiencies, high pumping power requirements, or significant sensible heat losses required to heat the inert gas, a combination of mechanical and chemical techniques to reduce the oxygen partial pressure were proposed. Specifically, scheme (a) in combination with a chemical oxygen scavenger made of magnesium (scheme (c)) was investigated. The magnesium acted as reducing agent and reacts with the oxygen before it enters the reduction chamber. Magnesium is a strong reducing agent and is able to reduce the partial pressure of oxygen in sweep gas to values lower than  $10^{-17}$  atm [101]. The calculated efficiencies of scheme (c) under different  $p_{\text{O}_2,1}$  are shown in figure 2.12a. The energy penalty introduced for MgO recycling was 3600 kJ/mol assuming MgO reduction by the Bolzano process [100]. The chemical reduction of  $p_{\text{O}_2,1}$  in the sweep gas led to higher  $\eta_{\text{STF}}$  for the optimal cases because of a further reduction in the required sweep gas. For isothermal operation, the use of an oxygen scavenger showed no increase in  $\eta_{\text{STF}}$  as the energy penalty caused by the large amount of magnesium required to scavenge the oxygen of the large amount of sweep gas traded off the increase in efficiency due by lower  $p_{\text{O}_2,1}$ .

The effect of  $\dot{Q}_{\text{Mg,pr}}$  on the STF efficiency of the system is depicted in figure 2.12a and showed no significant efficiency penalty for the selected values of  $\dot{Q}_{\text{Mg,pr}}$  between 0 to 9000 kJ/mol, which corresponded to free MgO recycling and MgO recycling by the Pidgeon process [100].

A combination of sweep gassing, vacuum pumping, and chemical scavenger (scheme e) allowed for a further increase in efficiency due to a decrease in system pressure. The basic idea of this combination was to reduce  $p_{\text{O}_2,1}$  in the sweep gas from the baseline value (1 Pa), to a target value (0.1 Pa) through the oxygen scavenger. The vacuum pump was then used to further reduce the  $p_{\text{O}_2,1}$  in reduction chamber by reducing the system pressure,  $p_{\text{system}}$ . Figure 2.13 depicts the change of  $\eta_{\text{STF}}$  with different  $p_{\text{system}}$  for both optimal and isothermal operations when varying  $p_{\text{system}}$  between 1 atm and 0.1 atm. For isothermal operation, a minimum in  $\eta_{\text{STF}}$  was observed when decreasing  $p_{\text{system}}$  from 1 atm to 0.1 atm. The maximal  $\eta_{\text{STF}}$  was observed at  $p_{\text{system}} = 1$  atm as the gain in efficiency with decreasing  $\delta_{\text{red}}$  at low oxygen partial pressure was overruled by the large pumping work due to the large amount of sweep gas needed in isothermal operation. For the optimal cases, a reduction in  $p_{\text{system}}$  increased the efficiency. This effect was less pronounced at higher temperatures as the amount of sweep gas required was higher at higher  $T_{\text{red}}$  which makes pumping work costly.

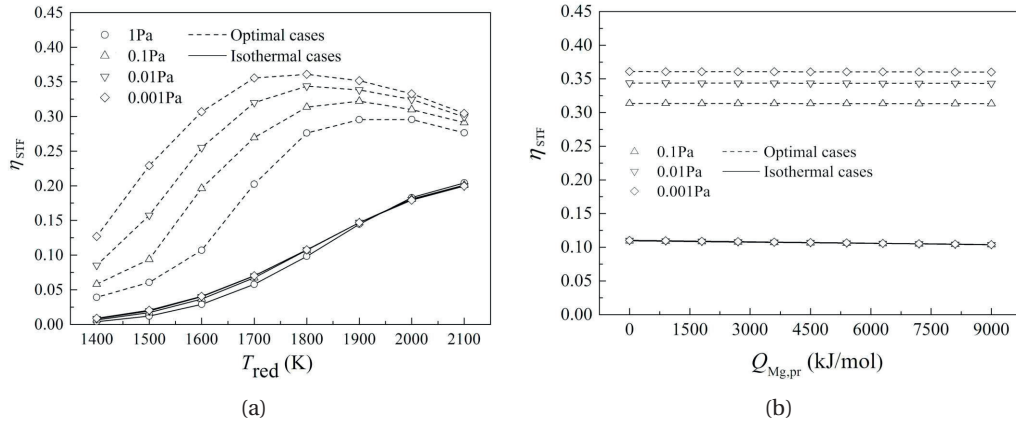


Figure 2.12 – (a)  $\eta_{STF}$  as a function of  $T_{red}$  at various  $p_{O_2,1}$  for  $\dot{Q}_{Mg,pr} = 3600$  kJ/mol for optimal and isothermal cases. (b)  $\eta_{STF}$  as a function of  $\dot{Q}_{Mg,pr}$  for various of  $p_{O_2,1}$  at  $T_{red} = 1800$  K for optimal and isothermal cases.

The use of vacuum pumping to lower the system pressure indicated less improvement in efficiency compared to the use of an oxygen scavenger in combination with sweep gassing (figure 2.12). This conclusion also held for the combination of the mechanical methods (sweep gassing + vacuum pumping, scheme (d)), where the same behavior as indicated in figure 2.13 was observed.

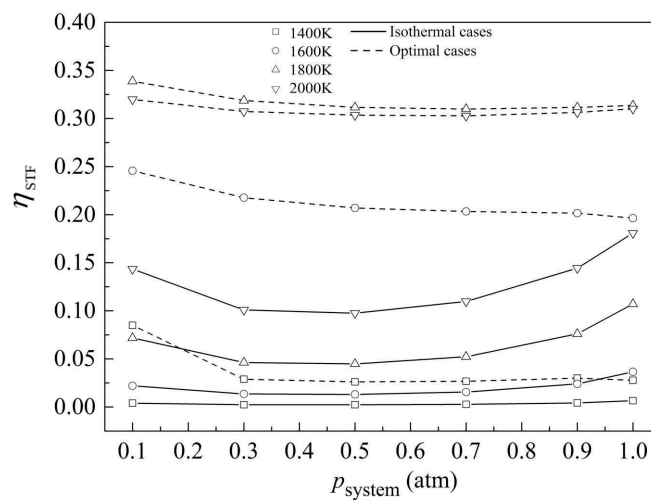


Figure 2.13 –  $\eta_{STF}$  as a function of  $p_{system}$  for various  $T_{red}$  at  $\dot{Q}_{Mg,pr} = 3600$  kJ/mol for both optimal and isothermal cases for scheme (c).

**2.2.9 Counterflow versus ideal mixing reactor configurations**

A counterflow arrangement represents a counter-current flow between ceria and the gases which assumes that the gases are well mixed in the radial direction and only vary in the axial direction. The ideal mixing arrangement models a well-mixed reactor, resulting in no spatial variation of temperature, pressure, and species concentrations [102]. Compared to the counter-flow arrangement, the ideal mixing arrangement required enormous amounts of sweep gas due to the need to maintain the whole reduction chamber at a low  $p_{O_2,1}$ . Owing to the large amount of sweep gas input, the previous studies utilizing ideal mixing arrangements [23, 24] predicted that larger  $p_{O_2,1}$  (of about 1000 Pa) favor larger efficiencies and operation at large  $\Delta T$  (to ensure a complete oxidation of ceria).

The efficiencies of schemes (a) and (b) at various operating conditions for an ideal mixing arrangement are shown in figures B.2 to B.6. Scheme (a) always worked at low efficiencies ( $\eta_{STF} < 15\%$ ) and favored isothermal operation. The small efficiencies were caused by the large sweep gas and water input flow rates, respectively, which dominated the energy demand (figure B.3). Scheme (b) showed efficiencies significantly larger than for scheme (a) due to a large decrease in the energy consumption to keep the  $p_{O_2,1}$  in the reduction chamber low. Compared to the counterflow arrangement, the ideal mixing model tended to inefficiently use the water inflow and requires more sweep gas input, all of which led to significant lower efficiencies. The effect of changing  $\varepsilon_g$  on the system performance is shown in figure B.5. As for the counterflow arrangement, for scheme (a) at isothermal conditions and in ideal mixing arrangement, larger  $\varepsilon_g$  resulted in larger efficiencies. This increase became more significant for  $\varepsilon_g > 0.9$ . Isothermal operation was favored in the ideal mixing arrangement as the reduction in  $\dot{Q}_{gas,red}$  with increasing  $\Delta T$  was too small to overcome the increase in  $\dot{Q}_{ceria}$  and  $\dot{Q}_{gas,ox}$  (figure B.3c). Similar behavior in efficiency variation was observed for scheme (b) for the ideal mixing arrangement. However, scheme (b) could achieve larger efficiencies than scheme (a) as vacuum pumping required less energy than sweep gassing to maintain a low-oxygen atmosphere in the reaction chamber.

The influence  $\varepsilon_s$  on the solar-to fuel efficiency is shown in figure B.6a, and indicated negligible impact on scheme (a) in an ideal mixing arrangement due to the extremely low ceria flow rates. For scheme (b), the increase of  $\varepsilon_s$  led to higher efficiencies. However, this increase was small for large  $\Delta T$  (figure B.6b) due to the decreasing  $\dot{Q}_{ceria}$  resulting from the decreasing ceria flow rate.

Generally, the ideal mixing arrangement is inferior to counterflow arrangement for schemes (a) and (b) because of significantly lower water utilization and the requirement of extremely large rates of sweep gas.

### 2.3. High temperature electrolysis vs. thermochemical cycles

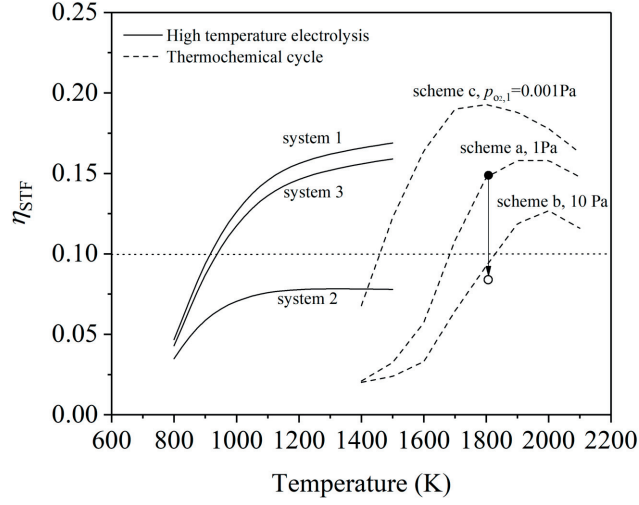


Figure 2.14 –  $\eta_{STF}$  as a function of  $T$  for high temperature electrolysis systems (solid lines, system 1,2, and 3 with ambient pressure), and thermochemical cycles (dashed lines, scheme a, b, and c with selected  $p_{O_2,1}$ ). The arrow indicates the STF efficiency drop for schema a when  $\epsilon_g$  decreased from 0.955 to 0.8.

### 2.3 High temperature electrolysis vs. thermochemical cycles

Two high-temperature routes for solar fuel production are compared in this section in terms of  $\eta_{STF}$  based on the studies from chapter 1 and 2. The  $\eta_{STF}$  definitions for thermochemical cycles and high-temperature electrolysis systems are different in two aspects: *i*) the optical efficiency of the solar concentrator, and *ii*) the diffuse part of the solar irradiance were not considered in thermochemical cycles' analysis (eq. 1.12). For a direct comparison between two routes, we unified the  $\eta_{STF}$  for two high-temperature routes by adapting the  $\eta_{STF}$  definition in eq. 1.12 consistent with eq. 1.24 considering an optical efficiency of solar concentrator (solar tower) of 0.64 and  $RHN$  of 0.165. The results under  $\eta_{STF}$  for *i*) thermochemical cycles with inert gas sweep, vacuum pump, and chemical scavenger schemes for selected  $p_{O_2,1}$  levels and reduction temperature range of 1400 K to 2100 K, and *ii*) high-temperature electrolysis systems at 1 atm and a operation temperature range of 800 K to 1400 K are shown in figure 2.14. For high-temperature electrolysis systems, the STF efficiencies are plotted as a function of electrolyzer operation temperature at 1 atm with other parameters kept at reference values (see table 1.3). For thermochemical cycles, *i*) the optimal  $\eta_{STF}$  for scheme (a) under  $p_{O_2,1} = 1$  Pa (the  $p_{O_2} = 1$  Pa can be achieved by industrial  $N_2$  with purity of 99.999% [104]), *ii*) the optimal  $\eta_{STF}$  for scheme (b) under  $p_{O_2,1} = 10$  Pa with realistic vacuum efficiency (best performance according to figure 2.8a), and *iii*) scheme (c) under  $p_{O_2,1} = 0.001$  Pa (the best performing case according to figure 2.12a) with other parameters at reference conditions are selected.

In general, the two high-temperature solar fuel production routes showed comparable achiev-

able efficiency ranges (3% to 17% for high-temperature electrolysis systems, and 2% to 19% for thermochemical cycles), while operating at distinctly temperature ranges (800 K to 1500 K for high-temperature electrolysis systems, and 1400 K to 2100 K for thermochemical cycles). Note that the heat exchanger effectiveness for high-temperature electrolysis systems was 0.8, while 0.955 for thermochemical cycles in figure 2.14. Due to much higher operation temperature of thermochemical cycles, the requirement for gas phase recovery is more stringent. For example, the  $\eta_{\text{STF}}$  for scheme (a) at  $p_{\text{O}_2,1} = 1$  Pa,  $T_{\text{red}} = 1800$  K, and  $\epsilon_g = 0.955$  was 14.8% and dropped to 8.4% at  $\epsilon_g = 0.8$  (see figure 2.14 the black filled dots to the unfilled circle). The thermochemical cycles' efficiency were also sensitive to the variation in  $p_{\text{O}_2,1}$  at reduction step, the lower the pressure, the higher the system efficiency (see figure 2.14). In this thesis, special focus was paid to the high-temperature electrolysis systems due to its lower temperature requirement, less stringent partial pressure of oxygen environment, and highly efficient gas phase heat recovery. In addition, high-temperature electrolysis systems are operation in a continuous one-step manner which simplifies the reactor design compared to the two-step thermochemical cycles where high-temperature solid material cycling [24, 105] or multiple reactor chambers/channels with alternative reduction/oxidation operations [106] for a continuous fuel production. This thesis focuses on improving the efficiency of solar-driven high-temperature electrolysis systems via integrated solar reactor design coupling solar absorber and solid oxide electrolyzer into one reactor to reduce the heat losses related to high-temperature fluids transportation.

## 2.4 Summary and conclusions

A thermodynamic analysis was developed based on [29, 23, 24] to evaluate the solar fuel processing performance of a ceria-based thermochemical cycling scheme at various working conditions. Mechanical and chemical methods for the decrease of the oxygen partial pressure in the reduction chamber were proposed, compared, and combined. The impact of flow arrangement in the reactors (counterflow versus ideal mixing), temperature, pressure, solid and gas heat recovery effectiveness, and concentration ratio were discussed. Both isothermal and non-isothermal operation for ceria based redox cycles were studied to find the optimal configurations for best STF efficiency. For the scheme using sweep gassing to reduce (scheme (a)), the non-isothermal operation predicted significant higher efficiency than isothermal operation even without solid phase heat recover. The optimal temperature difference between the reduction and oxidation temperature was in the range of 100K to 150K and this slight temperature difference between reduction and oxidation reactions ensured a high STF efficiency trading off the energy consumption caused by solid phase heating and recycling of large amounts of sweep gas.

For the scheme using vacuum pumping to reduce (scheme (b)), the optimal efficiencies were

obtained at isothermal operation, indicating a promising way to conduct isothermal operation bearing both high efficiency as well as simple design and operation. The efficiency of the vacuum pump was crucial in dictating a high efficiency and was predicted to be around 40% throughout the operational range.

The gas phase heat recovery significantly increased the efficiency for sweep gassing and vacuum pumping schemes. A minimum  $\varepsilon_g$  of 0.9 was required for efficiencies of 25% for both scheme (a) and scheme (b), working at conditions leading to the optimal efficiency. The requirement for  $\varepsilon_g$  could be relaxed by imposing a small  $\Delta T$  (of around 100 – 200 K) with minimal efficiency reduction (below 3% when reducing  $\varepsilon_g$  from 0.975 to 0.9) for scheme (a) and scheme (b). The addition of solid phase heat recovery could further increase the efficiency. However, the absence of solid heat recovery didn't show a detrimental effect on the efficiency (efficiency reduction of 13.9% (scheme (a)) and 0.4% (scheme (b)) when changing  $\varepsilon_s$  from 1 to 0 at  $T_{\text{red}} = 1800$  K and  $p_{\text{O}_2,1} = 1$  Pa).

A high irradiation concentration led to lower radiation heat losses due to a reduced aperture area at the same solar energy input. The heat losses were dominating at large working temperatures due to the rapid increase of the radiation loss. The enhancement of the efficiency by increasing the concentration ratio became insignificant for concentrations above 5000. A novel scheme combining mechanical approaches (sweep gassing) and chemical approaches (chemical scavenger) to reduce the oxygen partial pressures showed promise in further increasing the system efficiency at non-isothermal conditions. The energy penalty caused by using active metal was in a reasonable range (below 0.5% of input energy for optimal cases of scheme (c)) as the amount of required sweep gas was minimized at non-isothermal conditions. Consequently, the combination of sweep gassing with a chemical scavenger provided a significant jump in efficiency from 28% to 36% for optimal cases at 1800 K. For isothermal operation, the combined mechanical-chemical approach showed no enhancement effected by the large amount of required sweep gas. The combination of sweep gas, vacuum pumping, and a chemical oxygen scavenger could further improve the system efficiency, but less efficiently as solely combining sweep gassing with an oxygen scavenger.

The counterflow and ideal mixing arrangement for fluid flow in reactor were implemented and compared. Generally speaking, the ideal mixing model is inferior to counterflow due to its inefficient use of sweep gas leading to extreme energy consumption in sweep gas heating, i.e. the maximum STF efficiency achieved for counter flow and ideal mixing arrangement was 18.2% and 4.3%, respectively, at  $T_{\text{red}} = 1800$  K and  $p_{\text{O}_2,1} = 10$  Pa.

The developed thermodynamic model of ceria-based cycling for solar fuel processing offers guidelines for the design and operation of redox cycles for solar fuel processing and can straightforward be applied to other promising redox materials such as perovskites[107, 108,



109].

The two high-temperature routes (HTE and TCC) were compared and discussed. It was found that the two technologies lied in similar achievable solar-to-efficiency ranges while operating at two distinct temperature ranges. The solar-driven HTE systems are of special interest due its less stringent requirements for operation temperature, low partial pressure of oxygen environment, and highly efficient gas phase heat recovery.



### 3 Tubular solar receiver for direct steam generation<sup>1</sup>

In this chapter, a coupled heat and mass transfer model of cavity receivers with tubular absorbers is developed to guide the design of solar-driven direct steam generation. Indirectly irradiated solar receiver designs utilizing tubular absorbers enclosed by a cavity are possible candidates for direct steam generation to feed the high-temperature electrolysis cell (stack), allowing for design flexibility and high solar thermal efficiency. The numerical model consisted of a detailed 1D two-phase flow model of the absorber tubes coupled to a 3D heat transfer model of the cavity receiver. The absorber tube model simulated the flow boiling phenomena inside the tubes by solving 1D continuity, momentum, and energy conservation equations based on a control volume formulation. The Thome-El Hajal flow pattern maps were used to predict liquid-gas distributions in the tubular cross-sections, and heat transfer coefficients and pressure drop along the tubes. The heat transfer coefficient and fluid temperature of the absorber tubes' inner surfaces were then extrapolated to the circumferential of the tube and input to the 3D cavity receiver model. The 3D steady state model of the cavity receiver coupled radiative, convective, and conductive heat transfer. The model was validated with experimental data and used to analyze different receiver types and designs made of different materials and exposed to various operational conditions. The proposed numerical model and the obtained results provide an engineering design tool for cavity receivers with tubular absorbers (in terms of tube shapes, tube diameter, and water-cooled front), support the choice of best-performant operation (in terms of radiative flux, mass flow rate, and pressure), and aid in the choice of the component materials. The model allows for an in-depth understanding of the coupled heat and mass transfer in the solar receiver for direct steam generation and can be exploited to quantify the optimization potential of such solar receivers.

---

<sup>1</sup>Material from this chapter has been submitted for publication as: M. Lin, J. Reinhold, N. Monnerie, and S. Haussener, "Modeling and design guidelines for direct steam generation solar receivers," *Appl. Energy*, vol. 216, pp. 761–776, 2018. [46]

### 3.1 Receiver model development

The development of a full 3D mechanistic model of the flow boiling process is challenging [110] due to the complex nature of the processes involved (activation of nucleation sites, bubble dynamics, and interfacial heat transfers) and the computational needs required for the solution of the direct numerical problem incorporating a large number of bubbles and surfaces with complex geometries [111, 112]. To overcome this challenge, semi-mechanistic approaches are proposed [113, 114, 115, 116, 117, 118]. For example, Kurul and Podowski developed a 3D model which couples an Euler-Euler two-phase flow model (for bulk fluid flow) with a wall boiling model. The wall boiling model partitioned the heat flux between the tube wall and the fluid into three parts: liquid phase convective heat flux, quenching heat flux, and evaporation heat flux (wall boiling phenomena), predicting each heat flux by empirical and mechanistic correlations. Due to the numerical instability and large computational cost of the wall boiling model, a bulk boiling model was used instead and coupled with an Euler-Euler two-phase flow model in the modeling of a PWR nuclear steam generator [119]. The bulk boiling model agreed well with the experimental data. In the engineering design of evaporators and steam generators, the wall-fluid heat transfer is more important in determining the thermal performance than the detailed in-tube liquid-vapor interfacial heat and mass transfer. Hence less computationally expensive 1D two-fluid (separated or homogeneous) two-phase flow models with empirical correlations (single equation correlations [120, 121] and flow pattern based correlations [122, 123]) for the wall-fluid heat transfer coefficients are commonly employed [124, 125, 126] without resolving the local non-uniformity of the wall-liquid heat transfer. An obvious disadvantage of a simplified 1D two-phase model with empirical correlations is that the local heat transfer and temperature distribution cannot be accurately captured. However, this might be extremely important for the determination of the critical point. Olliet et al. [126] proposed an integrated model for a fin-and-tube evaporator by linking a fin-and-tube solid core 2D heat transfer model and an 1D in-tube separated two-phase flow model. They showed accurate and computationally cost effective predictions for fin-and-tube local temperature distributions, based on calculated non-uniform wall-fluid heat transfer coefficients captured by using advanced flow pattern maps based on wall wetting conditions for different flow regimes [127].

The modeling efforts for solar-driven tubular cavity receivers and reactors have been extensively reported [37, 128, 38, 129, 130, 131]. Martinek et al. [37, 38] developed a 3D steady-state model for a multi-tubular solar reactor for steam gasification of carbon using a hybrid Monte Carlo/Finite Volume method for radiative heat transfer and a single-phase fluid flow model with volume-averaged mixture properties. However, 3D models cannot be directly used for accurate modeling of a tubular cavity solar receiver for direct steam generation since the 3D direct numerical simulation of two-phase boiling flow is difficult and computational

expensive.

Inspired by the two-phase flow modeling methods for the conventional steam generator and evaporator and of the solar receiver modeling community, a solar receiver model for direct steam generation considering the in-tube two-phase flow phenomena is presented here. The approach is the following: a 1D two-phase flow model for the in-tube two-phase flow is coupled to a 3D heat transfer model of the receiver cavity, providing a simplified but accurate and computationally efficient model. A similar approach has been used by Zapata et al. [132], one of the view reported modeling studies for solar-driven steam generation [132, 133, 134]. They used a 3D multi-model receiver model, however, they solved only a homogeneous two-phase 1D model inside the absorber tube utilizing empirical correlations to predict the heat transfer between the tube surface and the working fluid without resolving the circumferential variations in the heat transfer coefficient. However, the non-uniform heat transfer together with the non-uniform solar irradiation will potentially lead to large temperature gradients in the absorber tube and is responsible for hot spots. Circumferentially resolved heat transfer is required to accurately identify hot spots. Here, specially attention was paid to hot spots induced by the dryout of the in-tube two-phase flow where the temperature gradients are large (temperature jump between two mesh elements larger than 100 K) and therefore worked with a method that allows for the resolution of the non-uniform heat transfer, also in the circumferential direction of the tube.

These issues can be addressed by utilizing a 1D two-phase flow absorber tube model and couple it to flow pattern maps to accurately account for and extrapolate for the circumferentially varying heat transfer behavior in the tube. The schematic of the two types of receivers investigated and the calculation domains (consisting of insulation, cavity, and tubes) are shown in figure 3.1. The heat transfer and fluid flow inside the absorber tubes are analyzed by a separated 1D two-phase flow model considering continuity, energy, and momentum equations (the conservation equations are solved for the combined flow while the velocities are different for the two phases [133]) to calculate the fluid temperature, phase velocity, liquid-vapor velocity slip, and heat transfer coefficient in the absorber tubes based on the absorbed radiation calculated from the 3D heat transfer model in the cavity. The fluid temperature and the heat transfer coefficient obtained by the 1D two-phase flow model are then extrapolated to a 3D temperature and heat transfer coefficient profile utilizing two-phase flow pattern maps. The obtained temperature and heat transfer coefficient at the inner absorber tube provide a convective boundary condition to the heat transfer model in the cavity.

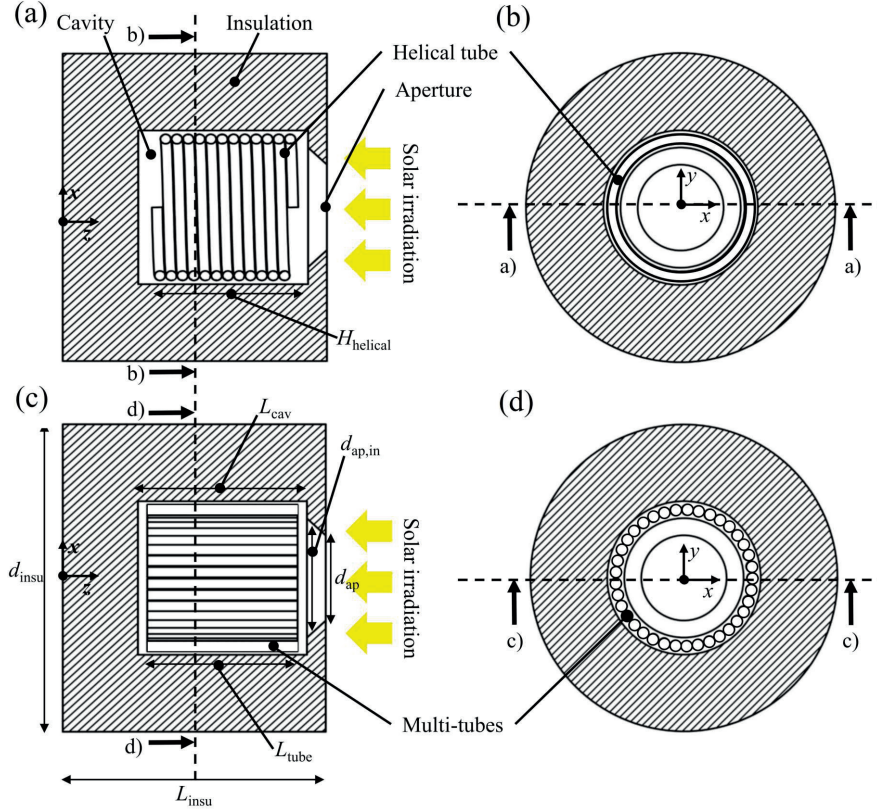


Figure 3.1 – Schematic of the two investigated types of cavity receivers with tubular absorber tubes, receiver 1 utilizing a helical absorber tube: (a) and (b), and receiver 2 utilizing multiple connected straight absorber tubes: (c) and (d).

### 3.1.1 Cavity model

#### Radiation model

##### *Solar flux characteristics at the receiver aperture boundary*

The spatial distribution of the solar irradiation magnitude at the aperture of the cavity was approximated by a Gaussian distribution [134]. The angular distribution was assumed to be diffuse. This assumption was made in order to ensure a broader applicability of the results as the angular distribution of concentrating solar facilities is highly dependent on the design of the primary concentrator and position of the receiver. The receiver aperture boundary was treated as a high-temperature black body emitting into the receiver at an equivalent temperature described by:

$$T_i^{\text{eff}} = \left( \frac{q_{\text{solar},i} + \sigma T_{\text{amb}}^4}{\sigma} \right)^{\frac{1}{4}}, \quad (3.1)$$

$$q_{\text{solar},i} = q_{\text{peak}} \exp\left(-\frac{(x_i - x_0)^2}{2\delta_x} - \frac{(y_i - y_0)^2}{2\delta_y}\right). \quad (3.2)$$

where  $T_i^{\text{eff}}$  is the effective temperature for surface element  $i$  at the aperture,  $\delta_x$  and  $\delta_y$  are the standard deviations of the Gaussian flux approximation for the  $x$ - and  $y$ -axis (equal in our case as the profile is symmetric),  $x_i$  and  $y_i$  are the location at the aperture,  $x_0$  and  $y_0$  are the coordinates of the aperture center,  $q_{\text{solar},i}$  is the local solar irradiation at the aperture surface element  $i$ ,  $q_{\text{peak}}$  is the peak flux density, and  $\sigma$  is the Stefan-Boltzmann constant. Figure C.1 shows the sensitivity of the results with respect to the exact choice of  $\delta_x$ , indicating that the impact of  $\delta_x$  on the thermal performance of both receiver types (receiver 1 and 2) is negligible.

#### ***Radiative heat transfer inside the receiver cavity***

The surfaces inside the receiver cavity were assumed grey and diffuse, and the air inside the cavity was treated as a radiatively nonparticipating medium. The heat conduction and fluid flow inside the cavity was not numerically computed. Instead a surface heat sink was used with a semi-empirical heat transfer coefficient (see section 3.1.1). The radiative heat transfer within the receiver cavity was described by a surface-to-surface radiation model,

$$J_i = E_i + \rho_i \sum_{j=1}^N F_{ij} J_j, \quad (3.3)$$

$$F_{ij} = \frac{1}{A_i} \int_{A_i} \int_{A_j} \frac{\cos\theta_i \cos\theta_j}{\pi r_{ij}^2} \delta_{ij} dA_i dA_j. \quad (3.4)$$

where  $J_i$  represents the radiosity of surface  $i$ ,  $E_i$  is the emissive power,  $N$  is the total number of surfaces,  $F_{ij}$  is the view factor between surfaces  $i$  and  $j$ ,  $A$  is the surface area,  $r_{ij}$  is the distance between two area-centroids of two surfaces,  $\theta$  is the angle between the surface normal and the vector connecting area centers  $i$  and  $j$ , and  $\delta_{ij}$  is a dirac function determined by the visibility of surface  $i$  and  $j$  ( $\delta_{ij} = 1$  if  $dA_j$  is visible to  $dA_i$  and 0 otherwise). The radiative heat transfer model was applied to all inner cavity surfaces and the aperture. The re-radiation loss,  $\dot{Q}_{\text{rerad}}$ , was defined as the total emitted power from the inner cavity surfaces toward the aperture.

#### **Natural convection model**

The convective heat loss through the cavity receiver aperture was quantified by utilizing an empirical correlation. This correlation has been based on 3D numerical heat and flow simulations adjusted by considering experimentally measured heat transfer rates reported in [135]. The total natural convection heat loss from the aperture was given as:

$$\dot{Q}_{\text{nc}} = A_{\text{cav,in}} h_{\text{nc}} (\bar{T}_{\text{cav,in}} - T_{\text{amb}}), \quad (3.5)$$

$$\text{Nu}_L = 0.0196 \text{Ra}_L^{0.41} \text{Pr}^{0.13}, \quad (3.6)$$

$$L = \left| \sum_{i=1}^3 a_i \cos(\phi + \phi_i)^{b_i} L_i \right|, \quad (3.7)$$

where  $A_{\text{cav, in}}$  is the total inner surface area of the receiver cavity, the Rayleigh number is given by  $\text{Ra}_L = \frac{g\beta(\bar{T}_{\text{cav, in}} - T_{\text{amb}})L^3}{\nu a_{\text{td}}}$  [72],  $a_{\text{td}}$  the thermal diffusivity, and  $L$  the ensemble length.  $L$  was calculated using the cavity receiver tilt angle  $\varphi$  (considered to be  $\theta_0$  in this study), the cavity inner diameter  $L_1$ , the cavity depth  $L_2$ , the cavity open aperture diameter  $L_3$ , and the fitting coefficients  $a_i$ ,  $b_i$ , and  $\phi_i$  (the schematic representation of the cavity and the coefficients' values are given in [135]).  $\bar{T}_{\text{cav, in}}$  is the average temperature of the cavity's inner surfaces, including the absorber tubes' surfaces. An averaged heat transfer coefficient,  $\bar{h}_{\text{nc}}$ , of the absorber tube surfaces was defined in order to estimate the local cooling effect by natural convection:

$$\bar{h}_{\text{nc}} = \frac{\dot{Q}_{\text{nc}}}{A_{\text{tube}}(\bar{T}_{\text{tube}} - T_{\text{amb}})}, \quad (3.8)$$

where  $A_{\text{tube}}$  is the total absorber tube area, and  $\bar{T}_{\text{tube}}$  is the tube surface-averaged temperature. A boundary heat sink term was calculated and applied to the tube surfaces using a thin wall conduction model ( $t_{\text{wall}}$  was  $10^{-6}$  m, the results were not sensitive to  $t_{\text{wall}}$ , see figure C.2):

$$q'''_{\text{nc, sink}} = -\bar{h}_{\text{nc}}(T_{i, \text{tube}} - T_{\text{amb}})/t_{\text{wall}}. \quad (3.9)$$

The convective heat loss,  $\dot{Q}_{\text{conv}}$ , was the integration of the heat sink term over the tubes' thin walls and was – by definition – equals to  $\dot{Q}_{\text{nc}}$ . This correlation-based natural convection model can reasonably well predict the overall heat losses due to natural convection at a low computational cost as there is no need for a numerical solution of the heat transfer and fluid flow within the cavity inner and ambient air domains [38, 129]. However, this global approach can lead to inaccuracies in predicting the local flux as the local natural convection heat flux is only a function of the local surface temperature, neglecting any effects from locally present flow zones (main flow, stagnant zone, and the counterflow zone [136]). This may lead to inaccuracy in predicting the local surface temperature which in turn leads to inaccuracy in predicting the hot spots. However, the dominating effect for hot spots is the sharp decrease in the in-tube wall-fluid heat transfer coefficient while the natural convection heat transfer coefficient played only a minor role. For example, the heat transfer coefficient reduced from  $11000 \text{ W/m}^2/\text{K}$  to  $1000 \text{ W/m}^2/\text{K}$  at the dryout point for the receiver 1 at the reference condition, while the predicted natural convection heat transfer coefficient was only around  $4 \text{ W/m}^2/\text{K}$ .

#### Conduction model

The energy conservation for solid domains of the receiver (insulation and tubes' walls) was described by,

$$\nabla \cdot (k \nabla T) = 0 \quad (3.10)$$

where  $k$  is the thermal conductivity of the solid material. The boundary condition for the tubes' outer surfaces was the net surface energy flux by natural convection and radiation. The inner tubes' surface boundary condition was set as the convection boundary, coupling the 3D receiver model to the 1D tube model (see section 3.1.2). A combined radiation and convection boundary condition was applied at the outer surfaces of the insulation with the ambient temperature 298 K, surface emissivity of 0.8, and heat transfer coefficient of 5 W/m<sup>2</sup>/K (a reasonable estimation for natural convection from external cavity walls [137]). The conductive heat loss,  $\dot{Q}_{\text{cond}}$ , was the total heat transfer from the cavity inner surface wall to the outer surface wall through conduction.

#### 3.1.2 Tube model

##### Two-phase flow model inside tubes

The two-phase flow phenomena were modeled by a steady state 1D separated two-phase flow model [124, 133] which assumed the same pressure and temperature in each phase at any cross section of the tube while allowing for a slip velocity between the liquid and vapor phases. Compared to a homogenous flow model, a separated flow model can capture – while simple in formulation – more accurately the physical flow behavior with each phase having different properties and velocities. A two fluids model could alternatively be used to predict more precisely the flow behavior by separately solving the conservation equations for two phases without needing empirical correlations for the prediction of the void fraction. However at the expense of significant computational costs and potentially numerical instability. Here, the separated flow model was chosen as a good compromise between computational cost and model accuracy.

The two-phase continuity equation,

$$\frac{d}{dz} [\rho_g v_g \varepsilon_g + \rho_l v_l (1 - \varepsilon_g)] = 0, \quad (3.11)$$

was solved, where  $\rho_g$  and  $\rho_l$  are the density of the gas and liquid phases,  $v_g$  and  $v_l$  are the



velocities, and  $\varepsilon_g$  is the void fraction of the gas phase. The momentum equation,

$$-\frac{dp}{dz} = \frac{d}{dz} \left[ \rho_g v_g^2 \varepsilon_g + \rho_l v_l^2 (1 - \varepsilon_g) \right] + g \rho \cos \theta + \frac{\tau_w P}{A_{\text{tube,in}}}, \quad (3.12)$$

was solved, where  $p$  is the pressure,  $\rho = (1 - \varepsilon_g)\rho_l + \varepsilon_g\rho_g$  is the volume-averaged density,  $P$  is the tubes' inner circumferences,  $A_{\text{tube,in}} = \pi d_{\text{tube,in}}^2/4$  is the cross sectional area of tube,  $\tau_w = (f/4)(\dot{m}^2/2\rho A_{\text{tube,cross}}^2)$  is the wall shear stress, and  $\theta$  is the inclination angle of the tube.  $\theta$  was determined locally for each tube segment according to the tube orientation. The first term on the right side of eq. 3.12 is the momentum pressure drop, the second term represents the static pressure change, and the third term is the frictional pressure drop. The friction factor,  $f$ , was estimated by empirical correlations. In the single phase flow region,  $f$  was predicted by the Blasius equation [28]. In the two-phase flow region,  $f$  was predicted by the Friedel correction [138], implemented by utilizing a two-phase multiplier on the liquid phase friction factor.

The energy equation,

$$\frac{d}{dz} \left[ \rho_g v_g \varepsilon_g \left( h_g + \frac{v_g^2}{2} + g z \cos \theta \right) + \rho_l v_l (1 - \varepsilon_g) \left( h_l + \frac{v_l^2}{2} + g z \cos \theta \right) \right] = \frac{P q_w}{A_{\text{tube,in}}}, \quad (3.13)$$

was solved, where  $h_g$  and  $h_l$  are the enthalpy of gas and liquid phases evaluated based on local temperature and pressure, and  $q_w$  is the heat flux at the tube inner wall which was obtained by the calculation of a surface-averaged heat flux obtained from the cavity receiver 3D heat transfer model.

The fluid properties were evaluated by using the open-access thermodynamic properties database, Coolprop [139]. If an incondensable gas was additionally injected into the liquid water in the tube (for example  $\text{CO}_2$ ), the gas phases were assumed well mixed with properties calculated based on the molar fractions. Solving the separated flow model requires information on the cross-sectional void fraction,  $\varepsilon_g$ , which was predicted by using an empirical correlation [140]:

$$\varepsilon_g = \frac{x_g}{\rho_g} \left[ (1 + 0.12(1 - x_g)) \left( \frac{x_g}{\rho_g} + \frac{1 - x_g}{\rho_l} \right) + \frac{1.18(1 - x_g)(g \sigma_t (\rho_l - \rho_g))^{0.25}}{\dot{m}'' \rho_l^{0.5}} \right]^{-1}, \quad (3.14)$$

where  $x_g$  is the vapor quality in cases when there is no gas injection (i.e. the injection of  $\text{CO}_2$  for concurrent heating of  $\text{H}_2\text{O}$  and  $\text{CO}_2$  for HTE syngas generation) or the gas quality (ratio of the total gas mass to the total fluid mass) in cases when there is gas injection.  $\sigma_t$  is the temperature-dependent surface tension (obtained from Coolprop) and  $\dot{m}''$  is the total mass flux. This correlation is the Steiner version of the Rouhani–Axelsson drift flux model, originally proposed for horizontal tubes [141]. It is easy to implement because the void



fraction is expressed as an explicit function of the total mass flux. It has been shown that the Steiner version of the Rouhani–Axelsson drift flux model can also be used to estimate the void fraction for inclined and vertical flows with reasonable accuracy (capturing > 80% data points with < 15% error) [142]. The Steiner version of the Rouhani-Axelsson drift flux model was consequently an accurate model to flexibly investigate either horizontal, inclined or vertical configurations. Only few other models provide the same flexibility.

#### **Non-uniform heat transfer coefficients at the inner tube surface**

The heat transfer coefficient between the two-phase mixture and the tube wall were obtained by empirical correlations. The liquid-vapor distribution within the tube has to be known for this and suitable heat transfer coefficient correlations were used for the wetted and non-wetted surfaces. For horizontal tubes, the Thome-El Hajal flow pattern map [8] was used to locally determine the liquid-vapor distribution, i.e. the local flow regimes. This flow pattern map is a modification of the Kattan-Thome-Favrat map [127] which was developed based on Taitel-Dukler map [143]. The Taitel-Dukler map was developed based on water but adiabatic boundary conditions. The Thome-El Hajal flow pattern map was developed based on experimental data for several refrigerants (R-22, R-410A, R-134A, R407C, etc.) for tube diameters from 8 to 14 mm, fluid mass fluxes from 16 to 700 kg/m<sup>2</sup>/s, and heat fluxes from 440 to 57'500 W/m<sup>2</sup>. The Thome-El Hajal flow pattern map was used for the various heat fluxes, assuming it is also valid for water. The accuracy of this assumption was validated and confirmed by predicting the water-steam flow regimes in a parabolic trough solar collector for direct steam generation (see section 3.2.1). The results showed agreement with the experiments with a maximum relative error of 1.2% for temperature results and 2.2% for pressure results [144]. The same extrapolation approach was then used for our receiver as the operational conditions were in similar conditions with relatively similar tube geometries and arrangements.

For vertical tubes, the Gungor-Winterton correlation [145] was used to predict the heat transfer before dryout region, and the Groeneveld method [146] in the dryout region. In the 1D two-phase flow model, averaged heat transfer coefficients between the wall and the two-phase fluid were used based on the circumference ratio covered by gas and liquid. The 3D inner tube surface heat transfer coefficient profiles (varying in axial and azimuthal direction) were generated by assigning different heat transfer coefficient values (dry or wet) locally for each azimuthal segment. 3D free stream temperature profiles were obtained by assuming a constant temperature within each axial tube segment and, hence, also a constant temperature in azimuthal direction. The heat transfer coefficient and free stream temperature profiles generated from the 1D tube model were then used as the convective boundary conditions at the inner tube wall in the 3D cavity heat transfer model.

### Flow pattern maps and heat transfer coefficient for horizontal tubes

The Thome-El Hajal maps predict five flow regimes: stratified flow, stratified wavy flow, intermittent flow, annular flow, and mist flow. The mass flux,  $\dot{m}''_{\text{strat}}$ , of the fluids, the heat flux,  $q_w$ , and the vapor quality,  $x_g$ , are required for the determination of the flow regime. The transitions between different flow regimes are summarized below.

**Stratified flow to stratified wavy flow** was defined as:

$$\dot{m}''_{\text{strat}} = \left[ \frac{226.3^2 A_g A_l^2 \rho_g (\rho_l - \rho_g) \nu_l g}{x_g^2 (1 - x_g) \pi^3 d_{\text{tube,in}}^6} \right]^{1/3}, \quad (3.15)$$

where  $A_g$  and  $A_l$  are the corresponding cross-sectional areas for gas and liquid.

**Stratified wavy flow to annular and intermittent flows** was defined as:

$$\dot{m}''_{\text{wavy}} = \left\{ \frac{16 A_g^3 g \rho_g \rho_l}{x_g^2 \pi^2 d_{\text{tube,in}}^5 [1 - (\frac{2h_l}{d_{\text{tube,in}}} - 1)^2]^{0.5}} \left[ \frac{\pi^2 d_{\text{tube,in}}^2}{25 h_l^2} (1 - x)^{-f_1(q)} \left( \frac{We_l}{Fr_l} \right)^{-f_2(q)} \right] \right\}^{0.5} + 50 - 75 e^{-\frac{(x_g^2 - 0.97)^2}{x_g(1 - x_g)}}, \quad (3.16)$$

where  $h_l$  is the liquid level,  $We_l = \frac{\dot{m}_l'^2 d_{\text{tube,in}}}{\rho_l \sigma_t}$  the Weber number for the liquid phase, and  $Fr_l = \frac{\dot{m}_l'^2}{g \rho_l^2 d_{\text{tube,in}}}$  the Froude number for the liquid phase.  $f_1(q)$  and  $f_2(q)$  are two empirical exponents accounting for the effect of the heat flux on the onset of dryout of the annular film,

$$\begin{aligned} f_1(q) &= 646 \left( \frac{q_w}{q_{\text{DNB}}} \right)^2 + 64.8 \frac{q_w}{q_{\text{DNB}}}, \\ f_2(q) &= 18.8 \left( \frac{q_w}{q_{\text{DNB}}} \right)^2 + 1.023, \end{aligned} \quad (3.17)$$

where  $q_{\text{DNB}} = 0.131 \rho_g h_{lg} [g(\rho_g - \rho_l)]^{0.25}$  is the heat flux of departure from nucleate boiling. If the mass flux is larger than eq. 3.16, it is either in an intermittent or annular flow regime.

**Intermittent flow to annular flow** was differentiated by:

$$x_{g,IA} = \left[ 0.2914 \left( \frac{\rho_g}{\rho_l} \right)^{-1/1.75} \left( \frac{\nu_l}{\nu_g} \right)^{-1/7} \right]^{-1}. \quad (3.18)$$

**Annular flow to mist flow** was defined as:

$$\dot{m}''_{\text{mist}} = \left( \frac{7680 A_g^2 g \rho_g \rho_l \nu_l Fr_l}{x_g^2 \pi^2 d_{\text{tube,in}}^3 \xi_{ph} We_l} \right)^{0.5}, \quad (3.19)$$

Table 3.1 – Summary of  $\theta_{\text{dry}}$  and  $\delta_{\text{lf}}$  for different flow patterns in horizontal tube [8]

Flow pattern	Sub-regions	$\theta_{\text{dry}}$	$\delta_{\text{lf}}$
Stratified	None	$\theta_{\text{dry}}$	
Stratified wavy	$x_g < x_{\text{max}}$	$\theta_{\text{strat}} \frac{\dot{m}''_{\text{wavy}}(x_g) - \dot{m}''}{\dot{m}''_{\text{wavy}}(x_g) - \dot{m}''_{\text{strat}}(x_g)}$	$\frac{\pi d_{\text{tube,in}}(1-\varepsilon)}{2(2\pi - \theta_{\text{dry}})}$
	$x_g > x_{\text{max}}$	$(2\pi - \theta_{\text{max}}) \frac{x_g - x_{\text{max}}}{1 - x_{\text{max}}} + \theta_{\text{max}}$	
Annular and Intermittent	None	0	
Mist	None	$2\pi$	0

Note: if  $\delta_{\text{lf}} > 0.5d_{\text{tube,in}}$ ,  $\delta_{\text{lf}} = 0.5d_{\text{tube,in}}$ .

where  $\xi_{\text{ph}} = [1.138 + 2 \log \left( \frac{\pi d_{\text{tube,in}}^2}{1.5 A_l} \right)]^{-2}$  is the liquid-vapor interfacial friction factor. The transition boundary was adapted by finding the vapor quality,  $x_{\text{mist,min}}$ , that minimized the mass flux,  $\dot{m}''_{\text{mist,min}}$ , of the mist flow transition curve while enforcing  $\dot{m}''_{\text{mist}} = \dot{m}''_{\text{mist,min}}$  when  $x_g > x_{\text{mist,min}}$ .

Once the flow regime is identified, it is able to estimate how much of the tube area was wetted utilizing the dry angle,  $\theta_{\text{dry}}$ , defined by the ratio of the dry perimeter to the tube radius. For convenience, the liquid quantity was assumed to be uniformly distributed along the wetting wall by forming a film with a mean thickness,  $\delta_{\text{lf}}$ . The detailed definition for  $\theta_{\text{dry}}$  and  $\delta_{\text{lf}}$  for the different flow patterns in horizontal tubes are summarized in table 3.1.  $x_{\text{max}}$  is the intersection point between  $\dot{m}''_{\text{wavy}}$  and  $\dot{m}''_{\text{mist}}$ . In stratified wavy flow and for  $x_g < x_{\text{max}}$ , a linear interpolation between  $\dot{m}''_{\text{wavy}}$  and  $\dot{m}''_{\text{mist}}$  was used to predict  $\theta_{\text{dry}}$  for a given  $\dot{m}$ . For  $x_g \geq x_{\text{max}}$ , the  $\theta_{\text{dry}}$  increased linearly from  $\theta_{\text{max}}$  to  $2\pi$  with increasing  $x_g$ . By using an explicit expression of  $\varepsilon_g$  as a function of  $\dot{m}$  and an approximated geometrical expression for the stratified angle ( $\theta_{\text{strat}}$ , the  $\theta_{\text{dry}}$  for stratified flow) in terms of  $\varepsilon$  [147], the iterative method in the Taitel-Dukler map for the evaluation of  $\varepsilon$  and  $\theta_{\text{strat}}$  was avoided.

The heat transfer coefficients between the two-phase fluid and tube wall surface for dry,  $h_{\text{dry}}$ , and wet,  $h_{\text{wet}}$ , areas were separately calculated using empirical correlations. For  $h_{\text{dry}}$ , the Dittus-Boelter correlation [148] was used:

$$h_{\text{dry}} = 0.023 \left( \frac{\dot{m}'' x_g d_{\text{tube,in}}}{\varepsilon_g \mu_g} \right)^{0.8} \left( \frac{c_{p,g} \mu_g}{k_g} \right)^{0.4} \frac{k_g}{d_{\text{tube,in}}}, \quad (3.20)$$

where  $c_{p,g}$  is the heat capacity of the gas phase,  $k_g$  is the gas phase thermal conductivity, and  $\mu_g$  is the dynamic viscosity of the gas phase.  $h_{\text{wet}}$  was obtained from an asymptotic expression ( $h_{\text{wet}} = (h_{\text{nb}}^3 + h_{\text{cb}}^3)^{1/3}$ ) that combines the nucleate boiling,  $h_{\text{nb}}$ , and convective boiling,  $h_{\text{cb}}$ , using an exponent of three, indicating the transition range between the nucleate and convection components.  $h_{\text{nb}}$  was determined by an empirical correlation of Cooper [145],

$$h_{\text{nb}} = 55 p_r^{0.12} (-\log p_r)^{-0.55} M_{\text{H}_2\text{O}}^{-0.5} q_w^{0.67}, \quad (3.21)$$

where  $p_r$  is the reduced pressure (ratio between fluid pressure and the critical pressure) and  $M_{H_2O}$  is the molar weight of water.  $h_{cb}$  [149] was predicted as,

$$h_{cb} = 0.0133 \left[ \frac{4\dot{m}''(1 - x_g)\delta_{lf}}{(1 - \varepsilon_g)\mu_l} \right]^{0.69} \left( \frac{c_{pl}\mu_l}{k_l} \right)^{0.4} \frac{k_l}{\delta_{lf}}, \quad (3.22)$$

where  $c_{pl}$  is the heat capacity of the liquid phase,  $k_l$  is the liquid phase thermal conductivity, and  $\mu_l$  is the dynamic viscosity of the liquid phase.

#### Flow pattern maps and heat transfer coefficient for vertical tubes

The flow patterns for flow boiling inside vertical tubes can be classified as bubbly flow, churn flow, annular flow, and mist flow. The dry angle before dryout (mist flow) can be considered as 0 and directly turns into  $2\pi$  at the presence of mist flow. Here, we paid attention to the transition from the annular flow to the mist flow while the flow patterns were not specifically identified. The transition from annular flow to mist flow was defined by the critical vapor quality,  $x_{crit}$ , which was predicted by an empirical correlation [150] giving a relation between  $x_{crit}$  and mass flux, pressure, heat flux, and tube diameter:

$$x_{g,crit} = 10.795 q_w^{-0.125} \dot{m}''^{-0.333} (1000 d_{tube,in})^{-0.07} e^{1715p}. \quad (3.23)$$

This correlation is valid for  $p < 30$  bar. When  $x_{g,crit} > 0.9$ ,  $x_{g,crit}$  was enforced to be 0.9. The Gungor-Winterton correlation [151] was used to predict the heat transfer coefficient,  $h_{wet}$ , before dryout, being the sum of convective heat transfer of the liquid phase,  $h_{cb}$ , using the Dittus-Boelter correlation and nucleate pool boiling,  $h_{nb}$ , from the Coop correlation [145]:

$$h_{wet} = E_{tcm} h_{cb} + S_{bsf} h_{nb}, \quad (3.24)$$

where  $E_{tcm}$  is the two-phase convection multiplier which is a function of the Martinelli parameter, heat flux, and  $S_{bsf}$ , which is the boiling suppression factor based on  $E_{tcm}$  and Reynold number of the liquid phase. The heat transfer coefficient of the dryout region,  $h_{dry}$ , was predicted by the Groeneveld method [146].

#### Heat transfer coefficient in titled and helical tubes

Since the reported flow pattern maps for the flow boiling phenomena in titled and helical tubes are very limited, approximations and interpolations were used based on the horizontal and vertical flow maps and correlations to predict the heat transfer coefficient. The horizontal flow was considered when the control volume has an inclination angle in the range of 0 to 30°. The flow was treated as vertical flow when the inclination angle was between 60° and 90°. A linear interpolation of heat transfer coefficient between horizontal and vertical flows was implemented for the control volumes with inclination angle between 30° and 60°. In the

curved helical tube, slower moving fluid elements move toward the inner wall of the curved tube as a result of the momentum balance between the momentum change caused by the centrifugal force and the momentum change induced by the pressure gradient. This drift leads to the occurrence of secondary flows in the flowing fluid [152]. Secondary flows, in turn, lead to an augmentation in heat transfer with the magnitude of this increase depending on the coil curvature ( $d_{\text{tube,in}}$  and  $r_{\text{turn}}$ ). Here, the secondary flow was not considered in the fluid flow model. However, the enhancement due to secondary flow was considered in helical tube by correcting the heat transfer coefficient based on the helical turning radius and the tube radius. Two heat transfer enhancement factors ( $1 + 1.77d_{\text{tube,in}}/r_{\text{turn}}$  for gas phase and  $1 + 10.3(d_{\text{tube,in}}/r_{\text{turn}})^3$  for liquid phase) [153] were considered for helical tube receivers, accounting for heat transfer enhancement induced by secondary flows.

#### Heat transfer in single phase flow region

The local heat transfer coefficients for the liquid single phase flow region was predicted using an empirical correlation proposed by Liu et al. [121] considering both forced convective contribution and subcooled boiling (based on temperature differences between tube wall and bulk fluid as well as tube wall and saturation temperature). The heat transfer coefficient for gas single phase flow region was simply predicted by the Dittus-Boelter correlation (eq. 3.20).

#### 3.1.3 Model coupling

The 3D receiver cavity heat transfer model and the 1D tube fluid flow model were solved iteratively using a simulation flow as shown in figure 3.2. The calculation started with the 1D tube model using the input parameters (i.e.  $\dot{m}$ ,  $p$ , and  $T_{\text{inlet}}$ ) and an initial guess for the heat flux,  $q_{w,\text{ini}}$ . A 3D heat transfer coefficient profile and a 3D fluid temperature profile along the tube inner wall surface were generated based on the model described in section 3.1.2. These two profiles were then applied to the 3D receiver cavity model as a convective boundary condition at the inner tube wall. The results of the 3D receiver cavity model provided a 1D heat flux profile to the 1D tube model by azimuthal-averaging the heat flux calculated from the 3D cavity model for each axial tube segment and applying it to the inner tube surfaces. The overall convergence was controlled by the relative error in the temperature ( $T_j$ , temperature for each node  $j$ ) between two iterations (i.e. between iteration  $i$  and  $i-1$ ) with a tolerance of  $10^{-3}$  to ensure an overall energy imbalance smaller than 0.5%.

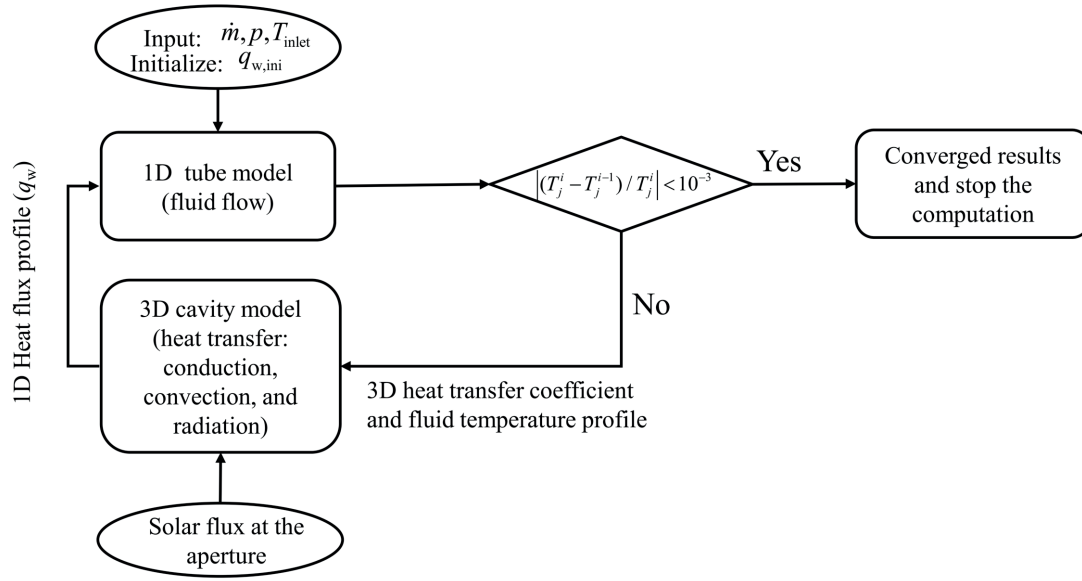


Figure 3.2 – Schematic of the coupling between the 1D tube model and the 3D - receiver cavity heat transfer model.

### 3.1.4 Numerical solution

The numerical discretization of the 1D tube model for the two-phase flow inside the receiver tubes relied on the control volume formulation, solved with an implicit step-by-step method in the flow direction [124, 125]. The convergence criterion in each control volume for continuity, momentum, and energy equations were set to  $10^{-8}$ . The 3D receiver cavity heat transfer model was implemented with a commercial solver, ANSYS FLUENT version 17.2 [154]. The surface-to-surface radiation model was solved with a residual of  $10^{-8}$ . The energy equation was discretized by a second order upwind scheme with a residual value of  $10^{-7}$ . The global convergence criterion of the coupled 1D and 3D model was the fluid temperature between two successive global iterations, where the convergence criterion was set to  $10^{-3}$ . All convergence criterion values were chosen to ensure an energy imbalance for all studied cases smaller than 0.5%.

A workstation with 24GB RAM and 10 cores was utilized to compute the coupled model. A mesh independence study showed that a reasonable meshing scheme for the tubes consisted of 1000 uniform elements (330 elements per meter) in flow direction (keeping the same for the 1D fluid flow model) and 30 uniform elements in azimuthal direction (30 elements over  $360^\circ$ ), resulting in a total mesh element number of about 1 million cells for the 3D heat transfer model. Further increase in the mesh element number resulted in less than 1 K difference for the predicted outlet fluid temperature. For the receiver 1 at the reference conditions, it took 4 hours to have the final convergence (16 iterations between the receiver cavity heat transfer

model and the tube fluid flow model). For receiver 2 at the reference conditions, it took 4.5 hours for a complete convergence (17 iterations between cavity model and the tube model). The computational time for cases with varying operational and geometrical conditions took a similar amount of time (for each calculation).

## 3.2 Results and discussion

### 3.2.1 Model validation

#### Comparison to parabolic trough concentrator

Due to lack of reported experimental data for direct steam generation receiver demonstrations in solar point-focusing concentrating facilities (towers and dishes), experimental data was utilized for direct steam generation in a parabolic trough solar collector for the validation of our two-phase flow model and for checking if our flow pattern map extrapolation approach (see section 3.1.2) was accurate. The geometrical data and operational conditions were set to be identical to what has been reported by Lobon et al. [2]. The validation with their example case 1 is shown in figure 3.3.

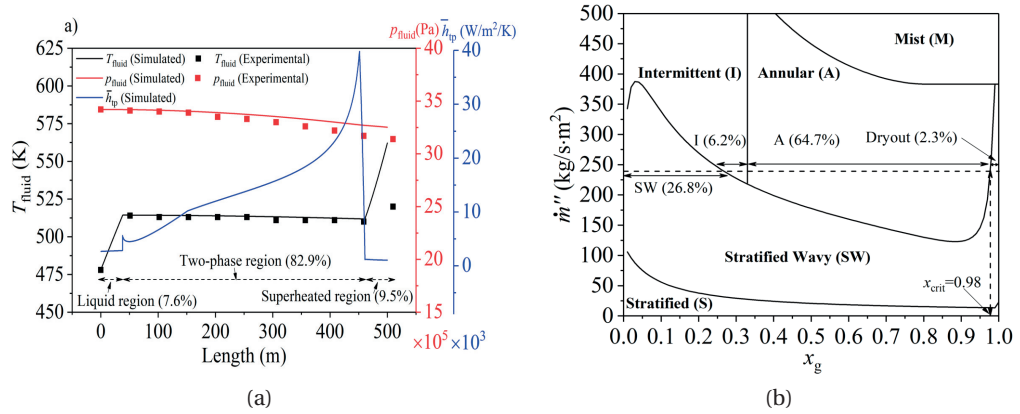


Figure 3.3 – (a) Experimentally measured fluid temperature and pressure profiles along the absorber tube given for case 1 in [2] compared with our numerical model results, and (b) the calculated flow pattern evolution for case 1 at  $q_w = 12.3 \text{ kW/m}^2$  (calculated peak flux was up to  $25.7 \text{ kW/m}^2$ ).

The detailed parameters used for the model validation are summarized in table 3.2. Our model accurately predicted the evolution of the temperature, pressure, and heat transfer coefficient (averaged value over azimuthal direction for each axial segment) along the flow direction. A slight over estimation in the temperature and underestimation in the pressure in the superheated region were observed (figure 3.3a).

### Chapter 3. Tubular solar receiver for direct steam generation

This agreement led us to conclude that the flow pattern maps can indeed be used for diabatic watersteam flows. The discrepancy between experimental data and the predicted value was associated with the inaccurate heat loss data from reference [2] in the superheating region. Our model was then used to predict the flow pattern evolution along the flow direction, information inaccessible in an actual experiment. 82.9% of the tube length was exposed to two-phase flow. As shown in figure 3.3a, the two-phase flow started with stratified wavy flow (26.8% of two-phase flow region or tube length) and switched to intermittent (6.2% of two-phase flow region or tube length) and to annular flow (64.7% of two-phase flow region or tube length) when the vapor quality reached 0.27. The flow started to dry out at a critical vapor quality of 0.98 for the last 2% of the tube length.

Table 3.2 – Parameters and conditions used in Lobon et al. [2] case 1

Parameters	Vaule
Inner diameter of the absorber	0.05 m
Outer diameter of the absorber	0.07 m
Total length of the absorber	510 m
Pressure at inlet	3.42 MPa
Temperature at inlet	205 °C
Direct normal insolation	822 W/m <sup>2</sup>
Flux concentration ratio	45
Optical efficiency	0.632
Heat loss in preheating collectors	1278 W/m <sup>2</sup>
Heat loss in boiling collectors	1828 W/m <sup>2</sup>
Heat loss in superheating collectors	2323 W/m <sup>2</sup>

#### Comparison to DLR receiver experiment utilizing a high-flux solar simulator

The temperature measurements for a helical tube receiver from the experimental campaigns at DLR in the high-flux solar simulator in Cologne were used for the helical tube model validation. A helical tube with height,  $H_{\text{helical}}$ , of 310 mm, tube outer diameter,  $d_{\text{tube,out}}$ , of 10 mm, tube thickness of 1 mm, and turning radius,  $r_{\text{turn}}$ , of 75 mm was used. The major components of the experimental setup at DLR are shown in figure 3.4a. The inlet water mass flow was controlled by a mass flow controller with an accuracy of  $\pm 0.4\%$ . The pump was connected to an independent, closed-loop water system to guarantee a constant pressure level (6 bar) at the flow inlet. A steam separator was used to separate liquid water and vapor in the outlet fluids. The vapor flow was then condensed in a water-cooled condenser. Three pressure transducers were used to measure the inlet (one transducer) and outlet (two transducers: one



for the pressure before the steam generator, and one for the vapor pressure after the steam generator) fluid pressures with an accuracy of  $\pm 0.2\%$ . K-type thermocouples were welded to the helical tube surface for the measurement of the tube surface temperatures. K-type thermocouples inserted into T-connectors were used to measure the inlet and outlet fluid temperatures. The thermocouples were calibrated by a Klasmeier thermocouple calibrator and showed an accuracy of  $\pm 1$  K. Figure 3.5a shows a side view of the helical tube indicating the positions of the thermocouples used for the temperature measurements. Their exact positions are listed in table 3.3. A conically shaped diffuser was added in the receiver with a bottom diameter of 100 mm and a height of 260 mm with the purpose of achieving a more uniform temperature distribution on the helical tube. Measured temperatures and inlet pressures over time are shown in figure 3.5b with an inflow of liquid water of 3 kg/h at an inlet temperature of 416 K, inlet pressure of 4.4 bar, and 1.51 kW solar power input (peak irradiation at aperture  $750 \text{ kW/m}^2$ , predicted local peak heat flux on tube surface is  $47.6 \text{ kW/m}^2$ , which is within the upper limit for the flow pattern map).

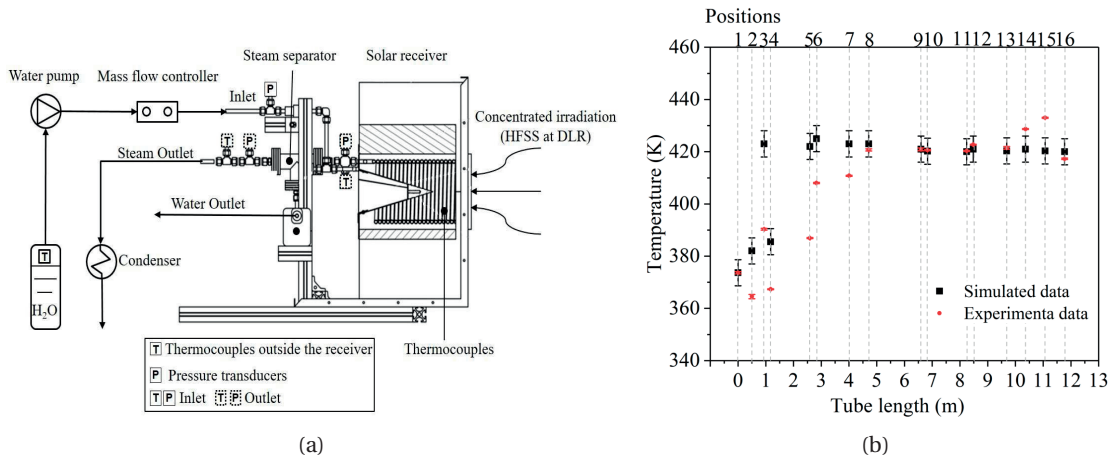


Figure 3.4 – (a) Schematics and main components of the experimental receiver setup at DLR's high-flux solar simulator (HFSS), and (b) comparison of the simulated temperatures and the measured values along the helical tube (at positions indicated in figure 3.5a). The positions 1 and 16 stand for the inlet and outlet fluid temperatures, respectively. Other positions represent surface temperatures of the absorber tube. Red symbols indicate experimental data and the black symbols indicate the simulated data. Error bars for the simulated data indicate the position uncertainties of thermocouples ( $\pm 1$  mm) and errors bars for experiment data result from the standard deviation over the steady state testing time of 2 hours

Figure 3.4 compares our calculated temperatures with the experimental data. In general, the model accurately predicted the tube surface temperatures. The deviation between the simulated and experimental data in the front (positions 2 to 6) are associated with a non-diffuse irradiation in the experiment and the detachment of one thermocouple from the

### Chapter 3. Tubular solar receiver for direct steam generation

surface (position 13). The measured fluid outlet temperature was 417 K with vapor quality of 0.57. The model accurately predicted the outlet fluid conditions with relative deviations of 0.65% and 7% for the temperature (predicted value: 420 K) and vapor quality (predicted value: 0.61), respectively.

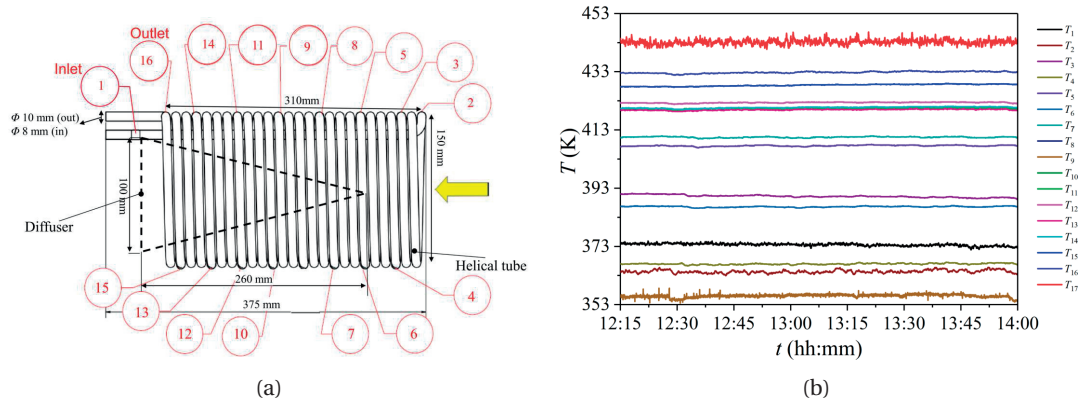


Figure 3.5 – (a) Side view of the helical tube indicating the locations of the thermocouples used for the temperature measurements, and (b) recorded temperature measurements during the experimental run at DLR. The time (12:15 to 14:00) was selected as steady state period for the model validation. This steady state was defined by ensuring that the standard deviation of the measured temperatures ( $T_1 - T_{16}$ ) was within 0.5 K during the selected period.

Table 3.3 – Locations of the thermocouples for the solar receiver tested at DLR.

Thermocouple	Location	Thermocouple	Location
1	0 m	9	6.59 m
2	0.5 m	10	6.83 m
3	0.94 m	11	8.48 m
4	1.18 m	12	8.24 m
5	2.83 m	13	9.69 m
6	2.59 m	14	10.36 m
7	4 m	15	11.07 m
8	4.71 m	16	11.78 m

Note: The locations of thermocouples are shown schematically in figure 3.3a.

#### 3.2.2 Reference cases results

One reference case for two types of receivers was defined (see table 3.4). The number of tubes in receiver 2 was determined by approximating closely the same total tube length as the helical

tube in receiver 1 (3.02 m for receiver 1, and 3.04 m for receiver 2). The fluid inlet was assumed to be at the rear of the cavity (see figure C.1) for receiver 1. The tubes in receiver 2 were connected in series with the outlet of one tube connected to the inlet of the successive tube. The fluid temperature profiles along the tube and the pressure for the two receivers under reference conditions are shown in figure 3.6a and the detailed energy balance are presented in figure 3.6b. The local heat flux along the tube length is shown in figure 3.12 indicating the maximum heat flux may exceed  $90 \text{ kW/m}^2$ , a flux magnitude beyond the validated heat flux for the flow pattern map. The extrapolation of the map to these heat fluxes was not validated. Under reference conditions with 1.5 kW incident solar power at the aperture, the receiver 1 (80.3%) showed better solar-to-thermal efficiency,  $\eta_{\text{STT}}$ , than receiver 2 (78.6%). The  $T_{\text{fluid,out}}$  for receiver 1 was 1068 K, and 1029 K for receiver 2. The pressure drop for receiver 2 was higher compared to receiver 1 due to a longer, higher velocity superheating region. Receiver 1 showed higher  $\dot{Q}_{\text{rerad}}$  (8.4%) than receiver 2 (7.9%) due to higher surface temperatures close to the aperture (see figure 3.6c and 3.6d). Receiver 2 showed larger  $\dot{Q}_{\text{conv}}$  and  $\dot{Q}_{\text{cond}}$  compared to receiver 1 (see figure 3.6b) due to a larger averaged tube surface temperature (741 K for receiver 2, and 609 K for receiver 1).

A larger input power scenario of  $\dot{Q}_{\text{solar}} = 10 \text{ kW}$  was created for which an increased flow rate of 0.0021 kg/s was used. This flow rate was determined by multiplying the 0.0003 kg/s (reference value at  $\dot{Q}_{\text{solar}} = 1.5 \text{ kW}$ ) with the solar power ratio and artificially increasing it by 5% to ensure that the outlet temperature was smaller than 1200 K (an upper temperature considered safe for stainless steel tubes).  $\eta_{\text{STT}}$  of both receivers increased (91.5% for receiver 1 and 90.5% for receiver 2) for the larger input power scenario. The increase of  $\eta_{\text{STT}}$  was attributed to the increasing average concentration ratio (increased from 764 to 5093 for receivers 1 and 2) and increasing surface-averaged heat transfer coefficients (increased from  $3022 \text{ W/m}^2/\text{K}$  to  $8567 \text{ W/m}^2/\text{K}$  for receiver 1, and from  $882 \text{ W/m}^2/\text{K}$  to  $4825 \text{ W/m}^2/\text{K}$  for receiver 2) when  $\dot{Q}_{\text{solar}}$  increased from 1.5 kW to 10 kW. The  $\dot{Q}_{\text{rerad}}$  dominated the heat losses at  $\dot{Q}_{\text{solar}} = 10 \text{ kW}$  due to increased average tube surface temperature (666 K for receiver 1 and 780 K receiver 2). However, the efficiency of receiver 2 was still inferior to the one of receiver 1 due to much higher  $\dot{Q}_{\text{cond}}$  which counteracted the benefit from lower  $\dot{Q}_{\text{rerad}}$  (figure 3.6b). This efficiency difference was reduced at larger  $\dot{Q}_{\text{solar}}$  due to increased difference in  $\dot{Q}_{\text{rerad}}$ . For instance, the absolute efficiency difference between receiver 1 and receiver 2 was 1.7% at  $\dot{Q}_{\text{solar}} = 1.5 \text{ kW}$  and 1% at  $\dot{Q}_{\text{solar}} = 10 \text{ kW}$ .

### Chapter 3. Tubular solar receiver for direct steam generation

Table 3.4 – Reference case parameters used for the comparison of the five different models of the ceria cycling.

Parameters	Value
Cavity inner diameter, $d_{\text{cav}}$	0.09 m
Cavity length, $L_{\text{cav}}$	0.09 m
Aperture outer diameter, $d_{\text{ap}}$	0.05 m
Aperture inner diameter, $d_{\text{ap,in}}$	0.07 m
Insulation diameter, $d_{\text{insu}}$	0.18 m
Insulation length, $L_{\text{insu}}$	0.14 m
Height of helical tube (receiver 1), $H_{\text{helical}}$	0.08 m
Helical turning radius (receiver 1), $r_{\text{turn}}$	0.04 m
Length of helical tube (receiver 1), $L_{\text{tube},1}$	3.02 m
Length of single tube (receiver 2), $L_{\text{tube},2}$	0.08 m
Number of tubes (receiver 1), $N_{\text{tube},1}$	1
Number of tubes (receiver 2), $N_{\text{tube},2}$	38
Tube outer diameter, $d_{\text{tube,out}}$	0.006 m
Tube inner diameter, $d_{\text{tube,in}}$	0.005 m
Surface emissivity of insulation, $\varepsilon_{\text{insu}}$	0.5
Surface emissivity of tube, $\varepsilon_{\text{tube}}$	0.9
Fluid inlet temperature, $T_{\text{fluid,in}}$	303.15 K
Fluid inlet pressure, $p_{\text{fluid,in}}$	5 bar
Inlet flow rate, $\dot{m}_{\text{tube,in}}$	$3 \cdot 10^{-4}$ kg/s
Incident solar power at aperture, $\dot{Q}_{\text{solar}}$	1.5 kW and 10 kW
Standard deviation of flux distribution, $\delta_x$	0.026 m

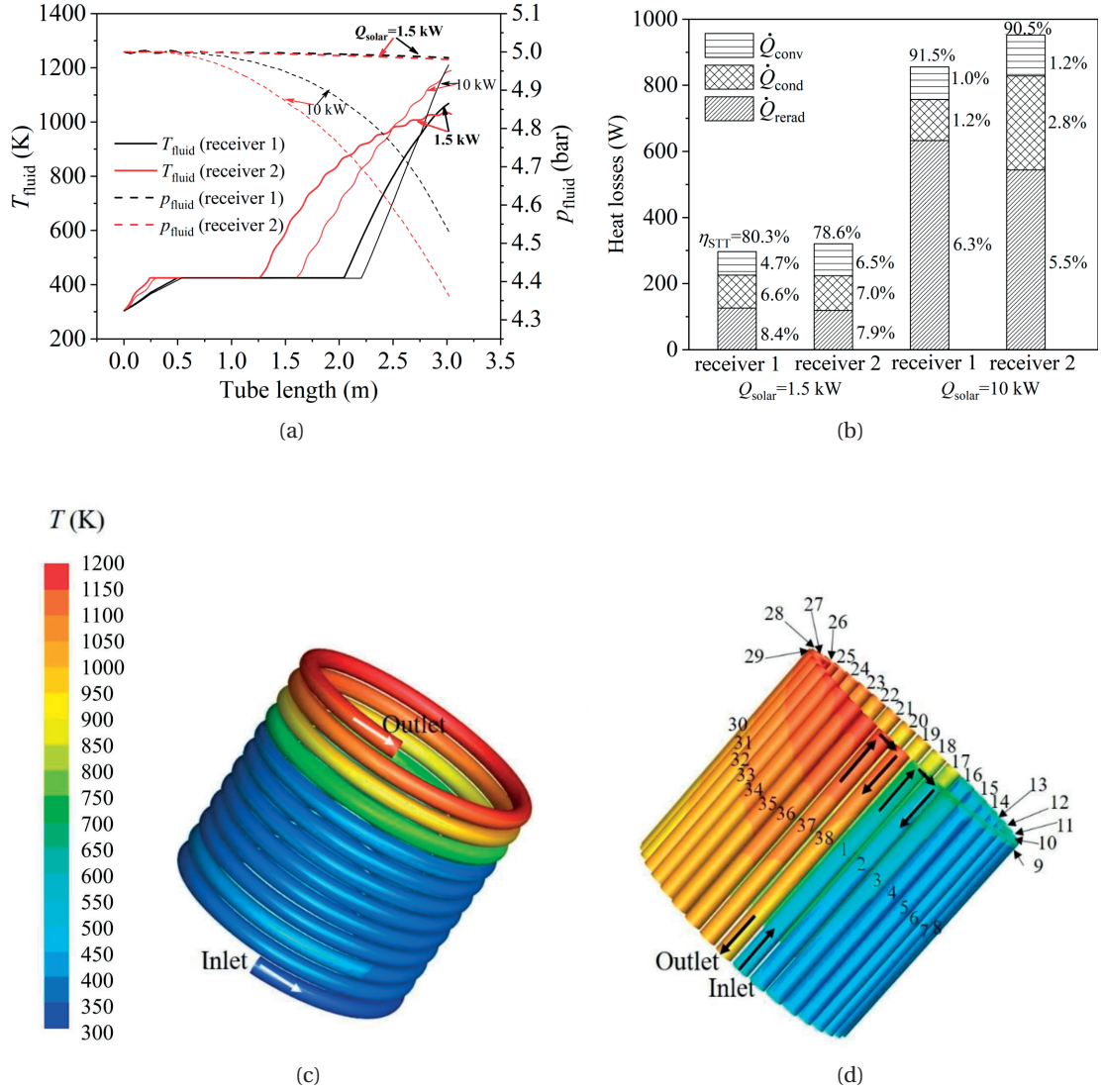


Figure 3.6 – (a) Computed fluid temperature (solid lines) and fluid pressure (dashed lines) along the absorber tube, (b) the fractions of energy losses due to convection, conduction, and re-radiation from the receiver, (c) tube surface temperature for receiver 1 at reference conditions with solar energy input of 1.5 kW, and (d) tube surface temperature for receiver 2 at reference conditions with solar energy input of 1.5 kW. In (a), the thick lines represent the reference case with input solar energy of 1.5 kW and water flow rate of 0.0003 kg/s, and the thin lines stand for the reference case with input solar energy of 10 kW and flow rate of 0.0021 kg/s. Inlet and outlet positions and directions for receiver 1 and receiver 2 are indicated with arrows. Tube connection sequence for receiver 2 is indicated by tube numbers (from 1 - 38).

This model can also be used for the concurrent heating of a water and CO<sub>2</sub> mixture, a scenario interesting for studying syngas production in HTE applications. The corresponding reference

case results are shown in figure 3.7 with the  $\text{CO}_2$  molar fraction varying from 0 to 1 while other parameters were kept at the reference condition. In general, the  $\eta_{\text{STT}}$  decreases with an increasing inlet molar fraction of  $\text{CO}_2$  resulting from higher fluid outlet temperatures for the same solar input (see figure 3.7), which led to higher averaged tube surface temperatures and, correspondingly, higher heat losses. The increase in the fluid outlet temperature with increasing inlet molar fraction of  $\text{CO}_2$  resulted from the reduced (latent) heat demand with the decreasing water flow at the inlet. The addition of  $\text{CO}_2$  to the water led to two competing effects in terms of heat transfer: *i*) its increase in the subcooled region due to the higher fluid velocity, and *ii*) its decrease due to the reduced length of the two-phase flow region. At a small inlet molar fraction of  $\text{CO}_2$  (10 - 20%), the decrease in  $\eta_{\text{STT}}$  due to reduced heating demand is minor while the heat transfer coefficient enhancement in the subcooled region is significant leading to a more efficiency mixture heating than individual heating of water and  $\text{CO}_2$ .

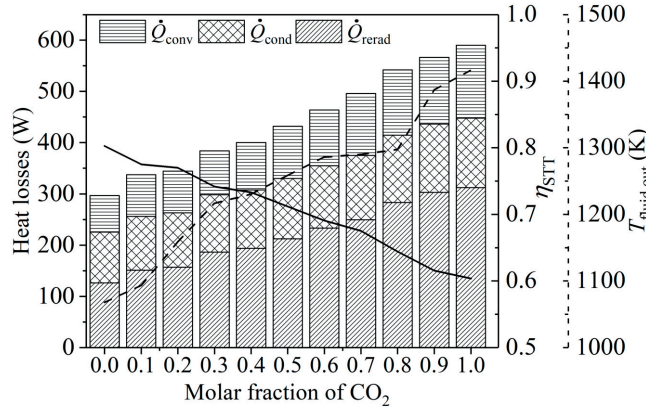


Figure 3.7 – Heat losses (bar), solar-to-thermal efficiency (solid line, decreasing), and fluid outlet temperature (dashed line, increasing) as a function of molar fraction of  $\text{CO}_2$  at the inlet. The three bar types represent convection, conduction, and re-radiation losses.

#### 3.2.3 Flow rates

The outlet fluid temperature  $T_{\text{fluid,out}}$ ,  $\eta_{\text{STT}}$ , and outlet vapor quality,  $x_{\text{out}}$ , are shown as a function of the fluid flow rate,  $\dot{m}_{\text{H}_2\text{O,in}}$ , in figure 3.8a. As  $\dot{m}_{\text{H}_2\text{O,in}}$  increased from 0.3 g/s to 1 g/s, for receiver 1,  $T_{\text{fluid,out}}$  decreased from 1068 K to 425 K,  $\eta_{\text{STT}}$  decreases from 80.4% to 89.3%, and  $x_{\text{out}}$  decreased from 1 (superheated steam) to 0.39. The significant increase in  $\eta_{\text{STT}}$  with increasing  $\dot{m}_{\text{H}_2\text{O,in}}$  can be attributed to significant decrease of  $\dot{Q}_{\text{rerad}}$  ( $\dot{Q}_{\text{rerad}}$  was 161.1 W at 0.3 g/s and 57.2 W at 1 g/s, see figure 3.8b). Receiver 2 showed similar behavior as receiver 1 in a flow rate range of 0.3 g/s to 1 g/s. The increase in  $\eta_{\text{STT}}$  reduced when  $\dot{m}_{\text{H}_2\text{O,in}}$  was larger than 0.45 g/s for receiver 1 and 0.41 g/s for receiver 2 (see figure 3.8a), respectively, both due to the reduced benefit from the decreasing re-radiation losses with increasing flow rate. Note that receiver 1 and receiver 2 were not able to produce superheated steam when the flow rate



was above 0.55 g/s and 0.5 g/s, respectively, both at reference conditions.

As  $\dot{m}_{\text{H}_2\text{O},\text{in}}$  further increased from 1 g/s to 1.6 g/s,  $\eta_{\text{STT}}$  of receiver 1 continued to increase from 89.3 to 89.5% while for receiver 2 it decreased from 87.0% to 86.3%. This further increase of  $\eta_{\text{STT}}$  for receiver 1 with increasing flow rate was mostly due to a decrease of  $\dot{Q}_{\text{conv}}$  (from 33.6 W to 30.7 W) and  $\dot{Q}_{\text{cond}}$  (from 74.1 W to 73.1 W). As for receiver 2, the decrease in  $\eta_{\text{STT}}$  resulted from the increase in all three heat loss terms (see figure 3.8b), attributed to the reduction in heat transfer coefficient resulting from reduced tubular length in the two-phase flow region ( $x_{\text{out}} = 0.38$  at 1 g/s and  $x_{\text{out}} = 0.14$  at 1.6 g/s).

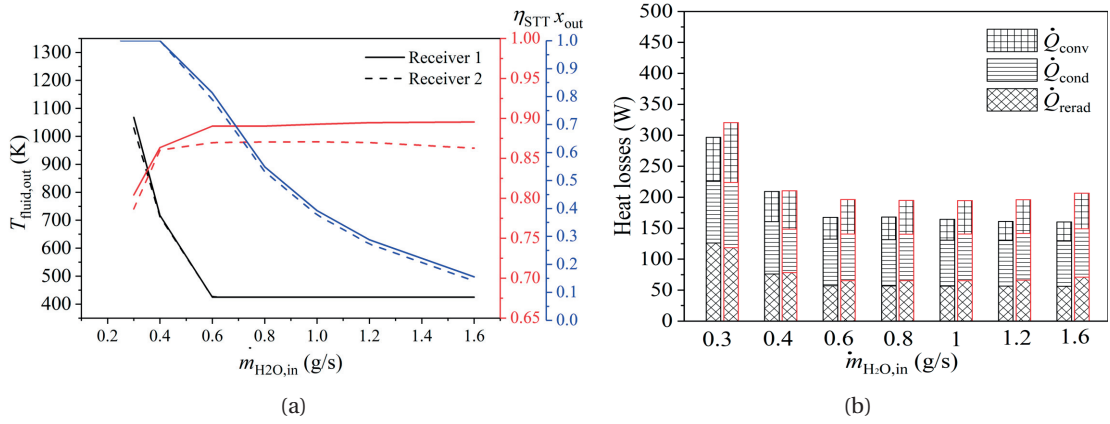


Figure 3.8 – (a) Fluid outlet temperature, solar-to-thermal efficiency, and vapor quality as a function of the flow rate for both receiver types, and (b) composition of the different heat loss terms as a function of the flow rate for receiver 1 (black frame) and receiver 2 (red frame).

The receiver's thermal performance with varying flow rates offers useful information for designing direct steam generation solar receivers with a desired outlet temperature. For example, for a desired fluid outlet temperature of 950 K, receiver 2 is the more reasonable choice as both receiver have identical  $\eta_{\text{STT}}$  while receiver 2 exhibits less stringent temperature gradients (see figure 3.6c and 3.6d).

### 3.2.4 Pressure

The fluid inlet pressure was varied from 1 to 25 bar. The corresponding fluid outlet temperature and solar-to-thermal efficiency are shown in figure 3.9, and the heat loss compositions in figure 3.9b. When the fluid inlet pressure increased from 1 to 10 bar, the solar-to-thermal efficiency slightly decreased for receiver 1 (from 80.3% to 80.1%) while it stayed constant for receiver 2 (78.6%). The decrease in efficiency for receiver 1 was attributed to the increasing conductive and convective heat losses (see figure 3.9b). It is interesting to note that the

outlet temperature increased from 1065 K to 1070 K although the efficiency decreased under reference conditions. This resulted from the decreased enthalpy difference with increasing pressure required to achieve the same temperature. When pressure was further increased from 10 bar to 15 bar, receiver 1 showed a decrease in the solar-to-thermal efficiency (80.4% to 79.5%) due to the higher saturation temperatures at higher pressure and the corresponding increase in the average surface temperature (620 K to 640 K), which dominated and increased the heat losses (see figure 3.9b). For pressures above 15 bars, the solar-to-thermal efficiency was constant for receiver 1 as the benefit from the increased enthalpy difference counteracted the disadvantage in heat transfer losses. The performance of receiver 2 was not sensitive to changes in pressure as the temperature was more uniformly distributed in the receiver.

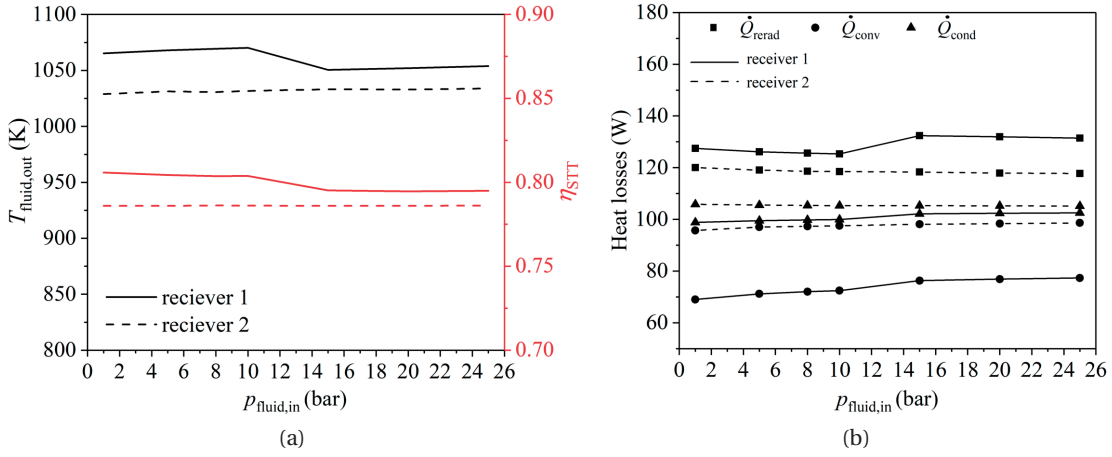


Figure 3.9 – (a) Fluid outlet temperatures (black lines) and solar-to-thermal efficiencies (red lines) as a function of inlet fluid pressure, and (b) composition of heat losses, both for receiver 1 (solid lines) and receiver 2 (dotted lines).

#### 3.2.5 Surface emissivity

The fluid outlet temperature and solar-to-thermal efficiency as a function of the tube surface emissivity are shown in figure 3.10a. The emissivity of the receiver cavity inner surfaces was kept at our reference value of 0.5. In general, the solar-to-thermal efficiency and the fluid outlet temperature increased with increasing surface emissivity (see figure 8a), resulting from sharply reduced re-radiation losses (see figure 3.10b). Receiver 2 showed larger solar-to-thermal efficiencies than receiver 1, in the case when  $\epsilon_{\text{tube}}$  was smaller than 0.58. This was due lower re-radiation losses for receiver 2 compared to receiver 1 (i.e.  $\dot{Q}_{\text{rerad}} = 505$  W for receiver 1 and 437 W for receiver 2 at  $\epsilon_{\text{tube}} = 0.1$ ), which compensated the higher conductive and convective losses for receiver 2. At  $\epsilon_{\text{tube}} = 0.58$ , both receiver types show identical performance. Further increase of  $\epsilon_{\text{tube}}$  (above 0.58) led to higher performance for receiver 1, caused by a reduced difference in the re-radiation losses due to better absorption behavior.



These results provide guidance for the best surface emissivity and correspondingly guide the choice of coating materials (emissivities above 0.8 increase the efficiency only minimal, by less than 0.5%). In addition, the receiver selection (helical tube or multi-tube) can be adapted depending on the choice or availability of the emissivity of the solar absorber surfaces.

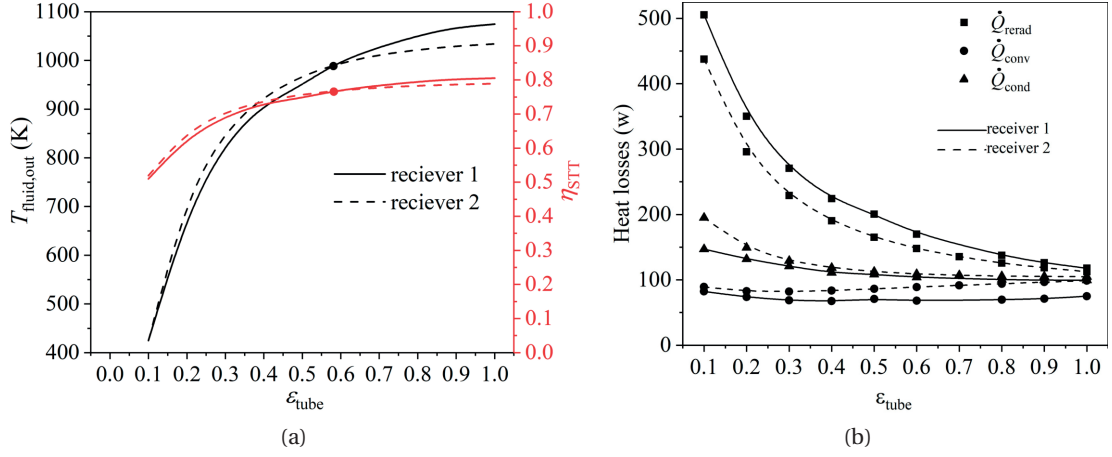


Figure 3.10 – (a) Fluid outlet temperatures (black lines) and solar-to-thermal efficiencies (red lines) as a function of tube surface emissivity, and (b) composition of the heat losses, both for receiver 1 (solid lines) and receiver 2 (dotted lines).

### 3.2.6 Effect of fluid inlet position

The effect of the fluid inlet position on the performance of receiver 1 is shown in figure 3.11. The fluid inlet position was assumed to be at the rear in the reference case. This inlet configuration showed better  $\eta_{\text{STT}}$  at  $\dot{Q}_{\text{solar}} = 1.5$  kW ( $\eta_{\text{STT}} = 80.3\%$ ) than the case with inlet position at the front (co-located with the solar irradiation position) of the receiver ( $\eta_{\text{STT}} = 78.6\%$ ). This advantage in  $\eta_{\text{STT}}$  led to higher outlet fluid temperature (1068 K at rear vs. 1030 K front). The inlet position at the front led to longer sub-cooled and two-phase flow regions than the case with the inlet position at the rear, which led to a lower average tube surface temperature (610 K at front vs. 816 K rear). This in turn resulted in lower  $\dot{Q}_{\text{conv}}$  and  $\dot{Q}_{\text{cond}}$  with a front inlet.  $\dot{Q}_{\text{conv}}$  and  $\dot{Q}_{\text{cond}}$  dominated the heat losses at  $\dot{Q}_{\text{solar}} = 1.5$  kW (see figure 3.11) which favored the rear inlet case. However, the front inlet case showed lower re-radiation heat losses because of the better heat transfer near the aperture which, in turn, led to lower tube surface temperatures near the aperture. Compared to the front inlet case, the decrease of  $\dot{Q}_{\text{conv}}$  and  $\dot{Q}_{\text{cond}}$  with the inlet position at the rear counteracted the increase of  $\dot{Q}_{\text{rerad}}$ , which caused a decrease in  $\eta_{\text{STT}}$ . When the increased from 1.5 kW to 10 kW, the front inlet position showed larger  $\eta_{\text{STT}}$  (92.3%) than the rear inlet position (91.4%). This was due to the domination of  $\dot{Q}_{\text{rerad}}$  (see figure 3.11b) at higher  $\dot{Q}_{\text{solar}}$  and the advantage of having smaller  $\dot{Q}_{\text{rerad}}$  (498 W) for the front inlet case (633 W) than the rear inlet case, which overshadowed the larger convective

### Chapter 3. Tubular solar receiver for direct steam generation

and conductive heat losses for the front inlet case ( $\dot{Q}_{\text{conv}} + \dot{Q}_{\text{cond}} = 223$  W for rear inlet case, and 269 W for front inlet case). Consequently, a smart choice of the flow inlet position can boost the receiver's performance, however dependent on the solar input power magnitude, i.e. the receiver size.

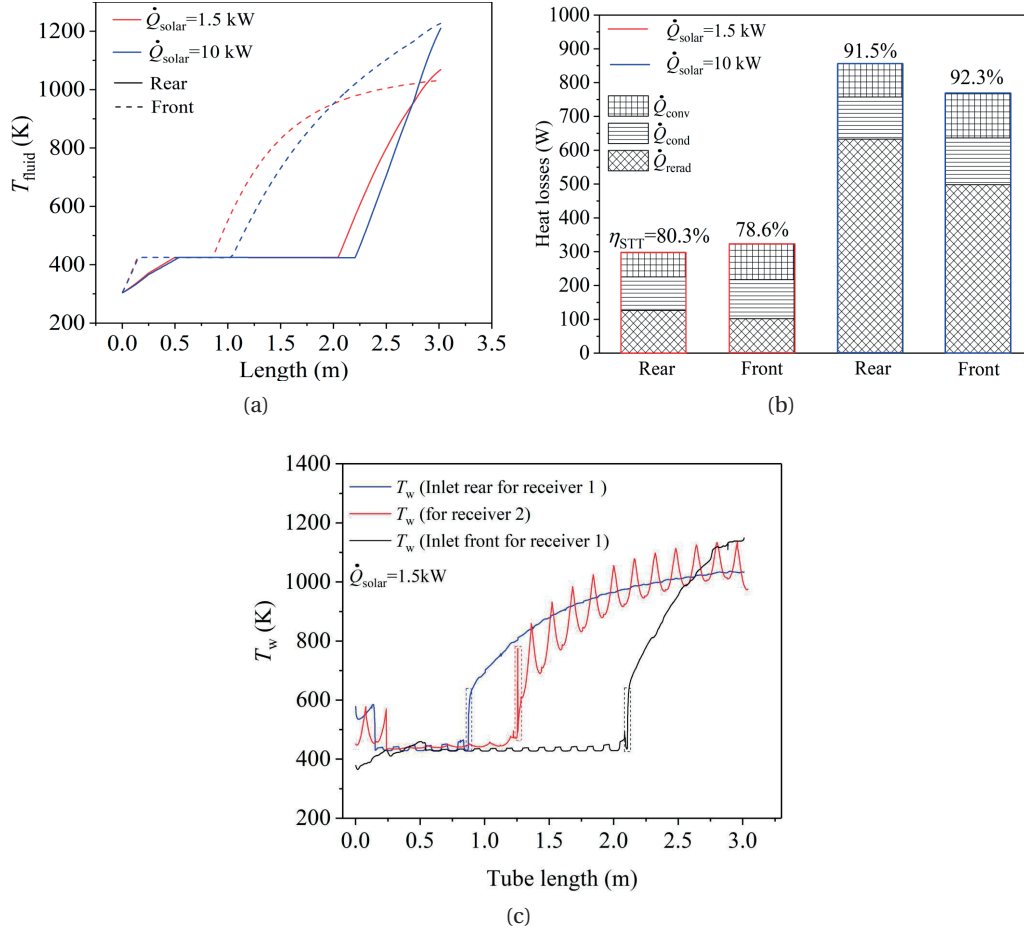


Figure 3.11 – (a) Fluid temperature along the tube for receiver 1 with inlet position at front (solid lines) and rear (dashed lines) and for input solar energy input of 1.5 kW (red lines) and 10 kW (blue lines), (b) composition of heat losses for receiver 1 with front and rear inlet positions and for solar energy input of 1.5 kW (red frame) and 10 kW (blue frame), and (c) averaged inner tube wall temperature along the tube (from inlet to outlet) for inlet at rear (blue line) and front (black line) for receiver 1 and for receiver 2 (red line). The dashed line boxes are for the indication of dryout point.

The hot spots due to the dryout of two-phase can be identified based on the predicted tube surface temperature. The tube surface temperature evaluations along the tube length from the inlet to the outlet for receiver 1 with inlet from the front and rear as well as for receiver 2, both at  $\dot{Q}_{\text{solar}} = 1.5$  kW, is shown in figure 3.11c. Receiver 2 showed the highest temperature jump at the dryout point (from 475 K - 775 K) due to the horizontally positioned absorber

tubes, leading to lower heat transfer coefficient than the helical tube absorber (which can be treated as a combination of horizontal and vertical tubes). The hot spots due to dryout can be used as an indicator for the critical point where thermo-mechanical stresses might be high given by the large temperature gradient. In addition to a large temperature jump at the dryout point, receiver 2 showed a wave-like behavior in the tube inner surface temperature for each tube, given by the configuration of the fluid passing through the receiver from rear to front (or front to rear) with a large heat flux difference (figure 3.12 shows the heat flux profile). In contrast, receiver 1 showed smaller temperature variation in both the subcooled region and the superheated region due to smoother heat flux profiles (figure 3.12). The two cases with fluid inlet from the front and from the rear had very similar temperature jumps at the dryout hot spot (430 K - 635 K for inlet from the rear and 438 K - 637 K for inlet from the front). However, the case with the fluid inlet from the front had less stringent temperature gradients in the dryout hot spot superheated region than the case with inlet from rear (see figure 3.11c), which can potentially lead to smaller thermal stresses.

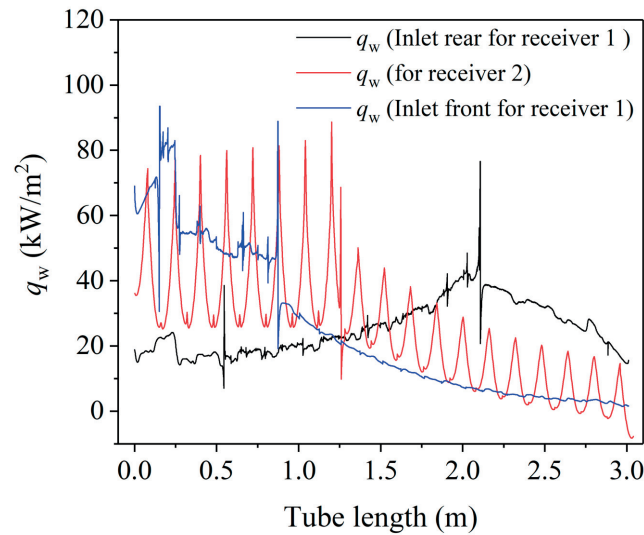


Figure 3.12 – Averaged inner tube wall net heat flux along the tube (from inlet to outlet) for inlet at rear (blue line) and front (black line) for receiver 1, and for receiver 2 (red line).

#### 3.2.7 Tube diameter

The effect of different tube diameters,  $d_{\text{tube,in}}$ , on the receiver thermal performance were investigated which can be used to guide the choice of optimal tube diameter. The tube inner diameters were varied from 4 mm to 12 mm, details on the position are indicated in table 3.5. The cavity size was kept to be unchanged, resulting in a decrease in the total tube length with increasing tube diameter. In general, the total tube length for receiver 1 and receiver 2 were close (within 8 cm for most of the cases and is changing due to the use of integer tube numbers

Table 3.5 – Tube configurations for changing tube diameters, for receiver 1 and receiver 2

	$d_{\text{tube,in}}$ (mm)	4	5	8	10	12
Receiver 1	Total length (m)	3.52	3.01	2.01	1.5	1.26
	Tube number	45	38	25	19	16
Receiver 2	Total length (m)	3.6	3.04	2	1.52	1.28

only for receiver 2). For receiver 1 and receiver 2, the tubes were placed close to the cavity walls, with 1mm distance between the tube wall and cavity wall. This was done in order to avoid direct contact of the absorber tubes with the insulation and benefit from the low thermal conductivity of air. For receiver 2, the tubes were uniformly arranged inside the cavity with 0.5 mm distance between two neighboring tubes. In general, receiver 1 and receiver 2 showed decreasing solar-to-thermal efficiency with increasing  $d_{\text{tube,in}}$ , due to reduced absorbing surface area and fluid residence time in the tubes. Receiver 1 showed better solar-to-thermal efficiency than receiver 2 when  $d_{\text{tube,in}}$  was smaller than 7.5 mm (figure 3.13a). Receiver 1 benefited from lower convective heat losses ( $\dot{Q}_{\text{conv}} = 71.8$  W for receiver 1 and  $\dot{Q}_{\text{conv}} = 96.5$  W for receiver 2 at  $d_{\text{tube,in}} = 4$  mm) at lower tube diameters. At larger  $d_{\text{tube,in}}$  (larger than 7.5 mm), the lower convective losses were counteracted by the dominating  $\dot{Q}_{\text{rerad}}$ , caused by increasing average tube surface temperature at large inner tube diameter (see figure 3.13b), similar as for the emissivity variation investigation (see section 3.2.5)

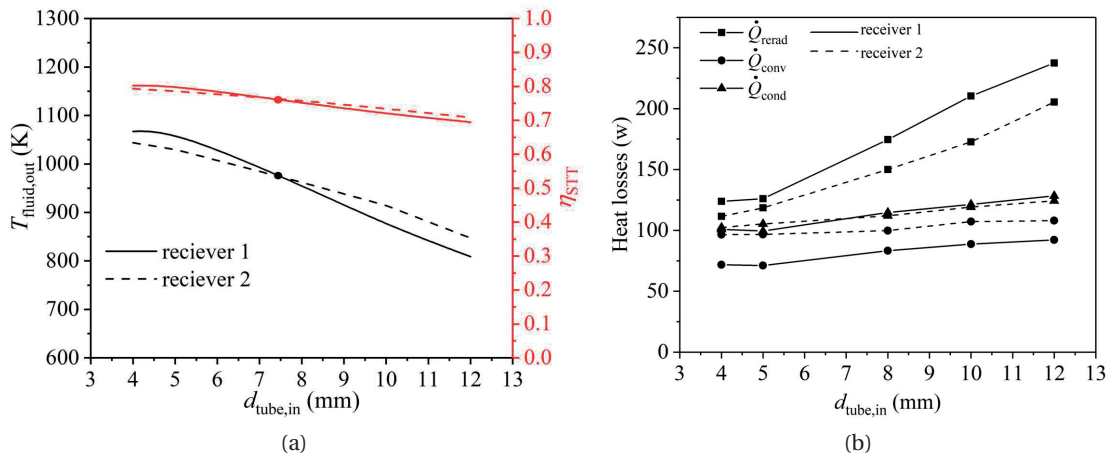


Figure 3.13 – (a) Fluid outlet temperatures (left y-axis in black) and solar-to-thermal efficiencies (right y-axis in red) plotted as a function of tube inner diameter at reference conditions, and (b) composition of the heat losses plotted as a function of tube inner diameter at reference conditions. The solid lines are for receiver 1 and dotted lines are for receiver 2.

### 3.2.8 Shape of the helical tube

Two conical shaped helical tubes (shape 1 and shape 2, see figure 3.14) for receiver 1 were investigated with  $H_{\text{helical}}$  kept at the reference condition (0.08 m). For shape 1, the bottom turning radius was 0.02 m and the top turning radius was 0.04 m. For shape 2, the top and bottom turning radius was reversed, compared to shape 1. Compared with shape 1 and shape 2, the reference shape showed larger solar-to-thermal efficiency, independent of the magnitude of the solar irradiation input power at the aperture (figure 3.14). For example, shape 1 receiver exhibited a solar-to-thermal efficiency of 79.7% and shape 2 receiver showed an efficiency of only 73.2%, while the reference shape reached an efficiency of 80.3%, all at reference conditions. Shape 1 showed slightly higher conductive (76.9 W for Shape 1 and 71.2 W for reference shape) and re-radiative (128.9 W for Shape 1 and 126.1 W for reference shape) heat losses than the reference shape. The significantly lower efficiency of the shape 2 receiver resulted from much higher re-radiation losses (292.6 W) compared to the shape 1 and reference shape receivers. This disadvantage in the re-radiation losses was even more significant at larger solar irradiation input power. For example, when  $\dot{Q}_{\text{solar}} = 10$  kW, shape 1 and reference shape receivers reached efficiencies as high as 91.1% and 91.5%, respectively, while shape 2 reached only 73.4%. Based on our analysis, it is reasonable to choose the cylindrically shaped helical tube. Receivers with this tube shape achieve high efficiency and are reasonably simple to manufacture.

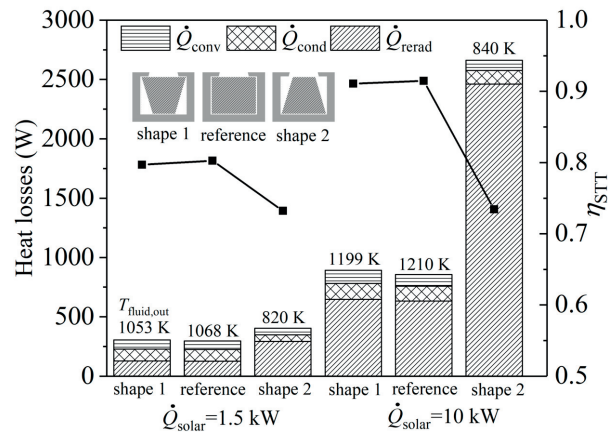


Figure 3.14 – Heat losses, STT efficiency, and fluid outlet temperature for the three different shapes of helical tubes (shape 1, shape 2, and reference case) and two different solar irradiation energies at the aperture (1.5 kW and 10 kW). The different shapes are illustrated in the top left corner. The solid lines with square symbols indicate the solar-to-thermal efficiency. The fluid outlet temperatures are shown on top of each bar.

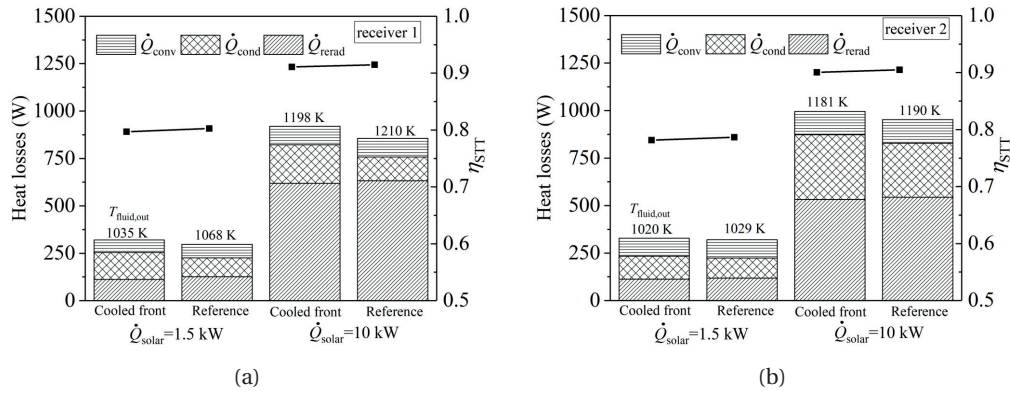


Figure 3.15 – Heat losses, STT efficiency, and fluid outlet temperature for receivers with and without a water-cooled front and for two different solar irradiation magnitudes (1.5 kW and 10 kW). (a) shows the results for receiver 1, and (b) for receiver 2. The solid lines with square symbols indicate solar-to-thermal efficiency. The fluid outlet temperatures are shown on top of each bar.

### 3.2.9 Cooled receiver front

In a practical implementation of the receiver, a water-cooled receiver front is usually employed to avoid overheating and damage caused by spillage irradiation at the receiver front. To simulate the effect of the water-cooled receiver front, a fixed temperature boundary condition was used at the receiver front surface ( $T_{front} = 300$  K) instead of the mixed convective and radiation boundary (see section 2.1.4 ). In figure 3.15, the effect of using a cooled front on the solar-to-thermal efficiency at two solar irradiation conditions (1.5 kW and 10 kW) was investigated. In general, the utilization of water-cooled receiver fronts leads to an increase in conductive heat losses from the front, decreasing the solar-to-thermal efficiency of the receiver. For example, the conductive heat loss for receiver 1 at  $\dot{Q}_{solar} = 1.5$  kW was 99.5 W and increased to 142.1 W when a water-cooled front was used. Consequently, a temperature decrease of 33 K in the fluid outlet temperature was observed and the solar-to-thermal efficiency decreased from 80.3% to 79.7% (figure 3.15a). For  $\dot{Q}_{solar} = 10$  kW, the conductive heat losses increased from 124.7 W to 203.2 W leading to 12 K decrease in the outlet fluid temperature and an 0.4% decrease in efficiency. This indicates that the increase of the incidence solar irradiance could reduce the negative impact of the water-cooled front on the receiver efficiency. Similar behavior was observed for receiver 2. The introduction of the cooled front led to a reduced fluid outlet temperature of 9 K and a reduction in solar-to-thermal efficiency by absolute 0.5%. Similar effects of the cooled front on the thermal performance of receiver 2 was found (figure 3.15b).

The introduction of a water-cooled receiver front, protecting the receiver from spillage irradi-



ation, is accompanied by large heat losses. However, this heat loss becomes less significant when the receiver is scaled.

### 3.2.10 Double helical tube receiver

In the application of solar-driven high temperature electrolysis, two high temperature streams are generally required to feed the SOEC stack: *i*) feed water vapor for the cathode, and *ii*) sweep gas (air/N<sub>2</sub>/Ar) for anode product (i.e. O<sub>2</sub>) remove. Here a double helical tube configuration was proposed using two parallel helical tubes for high temperature water vapor and N<sub>2</sub> generation separately. The geometrical parameters designed for this solar receiver are given in tabel 3.6. The front inlet positions were chosen for both tubes and the fluid temperature evolutions along each tube in the fluid flow directions are shown in figure 3.16. The outlet temperature of fluids are found to be 1024 K for water vapor and 1033 K for nitrogen with temperature difference of 9 K. This small temperature difference between two fluid outlets could guarantee a small temperature gradient at the SOEC stack inlet. For example, by assuming the two fluid inlets have a gap of 2 cm, the inlet temperature gradient is 4.5 K/cm which is well within the required temperature gradient (10 K/cm reported by Aguiar et al. [155]). Figure 3.16b shows the surfaces temperature profiles for two helical tubes with longer blue region (low temperature region,  $T < 400$  K) for the water tube compared to the nitrogen tube due to the presence of two-phase boiling region (corresponding to the flat region for water fluid temperature in figure 3.16a). Based on the modeling efforts presented in this chapter, a compact solar reactor coupling a double helical tube receiver and a SOEC stack was designed, fabricated, and tested which is discussed in the next chapter.

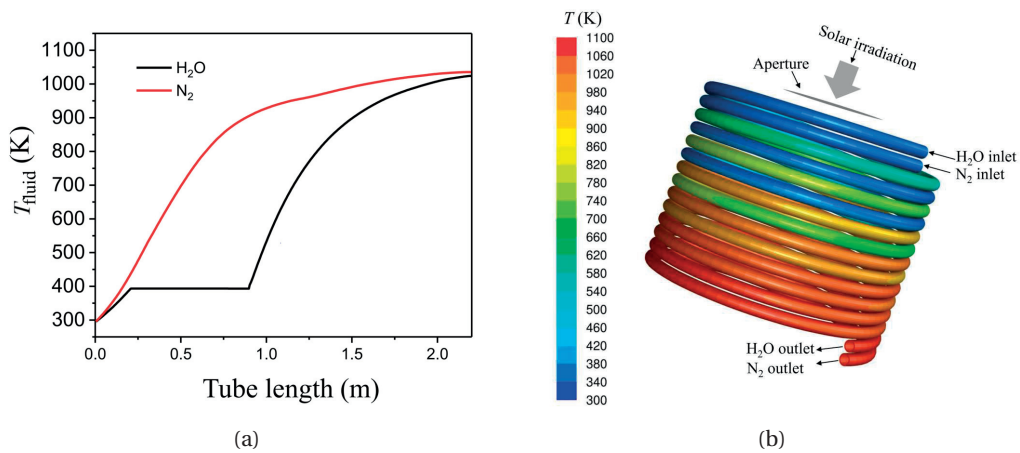


Figure 3.16 – (a) Fluids' temperature as a function of tube length. (b) Temperature profiles for the outer surfaces of two helical tubes.

Table 3.6 – Parameters used for the duoble helical tube receiver modeling

Parameters	Value
Cavity inner diameter, $d_{cav}$	0.11 m
Cavity length, $L_{cav}$	0.11 m
Aperture, $d_{ap}$	0.04 m
Insulation diameter, $d_{insu}$	0.3 m
Insulation length, $L_{insu}$	0.3 m
Height of single helical tube, $H_{helical}$	0.08 m
Helical turning radius, $r_{turn}$	0.05 m
Length of single helical tube, $L_{tube,1}$	2.2 m
Tube outer diameter, $d_{tube,out}$	0.0055 m
Tube inner diameter, $d_{tube,in}$	0.005 m
Fluid inlet temperature, $T_{fluid,in}$	303.15 K
Fluid inlet pressure, $p_{fluid,in}$	1 atm
Inlet flow rate of water	0.2 g/s
Inlet flow rate of nitrogen	0.46 g/s
Incident solar power at aperture, $\dot{Q}_{solar}$	1.5 kW

### 3.3 Summary and conclusions

Under reference conditions, receiver 1 exhibited larger re-radiation heat losses and smaller conductive and convective heat losses compared to receiver 2. The STT efficiency was always higher for receiver 1 than receiver 2 due to higher conductive and convective heat losses. This inferiority in solar-to-thermal efficiency for receiver 2 could be alleviated when a larger solar power was applied, resulting from the dominance of re-radiation heat losses.

The flow rate had a significant effect on the STT efficiency and the fluid outlet conditions. In general, the efficiency increased with the increasing flow rate for receiver 1 and this increase reduced when the flow rate was larger than 0.55 g/s under reference conditions. Receiver 2 showed an increasing efficiency with flow rate when the flow rate was smaller than 1 g/s. Further increase in flow rate lead to a light decrease in solar-to-thermal efficiency resulted from increased heat losses.

Receiver 1 was more sensitive to the variation in pressure than receiver 2. In general, the solar-to-thermal efficiency decreases with increasing inlet fluid pressure. Under reference conditions, there existed a pressure region (10 bar-15 bar) where the decrease in efficiency was more prominent. Higher tube surface emissivity always favored higher solar-to-thermal



efficiency. Receiver 2 showed larger solar-to-thermal efficiency than receiver 1 when  $\epsilon_{\text{tube}}$  was smaller than 0.58. This offers a guideline to choose receiver designs and tube materials. Additionally, receiver 2 might be the choice in cases where pressure variations are not well tolerated in downstream applications.

For receiver 1, the fluid inlet position played an important role in determining the solar-to-thermal efficiency of the receiver. When the re-radiation heat loss dominated (at large input solar power, 10 kW in this study), the rear inlet case showed better performance as the re-radiation reduced when cold fluid passed through tube parts close to aperture. The front inlet is recommended in cases where the conductive and convective heat losses dominate (at small input solar power, 1.5 kW in this study).

Smaller tube diameters always led to higher efficiency of the receivers. Receiver 1 had better efficiency than receiver 2 under reference conditions when the inner tube diameter was smaller than 7.5 mm. While receiver 2 showed larger efficiency at inner tube diameter larger than 7.5 mm. This transition resulted from the smaller  $\dot{Q}_{\text{rerad}}$  for receiver 2 which dominated the heat losses. The reference shape (cylindrical) of helical tube for receiver 1 exhibited a higher solar-to-thermal efficiency than two conical shapes of the helical tube (shape 1 and shape 2). Shape 1 showed very close performance to the reference case and the difference was further reduced by larger solar power input. A significant reduction in efficiency was found in the case with shape 2, resulting from very high re-radiation losses which were even more prominent at higher solar power input.

The use of a water-cooled front can protect the receiver front from overheating caused by spillage irradiation. The introduction of a water-cooled front led to higher conductive heat losses which, in turn, resulted in lower solar-to-thermal efficiency, in the range of 0.5%-1.5%. This decrease in efficiency could be reduced by going to higher solar power input, favoring scaled-up designs of the receiver.

For the scaled receiver, the inlet flow rate will be significantly larger which will lead to a bypassing or reduction of the stratified flow/stratified-wavy flow while elongating the annular flow region in horizontal tubes (see figure 3.3b as an example). This may lead to further enhancement in the thermal efficiency given by the improved in-tube heat transfer. Consequently, a scale-up of the receiver might generally show enhanced efficiencies.

Here, the development of a comprehensive and computationally-effective solar receiver model is reported with special focus on the modeling of the two-phase flow in the solar-driven direct steam generation systems. The thermal efficiency and each heat loss mechanism for two types of tubular receivers were quantified under various operational conditions, material properties, and tube geometries. Results showed that receiver designs achieving high performance in the

### **Chapter 3. Tubular solar receiver for direct steam generation**

---

direct steam generation are possible when carefully considering tube types (multiple tubes and helical tube), surface emissivity, fluid inlet position, target operation temperature, flow rates, and incoming solar power which offers practical design guidelines for direct steam generation solar receiver.

## 4 A compact solar reactor design and experimentation

In this chapter, the design for a 1 kW<sub>th</sub> compact solar reactor which couples a double helical tube solar absorber and a 16-cell SOEC stack in one single reactor is presented. The integration of two components is expected to reduce heat losses in high-temperature fluids transportation. The double helical tube, serving as the solar absorber, is comprised of two parallel placed helical tubes for heating up of N<sub>2</sub>/Air for anode sweeping and feeding reactants (H<sub>2</sub>O and H<sub>2</sub>) for the cathode, respectively, to the required operation temperature (in the range of 550 °C to 700 °C). The outlets of the double helical tubes were directly connected to a SOEC stack mounted on the back of the double helical tubes (avoiding direct illumination by solar irradiation) to feed the cathode and anode sides for the H<sub>2</sub> production via electrochemical reactions in the stack. The design of the compact solar reactor was based on our numerical model (detailed in chapter 3). The two major components, namely the double helical receiver (solar absorber together with steel frame supported insulation) and the SOEC stack, were designed, fabricated, and experimentally characterized separately (campaign 1 and 2). The two components were then coupled to form the compact reactor (campaign 3). The tests for the compact reactor were performed with the high-flux solar simulator (HFSS) at EPFL.

### 4.1 Reactor design

A schematic of the compact 1 kW<sub>th</sub> solar reactor configuration is shown in figure 4.1. It consists of a cylindrical cavity with a double helical tube (tube inner diameter 4 mm, outer diameter 6 mm, helical turning radius 40 mm, and the pitch of each helix 12.2 mm made of Inconel 600) mounted close to the reactor aperture (cone top diameter of 40 mm, and cone bottom diameter 72 mm). The aperture is an open-cavity (windowless) allowing for the direct entering of the incoming irradiation. A 45° cone was design to extend the aperture towards the inner reactor cavity to minimize the irradiation block by water-cooled front (30 mm). The cone angle (45°) of the aperture was chosen to be equal (or larger) than the cone angle of the

## Chapter 4. A compact solar reactor design and experimentation

incident solar irradiation at the focal plane from the source (HFSS at LRESE, EPFL) [156]. To avoid the potential overheating by spillage incident irradiation at the aperture, the reactor front was water-cooled by internal channels (see figure D.1 for the technical drawing for the water-cooled reactor front designs, the water-cooled front temperature can be well controlled within 30 °C). On the back of the solar absorber, a 16-cell SOEC stack was mounted with its inlets (cathode and anode) directly connected to the outlets of the double helical tube for directly feeding by the solar absorber (cathode: helical tube 1 (H<sub>2</sub>O and H<sub>2</sub>), and anode: helical tube 2 (Air or N<sub>2</sub>)). The SOEC stack was composed of 16 square cathode-supported SOEC cells. Each SOEC has a size of 36 cm<sup>2</sup> and an active of 27 cm<sup>2</sup>. Cells were stacked in a series sequence electrically connected by bipolar plates (see figure D.2 for the bipolar plate design). The cathode of the SOEC cell was made of Ni-cermet with a thickness of 250 μm. The YSZ with a thickness of 13 μm acted as the solid electrolyte for ion transportation. The anode was made of LSM with a thickness of 50 μm. The stack was designed to operate at a temperature range from 550 °C to 700 °C.

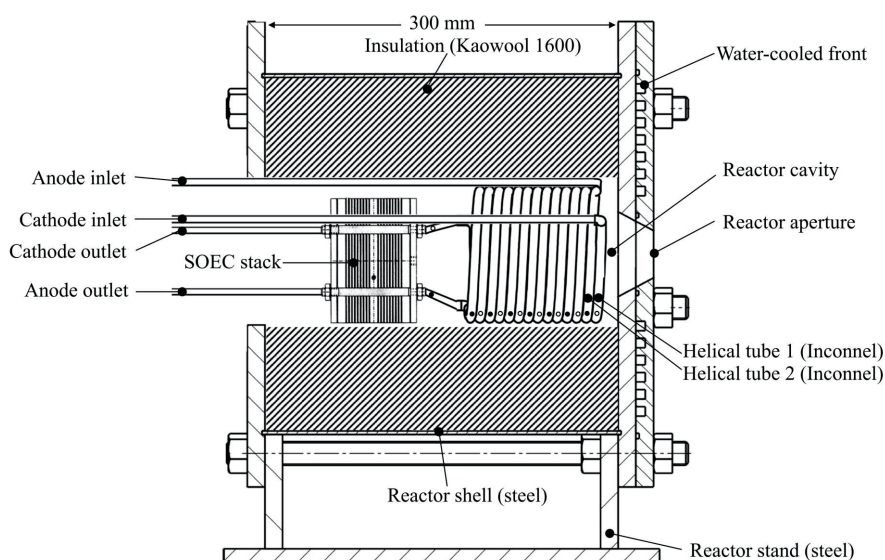


Figure 4.1 – Schematic of the novel compact solar reactor with a double helical tubes solar absorber and a 16-cell SOEC stack directly connected on the back of the solar absorber.

Air or otherwise N<sub>2</sub>, representing the anode flow, and liquid water premixed with H<sub>2</sub>, representing the cathode flow, are separately piped at ambient temperature and 1 atm to the two inlets of the solar absorber and heated up by incoming solar irradiation to the operation temperature of the SOEC stack. The high temperature fluids from the two outlets of the double helical tube entered the cathode inlet (indicated by small unfilled dots) and anode inlet (indicated by small black filled dots). The water vapor in the stack cathode was then electrochemically reduced into H<sub>2</sub> with electrical power externally supplied to the SOEC stack.

The products ( $H_2$  from the cathode, and  $O_2$  from the anode) collected at the two stack outlets.

The solar absorber-SOEC stack assembly was thermally insulated by alumina fiber paper (Kaowool 1600, thermal conductivity:  $-0.02923 + 0.0001568T$  (W/m/K), thickness: 7.5 cm) which filled the gap between the assembly and the reactor shell (steel frame). The voids between the double helical tube and the stack, and from the stack back to the reactor back were filled with Kaowool pellets.

## 4.2 Performance definitions

The electrical electrolysis efficiency,  $\eta_{el,electric}$ , was defined by the ratio between the HHV of the hydrogen (fuel) produced by electrolysis and the electrical power consumed by the stack:

$$\eta_{el,electric} = \frac{\dot{n}_{H_2} \Delta h_{H_2}}{I_{op} V_{op}}, \quad (4.1)$$

where  $I_{op}$  and  $V_{op}$  are the operation current and voltage of the stack.  $\Delta h$  is the enthalpy difference of the water splitting reaction and  $\dot{n}_{H_2}$  the hydrogen production rate. The Faradic efficiency for water splitting is assumed to be 100% resulting in  $\dot{n}_{H_2} \Delta h_{H_2} = I_{op} V_{tn}$ , where  $V_{tn}$  is the thermoneutral voltage (1.3 V [157]). Hence,  $\eta_{el,electric}$  can be defined as:  $1.3 / V_{op}$ .

The solar thermal efficiency,  $\eta_{STT}$ , of the compact solar reactor (without SOEC stack, hence no reactions considered) was the ratio between the enthalpy gain of the fluids and the incident solar irradiation at the reactor aperture:

$$\eta_{STT} = \frac{\sum_i \dot{n}_{i,out} h_{i,out} - \sum_i \dot{n}_{i,in} h_{i,in}}{\dot{Q}_{solar}}, \quad (4.2)$$

where  $\dot{n}_i$  are the molar flow rate of fluid  $i$ ,  $h_i$  the enthalpy of fluid  $i$ , and  $\dot{Q}_{solar}$  the solar power at the aperture without considering the optical efficiency of the concentrator.

The solar-to-fuel efficiency,  $\eta_{STF}$ , was defined as

$$\eta_{STF} = \frac{\dot{n}_{H_2} HHV_{H_2}}{\frac{IV}{\eta_{STE} \eta_{DC-DC}} + \dot{Q}_{solar}}, \quad (4.3)$$

where  $\eta_{STE}$  is the solar-to-electrical efficiency, and  $\eta_{DC-DC}$  the electrical efficiency (0.93 in this study) of the DC-DC converter. The  $\eta_{STE}$  varies with different solar electricity technologies and the effect of which will be discussed in section 4.3.3.

### 4.3 Experimentation

Three experimental campaigns were carried out at GEM of EPFL Sion (campaign 1) and at LRESE of EPFL Lausanne (campaign 2 and campaign 3). Campaign 1 was the testing of the 16-cell SOEC stack under controlled conditions, campaign 2 was the characterization of the thermal performance of the solar receiver without the stack, and campaign 3 was the testing for the compact reactor (receiver + SOEC stack).

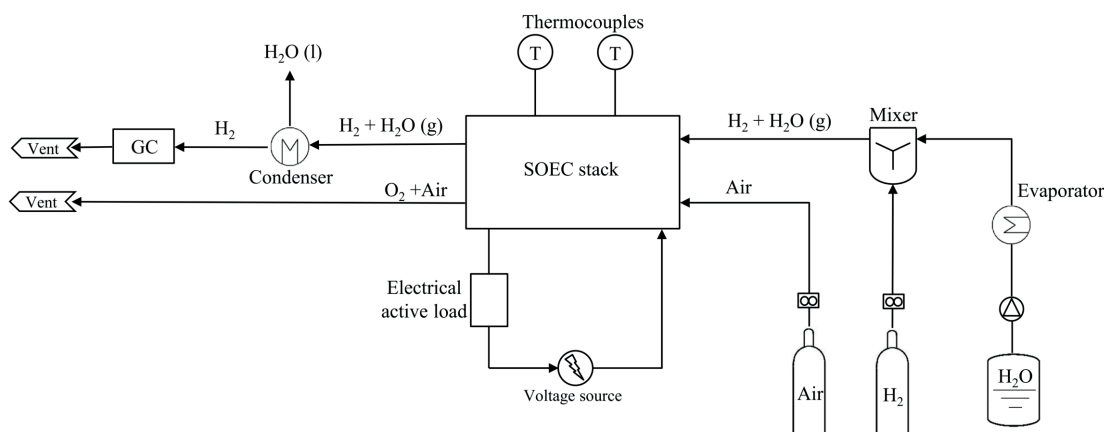


Figure 4.2 – Schematic of the test setup for the SOEC stack under controlled condition at EPFL Sion (campaign 1). The MFC represents mass flow controller and the GC represents gas chromatography.

#### 4.3.1 Characterization of the SOEC stack (campaign 1)

The test setup for the SOEC stack is shown in figure 4.2. The stack was mounted in a bell-furnace (Rohde, D). An electrical steam generator (in-house) was used for liquid water evaporation which was then mix with 10% (molar fraction) H<sub>2</sub>. H<sub>2</sub> was used to avoid re-oxidation of the Ni cathode catalyst. The anode was swept by air. The gas flows were controlled by Red-y mass flow controllers and the liquid water supply to the steam generator was regulated by a dosing pump (KNF). A voltage source (24V, TDK) connected in series with an electrical active load (Agilent) enabled the function for the required current supply to the stack. Two K-type thermocouples were used for the measurement of the stack center temperatures. Two thermocouples were inserted into the center holes at the stack (figure 4.3c).

The SOEC stack was tested under three inlet flow conditions: 4 Nml/min/cm<sup>2</sup>, 8 Nml/min/cm<sup>2</sup>, and 12 Nml/min/cm<sup>2</sup> (defined by the cathode, i.e. cathode area and cathode inlet flow rates were used to calculate these values). The stack was operated at 1 atm with the inlets for cathode and anode having the identical molar flow rates. The total active area of the stack was

$16 \cdot 27 \text{ cm}^2 = 432 \text{ cm}^2$ . Hence, the inlet flow rates for the flow condition of 4 Nml/min/cm<sup>2</sup> (as an example) are: 172.8 ml/min H<sub>2</sub> (cathode inlet), 1.555 g/min H<sub>2</sub>O (cathode inlet), and 1728 ml/min air (anode inlet). Three temperature levels (600 °C, 650 °C, and 700 °C) were tested for each flow condition with the *J-V* and stack center average temperature curves shown in figure 4.4.

The OCV decreased with increasing temperature. For example, the OCV reduced from 14.2 V to 13.4 V (for cell: 0.89 V to 0.84 V) when the stack temperature increased from 600 to 700 K at 8 Nml/min/cm<sup>2</sup>. The increase in the inlet flow rate led to increased OCV (e.g. stack OCV increased from 13.4 V to 13.7 V when the inlet flow increased from 4 Nml/min/cm<sup>2</sup> to 8 Nml/min/cm<sup>2</sup>).

The *J-V* curves showed very close behavior at temperatures of 600 °C and 650 °C all three inlet flow rates due to dominating of large ohmic overpotentials at low temperature due to low ionic conductivity of the YSZ electrolyte. At 700 °C, the cell potential increased with increasing flow rate. For example, from 4 Nml/min/cm<sup>2</sup> to 12 Nml/min/cm<sup>2</sup> due to the increased Nernst potential (OCV from 13.4 V to 13.7 V) and the slightly decreased stack temperature (699.2 °C to 696.1 °C). This indicates that a flow rate of 4 Nml/min/cm<sup>2</sup> is preferred for less electrical power consumption at high temperature (e.g. 700 °C) and less heating demand (smaller flow rate).

$\eta_{\text{el,electric}} = 1$  when the operation voltage for the stack is at 20.8 V (1.3 V per cell, see figure 4.4 the dashed lines). Larger operation voltage leads to reduction in  $\eta_{\text{el,electric}}$ , and lower operation voltage leads to increased  $\eta_{\text{el,electric}}$  (higher even than 1). For solar-driven high-temperature electrolysis systems, the solar thermal efficiency can be much higher than solar electrical efficiency, favoring higher  $\eta_{\text{el,electric}}$  which minimized the electrical demand and maximized the heat demand. In this regard, 4 Nml/min/cm<sup>2</sup> is still good choice as it has larger range of operation current for  $\eta_{\text{el,electric}} > 1$ . For example, 10.4 A is the maximum operation current to ensure  $\eta_{\text{el,electric}} \geq 1$  which is larger than for the flow rate of 8 Nml/min/cm<sup>2</sup> (10.1 A) and 12 Nml/min/cm<sup>2</sup> (8.5 A).

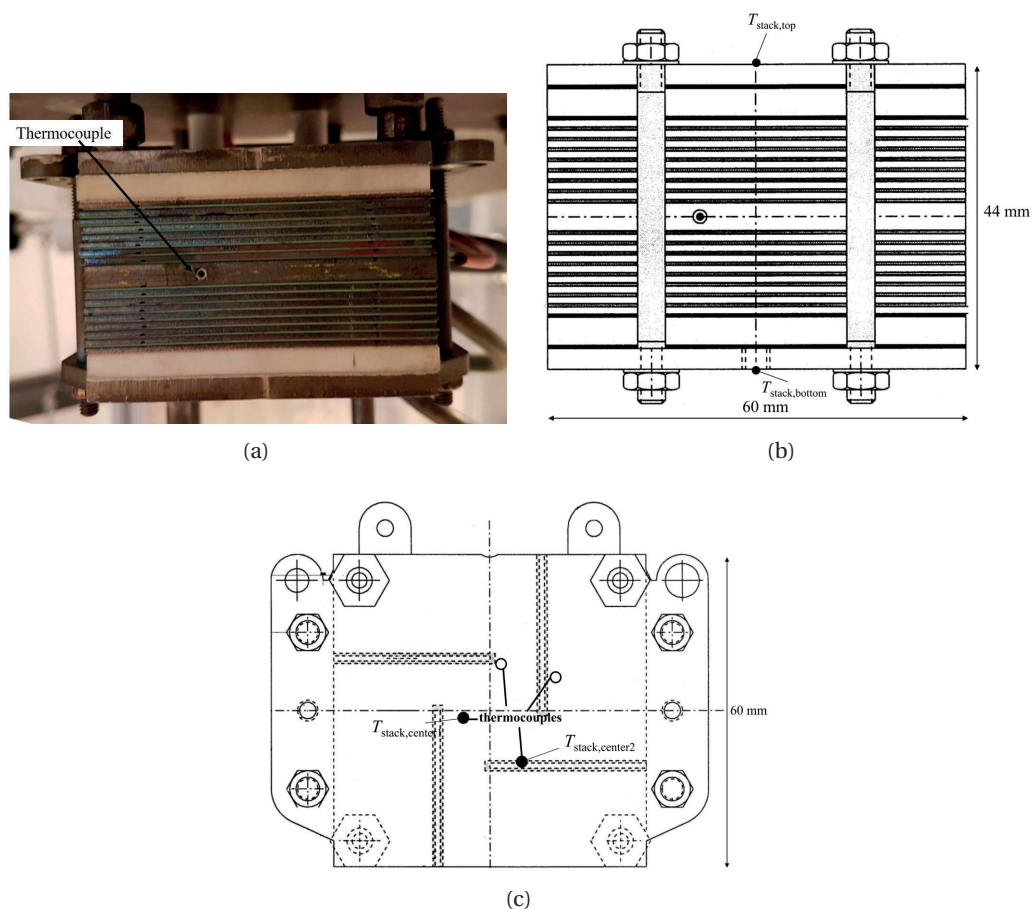


Figure 4.3 – Schematic and photography of the SOEC stack tested in this study: (a) The photography of the 16-cell SOEC stack, (b) the lateral view schematic for the stack, and (c) the top view of the stack showing four holes for install thermocouples. Two filled dots were inserted with thermocouples during our tests, while two unfilled dots were left unused.



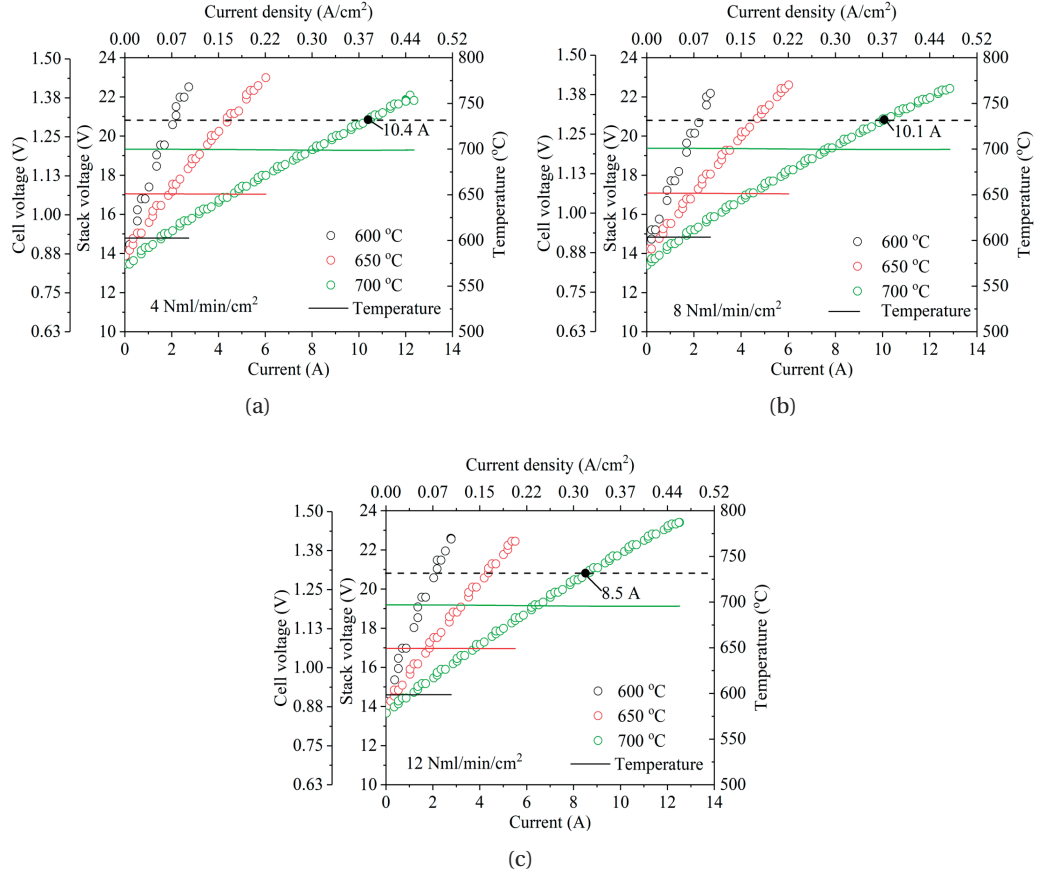


Figure 4.4 –  $J$ - $V$  characterization curves of the SOEC stack at 600 °C, 650 °C, and 700 °C with gas flows: (a) 4 Nml/min/cm<sup>2</sup>, (b) 8 Nml/min/cm<sup>2</sup>, and (c) 12 Nml/min/cm<sup>2</sup>. The colored dots are the current-voltage data. The solid lines are the average temperature at the stack center (y-axis). The stack voltage and the average cell potential (over 16 cells) are shown in left y-axis. The bottom x-axis is the stack operation current and the top x-axis is the cell current density correspondingly. The dashed lines represent the cell potential of 1.3 V (20.8 V for the stack).

#### 4.3.2 Thermal performance of the receiver (campaign 2)

Campaign 2 was performed under the HFSS at LRESE, EPFL for the thermal performance of the solar reactor without coupling the SOEC stack. Different temperature levels were achieved by tuning the incoming irradiation and fluids inlet flow rates.

##### High flux solar simulator

The HFSS is depicted in figure 4.5 and comprises an array of  $18 \times 2.5 \text{ kW}_{\text{el}}$  high-pressure xenon arcs arranged in two concentric circles, each closely coupled with truncated ellipsoidal specu-

lar reflectors of common focus. It provides an external source of intense thermal radiation (radiative power  $> 7.5$  kW, power flux  $> 20$  kW/m<sup>2</sup>) that mimics the heat transfer behaviors of high concentration solar systems, such as solar towers, dishes and furnaces. Meanwhile, it allows experimental work under controlled steady (or artificially created unsteady) conditions for reproducible measurements and model validation [158]. The radiative flux was calibrated as a function of the arc current by a flux gage (Vatell Corporation, TG1000 - 0, colloidal graphite coated, range 0 – 10 MW/m<sup>2</sup>, active area 1.82 mm<sup>2</sup>, repeatability  $< 3\%$ ) placed at the focal point. The radiative flux distribution is measured by using an Al<sub>2</sub>O<sub>3</sub>-plasma-coated Lambertian target (Haueter Engineering GmbH, 350 × 350 mm, water-cooled aluminum body, plasma spray-coated with alumina) by a CCD camera (Basler scA 1400 -17 gm, 1.5 MP, 12 bit pixel depth) equipped with a manual zoom lens (Computar M6Z1212,  $f = 12.5 - 75$  mm, Fujinon HE20 - 1, 2 × extender) and neutral density filters (Midwest ND400, optical density 4), and calibrated by the flux gage. The mismatch of the typical HFSS spectrum and the one the flux gage has been calibrated leads to an assumed uncertainty of 10% for the flux measurements [159]. The solar cavity-receiver is positioned at the focal plane of the HFSS. Radiative power entering into the receiver/reactor was computed by integrating the radiative flux over the reactor's aperture based on the flux measurement. The flux calibration was conducted for lamps 1, 3, 5 and lamps 2, 4, 6 with current supply for each lamp in the range of 70 A to 100 A.

### Thermal measurements

In the campaign 2, the reactor was tested without electrolyzer, only producing superheated steam and nitrogen (see figure 4.7). N<sub>2</sub> flow rates ranging from 0.16 L/min to 0.7 L/min were controlled using an electronic flow controller (Bronkhorst F-201CV, range 0-2 L/min). The liquid water flow rates ranging from 2.25 g/min to 10.8 g/min were ensured by a dosing pump (KNF SIMDOS 02, range 30 μL/min–20 ml/min, repeatability 1%). The two fluids are released to the vent after being heated up in the solar absorber. 6 K-type thermocouples (Material: Chromel – Alumel, tip shell: Inconel 600 1 mm, accuracy  $-40^{\circ}\text{C} < T < +375^{\circ}\text{C}$ , accuracy =  $\pm 1.5^{\circ}\text{C}$ ;  $375^{\circ}\text{C} < T < +1000^{\circ}\text{C}$ , accuracy =  $\pm 0.004T$ ) were used to monitor temperatures up to around 1000 K for the water tube ( $T_1$ ,  $T_2$ ,  $T_3$  for front, middle, and bottom) and the sweep gas tube (N<sub>2</sub>;  $T_4$ ,  $T_5$ ,  $T_6$  for front, middle, and bottom) at the outer surface of the tubes in the solar absorber (see figure 4.6). Four additional K-type thermocouples were used to measure the inlet temperatures ( $T_{\text{in,water}}$  and  $T_{\text{in,N}_2}$ ) and outlet temperatures ( $T_{\text{out,water}}$  and  $T_{\text{out,N}_2}$ ) for the solar absorber.

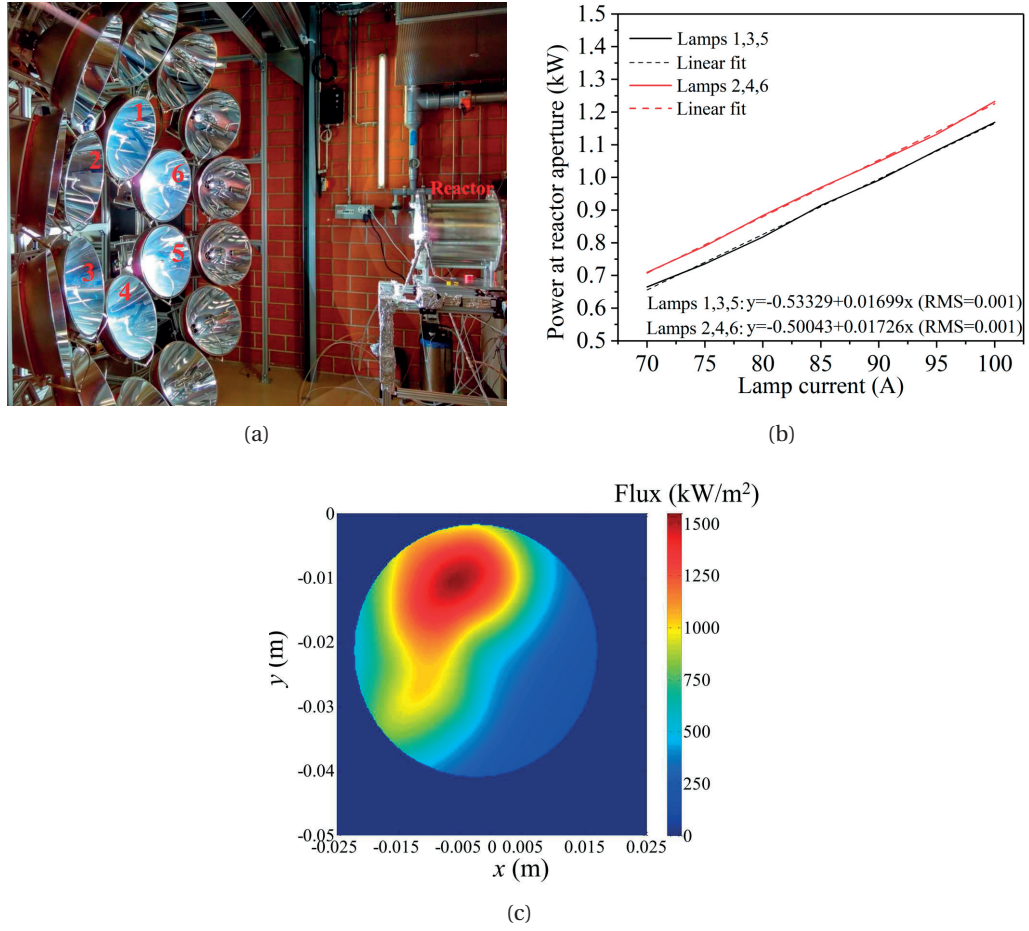


Figure 4.5 – (a) Photograph of the solar reactor operating at the HFSS of EPFL, (b) incident power at the reactor aperture under lamps 1, 3, and 5 and lamps 2, 4, and 6 with various current supplies, and (c) the flux map at the reactor aperture with lamps 1, 3, and 5 at 85 A current for each lamp. The red circle in (c) is the reactor aperture.

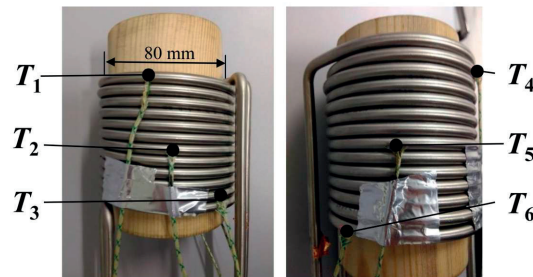


Figure 4.6 – Thermal couple positions on the double helical tube solar absorber.

6 experimental runs with different flow rates combinations of water and N<sub>2</sub> are shown in

## Chapter 4. A compact solar reactor design and experimentation

---

figure 4.8b (see figure 4.8a for more detailed experimental data sets). Solar thermal efficiency and outlet temperatures for 6 combinations of water and  $N_2$  flow rates are shown. In general, the solar thermal efficiency (range between 15.8% and 77.8%) increases and the outlet fluid temperature decreases (water outlet temperature in the range of 938 K to 736 K, and  $N_2$  outlet temperature in the range of 910 to 666 K) with increasing flow rates (water flow rate in range of 2.25 g/min to 12.6 g/min, and  $N_2$  flow rate in range of 0.18 L/min to 1 L/min). At lower flow rates (run 1 to run 3), the increase in flow rates led to a small outlet temperature drop (8 K for both water and  $N_2$  outlet temperatures) which led to a significant solar thermal efficiency increase (15.8% to 47.2%). Run 1 to run 3 were in the region where the re-radiation heat loss is dominant and the heat removal by the fluids were minimal, leading to a stagnation condition where the fluids outlet temperatures were inert to the change in flow rates.

Further increase in flow rates (runs 4 to 6) led to a significant drop fluid temperatures while solar thermal efficiency continued to increase (58.4% to 77.8% from run 4 to run 6). For run 4 to run 6, the temperature difference between the water and  $N_2$  outlets were increasing (from 11 K to 30 K) with increasing flow rates. In campaign 2, the fluid rates of fluids were increased proportionally with a fix flow rate ration (0.08 L( $N_2$ )/g ( $H_2O$ )). As flow rates increased while the solar power input at the aperture kept constant, the two-phase region in the water tube increased due to the increased flow rate (see figure 3.16). Since the incident irradiance on the tube surface did not change, the reduced super heating region led to decreased fluids' residence time for heat exchange between two tubes resulting in larger fluids' temperature difference.

A typical run in campaign 2 is shown in figure 4.9. The inlet temperatures ( $T_{in,water}$  and  $T_{in,N_2}$ ) were kept at 288 K. The flow rates for water and  $N_2$  were 9 g/min and 0.71 L/min, respectively. Three lamps (1, 3, and 5 at 85 A) of the HFSS were utilized resulting in a 0.91 kW input power. The inlet pressures of the inlet fluids were kept at 1 atm. At steady state, the standard deviations of measured temperatures were below 5 K. The outlet temperatures for the steam and  $N_2$  (average over 15 minutes steady state time) were 798 K and 809 K. The temperature different between the two outlets was 11 K.

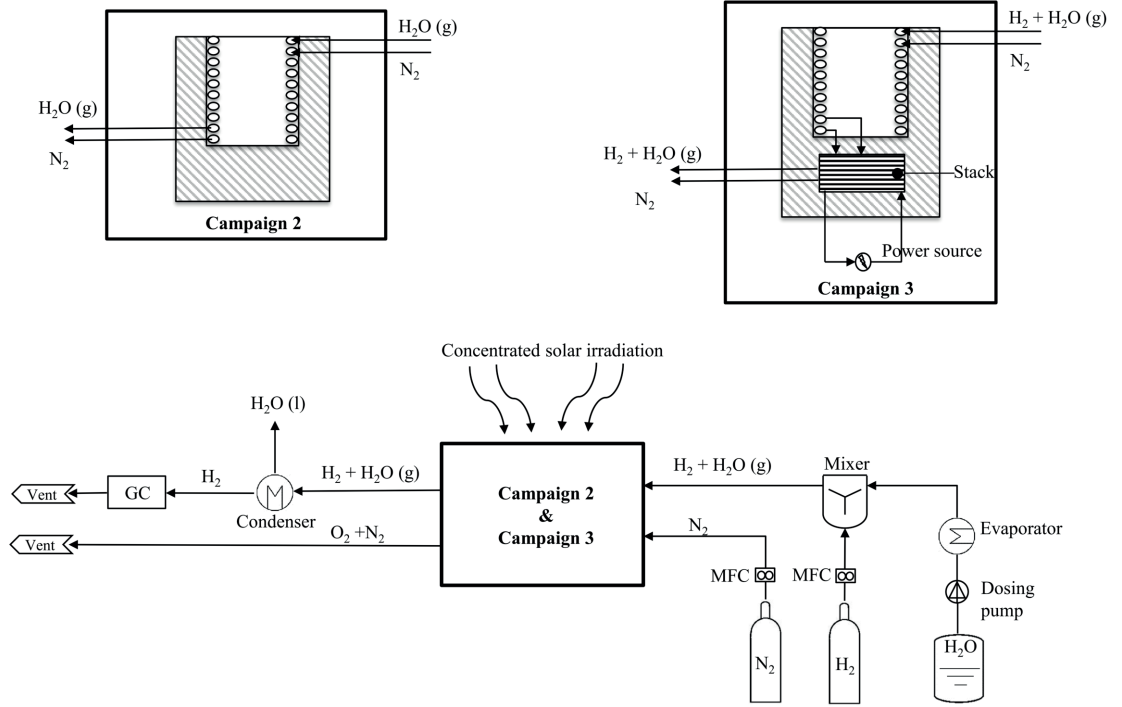


Figure 4.7 – Test setup for campaign 2 and campaign 3 performed under HFSS, LRESE. Campaign 2 is the receiver thermal test without integrating the SOEC stack. Campaign 3 is the compact reactor test with the SOEC stack and the tubular receiver compact.

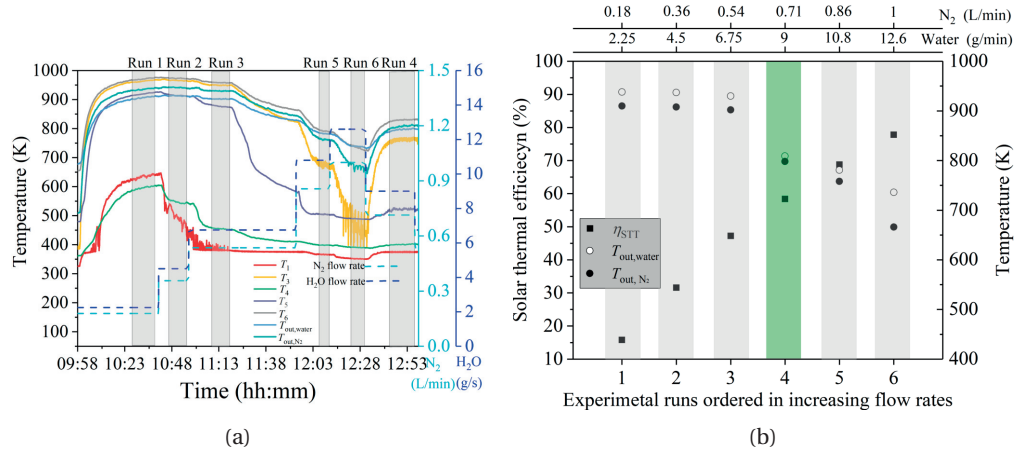


Figure 4.8 – (a) Measured temperature evolution vs. time for all 6 runs under various flow rates. (b) Solar thermal efficiency and fluid outlet temperatures for 6 runs of campaign 2 with changing flow rates under lamps 1, 3, and 5 at 85 A (power at aperture 0.91 kW). The flow rates for water and  $N_2$  are shown in top  $x$ -axis. Run 4 (green) represent the typical run showed in figure 4.9 with the minimal outlet temperature difference between water and  $N_2$  (11 K). Black squares are the solar thermal efficiencies, black circles for  $N_2$  outlet temperatures, and white filled circles for water outlet temperature.

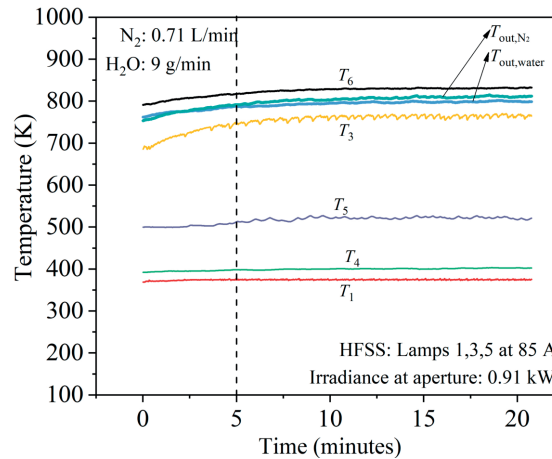


Figure 4.9 – Temperatures for a typical run of campaign 2. The dashed vertical line indicates the start of steady state.

### 4.3.3 Compact solar reactor testing (campaign 3)

In the campaign 3 (see Figure 4.7), the reactor thermal and electrical performances were tested in a compact manner. The thermal setup has been extended by directly connecting the outlets of the solar absorber (the double helical tubes) to the inlets of the SOEC stack (see figure 4.1). To avoid the re-oxidation of Ni catalyst at cathode of the SOEC stack 5% to 10%  $H_2$  (molar fraction) were supplied to the cathode inlet of the reactor. The liquid water and the hydrogen were mixed before introducing into the cathode inlet. The anode inlet was swept with  $N_2$  (partial pressure of oxygen < 2 ppm). The inlet flows were introduced with a pressure of 1 atm. After the heating in the solar absorber and the electrolysis in the stack, the anode flow ( $O_2 + N_2$ /air) was released to the vent whereas the cathode flow ( $H_2$  and steam) was cooled to ambient temperature by a condenser (Alfa Laval AN27-10H, counter flow, 5.5 kW). The  $H_2$  was skimmed from the remaining liquid water by a separator. In addition to the thermocouples for the surface temperature of the solar absorber ( $T_1$  to  $T_6$ ), 4 K-type thermocouples were introduced to measure the temperature of the SOEC stack ( $T_{stack,top}$ ,  $T_{stack,bottom}$ ,  $T_{stack,center1}$ , and  $T_{stack,center2}$ ). Current-voltage curves of the electrolyzer cell were measured using a potentiostat (Power Supply EA - PS 8080 - 60 DT, 0 - 80V, 0 - 1500 W, accuracy < 2%) forcing the current and an auxiliary voltmeter (DC Electronic Load EA-EL 3160-60, 0-160V, 0-400 W, accuracy < 2%) for the voltage measurement.

The required heat rate for the SOEC stack must be smaller than 200 °C/h (Almus AG) to avoid membrane (YSZ) crack due to thermal stress induced by rapid heating. Figure 4.10 shows the temperature evaluation for a typical test of the compact solar reactor. To ensure a heating rate of the SOEC stack smaller than 200 °C, the lamps of the HFSS were turned one by one (from lamp 1 to 6 with lamp current supply from 70 A to 90 A) with a flow combination of 2.57



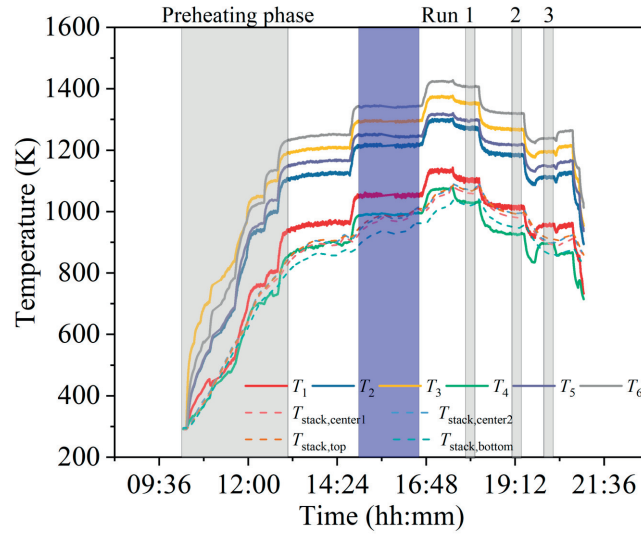


Figure 4.10 – Temperature evolution over the testing time for the thermocouples on the solar absorber ( $T_1$  to  $T_6$ ) and the SOEC stack ( $T_{\text{stack,top}}$ ,  $T_{\text{stack,bottom}}$ ,  $T_{\text{stack,center1}}$ , and  $T_{\text{stack,center2}}$ ).  $J$ - $V$  curves were measured at 3 selected flow and irradiation conditions (run 1 to run 3). Blue block covered region is one of a thermal behavior testing regions.

L/min  $\text{N}_2$  for anode inlet, 0.174 L/min  $\text{H}_2$  and 1.555 g/min  $\text{H}_2\text{O}$  for cathode inlet. As shown in figure 10, the whole preheating phase took about 2.75 hours heating up the stack temperature (averaged over the four measured temperatures on the SOEC stack) from 20 °C up to 560 °C giving a heat rate of 196.7 °C/h which was within the requirement. The maximum temperature different within the SOEC stack (different between  $T_{\text{stack,top}}$  and  $T_{\text{stack,bottom}}$ ) was around 42 K. Hence, for a stack height of 44 mm (see figure 4.3b), the average temperature gradient over the whole cell can be estimated to be 9.5 K/cm which is close to the acceptable 10 K/cm reported by Aguiar et al. [155].

3 runs were selected for three different distinct temperatures (average temperature over the SOEC stack: 783 °C, 707 °C, and 620 °C, see figure 4.10). Run 1 was performed under incident irradiation at the reactor aperture of 2.4 kW (Lamps 1 to 6 at a current supply of 100 A) with a flow of 3.5 L/min  $\text{N}_2$  for anode inlet and 0.36 L/min  $\text{H}_2$  and 3.11 g/min  $\text{H}_2\text{O}$  for cathode inlet (8 Nml/min/cm<sup>2</sup>). Run 2 was performed under incident irradiation at the reactor aperture of 2.04 kW (lamps 1 to 6 at a current supply of 90 A) with the same flow condition as the run 1. Run 3 was performed under the same incident irradiation as run 2 with as flow condition of 2.57 L/min  $\text{N}_2$  for the anode inlet and 0.174 L/min  $\text{H}_2$  and 1.555 g/min  $\text{H}_2\text{O}$  for cathode inlet (4 Nml/min/cm<sup>2</sup>).

The  $J$ - $V$  curves for 3 selected runs are shown in figure 4.11. A degraded electrical performance was found for the SOEC stack at high current density. Take run 2 as an example, the stack

voltage (line with red circles) was larger than the previously measured data under stable condition (red dots) when the current supply to the stack was larger than 6 A. This performance degradation may relate to the degradation/delamination of electrodes induced by enlarged temperature gradient over the stack when further increasing the stack temperature during the thermal testing (the period after the preheating phase and before run 1, see figure 4.10). For example, the average temperature gradient over the stack was found to be 12 K/cm (with an average stack temperature of 965 K) which was larger than the required 10 K/cm. However, significant lower stack voltages were found in the low current region (smaller than 6 A for run 2). This is due to the use of the N<sub>2</sub> (partial pressure of O<sub>2</sub> < 2 ppm) as the anode sweep gas in the compact reactor tests compared to using air in the previous tests, leading to significant reduction in the Nernst potential (see eq. 1.8 which is highly dependent on the partially pressures of the involved reactants. For example, the Nernst potential calculated using bulk concentration for H<sub>2</sub>, O<sub>2</sub>, and H<sub>2</sub>O for run 2 in the compact test (red dots in figure 4.11) is 0.58 V per cell while it is 0.89 V per cell for the stable test (filled red dots in figure 4.11) showing a reduction of 0.31 V (53% reduction). This low operation voltage at low current was also related to the stack degradation or cell break induced by high internal temperature gradient (12 K/cm) which needs to be further confirmed and improved in the future.

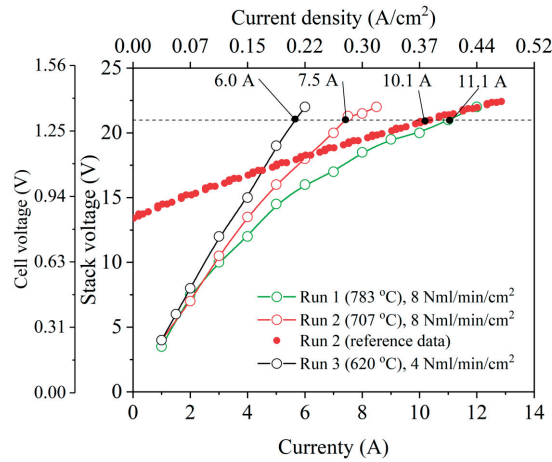


Figure 4.11 –  $J$ - $V$  curves for the selected 3 runs with 3 different averaged stack temperatures. The thermoneutral operations (cell voltage equal to 1.3V) of the stack are indicated by the filled black dots. Filled red dots are the data measured under stable conditions for the same flow (identical flow rate in cathode, while air instead of N<sub>2</sub> was used for anode sweeping) and temperature conditions (figure 4.4b for 8 NmL/min/cm<sup>2</sup> and 700 °C)

The compact reactor tests showed that the novel reactor concept can provide a relatively sufficient stable thermal operation conditions for SOEC stack. The STF efficiency can be estimated based on the measured compact solar reactor performance. The solar-to-electricity efficiency,  $\eta_{STE}$ , was assumed to be 15% by using commercialized single-crystalline silicon



PV cells [68] for electricity supplying to the SOEC stack of the solar reactor. The electrical efficiency for the DC-DC converter,  $\eta_{DC\_DC}$ , was 93% as mentioned in section 4.2. For the 3 runs tested in the compact solar reactor mode, the STF efficiency of the compact reactor was calculated without any heat recovery by assuming an thermoneutral operation (1.3 V per cell) and an 100% Faradic efficiency. The  $\eta_{STF}$  for run1 to run 3 were 5.7%, 4.9%, and 4.3%. If III-V based PV cell is used as the electrical source, for example a commercial III-V triple junction cell [10] with of 37% under 200 suns, the  $\eta_{STF}$  for run1 to run 3 increased to 7.5%, 6.3%, and 5.2%. For run 2, if the SOEC stack was operated without degradation and coupled to the III-V PV cells, the envisioned can be 7.9%.

The potential to increase  $\eta_{STF}$  further can be achieved by introducing heat recovery. For example, two heat exchangers can be used to recover heat of the cathode and anode outlets for preheating the cathode and anode inlets, respectively. Assuming a heat exchanger effectiveness of 0.7 based on the heat exchanger model in chapter 1 section 1.2.4 and a solar thermal efficiency of 50% for the receiver (an averaged values based on campaign 2). For run 1, 48% reduction in required incident solar irradiation was achieved with the  $\eta_{STF}$  can be further improved to 13.7% using III-V based PV cells with SOEC stack data from campaign 3. Similarly, for run 2 and run 3, the  $\eta_{STF}$  can be improved to 10.9% and 15.8%, respectively. The sharp increase in  $\eta_{STF}$  for run 3 shows the importance of the optimization for the flow rates (not only optimizing for the SOEC stack performance) which could possibly minimize the required solar energy for heating when the heat recovery is introduced.

#### 4.4 Summary and conclusions

A novel compact solar reactor which couples a double helical tube solar receiver and a 16-cell SOEC stack in one single reactor was proposed, fabricated, and experimentally tested for hydrogen production. The SOEC stack was initially tested under well-controlled stable conditions at GEM's test bench to characterize the electrochemical behavior of the SOEC stack under various temperature and flow rate conditions (campaign 1). Higher temperature always leads to better electrical performance of the SOEC stack. Lower flow rate (e.g. 4 Nml/min/cm<sup>2</sup>) showed better stack performance, especially at high temperature (e.g. 700 °C) due to lower Nernst potential and slightly higher stack temperature. In addition, low flow rate in compact reactor mode can reduce the required solar power for heating. The thermal behavior of the solar absorber was tested under various flow rates in campaign 2. A maximum solar-to-thermal efficiency of 78% was achieved for run 6 with inlet flow rates of 1 L/min N<sub>2</sub> and 12.6 g/min water and 0.91 kW incident irradiance at the reactor aperture. Re-radiation heat losses dominated at low flow rates (for N<sub>2</sub> between 0.18 L/min and 0.53 L/min, for water between 2.25 g/min and 6.75 g/min), for which the outlet temperatures were only slightly affected by

the flow rates (9 K increase with increasing flow rates). In the campaign 3, the thermal and electrical performance were tested for the compact solar reactor. The preheating phase showed good heating rates (196.7 °C/h) and maximum 9.5 K/cm temperature gradient over the stack. The further increasing in the stack temperature (blue region figure, average stack temperature 965 K) led to high temperature gradient (12 K/cm) which may lead to degradation in stack performance. Based on the measured performance of the stack, the solar-to-fuel efficiency of 5.3% can be achieved for run 3 (1056 K and 8 Nml/min/cm<sup>2</sup>) with a single-crystalline silicon PV. When III-V based PV cells were assumed (37% solar-to-electricity efficiency), the solar-to-fuel efficiency of the reactor can be improved to 7.5%. Further introduce of heat recovery may lead to a further efficiency increased can be envisioned to 13.7% (for run 3 with III-V based PV) by assuming a heat recovery effectiveness of 0.6.

The experimental results show the feasibility of this novel solar reactor concept, featuring direct steam generation and direct feeding of the reactant and sweep gas to the SOEC stack in order to reduce the transmission heat losses. This design is expected to enhance STF efficiency, reduce system complexity, and hence improve system sustainability compared to a separated approach.

Further improvements of the reactor include fabrication of higher performance SOEC stack and stable temperature (temperature gradient) control over the stack to avoid the fast degradation induced by fast heating and large temperature gradient over the stack. Our work on improving the compact reactor is on-going, the improvement will include a better performance stack and adding controlled electrical heating system on the solar absorber for the stabilization of the stack temperature.

## 5 An integrated concentrated solar fuel generator concept<sup>1</sup>

According to the discussion in chapter 1, the hybrid approach (PV + CST) was found to be the most promising strategy benefiting both high efficiency heating from concentrated solar technologies and cheap PV electricity. Typically, a 10% solar-to-hydrogen efficiency can be achieved by carefully choosing operation conditions using commercialized single crystalline silicon PV cells.

In the hybrid CST and PV approach, PV, solar receiver, and SOEC are considered to be three independent subsystems, electrically connected by wires and power electronics (between PV and SOEC) and fluidically connected by metal or ceramic pipes (between the solar receiver and SOEC) [160, 44]. These connections lead to transmission losses in, both, electricity and heat. An estimated temperature drop of 300 K and energy loss 100 W is predicted for two connecting pipes of 5 cm length each with a 15 cm thick Alumina insulation. All these losses are expected to reduce the system efficiency by 30% unless highly conductive electrical networks and well-insulated pipe networks are designed and used. Additionally, this system, made of several separate components, will require more auxiliary components and balance of system, expected to lead to increased cost and reduced sustainability. To minimize these transmission losses and to reduce the system complexity, we propose an integrated solar fuel reactor design which combines a cavity receiver (cavity chamber and thermal insulations) and a tubular solid oxide electrolyzer cell (SOEC) (anode and cathode channels and electrodes, and a solid oxide electrolyte) forming a compact monolithic device. The electricity need of the SOEC are provided by a concentrated III-V triple junction photovoltaic cell integrated on the water-cooled aperture of the reactor. The surface of the SOEC cell (see figure 5.1 the cathode channel outer surface) is simultaneously used as the solar absorber for reactant heating and the reactant channel. The heated-up reactants are then electrochemically and

---

<sup>1</sup>Material from this chapter is in preparation for a journal publication: M. Lin and S. Haussener, "An integrated concentrated solar fuel generator concept utilizing a tubular solid oxide electrolysis cell as the solar absorber," 2018.

thermochemically converted in the SOEC cell.

The solar energy partitioning between heat generation (in the absorber tube) and electricity generation (in the PV cell) is achieved by varying the radius of the reactor aperture for a specific size of the focus size.

The feasibility assessment and the quantification of the monolithic reactor performance under various operation conditions is key for the successful engineering of such a reactor concept. Various models of SOEC have been proposed [161, 162, 163, 164], assuming the SOEC is either placed in a well-controlled oven (constant outer surface temperature [165]) or well-insulated (adiabatic conditions [161, 164]). None of these modeling efforts considered the non-uniform heating conditions of the SOEC, which in turn leads to the spatial temperature and current variations. The SOEC performance corresponding to these non-uniform heating induced variations are of importance for the optimized integrated solar reactor design in terms of both performance and mechanical stability. Another key challenge for this integrated solar reactor design lies in the mechanical stability of the ceramic absorber/electrolyzer tube. Thermo-mechanical stresses are induced by the large temperature gradients within the ceramic absorber/electrolyzer tube, resulting from the non-uniform concentrated solar energy input and the intermittency of solar energy. To address these problems, the homogeneity of the temperature inside the reactor is of great interest. Design guidelines for the reactor need to be formulated so as to avoid unacceptable temperature gradients in the reactor.

In this study, we developed a multi-physics model for the performance prediction of the integrated solar reactor (see figure 5.1 for the reactor model domain) which solves the various coupled physical governing equations in 2D by a commercial finite element solver [166]: fluid flow and species transport in fluid channels and electrodes, electrochemistry and thermochemistry on the electrodes, current distribution on the whole SOEC, and heat transfer over the entire reactor. The III-V material based PV cell performance was predicted by the equivalent circuit model which was then coupled directly (direct wire connection) or indirectly (via a DC-DC converter) to the SOEC.

## 5.1 Reactor description

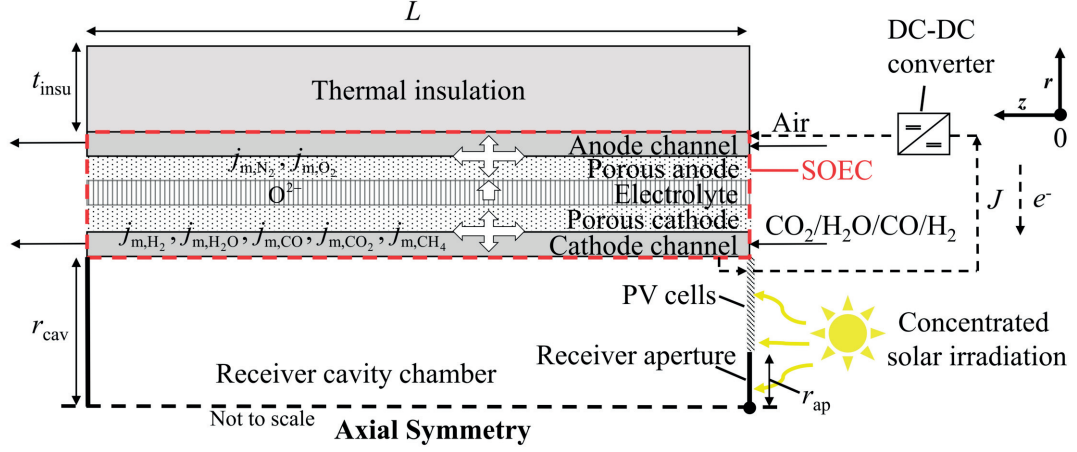


Figure 5.1 – Schematic of the axisymmetric calculation domain for the proposed integrated solar reactor (not to scale). The dashed red box is the SOEC cell domain. The white thick arrows stand for species transport and the dashed black lines stand for current flows. The coordinate 0 point (black dot) is on the aperture (black dot at the aperture domain). The DC-DC converter only appears in the indirect connected cases.

The multi-layered ceramic absorber tube (which also acts as SOEC cell) is the key component of the integrated reactor where the reactants ( $\text{H}_2\text{O}$  and  $\text{CO}_2$ ) are heated electrochemically converted into syngas while competing with two thermochemical reactions. In the porous cathode,  $\text{H}_2\text{O}$  and  $\text{CO}_2$  are reduced with electrons into  $\text{H}_2$ ,  $\text{CO}$ , and  $\text{O}^{2-}$  (eqs. 6 and 7).

The water reduction reaction (eq. 6) is termed as reaction 1 (R1) and the  $\text{CO}_2$  reduction reaction (eq. 7) is termed reaction 2 (R2) in this chapter.

In the porous anode, the oxygen ions are transported through the solid oxide electrolyte (i.e. YSZ) from the cathode to the anode, where they are oxidized into oxygen and electrons (eq. 8, termed R3).

Air acts as the sweep gas for the anode. In the case of syngas production, two additional reversible thermochemical reactions take place, i.e. water-gas shift reaction (WGSR) and steam reforming reaction (SRR) (termed R4 and R5):



The PV cell was placed at the water-cooled reactor front, around the receiver aperture, convert-

ing concentrated solar irradiation into electricity which is either directly provided to the SOEC or indirectly provided to the SOEC through a DC-DC. The latter approach provides better power matching between the SOEC and PV. Here, the solar energy partitioning for PV and solar receiver can be adjusted by tuning the aperture size, and the mean solar concentration can be different for the PV and solar receiver.

A numerical model for the integrated solar reactor is developed. The model simultaneously solves the governing equations for each component and couples the different components (sub-domains) with flux boundary conditions. The calculation domain (figure 5.1) was divided into several sub-domains: *i*) the receiver chamber domain (solving for radiative transfer and natural convection), *ii*) the tubular SOEC cell domain composed of two channels (cathode and anode channels), two porous electrodes (cathode and anode), and a solid electrolyte (solving for charge transport, fluid flow, species transport, and heat transfer), *iii*) the thermal insulation domain (solving for heat conduction), and *iv*) the PV cell domain placed at the front of the reactor (solving an equivalent circuit model for opto-electronic performance).

## 5.2 Model development

### 5.3 Cavity model

At the aperture of the cavity, the spatial distribution of the concentrated solar irradiation is estimated by a Gaussian distribution and the angular distribution is assumed to be diffuse. These characteristics largely dependent on the geometry of the concentrator and the position of the reactor relative to the focal plane of the concentrating facility and is characterized by the mean concentration ( $C_{ap}$ ). The receiver aperture boundary was treated as a high-temperature blackbody surface with an equivalent temperature [44]. The surface integration of the radiative flux over the receiver aperture gives the total solar power input into the receiver for heating use ( $\dot{Q}_{solar,ap}$ ).

The inner surfaces of the receiver cavity were considered grey and diffuse, and the air inside the cavity was assumed to be a non-participating media in the radiative heat transfer and was described by a surface-to-surface radiation model [167]. This model was applied to all inner cavity surfaces and the aperture. The re-radiation loss ( $\dot{Q}_{rerad}$ ) was defined as the total emitted power from the inner cavity surfaces toward the aperture. The heat conduction through the air in the cavity was not numerically computed but estimated with a surface heatsink. Similarly, also the fluid flow and natural convection was quantified by utilizing an empirical Nu correlation [135] and was applied to the receiver inner surfaces as heat sink [46]. The convective heat loss ( $\dot{Q}_{nc}$ ) was the integration of the convective heat transfer rate over the cavity walls. The net heat passing into the absorber tube/tubular SOEC was used for reactants

heating as well as providing thermal energy for chemical reactions (when needed).

## 5.4 SOEC models

### 5.4.1 Fluid flow and species transport

The two gas channels and two porous electrodes were modeled as porous media (materials properties given in tables 5.1, and E.1-E.4). Gas channels were comprised of multiple straight channels which were used as current collector/distributor and fluid distributor. Instead of modeling the detailed multi-channel geometry, the gas channels were modeled as porous domains with porosities (void channel volume over the total volume of the channel domain) and tortuosities (to be used in the species transport model, eqs. 5.3 and 5.4) [168]. The fluid flow in the two gas channels and the two porous electrodes were modeled by solving the mass conservation equation and Navier-Stokes equation with the Darcy extension [169],

$$\nabla \cdot (\rho u) = Q_M, \quad (5.3)$$

$$\frac{\rho}{\varepsilon} \left( u \cdot \nabla \frac{u}{\varepsilon} \right) = \nabla \cdot \left[ -p I_d + \frac{\mu}{\varepsilon} (\nabla u + (\nabla u)^T) - \frac{2\mu}{3\varepsilon} (\nabla \cdot u) I_d \right] - \left( \mu B^{-1} + \beta_F |u| + \frac{Q_M}{\varepsilon^2} \right) u, \quad (5.4)$$

where  $u$  is the superficial fluid velocity,  $\rho$  the gas mixture density,  $Q_M$  the mass source term (zero for gas channels and for porous electrodes based on the local electro- and thermochemical reactions, see below).  $\mu$  is the dynamic viscosity (obtained from Coolprop [139]),  $B$  the permeability, and  $\varepsilon$  the porosity of the channels and electrodes.

The species transport in the gas channels and porous electrodes was simulated by solving the Maxwell-Stefan model [170],

$$\nabla \cdot j_{m,i} + \rho(u \cdot \nabla) \omega_i = R_i, \quad (5.5)$$

where  $\omega_i$  is the mass fraction,  $j_{m,i}$  the mass flux relative to the mass averaged velocity, and  $R_i$  the reaction rate related to thermos- and electrochemical reactions. The species transport model was coupled to the fluid flow model (eqs. 5.3 and 5.4) by taking the velocity data and updating the local species' compositions for the effective gas mixture properties, which – in turn – were again used in the fluid flow model. The  $j_{m,i}$  was calculated by a mixture-averaging approximation [171],

$$j_{m,i} = - \left( \rho D_i^{\text{mk}} \nabla \omega_i + \rho \omega_i D_i^{\text{mk}} \frac{\nabla M_n}{M_n} \right), \quad (5.6)$$

where  $D_i^{\text{mk}} = \left( \frac{1}{D_i^{\text{m}}} + \frac{1}{D_i^{\text{k}}} \right)$  is the effective mixture-averaged diffusion coefficient,  $D_i^{\text{m}} = \frac{1-\omega_i}{\sum_{k \neq i}^n \frac{x_k}{D_{ik}}}$

is the mixture-averaged multicomponent Maxwell-Stefan diffusivities with the binary diffusivities  $D_{ik}$  predicted by Chapman-Enskog theory and the Knudsen diffusion coefficients  $D_i^k$  predicted by Knudsen theory, and  $M_n = \left( \sum_i^n \frac{\omega_i}{M_i} \right)^{-1}$  the mixture-averaged molar weight.

### 5.4.2 Charge conservation

Charge transport in electrodes, electrolyte, and gas channels (metal part as the current collector) is given by [172]:

$$\nabla \cdot J_k = S_k, \quad (5.7)$$

$$J_k = -\sigma_k \nabla V_k, \quad (5.8)$$

where  $k = cc$  for current collector,  $io$  for ionic conductor, and  $el$  for electrical conductor,  $\sigma_k$  the effective ionic/electronic conductivity,  $V_k$  the electrical potential,  $S_k = \sum A_{TPB} J_i$  is the sum of volumetric current sources (product of the electrochemically active specific surface area,  $A_{tpb}$ , and local current density,  $J_i$ ) due to electrochemical reactions. The effective conductivities and active surfaces areas were predicted using coordination number theory and percolation theory (section 5.4.7).

### 5.4.3 Electrochemical reactions

The two competing electrochemical reactions ( $H_2O$  and  $CO_2$  splitting reactions) were considered and the potential balance for the two electrically parallel-connected pathways is formulated by considering the equilibrium potential,  $E$ , activation overpotential,  $\eta_{act}$ , and ohmic overpotentials,  $\eta_{ohmic}$ .

$$V_{cell} = E + |\eta_{act,ca}| + \eta_{act,an} + \eta_{ohmic}, \quad (5.9)$$

$E$  was predicted by the Nernst equation [58] which comprised of the standard potential ( $E_0$ ) and the concentration overpotential ( $\eta_{conc}$ ):

$$E_{H_2} = E_{0,H_2} + \eta_{conc,H_2}, \quad (5.10)$$

$$E_{CO} = E_{0,CO} + \eta_{conc,CO}, \quad (5.11)$$

where  $E_{CO} = E_{0,CO} + \eta_{conc,CO}$ ,  $E_{0,CO} = 1.46713 - 4.527 \cdot 10^{-4} T$ ,  $\eta_{conc,H_2} = \frac{RT}{2F} \ln \left( \frac{p_{H_2}}{p_{H_2O}} \right) + \frac{RT}{2F} \ln (p_{O_2})^{0.5}$  and,  $\eta_{conc,CO} = \frac{RT}{2F} \ln \left( \frac{p_{CO}}{p_{CO_2}} \right) + \frac{RT}{2F} \ln (p_{O_2})^{0.5}$ .  $p_i$  are the local partial pressure of  $H_2$ ,  $H_2O$ ,  $CO$ ,  $CO_2$ , and  $O_2$  in the porous electrodes, obtained by solving species transport equations (section



5.4.1).

The kinetics of electrochemical reactions were described by the Butler-Volmer formulation:

$$J_{i,ca} = J_{0,i,ca} \left\{ \exp \left( \frac{2F\eta_{act,i,ca}}{RT} \right) - \exp \left( \frac{-F\eta_{act,i,ca}}{RT} \right) \right\}, \quad (5.12)$$

where  $J_{0,i,ca} = \frac{RT}{3F} s_{i,ca}$  is the exchange current density for  $i = \text{H}_2\text{O}$  or  $\text{CO}_2$  (for water or carbon dioxide splitting reactions at the porous cathode).  $s_{i,ca}$  is the cathode surface conductivity for  $\text{H}_2\text{O}$  and  $\text{CO}_2$  reductions, estimated by empirical correlations [9],

$$s_{\text{H}_2\text{O},ca} = \gamma_{0,\text{H}_2\text{O},ca} \exp \left( -\frac{E_{act,ca}}{RT} \right) \left( \frac{p_{\text{H}_2\text{O}}}{K_{eq,\text{H}_2\text{O}} p_{\text{H}_2}} \right)^{0.266}, \quad (5.13)$$

$$s_{\text{CO}_2,ca} = \gamma_{0,\text{CO}_2,ca} \exp \left( -\frac{E_{act,ca}}{RT} \right) \left( \frac{p_{\text{CO}_2}}{K_{eq,\text{CO}_2} p_{\text{CO}}} \right)^{0.266}, \quad (5.14)$$

where  $\gamma_{0,\text{H}_2\text{O},ca}$  and  $\gamma_{0,\text{CO}_2,ca}$  are the pre-exponential factors,  $p_i$  the local partial pressures of  $\text{H}_2$ ,  $\text{H}_2\text{O}$ ,  $\text{CO}$ , and  $\text{CO}_2$  at cathode which are solved by fluid flow and species transport models,  $E_{act,ca}$  is the activation energy for the cathode, and  $K_{eq,\text{H}_2\text{O}}$  and  $K_{eq,\text{CO}_2}$  are equilibrium constants for  $\text{H}_2\text{O}$  and  $\text{CO}_2$  splitting reactions. The equilibrium constants were fitted to equilibrium calculations in HSC Chemistry 5 [173]. The activation overpotential for  $2\text{O}$  oxidation reaction at the anode is given as [9]:

$$J_{i,an} = J_{0,i,an} \left\{ \exp \left( \frac{2F\eta_{act,i,an}}{RT} \right) - \exp \left( \frac{-2F\eta_{act,i,an}}{RT} \right) \right\}, \quad (5.15)$$

$$s_{\text{O}_2,an} = \gamma_{0,\text{O}_2,an} \exp \left( -\frac{E_{act,an}}{RT} \right) p_{\text{O}_2}^{0.5}. \quad (5.16)$$

Table 5.1 – Modeling parameters for electrochemical reactions [9].

Parameters	Vaule
Pre-exponential factor for R1, $\gamma_{0,\text{H}_2\text{O},ca}$	$2.1 \cdot 10^{11} \text{ A/m}^2$
Pre-exponential factor for R2, $\gamma_{0,\text{CO}_2,ca}$	$5.25 \cdot 10^{10} \text{ A/m}^2$
Pre-exponential factor for R3, $\gamma_{0,\text{O}_2,an}$	$2.5 \cdot 10^9 \text{ A/m}^2$
Activation energy for cathode, $E_{act,ca}$	$1.2 \cdot 10^5 \text{ J/mol}$
Activation energy for anode, $E_{act,an}$	$1.3 \cdot 10^5 \text{ J/mol}$

The parameters (pre-exponential factors and activation energy) used in this study are shown in table 5.1.

#### 5.4.4 Thermochemical reactions

The reaction rates for WGSR and SRR were predicted using Haberman and Young's model [57] and the volumetric reaction rates for WGSR ( $R_{\text{WGSR}}$ ) and SRR ( $R_{\text{SRR}}$ ):

$$R_{\text{WGSR}} = k_{\text{WGSR}} \left( p_{\text{H}_2\text{O}} p_{\text{CO}} - \frac{p_{\text{H}_2} p_{\text{CO}_2}}{K_{\text{WGSR}}} \right), \quad (5.17)$$

$$k_{\text{WGSR}} = 0.0171 \exp \left( \frac{-103191}{RT} \right), \quad (5.18)$$

$$K_{\text{WGSR}} = \exp \left( -0.2935Z^3 + 0.6351Z^2 + 4.1788Z + 0.3169 \right), \quad (5.19)$$

$$R_{\text{SRR}} = k_{\text{SRR}} \left( p_{\text{CH}_4} p_{\text{H}_2\text{O}} - \frac{p_{\text{H}_2} p_{\text{CO}}}{K_{\text{SRR}}} \right), \quad (5.20)$$

$$k_{\text{SRR}} = 2395 \exp \left( \frac{-231266}{RT} \right), \quad (5.21)$$

$$K_{\text{SRR}} = 1.0267 \times 10^{10} \exp \left( -0.2513Z^4 + 0.3665Z^3 + 0.5810Z^2 - 27.134Z + 3.277 \right), \quad (5.22)$$

where  $Z = \frac{1000}{T} - 1$ ,  $R$  the universal gas constant,  $p_i$  the partial pressure for each species locally at the porous cathode solved by the species transport model in section 5.4.1, and  $T$  is the local fluid temperature obtained from the heat transfer model in section 5.4.5.

#### 5.4.5 Heat transfer in SOEC

The steady state energy conservation equation is solved in all SOEC domains (including cathode and anode channels, electrodes, and electrolyte). The conductive and convective heat transfer dominates the heat transfer mechanism within the SOEC, while we neglect radiative heat transfer within the SOEC (radiative heat transfer only led to 2 K changes in the local temperature [174]). The energy conservation equation is given as,

$$\rho C_p u = \nabla \cdot (k \nabla T) + \dot{Q}_H, \quad (5.23)$$

where  $u$  is the superficial velocity fields in the fluid channels and porous electrodes, calculated from the mass and momentum conservation equations (section 5.4.1) or set to zero in the solid electrolyte domain.  $\dot{Q}_H$  is the total heat source term accounting for ohmic heat generation ( $\dot{Q}_{\text{ohmic}}$ ) in the electrolyte and porous electrodes, the reversible heating effects of the entropy change due to electrochemical (R1, R2, and R3) and thermochemical (R4 and R5) reactions ( $\dot{Q}_{\text{rev}} = \dot{Q}_{\text{rev,ca}} + \dot{Q}_{\text{rev,an}} + \dot{Q}_{\text{rev,WGSR}} + \dot{Q}_{\text{rev,SRR}}$ ) in the porous electrodes, and the irreversible heat generation induced by activation and overpotentials in the porous electrodes ( $\dot{Q}_{\text{act}}$  and  $\dot{Q}_{\text{conc}}$ ).  $k$  is the thermal conductivity for each computational domain. For porous domains (two gas channels, two electrodes),  $k = k_{\text{eff}}$  and is the volume-averaged conductivities of the

solid materials and fluid mixture. The temperature-dependent thermal conductivities for the fluid mixtures and the solid materials are given in table E.1. A similar method was used to calculate the heat capacities ( $c_p$ ) and densities ( $\rho$ ) of the fluid mixtures and the detailed values used in this study are listed in table E.2 and table E.3, respectively.

The ohmic heat source considered for different domains is given by:

$$\dot{Q}_{\text{ohmic}} = \frac{J_{\text{ion}}^2}{\sigma_{\text{ion}}} + \frac{J_{\text{elec}}^2}{\sigma_{\text{elec}}}, \quad (5.24)$$

where  $J_{\text{ion}}$  and  $J_{\text{elec}}$  are the current densities for ionic and electronic, respectively, conducting phases ( $j_{\text{el}}$  is 0 in the electrolyte domain), and  $\sigma_{\text{ion}}$  and  $\sigma_{\text{el}}$  the effective conductivity of ionic and electronic, respectively, conduction phases for the porous electrodes.

The reversible heat sources due to the electrochemical reactions are obtained based on the entropy changes,

$$\dot{Q}_{\text{rev,ca}} = \frac{A_{\text{TPB,ca}}(J_{\text{H}_2\text{O,ca}} T \Delta s_{\text{R1}} + J_{\text{CO}_2,\text{ca}} T \Delta s_{\text{R2}})}{2F}, \quad (5.25)$$

$$\dot{Q}_{\text{rev,an}} = \frac{A_{\text{TPB,an}} J_{\text{O}_2,\text{an}} T \Delta s_{\text{R3}}}{2F}, \quad (5.26)$$

where  $\Delta s_{\text{R1}}$ ,  $\Delta s_{\text{R2}}$ , and  $\Delta s_{\text{R3}}$  are the entropy generation for R1, R2, and R3, and  $J_{\text{H}_2\text{O,ca}}$ ,  $J_{\text{CO}_2,\text{ca}}$ , and  $J_{\text{O}_2,\text{an}}$  current densities for R1, R2, and R3, respectively. The reversible heat sources caused by two thermochemical reactions (R4 and R5) are calculated based on the reaction rates:

The reversible heat sources caused by the two thermochemical reactions (R4 and R5) are calculated based on the reaction rates:

$$\dot{Q}_{\text{rev,WGSR}} = R_{\text{WGSR}} \Delta h_{\text{WGSR}}, \quad (5.27)$$

$$\dot{Q}_{\text{rev,SRR}} = R_{\text{SRR}} \Delta h_{\text{SRR}}, \quad (5.28)$$

where  $\Delta h_{\text{WGSR}}$  and  $\Delta h_{\text{SRR}}$  are the reaction enthalpies for R4 and R5.

The irreversible heat generation induced by activation and overpotentials in the two porous electrodes are predicted by the products of the overpotentials and the current densities:

$$\dot{Q}_{\text{act}} = \eta_{\text{act,H}_2} J_{\text{H}_2\text{O,ca}} + \eta_{\text{act,CO}} J_{\text{CO}_2,\text{ca}}, \quad (5.29)$$

$$\dot{Q}_{\text{conc}} = \eta_{\text{conc,H}_2} J_{\text{H}_2\text{O,ca}} + \eta_{\text{conc,CO}} J_{\text{CO}_2,\text{ca}}. \quad (5.30)$$

#### 5.4.6 Carbon deposition boundaries in C-H-O ternary diagram

The carbon deposition must be avoided due to its deactivation effect on the cathode catalysts [175, 176]. Along the cathode (from the inlet to the outlet) during the syngas production, the carbon deposition tendency increases as the steam-to-carbon ratio of the gas mixture increases [177]. A smart choice of the inlet gas composition, pressure, temperature, and operation current density is required to avoid carbon deposition in the SOEC. We predicted the onset of carbon depositions based on a C-H-O ternary diagram, by minimizing the free energy of the gas mixture, considering 6 species (i.e.  $H_2$ ,  $H_2O$ ,  $CO$ ,  $CO_2$ ,  $O_2$ ,  $CH_4$ , and  $C$ ). The detailed thermodynamic model of Broers et al. [178] was implemented in an in-house MATLAB code. The preferable operation conditions were chosen to ensure there was no carbon deposition at the cathode outlet.

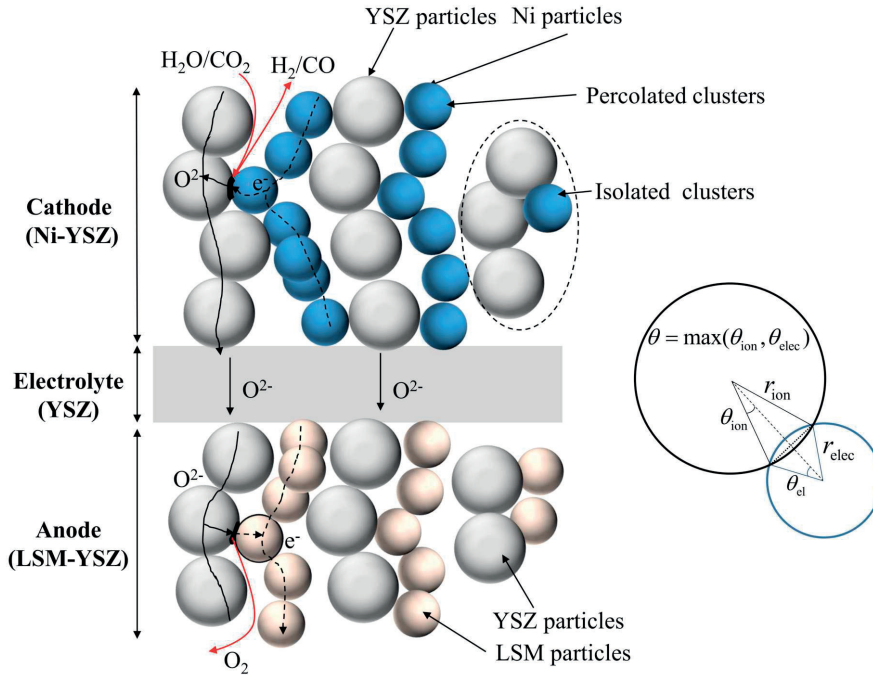


Figure 5.2 – Schematic of the SOEC and the random packing of binary spheres for electrodes. The definition of the contact angle,  $\theta$ , is schematically shown on the right side. Example electron, ion, and species transport at one triple phase boundary (TPB) well as the transport pathways are shown, for both cathode and anode. The solid-line paths are for ions and the dash-line paths are for electrons.

#### 5.4.7 Microstructure properties for the porous electrodes

Fluid, low-resistant electronic and ionic transport, and fast reaction kinetics are of crucial importance for a high-performance SOEC and are largely dependent on the microstructure

properties of the porous electrodes [179]. We modeled the microstructure of the porous SOFC/SOEC electrodes as a binary random spherical packing system comprised of void space, and electronic and ionic conducting particles (see figure 5.2). The microstructure characteristics, namely porosity, the volume fraction of the electronic and ionic phases ( $\phi_{\text{elec}}$  and  $\phi_{\text{ion}}$ ), and the mean radius of the electronic and the ionic phases ( $r_{\text{elec}}$  and  $r_{\text{ion}}$ ), have a decisive impact on the electrodes' transport characteristics. The accurate quantification of its morphological and effective properties, namely the active surface area per unit volume, tortuosity, effective electronic and ionic conductivities, and effective gas diffusion coefficients, is therefore crucial for the accuracy of the model. We used the coordination number theory to obtain the correlations between the microstructure and the effective properties [180]. The average coordination number for electronic and ionic particles can be estimated as:

$$Z_{\text{elec}} = 3 + \frac{(Z_{\text{tot}} - 3)r_{\text{elec}}^2}{\xi_{\text{elec}}r_{\text{elec}}^2 + \xi_{\text{ion}}r_{\text{ion}}^2}, \quad (5.31)$$

$$Z_{\text{ion}} = 3 + \frac{(Z_{\text{tot}} - 3)r_{\text{ion}}^2}{\xi_{\text{elec}}r_{\text{elec}}^2 + \xi_{\text{ion}}r_{\text{ion}}^2}, \quad (5.32)$$

where  $Z_{\text{tot}} = 6$  is the overall coordination number in a random packing of binary spheres, and  $\xi_{\text{elec}} = \frac{\phi_{\text{elec}}r_{\text{elec}}^3}{\phi_{\text{elec}}r_{\text{elec}}^3 + \phi_{\text{ion}}r_{\text{ion}}^3}$  and  $\xi_{\text{ion}} = \frac{\phi_{\text{ion}}r_{\text{ion}}^3}{\phi_{\text{elec}}r_{\text{elec}}^3 + \phi_{\text{ion}}r_{\text{ion}}^3}$  the number fractions of electronic and ionic conducting phases. The coordination number,  $Z_{i-j}$ , between  $i$ -phase and  $j$ -phase particles, representing the average number of  $j$ -phase particles in contact with an  $i$ -phase particle, was calculated as:

$$Z_{i-j} = \xi_j \frac{Z_i Z_j}{Z_{\text{tot}}}. \quad (5.33)$$

The probability of an  $i$ -phase particle belongs a percolated cluster of the same phase can be estimated by [181]:

$$P_i = \left[ 1 - \left( \frac{4.236 - Z_{i-i}}{2.472} \right)^{2.5} \right]^{0.4}. \quad (5.34)$$

The effective electronic ( $i = \text{elec}$ ) and ionic conductivities ( $i = \text{ion}$ ) of the porous electrodes are given based on the percolation theory:

$$\sigma_{i,\text{eff}} = \sigma_{i,0}(\phi_i P_i)^{1.5}, \quad (5.35)$$

where  $\sigma_{i,\text{eff}}$  is the effective conductivity and  $\sigma_{i,0}$  the intrinsic conductivity of phase  $i$ . The intrinsic electrical conductivities for YSZ, LSM, Ni, and gas channel (steel) are listed in table E.4. The active surface area of the porous electrode was given as [182]:

$$A_{\text{TPB}} = \pi \sin^2 \theta \min(r_{\text{elec}}^2, r_{\text{ion}}^2) n_{\text{tot}} \xi_{\text{el}} \xi_{\text{ion}} P_{\text{elec}} P_{\text{ion}} \frac{Z_{\text{elec}} Z_{\text{ion}}}{Z_{\text{tot}}}, \quad (5.36)$$

where  $A_{\text{tpb}}$  is the active surface area which is calculated separately for the porous cathode and anode,  $\theta$  the contact angle between electronic and ionic conducting particles, and  $n_{\text{tot}} = \frac{1-\varepsilon}{(4/3)\pi(\xi_{\text{elec}}r_{\text{elec}}^3 + \xi_{\text{ion}}r_{\text{ion}}^3)}$  the total number of particles of the porous electrode per unit volume.

In this study, Ni was considered as the catalyst and YSZ as the electrolyte at the cathode (hydrogen and CO electrode). Similarly, LSM and YSZ were considered as the catalyst and the electrolyte for the anode (oxygen electrode). The detailed membrane-electrode assembly (MEA) parameters are listed in table 5.2.

Table 5.2 – Reference geometrical and microstructure parameters for the SOEC membrane-electrolyte assembly.

Parameters	Vaule
Thickness of cathode, $t_{\text{ca}}$	500 $\mu\text{m}$
Thickness of electrolyte, $t_{\text{e}}$	50 $\mu\text{m}$
Thickness of anode, $t_{\text{an}}$	50 $\mu\text{m}$
Porosity of cathode	0.35
Porosity of anode	0.35
Ni particle radius at cathode	0.25 $\mu\text{m}$
YSZ particle radius at cathode	0.25 $\mu\text{m}$
LSM particle radius at anode	0.25 $\mu\text{m}$
YSZ particle radius at anode	0.25 $\mu\text{m}$
Tortuosity of cathode	2
Tortuosity of anode	2
Particle contact angle, $\theta$	15°

## 5.5 PV cell model

A simplified 0D two-diode equivalent circuit model [10] was used for modeling the III-V triple junction PV cells for various conditions (solar concentration and temperature). The active area of the PV cell was assumed to be the available area on the reactor front (see figure 5.1) and the PV cell operational temperature was tuned between 25 °C up to 120 °C, depending on the cooling power applied to the reactor front. The solar irradiation on the PV cell ( $\dot{Q}_{\text{solar,PV}}$ ) was assumed to be concentrated ( $C_{\text{PV}}$ ) and spatially uniform. The equivalent circuit for a triple junction cell is shown in figure 5.3. The  $J$ - $V$  relation for each sub-cell, neglecting the shunt resistance, was predicted by:

$$J_{\text{PV}} = J_{\text{SC},i} - J_{01,i} \left( e^{(q/k_{\text{B}}/T)(V_i + J_{\text{PV}}A_{\text{PV,ref}}R_{\text{s},i})} - 1 \right) - J_{02,i} \left( e^{(q/(2k_{\text{B}}/T))(V_i + J_{\text{PV}}A_{\text{PV,ref}}R_{\text{s},i})} - 1 \right), \quad (5.37)$$

where  $J_{PV}$  is the operation current density of PV,  $J_{SC,i}$  the short circuit current density,  $J_{01,i} = \kappa_{1,i} T^3 e^{(-E_{g,i}/k_B T)}$  and  $J_{02,i} = \kappa_{2,i} T^{3/2} e^{(-E_{g,i}/2k_B T)}$  the diode reverse saturation current densities for recombinations in the depletion and the quasi-neutral regions, respectively, and  $R_{s,i}$  the series resistance. We considered an InGaP/InGaAs/Ge triple junction cell from Sharp [183, 184]. The temperature-dependent bandgap information and the fitted data for  $A_{PV,ref}$ ,  $\kappa_{1,i}$ ,  $\kappa_{2,i}$ , and  $R_{s,i}$  are given in table E.5.

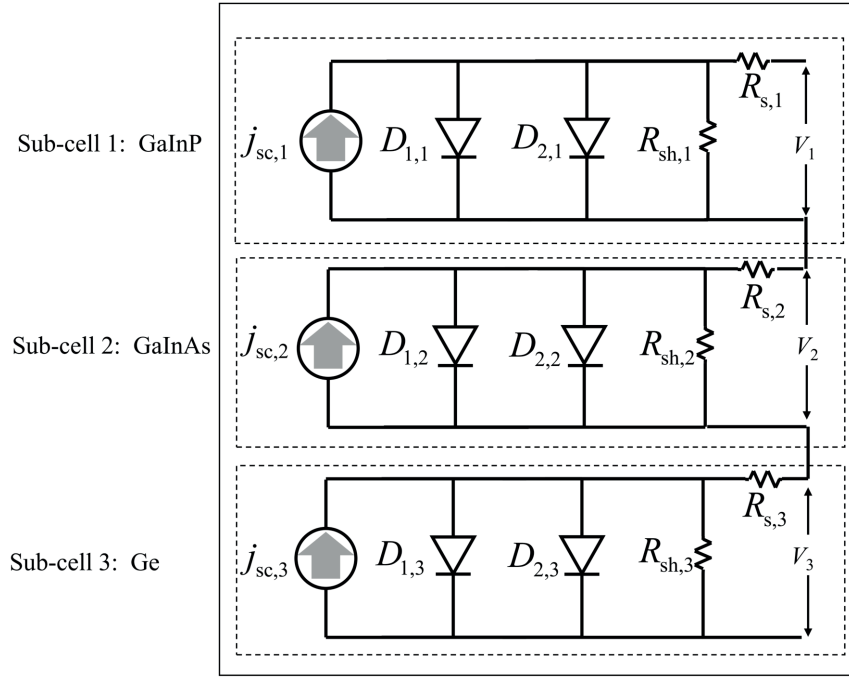


Figure 5.3 – Equivalent circuit model for the III-V triple junction PV cell.

Two PV-SOEC connection schemes were considered: *i*) the PV cell was directly connected to the SOEC and the operation point was determined by the intersection of the two current density-voltage curves ( $I_{PV} = I_{EC}$  and  $V_{PV} = V_{EC}$ ), and *ii*) the PV cell was indirectly connected to the SOEC, utilizing a DC-DC converter with a maximum power point tracker with an electrical efficiency of 93% [185]. In the latter case, the operation point for the EC and PV components were determined by the power matching between the two components ( $A_{PV} J_{PV} V_{PV} \eta_{DC-DC} = A_{EC} J_{EC} V_{EC}$ ). The total solar energy incident on the PV cell is  $\dot{Q}_{solar,PV} = DNI \cdot C_{PV} \cdot A_{PV}$ . The  $I_{solar}$  is the direct solar irradiation, assumed to be  $1000 \text{ W/m}^2$ .  $C_{PV}$  is the optical concentration defined as the ratio of energy incident on the solar concentrator to the area of the PV cell ( $A_{PV}$ ).  $A_{PV}$  is assumed to fully cover the water-cooled reactor front, except for the reactor aperture.

## 5.6 Performance definitions

Two parameters are defined to characterize and quantify the solar reactor performance: the STF efficiency ( $\eta_{\text{STF}}$ ) and the molar ratio of  $\text{H}_2$  and CO ( $R_{\text{HC}}$ ) at the cathode outlet.  $\eta_{\text{STF}}$  is defined as the ratio between the energy stored in the produced products ( $\text{H}_2$  and CO) and the total solar energy input into the reactor:

$$\eta_{\text{STF}} = \frac{2F \cdot E_{0,\text{H}_2} \cdot \dot{n}_{\text{H}_2 \text{ prod}} + 2F \cdot E_{0,\text{CO}} \cdot \dot{n}_{\text{CO prod}}}{\dot{Q}_{\text{solar,ap}} + \dot{Q}_{\text{solar,PV}}}, \quad (5.38)$$

where  $F$  is the Faraday constant,  $E_{0,\text{H}_2} = 1.23 \text{ V}$  and  $E_{0,\text{CO}} = 1.33 \text{ V}$  are the equilibrium potentials (or the Gibbs energies for  $\text{H}_2\text{O}$  and  $\text{CO}_2$  reactions, respectively) at 298 K and 1 atm,  $\dot{n}_{\text{H}_2 \text{ prod}}$  and  $\dot{n}_{\text{CO prod}}$  the produced molar rates for  $\text{H}_2$  and CO, respectively.

Eq. 5.38 uses the Gibbs free energy of reactions as the numerator, which represents the energy stored in the chemical bonds of  $\text{H}_2$  and CO that can be further used for the synthesis of different chemicals other than extracting heat via combustion. The  $\eta_{\text{STF}}$  can be also defined by using the HHV of  $\text{H}_2$  and CO which we used for chapters 1, 2, and 4:

$$\eta_{\text{STF}} = \frac{HHV_{\text{H}_2} \cdot \dot{n}_{\text{H}_2 \text{ prod}} + HHV_{\text{CO}} \cdot \dot{n}_{\text{CO prod}}}{\dot{Q}_{\text{solar,ap}} + \dot{Q}_{\text{solar,PV}}}, \quad (5.39)$$

where  $HHV_{\text{H}_2}$  and  $HHV_{\text{CO}}$  are the higher heating values for  $\text{H}_2$  and CO at 298 K. The quantitative impact of different  $\eta_{\text{STF}}$  definitions is discussed in section 5.8.7.

## 5.7 Numerical solutions

The numerical models were implemented in a finite elements solver, COMOSL Multiphysics V5.3. Two independent models were developed: *i)* the axisymmetric solar reactor model solving heat transfer in the receiver cavity, SOEC, thermal insulation, and fluid flow, species transport and thermo- and electrochemistry in the SOEC (model 1), and *ii)* the 0D two-diode equivalent circuit model for the PV cell (model 2). The models were solved separately for the electrical and thermal behavior of each component (i.e. SOEC reactor and PV cell) and then coupled by assuming an identical temperature for the water cooled front (thermal boundary condition) and the PV cell (cell temperature).

Model 1 was solved by a fully coupled solver (Newton method) with a direct linear solver (MUMPS). A relative tolerance of  $10^{-3}$  was chosen as the convergence criterion to ensure that the predicted fuel production variation was smaller than 0.1% with a further decrease in relative tolerance. The mesh elements number used was 23248, based on a mesh independent study performed at reference conditions. When further increasing the mesh element number,



the difference in the fluid outlet temperature and the molar fractions of  $H_2$  and  $CO$  was less than 0.5%. Note that a boundary mesh was created close to the electrode-electrolyte interface (8 boundary layers with a stretching factor of 1.5). The current-density versus voltage calculations for the reference case (current density range of  $0 \text{ A/m}^2$  to  $11000 \text{ A/m}^2$  with a step of  $100 \text{ A/m}^2$  applied at the outer surface of the anode gas channel) took 55 minutes on a workstation with 12 cores and 128GB RAM. Three ordinary differential equations were solved in model 2, using a fully coupled Newton method with a MUMPS linear solver system. A relative tolerance of  $10^{-3}$  was used for convergence to ensure a maximum 0.1% difference in the calculated current densities for a given range of voltages when further increasing the tolerance.

## 5.8 Results and discussion

### 5.8.1 Model validations

Given by the novelty of the reactor concept, no experimental data for the integrated reactor exist. Instead, the model validation was done based on separate validation of each major component, namely the receiver, the SOEC cell, and the PV cell. The receiver model implemented in this study was previously validated with experimental data (see 3) and is not detailed here. For the SOEC model, validation cases for  $H_2$  production [3],  $CO$  production [4], and syngas production [5] were performed individually. The experimental data has been reported for experiments in electrical ovens, where the temperature of the SOEC was controlled and, hence, a constant temperature was assumed. The model parameters were chosen to be identical to the references (table E.6 to E.8). In the  $H_2$  production case (figure 5.4a), the higher temperature cases (1223 K and 1273 K) showed good agreement between the experimental and numerical data with a root mean square (RMS) of 0.04 V for 1173 K, 0.041 V for 1223 K, and 0.008 V for 1273 K. The maximum relative difference between experimental and numerical cell voltage was 6.7 % and was found at 1173 K and  $4000 \text{ A/m}^2$ . For the  $CO$  production (figure 5.4b), the RMS between the experimental and simulated data was 0.0198 V for a 50/50  $CO_2/CO$  composition case, and was 0.0186 V for a 0.7/0.3  $CO_2/CO$  composition case. For the syngas production (figure 5.4c), the RMS between the experimental and simulated data was 0.06 V for an inlet molar composition of  $H_2/CO_2/H_2O$  to be 0.1/0.6/0.3 and at 1083 K.

The PV cell model is validated with the data provided by Nishioka et al. [6]. Experiments and our simulations for three solar concentrations ( $C_{PV} = 1, 17$ , and 200) and a cell temperature range (between 298 K and 393 K) were compared. The PV cell efficiency was defined as  $\frac{J_{PV} V_{PV}}{C_{PV} DNI}$ , with  $DNI = 1000 \text{ W/m}^2$ . The RMS between the experimental and numerical results was 0.06 V for the open circuit voltage and 0.8% for the cell efficiency. The model showed good agreement with the experimental data at a solar concentration of 1 for the cell efficiency (maximum

relative difference of 0.3% at 298 K). At higher  $C_{PV}$  (i.e. 17 and 200), the maximum relative difference between the predicted value and the experimental value grew, and was highest at the largest temperature and concentration (3.3% at  $C_{PV} = 200$  and 393 K).

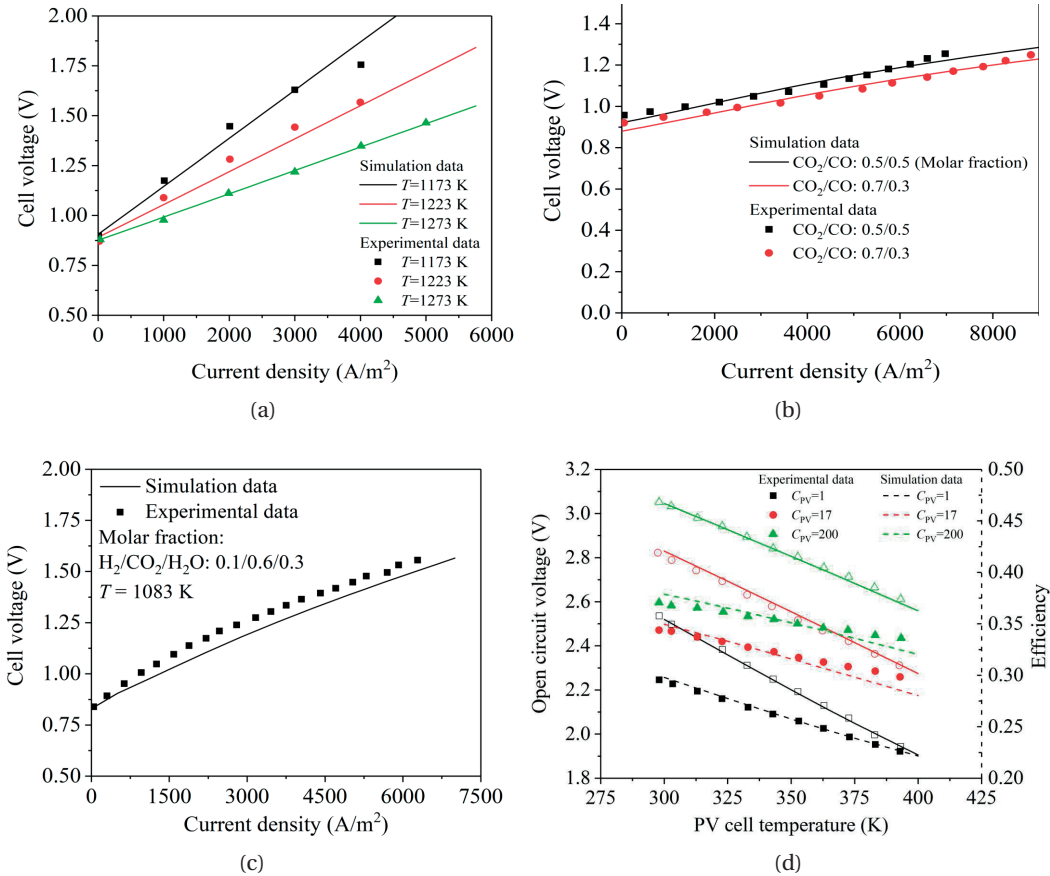


Figure 5.4 – Simulated  $J$ - $V$  results (lines) and the experimental (dots) [3, 4, 5] for (a) H<sub>2</sub> production at three different temperatures (1173 K, 1223 K, and 1273 K), (b) CO production for two inlet different CO<sub>2</sub>/CO compositions (0.5/0.5 and 0.7/0.3) at 1173 K [4], and (c) syngas production for a cathode inlet gas composition of H<sub>2</sub>/CO<sub>2</sub>/H<sub>2</sub>O : 0.25/0.25/0.5 at 1083 K [44]. (d) Simulated (lines) and experimentally obtained (dots) [6] PV open circuit voltage (left  $y$ -axis) and efficiency (right  $y$ -axis) as a function of the cell temperature.

### 5.8.2 Reference case

The reference case was defined for a solar power input to the reactor aperture ( $\dot{Q}_{\text{solar,ap}}$ ) of 100 W (surface average solar concentration  $C_{\text{ap}} = 1273$ ). The solar concentration on the PV cell was assumed adjustable in a range from of 1 to 1000 (corresponding to an additional between 6.3 to 6300 W), chosen to optimize  $\eta_{\text{STF}}$ , for direct and indirect PV-SOEC coupling schemes. The cathode and anode reactant inlet temperatures were assumed at 373 K. The inlet cathode

stream consisted of fully saturated vapor (the latent heat was assumed to be provided by heat recovery from the reactor exhaust via heat exchangers) premixed with CO<sub>2</sub>, CO, and H<sub>2</sub> (the latter two for kinetic reasons). A summary of the modeling parameters for the reference case is given in table 5.3.

### Reference case for the integrated reactor

The  $J$ - $V$  curve for the SOEC at reference conditions is shown in figure 5.5a. The SOEC potential first increased (from 0.9 V to 1.63 V) with increasing operation current density (from 0 A/m<sup>2</sup> to 6813 A/m<sup>2</sup>, zone 1), given by the increase in the overpotentials (ohmic, activation, and concentration overpotentials) which outweighed the decrease in equilibrium potential (figure 5.5b). A further increase in the current density (6813 A/m<sup>2</sup> to 9625 A/m<sup>2</sup>, zone 2) led to the decrease in the cell potential (from 1.63 V to 1.62 V), given by the decreasing equilibrium potential, activation overpotential, and concentration overpotential. These decreases resulted from the dominating temperature effect. With a further increase in the current density (from 9625 A/m<sup>2</sup> to 10375 A/m<sup>2</sup>, zone 3), the cell potential increased again (1.62 V to 1.64 V). The increasing concentration overpotential dominated zone 3, resulting from the mass transport limitation due to the depletion of the reactants (H<sub>2</sub>O and CO<sub>2</sub>). The reactants depletion is clearly visible when comparing the outlet species composition at high current densities (figure 5.5c).

The contributions of the electrochemical (R1 and R2) and thermochemical reactions (R4 and R5) to the H<sub>2</sub> and CO production rates are presented in figure 3d. The electrochemical reactions always dominated the fuel production. For example at 5000 A/m<sup>2</sup>, the electrochemical production of H<sub>2</sub> and CO was  $9 \cdot 10^{-5}$  mol/s and  $5.17 \cdot 10^{-5}$  mol/s, respectively, and the thermochemical production of H<sub>2</sub> and CO was  $-1.24 \cdot 10^{-5}$  mol/s and  $1.17 \cdot 10^{-5}$  mol/s, respectively. The WGSR was the dominating thermochemical reaction (WGSR rate was 3 to 4 orders of magnitude higher than the SRR rate, see figure 5.5d). Above a current of 1304 A/m<sup>2</sup>, the reaction rate of WGSR was negative (i.e. effectively a reverse WGSR) resulting from increased cell temperature. The CO production rate was smaller than the H<sub>2</sub> production rate in the case when the current density was smaller than 9250 A/m<sup>2</sup>. Current densities above 9250 A/m<sup>2</sup> led to higher CO production than H<sub>2</sub> product, given by decreased increasing rate electrochemistry contribution to H<sub>2</sub> production with increasing current density resulted from increased concentration overdetail for water splitting reaction as decreased equilibrium potential difference between H<sub>2</sub>O and CO<sub>2</sub> splitting reactions (see eqs. 5.10 and 5.11, and figure 5.5d).

## Chapter 5. An integrated concentrated solar fuel generator concept

Table 5.3 – Reactor geometry, anode and cathode inlet conditions, and irradiation concentration for the reference conditions.

Parameters	Values
<b>Reactor geometry</b>	
Length of the reactor, $L$	0.05 m
Receiver aperture radius, $r_{ap}$	0.005 m
Reactor front radius (aperture + PV), $r_{cav}$	0.015 m
Thickness of thermal insulation, $t_{insu}$	0.1 m
Solar power at the aperture, $\dot{Q}_{solar}$	100 W ( $C_{ap} = 1273$ )
Thickness of gas channels, $t_{ch}$	0.5 mm
<b>Cathode inlet conditions</b>	
Inlet gas mixture temperature	373.15 K
Inlet gas velocity	0.2 m/s
Inlet gas molar composition	$H_2/H_2O/CO/CO_2/CH_4:0.05/0.45/0.05/0.45/0$
<b>Anode inlet conditions</b>	
Inlet gas mixture temperature	373.15 K
Inlet gas velocity	0.2 m/s
Inlet gas molar composition	$O_2/N_2: 0.21/0.79$
<b>Solar concentration on PV cell, <math>C_{PV}</math></b>	50-600 ( $\dot{Q}_{solar,PV} = 31.4$ to $376.8$ W)

The outlet gas composition is important as different molar ratios of  $H_2/CO$  are required for different downstream applications. For example,  $R_{HC} = 2$  is desired for the synthesis of methanol [91].  $R_{HC}$  for the reference case for varying current densities is shown in figure 5.5d and varies between 1.44 and 0.98 for varying current densities between  $500 \text{ A/m}^2$  and  $10375 \text{ A/m}^2$ . Another important aspect regarding the cathode outlet gas compositions is the possibility of carbon deposition. Figure 5.6 shows the averaged C-H-O molar fractions for the cathode outlet for varying current densities (different colors represent different current densities). The carbon deposition boundaries are drawn for five selected temperatures (890 K, 950, 1000 K, 1050 K, and 1100 K). The carbon deposition boundary moves to the right side (i.e. allowing for larger fractions of C and enlarging the fully oxidized zone) with increasing temperature. The average temperature of the SOEC at open circuit condition ( $J_{EC} = 0 \text{ A/m}^2$ ) was 890 K. At open circuit conditions, operation in the fully oxidized zone is predicted (left side of the carbon deposition boundary) and no carbon depositions are expected. The intersection points between the SOEC operation curve and the five selected carbon deposition boundaries (for 890 K, 950, 1000 K, 1050 K, and 1100 K) are marked in red. If the SOEC temperature at the intersection point is larger than the carbon deposition boundary temperature, the point is within the fully oxidized zone. The temperatures for each carbon deposition boundary are

shown in black text and the averaged SOEC temperature for each operation point is shown in red text. The SOEC cell temperatures were higher than the carbon deposition boundary temperature for points 1 and 2 (i.e. points 1 and 2 are in the fully oxidized zone and no C deposition is expected as the predicted outlet temperatures at intersection points were larger than the C deposition boundary temperatures), while points 3, 4, and 5 were in the carbon deposition zone. Consequently, an operational guideline to avoid C deposition can be formulated: the reactor operation current density at reference conditions should be below 8725 A/m<sup>2</sup>.

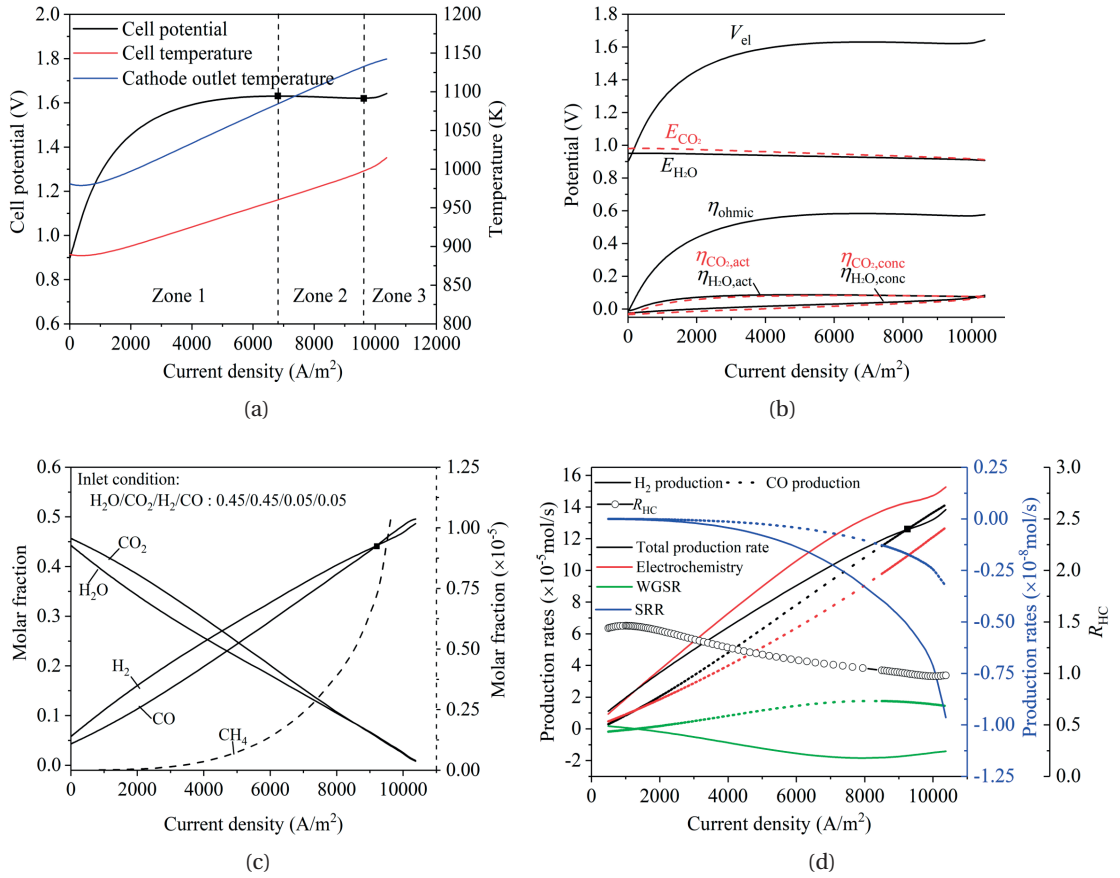


Figure 5.5 – SOEC performance at reference conditions. (a) The surface-averaged potential (left y-axis) and volume-averaged cell and surface-averaged cathode outlet temperatures (right y-axis) as a function of the current density. (b) The breakdown of the surface-averaged cell potential into the various overpotentials for varying current densities. (c) The molar fraction of cathode outlet species for varying current densities. (d) The contributions of electro- and thermochemistry to the syngas production for varying current densities.

Two PV-EC coupling strategies (direct and indirect connections) were investigated. Figure 5.7a shows the  $J$ - $V$  curves for the SOEC under different current densities and for the PV cell under

## Chapter 5. An integrated concentrated solar fuel generator concept

various solar concentrations. The operation points for the direct connection cases are marked with gray dots and the operation points for the indirect connection cases are indicated with colored dots (the dots with the same color represents the operation point for the SOEC and PV). The current density is given per area of SOEC area (i.e. the current density of the PV cell was normalized by  $F = A_{PV}/A_{EC} = 0.1205$  for the reference case).

Seven contributions to the energy balance are defined: the energy loss from the PV ( $f_{PV-loss} = (\dot{Q}_{solar,PV} - A_{PV} J_{PV} V_{PV}) / (\dot{Q}_{solar,ap} + \dot{Q}_{solar,PV})$ ), the fluid heating ( $f_{fluid}$ , defined as the total energy passing through the inlets and outlets boundaries relative to the total solar power input ( $\dot{Q}_{solar,ap} + \dot{Q}_{solar,PV}$ )), the energy loss from the cooling front ( $f_{cooling,re}$ , defined as the energy passing through the water cooled reactor front divided by the total solar power input), the natural convection loss through the reactor inner surfaces ( $f_{nc} = \dot{Q}_{nc} / (\dot{Q}_{solar,ap} + \dot{Q}_{solar,PV})$ ), the re-radiation heat loss through the aperture ( $f_{rerad} = \dot{Q}_{rerad} / (\dot{Q}_{solar,ap} + \dot{Q}_{solar,PV})$ ), the energy loss in the DC-DC converter ( $f_{DC-DC} = (1 - \eta_{DC-DC}) A_{PV} J_{PV} V_{PV} / (\dot{Q}_{solar,ap} + \dot{Q}_{solar,PV})$ ), and the energy stored in the produced fuels ( $f_{STF} = \eta_{STF}$ ).

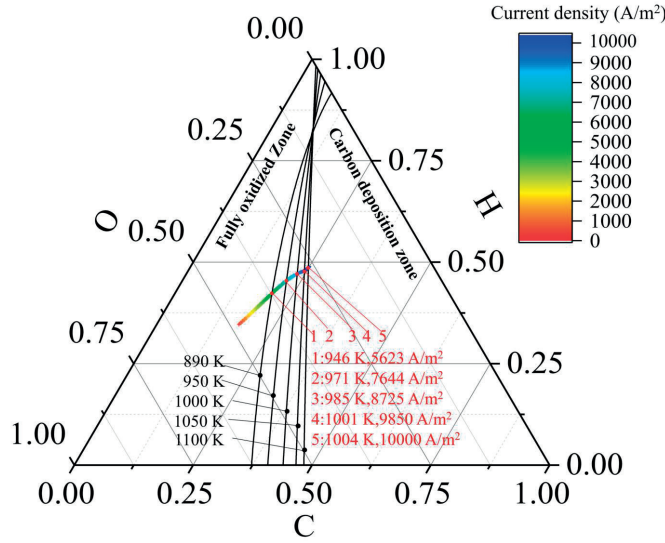


Figure 5.6 – The carbon deposition boundaries for 5 selected temperatures at 1 atm and their intersections (red dots) with the cathode outlet C-H-O curves for the reference case for various operation current densities. The SOEC surface-averaged temperature and operation current densities at intersections are indicated in red.

At reference conditions, the indirect connection strategy showed always better  $\eta_{STF}$  compared to the direct connection strategy. For example,  $\eta_{STF} = 4.3\%$  at  $C_{PV} = 50$  for the direct connection case while  $\eta_{STF} = 7.6\%$  for the indirect connection case (absolute difference of 3.3%). This was due to the oversizing (in terms of potential) of the PV cell for the direct connected case ( $f_{PV-loss} = 19.7\%$  for the direct connection case and 14.7% for the indirect connection case, both at



$C_{PV} = 50$  at reference conditions. In the direct connection case, the potential of the PV cannot be fully utilized. This difference in  $\eta_{STF}$  was further enlarged at higher  $C_{PV}$  (for example, the absolute difference was 6.3% at  $C_{PV} = 385$ ) due to a steeper current density increase with the voltage at higher SOEC cell temperatures at a higher current density as a result of higher  $C_{PV}$ .  $C_{PV} = 385$  was the maximum required solar concentration on the PV for the indirect connection case for a full conversion of reactants. The maximum required  $C_{PV}$  was 600 for the direct connection case. This favored a reactor design with the indirect connection strategy for the reference case.

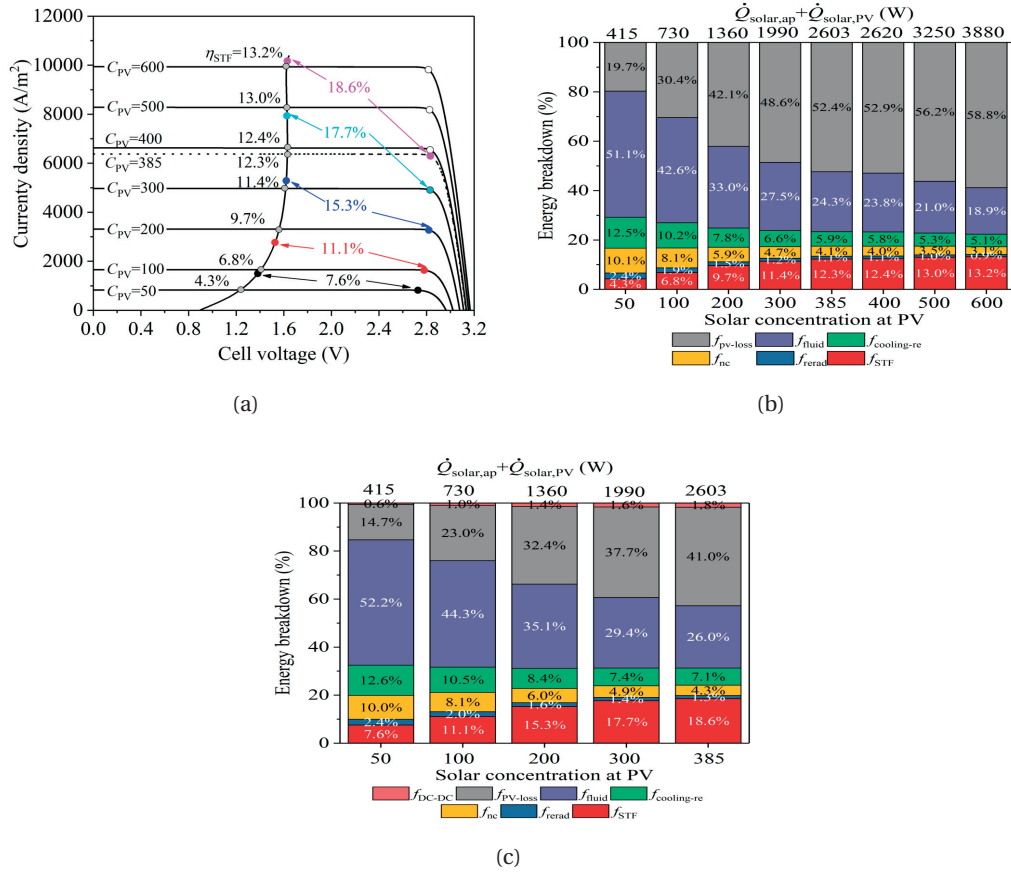


Figure 5.7 – (a) J-V curves for SOEC and PV for varying concentrations and corresponding STF efficiency for directly (grey dots) and indirectly (colored dots) coupled PV and SOEC. Energy breakdown for the solar reactor for (b) direct coupling and (c) indirect coupling cases. For (b) and (c), top x axis shows the total solar energy input to the system with  $\dot{Q}_{solar,ap} = 100$  W.

The energy breakdown in figure 5.7b and 5.7c shows dominating PV losses ( $f_{PV-loss}$ , 52.4% for direct connection case and 41.0% indirect connection case, both at  $C_{PV} = 385$ ) and high fluid heating losses ( $f_{fluid}$ , 24.3% for direct connection case and 26.4% for the indirect connection case, both at  $C_{PV} = 385$ ). The heat loss from the reactor cavity ( $f_{cooling,re} + f_{nc} + f_{reread} = 11.1\%$

for direct connection case and 12.7% indirect connection case, both at  $C_{PV} = 385$  ) chamber was small compared to  $f_{PV-loss}$  or  $f_{fluid}$ . The heat loss was increased with increasing  $C_{PV}$  due to the increasing SOEC temperature at a higher current density (figure 5.7a). With the increase in  $C_{PV}$ , the heat losses ( $f_{cooling, re}$ ,  $f_{nc}$ , and  $f_{reread}$ ) and  $f_{fluid}$  decreased due to the increasing share of  $\dot{Q}_{solar, PV}$  in the solar power input to the reactor front (hence a decrease in the share of  $\dot{Q}_{solar, ap}$ ). Similarly,  $f_{DC-DC}$  and  $f_{PV-loss}$  increased with the increasing  $C_{PV}$  as a result of increased  $\dot{Q}_{solar, PV}$ .

### Non-integrated system vs. integrated reactor

We compare a non-integrated fuel generation system with the here proposed, novel integrated generator using the same simulation framework. However, two equivalent domains (a receiver and a reactor domain) with connecting pipes have to be modeled for the non-integrated case. The model is adapted by (see figure 5.8 for the schematic): *i*) solving in the receiver domain the governing equations for the receiver cavity model and the heat transfer model in the SOEC cell (which acts as absorber only) while not considering any chemical reaction and reaction-induced heat sources, and *ii*) solving in the reactor domain the governing equations for the SOEC including chemical reactions. The two model domains are connected by an insulated pipe (5 m in length and 15 cm radius, Kaowool 1600 insulation) in which a temperature drop of 300 K was assumed (for both cathode and anode outlet). This temperature drop assumption was based on a 2D heat transfer simulation of an insulated pipe (figure E.1) and our experimental observations in chapter 4 (see figure 4.10).

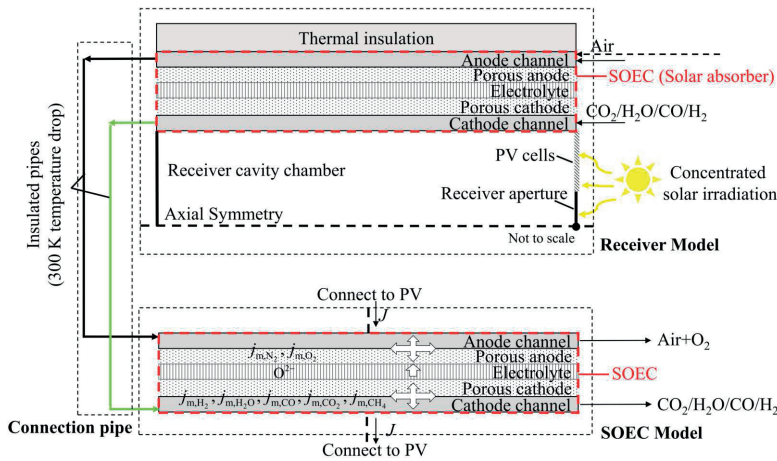
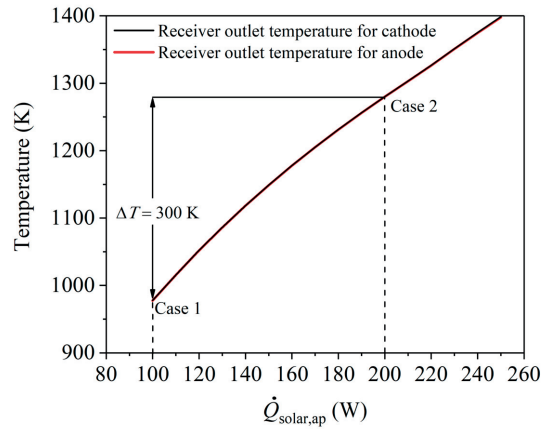
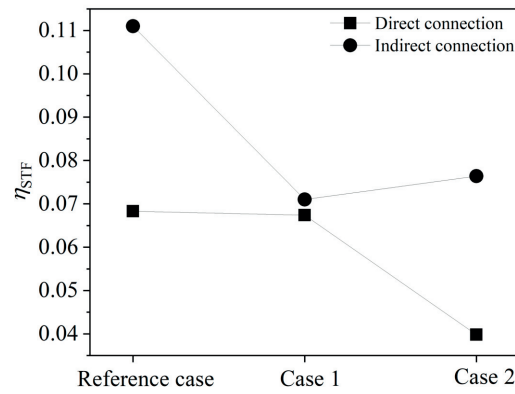


Figure 5.8 – Three sub-models are considered (dashed black boxes): *i*) Receiver model which uses the SOEC cell only as the solar absorber, *ii*) the insulated connection pipe with a temperature drop of 300 K, and *iii*) tubular SOEC cell model.





(a)



(b)

Figure 5.9 – (a) Fluid outlet temperatures under various  $\dot{Q}_{\text{solar,ap}}$ , and (b) the STF efficiency for the reference case, case 1, and case 2 with  $C_{\text{PV}} = 100$  for both direct and indirect PV - SOEC connections. Fill circle dots are for direct connection cases, and the filled square dots are for indirect connection cases.

In addition to the integrated reactor (as a reference case), we defined two different scenarios for the non-integrated system: *i*) a fixed solar power case (case 1), in which  $\dot{Q}_{\text{solar,ap}} = 100$  W, and *ii*) a case (case 2) in which  $\dot{Q}_{\text{solar,ap}}$  is increased to ensure a fixed inlet temperature to the SOEC cell. In case 2,  $\dot{Q}_{\text{solar,ap}}$  was increased ( $\dot{Q}_{\text{solar,ap}} = 200$  W) in order to compensate the 300 K drop in the connection pipes and to ensure the inlet temperatures to the SOEC were equals to the outlet temperatures of the receiver domain at  $\dot{Q}_{\text{solar,ap}} = 100$  W. The inlet temperatures for the SOEC were  $978 \text{ K} - 300 \text{ K} = 678 \text{ K}$  for the cathode and anode. For case 2, the inlet temperatures were 978 K for the cathode and anode. The comparison of the three cases at a selected  $C_{\text{PV}} = 100$  is shown in figure 5.9 for direct and indirect PV-SOEC connections. For the direct connection cases, the operation current density of the SOEC was always  $1654 \text{ A/m}^2$  while the operation voltages changed between the cases: 1.41 V for reference case, 2.45 V for

case 1, and 1.28 V for case 2. For the indirect connection cases, the PV cell's MPPT at  $C_{PV} = 100$  was 2.78 V and 1633.2 A/m<sup>2</sup> (normalized to SOEC area). The operation points under indirect connection are 1.52 V and 2778 A/m<sup>2</sup> for the reference case, 2.42 V and 1745 A/m<sup>2</sup> for case 1, and 1.38V and 3060 A/m<sup>2</sup> for case 2.

The reference case (integrated reactor) shows better STF efficiencies than cases 1 and 2, for the direct and indirect connection cases. For the direct connection case, the STF efficiency for the reference case was 6.8% while it was 6.7% for case 1 and 4.0% for case 2. The STF efficiency enhancement in the integrated reactor design over the two non-integrated systems (cases 1 and 2) was even larger (11.1% for reference case, while it was only 7.1% for case 1 and 7.6% for case 2).

### 5.8.3 Effect of inlet flow velocity

For a fix power input at the reactor aperture ( $\dot{Q}_{\text{solar,ap}} = 100$  W), an increasing cathode and anode inlet flow rate led to two conflicting effects: *i*) mass transport limitations were alleviated at high current densities, reducing concentration overpotentials, and *ii*) temperatures were reduced, increasing the required potential for the electrochemical operation (increased equilibrium potential, activation overpotential, and ohmic overpotential). As shown in figure 5.11b, the limiting current density current density (marked by dots in color) first increased with increasing inlet velocity (4970 A/m<sup>2</sup> to 19760 A/m<sup>2</sup> when increasing the velocity from 0.1 m/s to 1 m/s) due to no mass transport limitations, before it decreased when further increasing the inlet velocities (limiting current density equals 8760 A/m<sup>2</sup> at 1.5 m/s compared to 19760 A/m<sup>2</sup> at 1 m/s, resulting from reduced gas diffusivities at lower SOEC temperature).

The multi-dimensional nature of the modeled allowed us to further distinguish the origin of the mass transport limitations: either caused by bulk reactants depletion or local reactants depletion. We loosely define the bulk reactants depletion as the complete consumption of the reactant in the gas channels, while the local reactants depletion is defined as complete consumption of reactants at the reaction sites (even though the bulk reactants molar fractions in the gas channels are well above 0.05). The molar fraction of H<sub>2</sub>O along the cathode-electrolyte interface for five cathode inlet velocities at their the limiting current densities (color dots in figure 5.11a) is depicted in figure 5.11b along with the bulk H<sub>2</sub>O molar fraction (indicated for each case at the left bottom of figure 5.11b). For all five cases, the H<sub>2</sub>O molar fraction are gradually decreased to around 0 (below our threshold of 0.05) from the cathode inlet towards the outlet. For cathode inlet velocities of 0.1 m/s and 0.2 m/s, bulk (0.02 for 0.1 m/s and 0.025 for 0.2 m/s) and local (0.008 for 0.1 m/s and 0.002 for 0.2 m/s) reactant depletion was observed with the bulk reactant depletion most probably the origin of the transport limitation. For the cases with cathode inlet velocities larger than 0.2 m/s, the local

depletion was the origin of the mass transport limitation. The bulk molar fraction of  $\text{H}_2\text{O}$  at the cathode outlet was much larger (0.176, 0.285, and 0.38 for 0.5 m/s, 1 m/s, and 1.5 m/s, respectively) than the local molar fractions of  $\text{H}_2\text{O}$  at the outlet (0.025, 0, and 0 for these three cases).

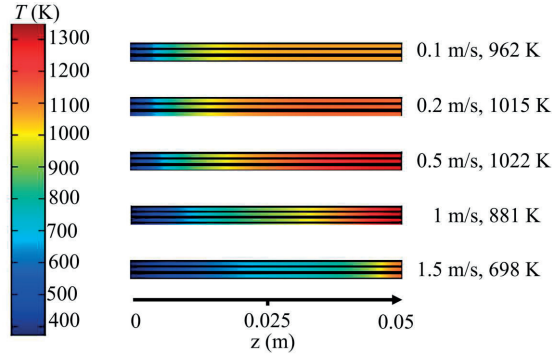


Figure 5.10 – Temperature profiles for five inlet flow velocities at their maximum achievable current densities for the reference arrangement. The 0 m position on the  $z$ -axis represents the fluid inlet position. The SOEC volume-averaged temperature are indicated on the right side of the figure.

The effect of the inlet velocity on the STF efficiency of the integrated reactor is shown in figure 5.11c. For the indirect connection cases at the same  $C_{PV}$ , the lower the inlet velocity the higher the STF efficiency, owing to the higher SOEC temperature at low velocity. However, higher inlet velocity led to higher achievable STF efficiencies (increased from 11.6% to 20.3% when the inlet velocity increased from 0.1 m/s to 0.5 m/s) by alleviating mass transport limitations at high current density. Further increase in inlet velocity (larger than 0.5 m/s) led to a decrease in the achievable STF efficiency (for example, only 15.9% and 9.5% for 1 m/s and 1.5 m/s, respectively). This decrease in the maximum achievable STF efficiency was due to the significant lowered SOEC temperature (see figure 5.10 for the temperature profiles) leading to a significant increase in the cell potential (see figure 5.11a, 2.1 V for 1 m/s and 3.6 V for 1.5 m/s at the maximum achievable current densities).

In the cases of direct connection, the efficiency curves for velocities of 0.1 m/s, 0.2 m/s, 0.5 m/s, 1 m/s were nearly overlapped since the operation points were within the plateau region of the PV  $J$ - $V$  curves (see figure 5.11a). However, the operation points for the cases with 1.5 m/s inlet velocity were found to be in the falling region of the PV  $J$ - $V$  curves, resulting from the rather low temperatures (below 700 K for all conditions) which significantly increased the SOEC potential (around 3 V at  $C_{PV} = 100$ ). Compared to the indirect connection cases, the direct cases showed always lower STF efficiency for a given flow velocity and PV solar concentration due to inefficient use of the PV (leading to high PV losses). An exception was found for the velocity of 0.5 m/s (blue lines in figure 5a) with  $C_{PV}$  in the range of in the range

of 100 to 450. For these cases, the operation points were close to the MPPT of the PV cell showing better performance than the indirect connection cases in which the efficiency of the DC-DC converter (93% efficiency) must be considered. This provides design guidelines for the integrated reactor which can avoid oversizing of PV cell as well as reduce the complexity of the reactor (avoid using DC-DC converter) by carefully choosing inlet flow rates and  $C_{PV}$ .

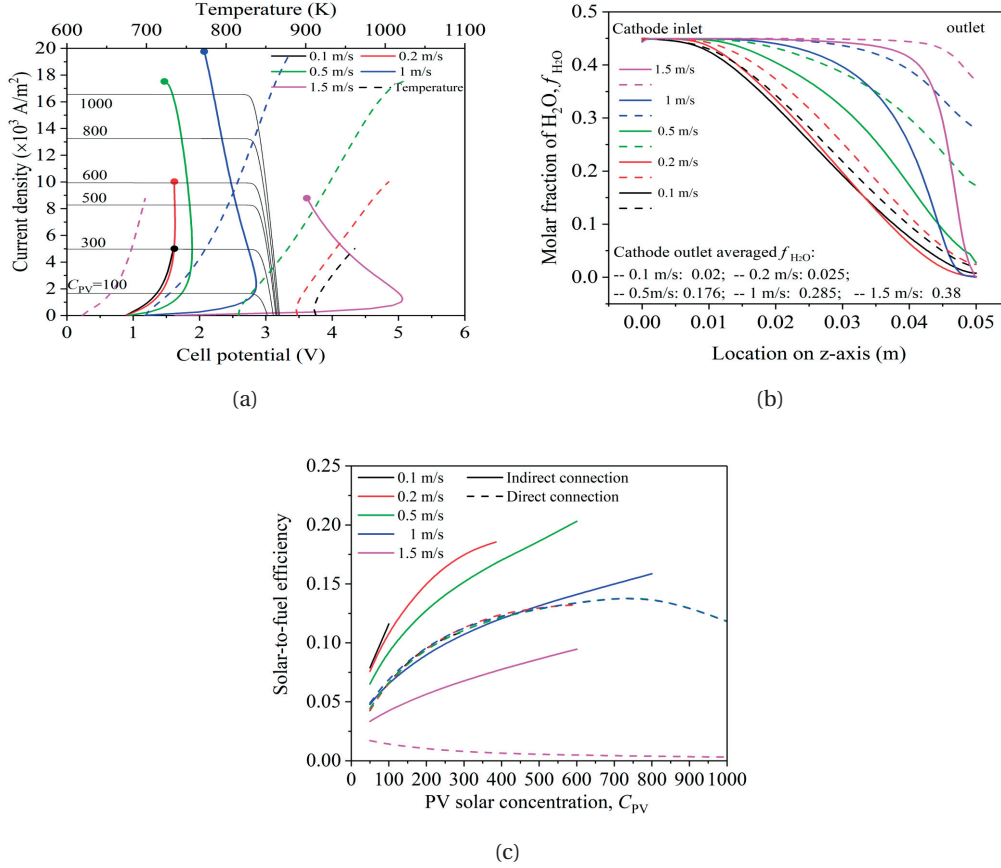


Figure 5.11 – (a) Operation cell potential (thick solid lines) and volume-averaged SOEC temperature (thick dashed lines) as a function of operation current density for various inlet flow velocities (differentiated by the colors), and the  $J$ - $V$  curves of the PV cell (thin solid black lines) for selected  $C_{PV}$ . (b) The  $\text{H}_2\text{O}$  molar fraction along the cathode-side triple phase boundaries at the cathode-electrolyte interface (solid lines) and channel-cathode interface (dashed lines) for various cathode inlet velocities at their limiting current density with the cathode outlet averaged  $\text{H}_2\text{O}$  molar fraction indicated on the bottom left. (c) STF efficiency for the direct (dashed lines) and indirect (solid lines) connections cases for varying flow rates and  $C_{PV}$ .

In the cases of direct connection, the efficiency curves for velocities of 0.1 m/s, 0.2 m/s, 0.5 m/s, 1 m/s nearly overlapped given by the operation points which were within the plateau region of the PV  $J$ - $V$  curves (see figure 5.11a). However, the operation points for the cases with

1.5 m/s inlet velocity were found to be in the falling region of the PV  $J$ - $V$  curves, resulting from the rather low temperatures (below 700 K for all conditions) which significantly increased the SOEC potential (around 3V at  $C_{PV} = 100$ ). Compared to the indirect connection cases, the direct cases showed always lower STF efficiency for a given flow velocity and PV solar concentration due to inefficient use of the PV (leading to high PV losses). An exception was found for the velocity of 0.5 m/s with  $C_{PV}$  in the range of 100 to 450. For these cases, the operation points were close to the MPPT of the PV cell, showing better performance than the indirect connection cases in which the efficiency penalty of the DC-DC converter (93% efficiency) becomes apparent.

#### 5.8.4 Flow arrangement

Four flow arrangements (schematically shown in figure 5.12a) are investigated in this section: the reference case (concurrent cathode-anode flow, inlets opposite to the reactor front), flow 1 (counter-flow, cathode inlet opposite to the solar inlet side), flow 2 (counter-flow, inlets at the solar inlet side), and flow 3 (counter-flow, cathode inlet at the solar inlet side).

In general, counter-flow arrangements led to two low temperature areas (close to the two inlets, see figure 5.12d) which led to higher heat losses through inlet boundaries, hence, leading to lower SOEC averaged temperature (938 K and 886 K for flow 1 and 3, respectively, and 831 K and 815 K for reference flow and flow 2, respectively). For the direct connection cases, concurrent flow arrangements showed smaller cell potentials for a specific operation current density than counter-current flow arrangements. For example at 5000 A/m<sup>2</sup> with direct connection, the cell potentials for the reference case and flow 2 were 1.62 V and 1.57 V, respectively, and 2.24 V and 2.29 V for flow 1 and flow 3. It is interesting to note that reference and flow 2  $J$ - $V$  curves cross at a current density of 7450 A/m<sup>2</sup>, i.e. at lower current density the operation potential of the flow 2 was smaller than for the reference case. This was due to the fact that the  $\eta_{ohmic}$  was higher in the reference case than in the flow 2 (0.57 V for reference case and 0.47 V for flow 2 at 5000 A/m<sup>2</sup>, see figure E.2). The ionic conductivity of YSZ exponentially decreases with the increasing temperature (see table E.4). For flow 2, the hot region close to outlet (0 m to 0.017 m) showed temperatures (1052 K to 1103 K) even higher than the maximum temperature (1052 K) leading to even higher ionic conductivity of electrolyte, although the surface averaged temperature for flow 2 was smaller than reference case (see figure 5.12d).

For the direct connection cases and for all four flow configurations operating with a  $C_{PV}$  in range of 50 to 500, the cell voltages are located in the flat region of the  $J$ - $V$  curve of the PV cell. For a specific  $C_{PV}$  (or current density), the operation current density was therefore constant but the STF efficiency still changed, resulting from the different molar ratio between the produced H<sub>2</sub> and CO (the lower the H<sub>2</sub>/CO ratio the higher the STF efficiency, see eq. 5.38).

## Chapter 5. An integrated concentrated solar fuel generator concept

As seen from figure 5.12b, flow 2 shows the largest STF efficiency, followed by the reference, followed by the two counter-current flow configurations. This observation is consistent with the products molar ratio plots for the SOEC cell under various current densities (see figure 5.12c, the flow 2 have the lowest ratio while flow 1 and 3 have the highest).

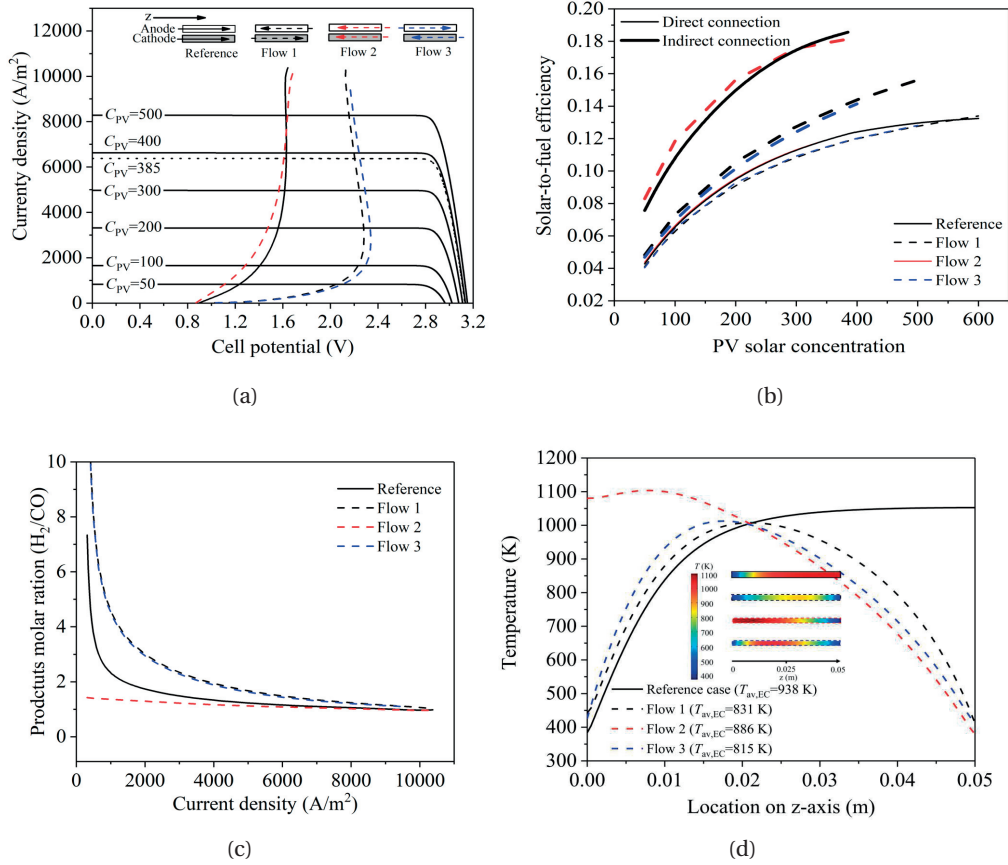


Figure 5.12 – (a)  $J$ - $V$  curves of the SOEC for the four flow arrangements at reference conditions and  $J$ - $V$  curves of the PV for varying  $C_{PV}$ . (b) STF efficiency for the four flow arrangements for varying solar concentrations for the indirect (thick lines) and direct (thin lines) cases. (c)  $H_2/CO$  molar ratio of the product gas at the SOEC cathode outlet for current densities between 300  $A/m^2$  and 10000  $A/m^2$ . (d) Temperature profiles along the cathode-side triple phase boundaries at the cathode-electrolyte interface and temperature distribution in the SOEC for the four flow arrangements at 5000  $A/m^2$ .

For the indirect connection cases, we observe the same grouping: reference and flow 2 show similar efficiencies and so do flow 1 and flow 3. However, the difference between the two groups is more significant compared to the direct connection cases. The two concurrent flow arrangements showed efficiencies of  $\eta_{STF} = 17.7\%$  and  $17.6\%$  (for the reference case at 7933  $A/m^2$  and for flow 2 at 7900  $A/m^2$ , both at  $C_{PV} = 300$ ), significantly larger than the STF

efficiencies of the two counter-current flow arrangements ( $\eta_{\text{STF}} = 12.8\%$  for flow 1 and  $12.5\%$  for flow 3). This resulted from higher volume-averaged SOEC temperature for the concurrent flow arrangements (see figure 5.12a) which led to lower cell potentials (see figure 5.12c for an example at  $5000 \text{ A/m}^2$ ). Flow 2 was inferior to the reference case for  $C_{\text{PV}} > 280$ , given by the higher  $f_{\text{fluid}}$  ( $29.4\%$  for reference case vs.  $35.9\%$  for flow 2 at  $C_{\text{PV}} = 300$ ). For  $C_{\text{PV}} < 280$ , the flow 2 showed higher STF efficiencies than the reference case. For example at  $C_{\text{PV}} = 100$ , the STF efficiency was  $11.1\%$  for the reference case while it was  $11.8\%$  for the flow 2, given by the lower cell potential and especially the lower ohmic overpotential (figure 5.12a and figure E.2).

### 5.8.5 Molar reactant composition at inlets

For the SOEC cathode inlet, we kept the molar fraction of CO and  $\text{H}_2$  constant at 0.05 to keep the reducing environment for the Ni catalysts. The molar fraction of  $\text{H}_2\text{O}/\text{CO}_2$  was however varied between 0 and 17. The STF efficiencies for the direct and indirect connection cases for 5 selected inlet  $\text{H}_2\text{O}/\text{CO}_2$  ratios and varying  $C_{\text{PV}}$  are shown in figure 5.13a. The operation current density for the direct connection cases can be read directly from the top x-axis and the operation current density for the indirect connection cases is shown in figure E.3. Generally, lower inlet  $\text{H}_2\text{O}/\text{CO}_2$  ratios led to higher STF efficiencies, resulting from a higher CO production (eq. 5.38), at a given  $C_{\text{PV}}$  (or current density). For example when the inlet  $\text{H}_2\text{O}/\text{CO}_2$  ratio increased from 0.125 to 8 at  $C_{\text{PV}} = 300$  for the direct connection case, the CO and  $\text{H}_2$  production decreased from  $1.21 \cdot 10^{-4} \text{ mol/s}$  and  $1.36 \cdot 10^{-5} \text{ mol/s}$ , respectively, to  $9.27 \cdot 10^{-6} \text{ mol/s}$  and  $1.253 \cdot 10^{-4} \text{ mol/s}$ , respectively, leading to an efficiency decrease from  $12.2\%$  to  $10.8\%$ . The efficiency became less sensitive to the inlet  $\text{H}_2\text{O}/\text{CO}_2$  ratio at high inlet  $\text{H}_2\text{O}/\text{CO}_2$  ratio. For example, the efficiency curves tended to overlap when the inlet  $\text{H}_2\text{O}/\text{CO}_2$  ratio increased above 2, given by the dominating  $\text{H}_2$  production at high inlet  $\text{H}_2\text{O}/\text{CO}_2$  ratio (see figure 5.13b). This was even more pronounced for the indirect connection cases, as (for a given  $C_{\text{PV}}$ ) the indirect connection cases achieved higher operation current densities. At high current densities, the  $\text{H}_2$  generation increased faster than at low current densities when increasing the inlet  $\text{H}_2\text{O}/\text{CO}_2$  ratio, resulting from a faster increase in the WGS rate (figure E.4a) and a faster increase in the electrochemical  $\text{H}_2$  production rate (see figure E.4d). The indirect connection cases showed always higher STF efficiencies compared to the direct connection cases, resulting from a better utilization of the PV cell and, in turn, leading to reduced energy losses from PV.



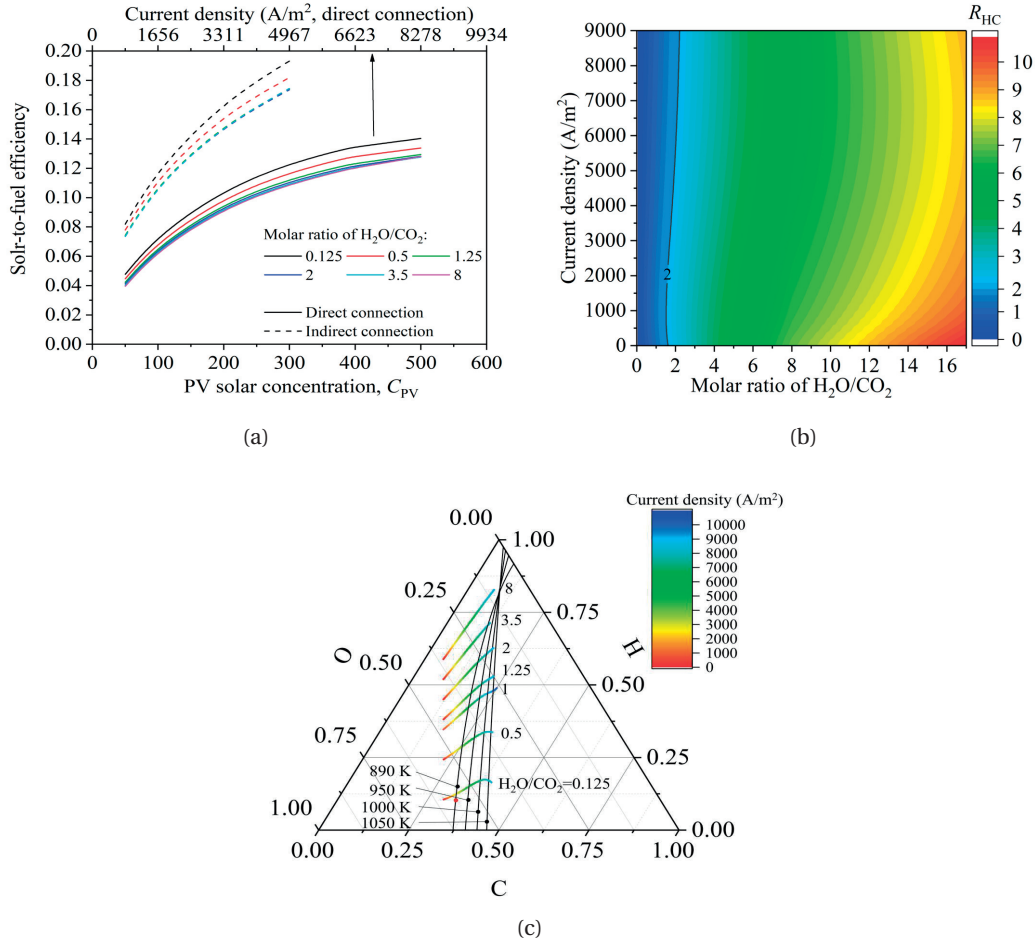


Figure 5.13 – (a) STF efficiency as a function of the PV solar concentration for direct (solid lines) and indirect (dashed lines) connection cases under varying current densities, (b) contour plot of the  $R_{HC}$  at the cathode outlet as a function of various inlet gas compositions ( $H_2O/CO_2$ ) and current densities, and (c) the C-H-O ternary diagram for various cathode inlet composition cases ( $0.125 < H_2O/CO_2 < 8$ ) with changing current densities and for five selected carbon deposition boundaries (for 890 K, 950 K, 1000 K, 1050 K and 1100 K at 1 atm).

Figure 5.13b shows  $R_{HC}$  at the SOEC cathode outlet as a function of cathode inlet  $H_2O/CO_2$  ratio and current density. To achieve  $R_{HC}$ , a higher inlet  $H_2O/CO_2$  ratio was required at higher current densities, resulting from the increase in the electrochemical  $H_2$  and CO production rates by around  $10^{-4}$  mol/s when increasing the current density from 1000  $A/m^2$  to 9000  $A/m^2$ . For the same increase in the current density, the absolute difference in the electrochemical  $H_2$  and CO production rates only increased by  $5 \cdot 10^{-5}$  mol/s (figure E.4d). In order to maintain  $R_{HC} = 2$ , larger  $H_2$  production rates were required, requiring, in turn, higher inlet  $H_2O/CO_2$  ratios.



Table 5.4 – The intersection points for 7 selected inlet  $\text{H}_2\text{O}/\text{CO}_2$  ratios and 4 carbon deposition boundaries.

Boundary temperature (K)		890		950		1000		1050	
inlet $\text{H}_2\text{O}/\text{CO}_2$ ratio		Current density ( $\text{A}/\text{m}^2$ )	SOEC temperature (K)	Current density ( $\text{A}/\text{m}^2$ )	SOEC temperature (K)	Current density ( $\text{A}/\text{m}^2$ )	SOEC temperature (K)	Current density ( $\text{A}/\text{m}^2$ )	SOEC temperature (K)
0.125		3261	916	5700	950	7600	978	8952	999
0.5		4481	930	6716	960	8342	981	9358	1000
1		5623	946	7644	971	8725	985	9850	1001
1.25		6309	954	8136	975	9256	992	9967	1003
2		7529	970	8952	987	9663	1000	-	-
3.5		8037	976	-	-	-	-	-	-
8		-	-	-	-	-	-	-	-

The cathode outlet C-H-O compositions for 7 selected inlet  $\text{H}_2\text{O}/\text{CO}_2$  ratios under varying operation current densities are shown in figure 5.13c. The variations in SOEC temperature due to different inlet  $\text{H}_2\text{O}/\text{CO}_2$  ratios were small ( $< 20$  K, figure E.5). For a straightforward comparison with the reference case in section 5.8.2, the lower boundary temperature for the analysis of carbon deposition was chosen to be 890 K, representing the SOEC temperature with an inlet  $\text{H}_2\text{O}/\text{CO}_2$  ratio of 0.5 at open circuit condition. Temperatures of 950 K, 1000 K, and 1050 K were chosen as the reference carbon deposition boundaries. The intersection points for the 7 select inlet  $\text{H}_2\text{O}/\text{CO}_2$  ratios with 4 reference carbon deposition boundaries are shown in table 4 with the points in carbon deposition zone marked in red. The SOEC temperature at the intersection points should be higher than the carbon deposition boundary to avoid carbon deposition. Higher inlet  $\text{H}_2\text{O}/\text{CO}_2$  ratio led to lower probability of carbon deposition. For example at inlet  $\text{H}_2\text{O}/\text{CO}_2 = 8$ , there is no carbon deposition expected for the whole range of operation current densities. With decreasing inlet  $\text{H}_2\text{O}/\text{CO}_2$  ratios, the current density at which carbon deposition is likely decreases ( $9663 \text{ A/m}^2$  at  $\text{H}_2\text{O}/\text{CO}_2 = 2$  and  $5700 \text{ A/m}^2$  at  $\text{H}_2\text{O}/\text{CO}_2 = 0.125$ ).

### 5.8.6 Reactor with multiple in-series SOEC stacks

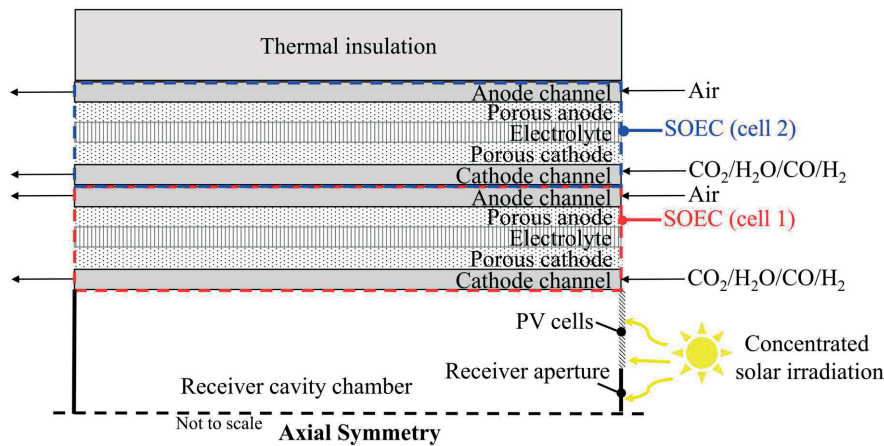


Figure 5.14 – Schematic of a possible design of an integrated reactor with two in-series connected SOEC cells (inner cell in dashed red box and outer cell in dashed black box). The two tubular SOEC cells are concentrically arranged.

The cell potential for a single cell SOEC in the integrated solar reactor (single-cell reactor) at reference conditions was found to be in a range of around 0.9 V to 1.6 V for current densities in the range of  $0 \text{ A/m}^2$  to  $10000 \text{ A/m}^2$ . These cell potentials are only 38% to 54% of the triple junction PV cell's open circuit voltage (2.97 V at  $C_{\text{PV}} = 50$ , and 3.17 V at  $C_{\text{PV}} = 600$ ). This indicates that higher efficiencies are achievable by connecting two SOECs in series to such a

triple junction PV cell, still ensuring operating close to the PV cell's MPPT. This enhanced the STF efficiency of the direct connection cases, leading to comparable or even higher efficiencies compared to the indirect connection cases (as the loss in the DC-DC converter is omitted in the direct connection cases). We investigated one example case of a reactor with two in-series connected SOECs (schematically shown in figure 5.14) with direct PV-SOEC connection (termed two-cell reactor). The second SOEC was placed concentrically around the first cell, with the cathodic channel of the outer cell in direct contact with the anodic channel of the inner cell (these two channels form a bipolar plate). The two SOECs had the same channel, electrode, and electrolyte thicknesses, and identical length. The cathode inlet fluid velocities for the two in-series SOEC cells were assumed to be the same.

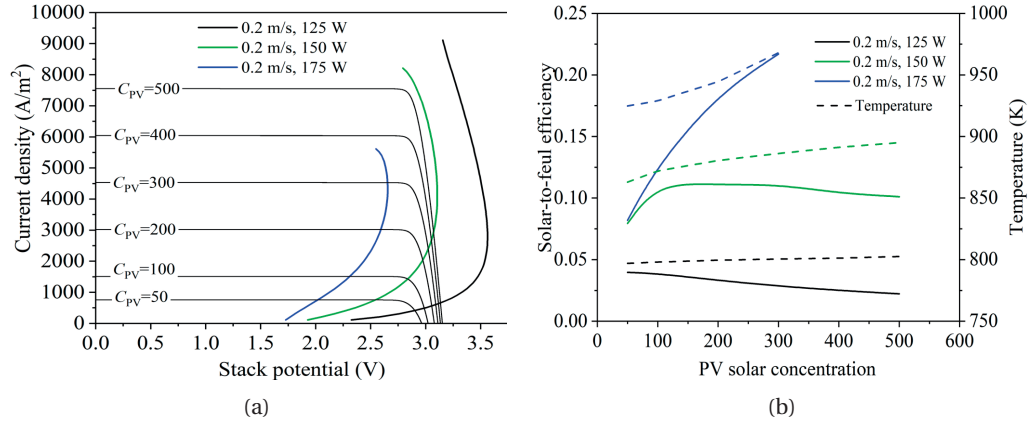


Figure 5.15 – (a)  $J$ - $V$  curves for the two-cell SOEC stacks and the PVs for three different solar energy inputs ( $\dot{Q}_{\text{solar,ap}} = 125$  W, 150 W, and 175 W) for direct connection cases, and (b) STF efficiencies (solid lines, left  $y$ -axis) and the average stack temperatures (dashed lines, right  $y$ -axis) as a function of the concentration for three different  $\dot{Q}_{\text{solar,ap}}$ .

For a cathode inlet velocity of 0.2 m/s and  $\dot{Q}_{\text{solar,ap}} = 125$  W, the two-cell reactor's open circuit potential was 1.7 V and its operating potential was 2.3 V at a current density of 410 A/m² and an STF efficiency of 4% ( $C_{PV} = 50$ ). The STF efficiency decreased with increasing current density (for 0.2 m/s and  $\dot{Q}_{\text{solar,ap}} = 125$  W) as the operation points were on the dropping region of the PV  $J$ - $V$  curve (figure 5.15a) given by the low SOECs temperature. This low STF efficiency was improved by increasing the  $\dot{Q}_{\text{solar,ap}}$ , which, in turn, significantly increased the SOECs temperature and therefore reduced the cell potential. For example, the STF efficiency increased from 4% to 7.9% at  $C_{PV} = 50$  when  $\dot{Q}_{\text{solar,ap}}$  increased from 125 W to 150 W with a temperature increase from 807 K to 864 K for SOEC cell 1 and 803 K to 861 K for SOEC cell 2. For  $\dot{Q}_{\text{solar,ap}} = 150$  W, the STF efficiency first increased with increasing  $C_{PV}$  (resulting from the increased temperature and reduced overpotentials) but then decreased when  $C_{PV}$  was larger than 100 (resulting from the operation point turning back to the PV falling region). Further

increasing  $\dot{Q}_{\text{solar,ap}}$  (from 150 W to 175 W) led to significant efficiency increases (especially at high current density) resulting from increased temperature and pushing the stack potential closer to the MPPT of the PV. It is worthwhile to note that at  $C_{\text{PV}} = 300$ , the STF efficiency reached 21.7%, which was higher than the highest value achieved for the single-cell reactor using an indirect connection strategy (18.6% at  $C_{\text{PV}} = 385$ ).

### 5.8.7 Effect of $\eta_{\text{STF}}$ definitions

The two definitions of  $\eta_{\text{STF}}$  given in section 5.6 are noted as definition 1 (eq. 5.38, based on Gibbs free energy) and definition 2 (eq. 5.39, based on enthalpy). In general, definition 2 shows larger  $\eta_{\text{STF}}$  values than definition 1 due to the consideration of latent heat of water in definition 2. The choice of these two definitions can be decided based on the end usage of the produced products. Definition 1 can be used for quantifying the systems' performance when the produced fuels are used for further chemical synthesis (e.g. methane, methanol, etc), while definition 2 can be chosen when the produced fuels are used for combustion. The effect on these two definitions on the final  $\eta_{\text{STF}}$  values under the reference condition are shown in figure 5.16 (see section 5.8.2 for the details of the reference case conditions). As expected, the definition 2 showed higher  $\eta_{\text{STF}}$  than definition 1. For example, at  $C_{\text{PV}} = 50$ , the efficiency for direct connection case with definition 1 was 4.28%, while 5.04% for definition 2. This means a 17.8% overestimation in  $\eta_{\text{STF}}$  by using definition 2 compared to definition 1 which indicates that the importance of unification of solar-to-fuel efficiency definitions when comparing different solar fuel technologies based on the fuel utilization.

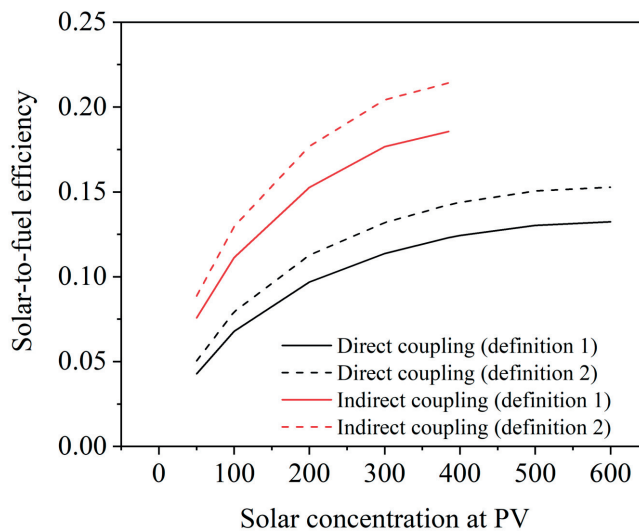


Figure 5.16 –  $\eta_{\text{STF}}$  as a function of solar concentration at PV cell under reference conditions for both direct (black lines) and indirect (red lines) connections for efficiency definition 1 (solid lines) and definition 2 (dashed lines)

## 5.9 Summary and conclusions

A novel integrated solar reactor concept is proposed in this chapter which integrates a solar receiver, a tubular solid oxide electrolyzer, and a PV cell for the solar fuel processing under concentrated irradiation. A numerical model was developed for this integrated solar reactor in order to do feasibility studies, quantify and assess the performance, optimize the design and operation for enhanced performance, and assess the potential of this technology. The model accounted for charge transfer in the membrane-electrolyte assembly, electro- and thermochemical reactions at the electrodes' reaction sites, species and fluid flow in the fluid channels and electrodes, and heat transfer for all reactor components. The STF efficiency, carbon deposition conditions, and product compositions were investigated for varying operation conditions and designs: reference case condition, flow fluid flow arrangements (two co-current flow and two counter-current flow), inlet fluid compositions, PV - SOEC coupling strategies, and two-cell reactor configuration.

At reference condition, the STF efficiency was higher for higher solar concentration due to the increased SOEC temperature with increasing operation current density. For the single-cell reactor, the indirect connection strategy generally showed higher efficiency (18.6% at  $C_{PV} = 385$ ) compared to the direct connection strategy (12.3% at  $C_{PV} = 385$ ) under the reference condition. The efficiency advantage of the indirect connection is even larger at higher PV concentrations. The current density threshold for carbon deposition was found to be  $7500 \text{ A/m}^2$  at reference condition for syngas production. The single SOEC reactor always favors the indirect connection between SOEC and PV for better use of triple junction PV cell voltage. The operation current density need to be carefully chosen in order not to exceed the carbon deposition boundary based on your inlet gas composition and operation conditions

The increase in the cathode inlet fluid velocity always led to a decrease in the solar-to-fuel efficiency for indirect connection cases, given by the reduced SOEC cell temperature. However, higher inlet velocity led to higher maximal solar-to-fuel efficiency (increased from 11.6% to 20.3% when the inlet velocity increased from 0.1 m/s to 0.5 m/s for the reference case) by alleviation mass transport limitation at high current densities. Further increase in inlet velocity (larger than 0.5 m/s) led to decreased achievable STF efficiency due to significant temperature reduction. When choosing the reactor inlet flow rates, an optimal velocity can be found to alleviate the mass transport limits as well as not significantly lowering the reactor temperature hence to maximize the STF efficiency.

Flow configuration is essential to the STF efficiency of the integrated reactor. Benefitting from lower thermal losses from the reaction, the concurrent flow arrangement with the front fluid inlet position showed better STF efficiency compared to counter-current flow configurations. At  $C_{PV} = 300$  for concurrent flows,  $\eta_{STF} = 17.7\%$  and  $17.6\%$  for the reference case and flow 2

## Chapter 5. An integrated concentrated solar fuel generator concept

---

under indirect connection, while only 12.8% and 12.5% for flow 1 and flow 3 (counter-current flows). There is a transition operation current density when the reference case showed better STF efficiency when operation above the transition value. This gives us useful design and operation guidelines for reactor engineering.

A large variation in the  $H_2/CO$  molar ratio (in the range of 0 - 11) in the product stream was achieved by varying the inlet  $H_2O/CO_2$  ratio (in the range of 0 - 17), the  $C_{PV}$  (in the range of 0 - 1000), and the operation current density (in the range of 0 - 10000 A/m<sup>2</sup>). Higher inlet  $H_2O/CO_2$  ratios led to lower probabilities of carbon deposition. With decreasing inlet  $H_2O/CO_2$  ratio, the carbon deposition threshold current density decreased. Hence the inlet gas ratio, as well as operation conditions, need to be optimized for the desired products compositions while avoiding carbon deposition.

The two-cell reactor could achieve even higher efficiency (21.7%) compared to the single-cell reactor by simply increasing the thermal energy ( $\dot{Q}_{solar,ap}$ ) input to the system. At low (0.2 m/s and  $\dot{Q}_{solar,ap} = 125$  W), the solar-to-fuel efficiency decreased with the increased current density as the operation points were on the falling region of the PV  $J$ - $V$  curve. The increasing in  $\dot{Q}_{solar,ap}$  could significantly increase the stack temperature resulting in reduced stack potential and hence increased solar-to-fuel efficiency. By a smart design of solar heating ( $\dot{Q}_{solar,ap}$ ) and solar electricity ( $\dot{Q}_{solar,PV}$ ) the direct connection cases could achieve even higher efficiency than the indirect connection cases.

The observation that the PV cell was highly oversized (in terms of open circuit potential) led to the design of an in-series stacked two SOEC cells reactor design. This two-cell reactor could achieve even higher efficiencies (maximal 21.7% for  $C_{PV} = 300$  and  $\dot{Q}_{solar,ap} = 175$  W) compared to the single-cell reactor by simply increasing the thermal energy input ( $\dot{Q}_{solar,ap}$ ) to the system. At low (0.2 m/s and  $\dot{Q}_{solar,ap} = 125$  W), the STF efficiency decreased with the increased current density as the operation points were on the falling region of the PV  $J$ - $V$  curve. The increase in  $\dot{Q}_{solar,ap}$  significantly increased the stack temperature, resulting in a reduced stack potential and, hence, an increased STF efficiency.

In sum, an integrated solar reactor concept was presented in this chapter which integrates a cavity receiver, a tubular solid oxide electrolyzer (SOEC), and the concentrated photovoltaic (PV) cell in a single reactor. This integrated reactor aims at overcoming transmission losses and reduce complexity while increasing the fuel processing efficiency for concentrated solar irradiation. A complete numerical model accounting for various coupled physics was developed, allowing for the performance prediction of the reactor under various operation conditions and design configurations. This study also offered initial design guidelines for the integrated solar reactor, which is useful for the design and engineering of both lab-scale prototypes (for proof-of-concept demonstrations) and scale-up plants.

## 6 Summary and outlook

This thesis studied two high-temperature routes for solar fuel processing with special focus on solar-driven HTE systems and reactors. The techno-economic performance of HTE systems was optimized under various system designs, operational conditions, and using various material and device choices. Direct steam generation solar receiver was then investigated in detailed based on an in-house coupled heat and mass transfer numerical model accounting for two-phase flow inside the tubular solar absorber as well as radiative, convective, and conductive heat transfer for the receiver cavity. Based on the model, a compact solar reactor was designed and demonstrated which was proven to have good thermal performance as well as promising solar-to-fuel efficiency. Further, an integrated solar reactor concept was proposed which used a tubular SOEC as the reactor as well as solar absorber to further reduce transmission heat losses. The novel reactor was investigated with a multi-physics model and showed better performance than the non-integrated reactor.

In chapter 1, based on the techno-economic model, the hybrid approach (concentrated solar heating and photovoltaics to provide heat and electricity) was found to be the optimal strategy to incorporate solar energy into HTE fuel generation systems. This strategy was found to produce hydrogen at a high efficiency and at a low costs showing a promising techno-economic performance towards large scale engineering of solar fuel plants. Further investigation on system 3 found that there is operation temperature for SOEC need to be optimized that balances the increased thermal receiver losses with the reduced electrolysis cell potential when increasing the temperature. Designing the system to work at ambient pressure always favors high system efficiency and low cost. The required product molar ratio ( $\text{H}_2/\text{CO}$ ) be achieved by tuning the inlet feeding molar ratio of  $\text{CO}_2/\text{H}_2\text{O}$ , temperature, and pressure for syngas production. This chapter introduced a flexible simulation framework of solar-driven HTE systems allowing for the assessment of competing solar integration approaches and for the guidance of the operational conditions maximizing efficiency and minimizing cost,



providing pathways for scalable solar fuel processing.

In chapter 2, a competing high-temperature route (i.e. ceria-based TCC), other than HTE, was discussed and compared. A thermodynamic analysis of five redox cycle designs to investigate the effects of working conditions on the fuel production. Focus was paid on the influence of approaches to reduce the partial pressure of oxygen in the reduction step, namely by mechanical approaches (sweep gassing or vacuum pumping), chemical approaches (chemical scavenger), and combinations thereof. The results indicated that the sweep gas schemes work more efficient at non-isothermal than isothermal conditions, and efficient gas phase heat recovery and sweep gas recycling was important to ensure efficient fuel processing. The vacuum pump scheme achieved best efficiencies at isothermal conditions, and at non-isothermal conditions heat recovery was less essential. The use of oxygen scavengers combined with sweep gas and vacuum pump schemes further increased the system efficiency. The present work can be used to predict the performance of solar-driven non-stoichiometric redox cycles and further offers quantifiable guidelines for system design and operation. Two high-temperature routes for solar fuel generation was compared at the end of chapter 2 showing that HTE can be a more promising technology due to lower operation temperature and less harsh requirement for low partial pressure of oxygen while still achieve identical STF efficiency as TCC.

In chapter 3, a validated numerical model for a solar receiver with indirectly irradiated absorber tubes for the direct steam generation was developed. The model coupled a 3D receiver cavity heat transfer model (accounting for conduction, natural convection, and radiation inside the receiver) with a 1D two-phase flow model (solving for two-phase flow inside the absorber tubes). This generalized numerical frameworks offers an accurate and fast tool for the performance evaluation as well as engineering design for indirectly irradiated tubular solar receiver. Two different receiver designs (i.e. receiver 1: with a helical absorber tube, and receiver 2: with straight, connected tubes) were investigated under various operation conditions and design parameters, i.e. fluid flow rates, pressure, surface emissivity, inlet position, tube diameter, helical shape, and the water-cooled receiver front. Higher solar thermal efficiency can be achieved for scaled-up receiver by using helical tube as the solar absorber, the fluid inlet at the receiver front, and a surface emissivity larger than 0.58. This numerical model enables design and optimization of direct steam generation solar receivers/reactors with a good accuracy as well as a reasonable computational cost which can be used as a fast design and prototyping tool of receivers/reactors for high-temperature solar thermal, thermochemical, and electrochemical applications.

In chapter 4, based on extensive numerical studies in chapter 3, the design, fabrication, and experimentation of a compact solar reactor (coupling a double helical tube solar receiver and a 16-cell SOEC stack in one single reactor) was performed. The SOEC stack test was firstly conducted in electrical oven at GEM's test bench to characterize the electrochemical behavior



---

of the SOEC stack under various temperature and flow rate conditions (campaign 1). Higher operation temperature led to better electrical performance of the SOEC stack. Lower flow rate had higher stack electrical efficiency. A maximum solar-to-thermal efficiency of 78% was achieved with inlet flow rates of 1 L/min N<sub>2</sub> and 12.6 g/min water and 0.91 kW incident irradiance at the reactor aperture. The thermal and electrical performance were tested for the compact solar reactor showing that the preheating phase showed good heating rates (196.7 °C/h) and maximum 9.5 K/cm temperature gradient over the stack. The solar-to-fuel efficiency of 5.3% can be achieved for run 3 (1056 K and 8 Nml/min/cm<sup>2</sup>) with a single-crystalline silicon PV cell. A solar-to-fuel efficiency of 7.5% can be envisioned when III-V based PV cells were used (37% solar-to-electricity efficiency). A further efficiency improvement can be achieved (9.8% for run 3 with III-V based PV) by assuming an 30% reduction in incident solar power at the aperture via heat recovery. The experimental results proofed feasibility of the compact solar reactor concept with direct steam generation and direct feeding to stack for the minimization of the heat losses. In addition, future improvements to higher STF efficiency can be achieved by improving SOEC stack performance as well as introducing of heat recovery.

In chapter 5, an integrated solar reactor concept was proposed which integrates a solar receiver, tubular solid oxide electrolyzer (used also as the solar absorber), and a III-V based PV cell for solar fuel processing under concentrated irradiation. A multi-physics numerical framework was developed for the solar reactor for performance prediction and design optimization. The STF efficiency, carbon deposition conditions and two PV-EC electrical coupling strategies have been discussed under various operation conditions and designs (fluid inlet velocity, fluid flow arrangements, inlet fluid compositions, and two-cell reactor configuration). The solar-to-fuel efficiency was higher with higher solar concentration due to the increased SOEC temperature with increasing operation current density. The indirect connection strategy showed better efficiency (18.6% at a PV concentration ( $C_{PV}$ ) equals to 385) compared to the direct connection (12.3% at  $C_{PV} = 385$ ) under the reference condition. The current density boundary for carbon deposition was 7500 A/m<sup>2</sup> for syngas production. The co-current flow arrangement with the front fluid inlet position close to the front (reference case) has better solar-to-fuel efficiency due to less thermal losses. The product H<sub>2</sub>/CO molar ratio can be achieved by tuning the inlet H<sub>2</sub>O/CO<sub>2</sub> ratio,  $C_{PV}$ , and operation current density. The decrease in inlet H<sub>2</sub>O/CO<sub>2</sub> ratio led to a reduction in the carbon deposition threshold current density. The two-cell reactor could achieve even higher efficiency (21.7%) compared to the single-cell reactor by simply increasing the thermal energy input to the system while the incident solar energy at the PV cell unchanged. This studies enables a promising route towards practical engineering of high efficient HTE solar fuel reactor.

The further successful engineering of the proposed solar reactor concepts depends largely on the mechanical stability of the SOEC stack/cell under integrated solar reactor mode which

is directly related to the local thermal stress induced by local temperature gradient [186]. To design integrated solar reactors with robust mechanical stability, thermal management over the integrated solar reactor together with thermal stress model in 3D is required for a comprehensive understanding of thermo-electrochemical-mechanical behavior of the reactor. The thermal stress induced by temperature gradient over the SOEC can be simulated using Young's modulus assuming that involved materials undergo elastic deformation [187]. This numerical framework can be used for scale-up engineering of the proposed solar reactors in this thesis.

The studies conducted in this thesis are based on macroscopic reactor/component modeling and experimentation. The fundamental understanding of the effects of electrodes' microstructure on the global SOEC performance is required for the optimal cell design and hence can further enhance the reactor performance [188]. The effective gas diffusivity, electrode electrical conductivity, intrinsic Knudsen diffusivity, and electrochemical reaction rates can be characterized based on real [189] or artificially generated [190] morphology of the electrodes which can then be coupled to the multi-physics numerical model in chapter 5 for more accurate performance prediction and optimization.

The discussion on chapter 3 indicated that the STF efficiency can be dominated by the efficiency of oxygen removal methods in the reduction step of the thermochemical cycle. Inert gas sweep route required very high heat exchanger effectiveness ( $> 0.955$ ) and the mechanical route (e.g. vacuum pump) suffered from low electrical efficiency at low oxygen pressure. In addition, both routes can hardly reach an oxygen pressure level of  $10^{-6}$  atm. The introduction of high-temperature electrochemical oxygen pump (e.g. YSZ-based membrane + LSM-based electrodes) can potentially provide an atmosphere with oxygen partial pressure in range of  $10^{-5}$  atm to  $10^{-30}$  atm [191, 192, 193, 194]. Hence, the concept of combining the thermochemistry (e.g. ceria-based redox pairs as the water/carbon dioxide catalysts) and electrochemistry (e.g. LSM/YSZ/LSM electrochemical cell for oxygen removal) can potentially overcome the drawbacks of existing thermochemical cycles and high-temperature electrolysis systems via providing efficient and stable low partial pressure of oxygen environment (compared to thermochemical cycles) and reducing the required electrical input (compared to the high-temperature electrolysis systems as only the oxygen pumping requires electricity input).

The PV cells discussed in this thesis are either Si-based or III-V based cells which need continuous cooling to ensure the solar-to-electricity efficiency. In this regards, two distinct temperature zones (high-temperature for SOEC while low temperature for PV cell) will be created leading to high heat losses as well as large temperature gradient over the reactor. The suggested future research could be on high-performance semiconductor materials working at elevated temperatures. For example, the PV cell with pn-junction formed by LSM (p-type)/TiO<sub>2</sub> (n-type) showed a knee voltage of 1.03 V at 723 K which was higher than 0.96 V (the equilibrium voltage

---

of water splitting at 723 K) [195] indicating a promising candidate as the electrical source for water splitting. A high-temperature photoelectrochemical (PEC) cell can be achieved by coupling the high-temperature PV and SOEC to split  $\text{H}_2\text{O}$  and  $\text{CO}_2$  at elevated temperature without cooling requirement for the PV. The success of this high-temperature PEC cell relies highly on the electron-hole separation ability of selected semiconductor materials and the electrochemical stability of catalysts at elevated temperature ( $> 700$  K). The screening of suitable semiconductor materials is essential and can be achieved by using density-functional theory (DFT) for the computation of the electronic band structure at elevated temperatures for various semiconductor materials.

To conclude, this thesis focused on paving the way for the optimization, design, and engineering of the HTE solar fuel processing systems and reactors. Modeling frameworks at multi-scales (system, reactor, and component) were developed to understand the system/reactor performance under various designs and operation conditions and hence to offer design and engineering guidelines for both prototypes and scaled-up plants. The successful demonstration of the compact solar reactor, as well as the proposal of the integrated reactor concept open a novel pathway for solar energy incorporation with HTE for high-performance solar fuel reactor engineering which in turn advance its future commercialization.



## **A Definition of energy fractions high-temperature electrolysis systems**

Table A.1 – Definition of energy fractions for all three systems.

System	System 1	System 2	System 3
$f_{el,power}$	$\frac{\dot{P}_{el}}{\eta_{CSP,STE} (DNI + DHI) A_{helio,stat}}$	$\frac{\dot{P}_{el}}{\eta_{PV,STE} (DNI + DHI) A_{PV,array}}$	$\frac{\dot{P}_{el}}{\eta_{PV,STE} (DNI + DHI) (A_{PV,array} + A_{helio,stat})}$
$f_{pump\&comp,power}$	$\frac{\dot{P}_{el}}{\eta_{CSP,STE} (DNI + DHI) A_{helio,stat}}$	$\frac{\dot{P}_{el}}{\eta_{PV,STE} (DNI + DHI) A_{PV,array}}$	$\frac{\dot{P}_{el}}{\eta_{PV,STE} (DNI + DHI) (A_{PV,array} + A_{helio,stat})}$
$f_{el,heat}$	$\frac{\dot{Q}_{el}}{\eta_{CSP,STT} (DNI + DHI) A_{helio,stat}}$	$\frac{\dot{Q}_{el}}{\eta_{PV,STT} (DNI + DHI) A_{PV,array}}$	$\frac{\dot{Q}_{el}}{\eta_{PV,STT} (DNI + DHI) (A_{PV,array} + A_{helio,stat})}$
$f_{fluid,heat}$	$\frac{(\dot{Q}_{fluid} - \dot{Q}_{fluid,electric}) / \eta_{CSP,STT} + \dot{Q}_{fluid,electric} / (\eta_{CSP,STE} \eta_{ETT})}{(DNI + DHI) A_{helio,stat}}$	$\frac{\dot{Q}_{fluid}}{\eta_{PV,STT} (DNI + DHI) A_{PV,array}}$	$\frac{(\dot{Q}_{fluid} - \dot{Q}_{fluid,electric}) / \eta_{CSP,STT} + \dot{Q}_{fluid,electric} / (\eta_{PV,STE} \eta_{ETT})}{(DNI + DHI) (A_{PV,array} + A_{helio,stat})}$

Note:  $\eta_{CSP,STE}$  and  $\eta_{PV,STE}$  are the solar to electricity efficiency for CSP and PV, respectively.  $\eta_{CSP,STT}$  is the solar-to-thermal efficiency of the CSP system and  $\eta_{ETT}$  is the electricity-to-thermal efficiency of the electrical heater which is 0.9 in this study.  $\dot{Q}_{fluid,electric}$  is the heat demand for the electrical temperature stabilizer (EH1 and EH2 in figure 1.1).

## B Supplementary data for two-step thermochemical cycles

### B.1 Efficiency curves for carbon dioxide splitting

Figure B.1 shows the efficiency of CO<sub>2</sub> splitting at various  $T_{\text{red}}$  and  $p_{\text{O}_2,1}$  for schemes (a) and (b). Compared to the hydrogen production (exemplary red curve for  $p_{\text{O}_2,1} = 1$  Pa), the CO production showed higher efficiencies (figure B.1a) due to a larger equilibrium constant, i.e. the equilibrium constant was  $5.34 \times 10^{-5}$  for H<sub>2</sub>O and  $2.05 \times 10^{-4}$  for  $p_{\text{O}_2,1}$  at 1800 K. Similar behavior for CO<sub>2</sub> and water splitting was observed for the efficiency dependency on  $T_{\text{red}}$  and  $p_{\text{O}_2,1}$ . E.g. scheme (a) had an optimal  $\Delta T$  for optimal efficiencies, and scheme (b) showed highest efficiencies at isothermal conditions.

### B.2 System performance behavior using ideal mixing model

In the ideal mixing model, the  $p_{\text{O}_2,1}$  was determined by its demand and hence the corresponding demand for sweep gas was calculated by

$$\dot{n}_{\text{N}_2} = \frac{p_{\text{system}}}{p_{\text{O}_2,1}} \dot{n}_{\text{O}_2,4}, \quad (\text{B.1})$$

where  $\dot{n}_{\text{O}_2,4}$  is the flow rate of oxygen produced by reduction. The  $p_{\text{O}_2,12}$  was the optimal value calculated - smaller than  $p_{\text{O}_2,11}$  - which led to the highest solar-to-fuel-efficiency. The baseline parameters used in ideal mixing models were identical to the ones used in the schemes using counterflow arrangement (table 2.1).

Figure B.2 shows the efficiency variation for various working conditions. Figures B.3 and B.4 show the corresponding energy breakdown. Schemes (a) and (b) showed increasing efficiencies with increasing  $T_{\text{red}}$ . For both schemes, the largest efficiencies were observed at isothermal conditions (for  $p_{\text{O}_2,1} < 1$  kPa). The scheme (a) showed significant lower efficiency

## Appendix B. Supplementary data for two-step thermochemical cycles

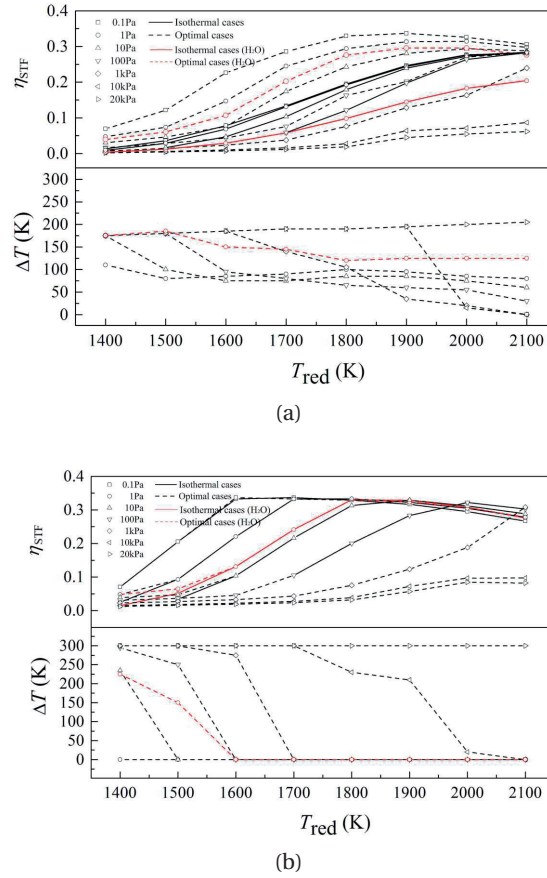


Figure B.1 – Optimal  $\eta_{STF}$  and corresponding  $\Delta T$  for various  $T_{red}$  and  $p_{O_2,1}$  combinations for (a) sweep gassing (scheme (a)), and (b) vacuum pumping (scheme (b)). The solid lines indicate the efficiency at corresponding  $T_{red}$  and  $p_{O_2,1}$  for isothermal operation ( $\Delta T=0$ ). The red lines show exemplary performance for a water splitting system at  $p_{O_2,1} = 1$  Pa.

compared to scheme (b) which was explained by the large quantity of sweep gas needed in the ideal mixing arrangement (i.e. the maximum efficiency for scheme (a) was below 0.15 and for scheme (b) around 0.3).

Figure B.5 depicts the impact of  $\varepsilon_g$  on the efficiency at condition of  $p_{O_2,1} = 10$  Pa under various working conditions for scheme (a) and (b). Larger  $\varepsilon_g$  led to higher efficiency. This increase in efficiency was more pronounced at higher  $\varepsilon_g$  which was analogous to the results for the counterflow arrangement. For scheme (a),  $\varepsilon_g$  was required to be higher than 0.98 to achieve the 10% efficiency. While, for scheme (b), the 10% efficiency could be obtained with  $\varepsilon_g$  of 0.95 at temperatures of 1800 K. Scheme (b) showed superior performance compared to the scheme (a).

Figure B.6 shows the effect of  $\varepsilon_s$  on the efficiency at  $T_{red} = 1800$  K and  $p_{O_2,1} = 1$  Pa for various  $\Delta T$ . The increase of  $\varepsilon_s$  showed no effect on the efficiency as the  $\dot{Q}_{gas,red}$ ,  $\dot{Q}_{gas,ox}$ , and  $\dot{Q}_{heat loss}$



## B.2. System performance behavior using ideal mixing model

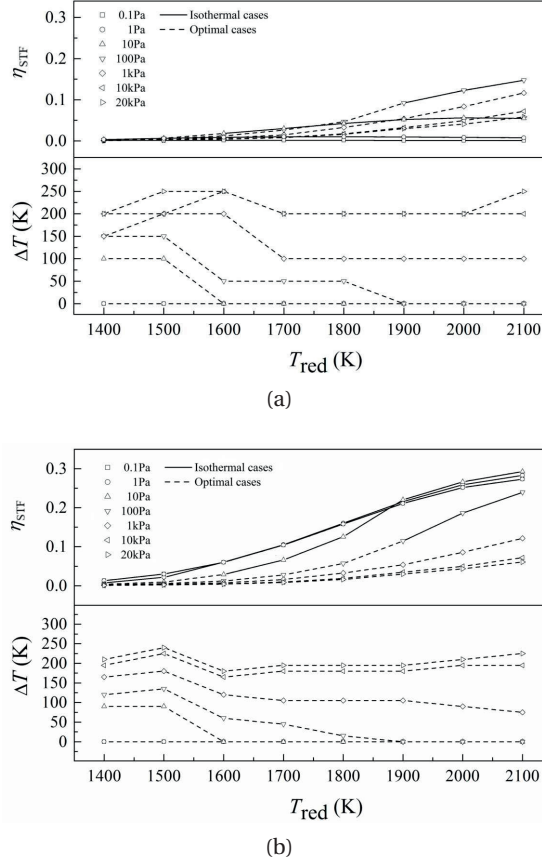


Figure B.2 – Optimal  $\eta_{STF}$  and corresponding  $\Delta T$  for various  $T_{red}$  and  $p_{O_{2,1}}$  combinations for (a) scheme (a), and (b) scheme (b) using an ideal mixing arrangement. The solid lines indicate the efficiency at corresponding  $T_{red}$  and  $p_{O_{2,1}}$  for isothermal operation ( $\Delta T=0$ ).

dominated the energy consumption while  $\dot{Q}_{solid}$  was minor in scheme (a). For scheme (b), an increase in  $\epsilon_s$  led to larger efficiencies. This efficiency enhancement reduced as  $\Delta T$  increased further ( $\Delta T > 25$  K) due to an increase in  $\dot{Q}_{gas,ox}$  and decrease in the ceria flow rate resulting from increasing  $\Delta\delta$ .

## Appendix B. Supplementary data for two-step thermochemical cycles

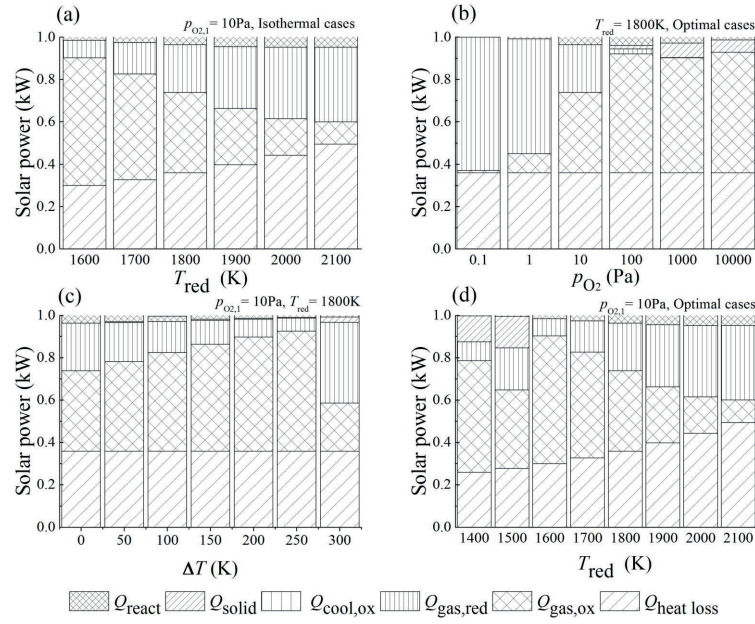


Figure B.3 – Energy balance for scheme (a) at 1 kW solar power input under various working conditions: (a) isothermal cases at  $p_{O_2,1} = 1$  Pa for varying  $T_{red}$ , (b) optimal cases at  $T_{red} = 1800$  K for varying  $p_{O_2,1}$ , (c) cases at  $p_{O_2,1} = 1$  Pa and  $T_{red} = 1800$  K for varying  $\Delta T$ , and (d) optimal cases at  $p_{O_2,1} = 1$  Pa for varying  $T_{red}$ .

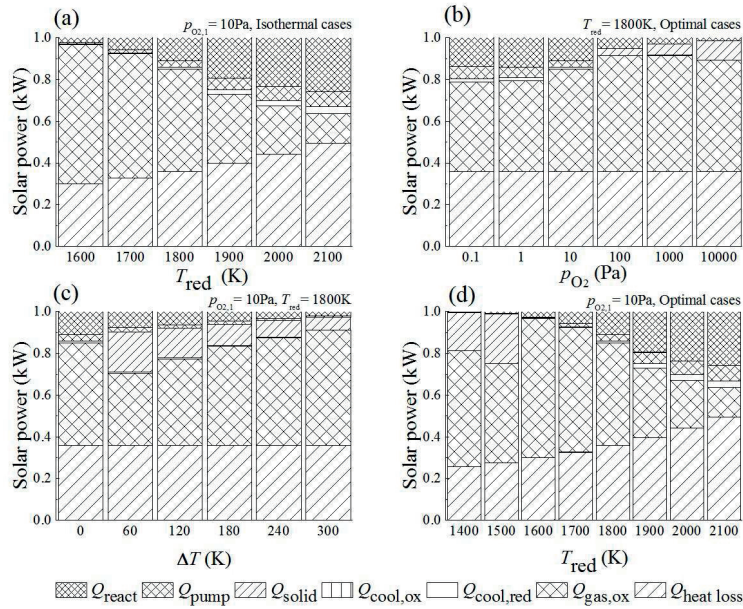


Figure B.4 – Energy balance for scheme (b) at 1 kW solar power input under various working conditions: (a) isothermal cases at  $p_{O_2,1} = 1$  Pa for varying  $T_{red}$ , (b) optimal cases at  $T_{red} = 1800$  K for varying  $p_{O_2,1}$ , (c) cases at  $p_{O_2,1} = 1$  Pa and  $T_{red} = 1800$  K for varying  $\Delta T$ , and (d) optimal cases at  $p_{O_2,1} = 1$  Pa for varying  $T_{red}$ .

## B.2. System performance behavior using ideal mixing model

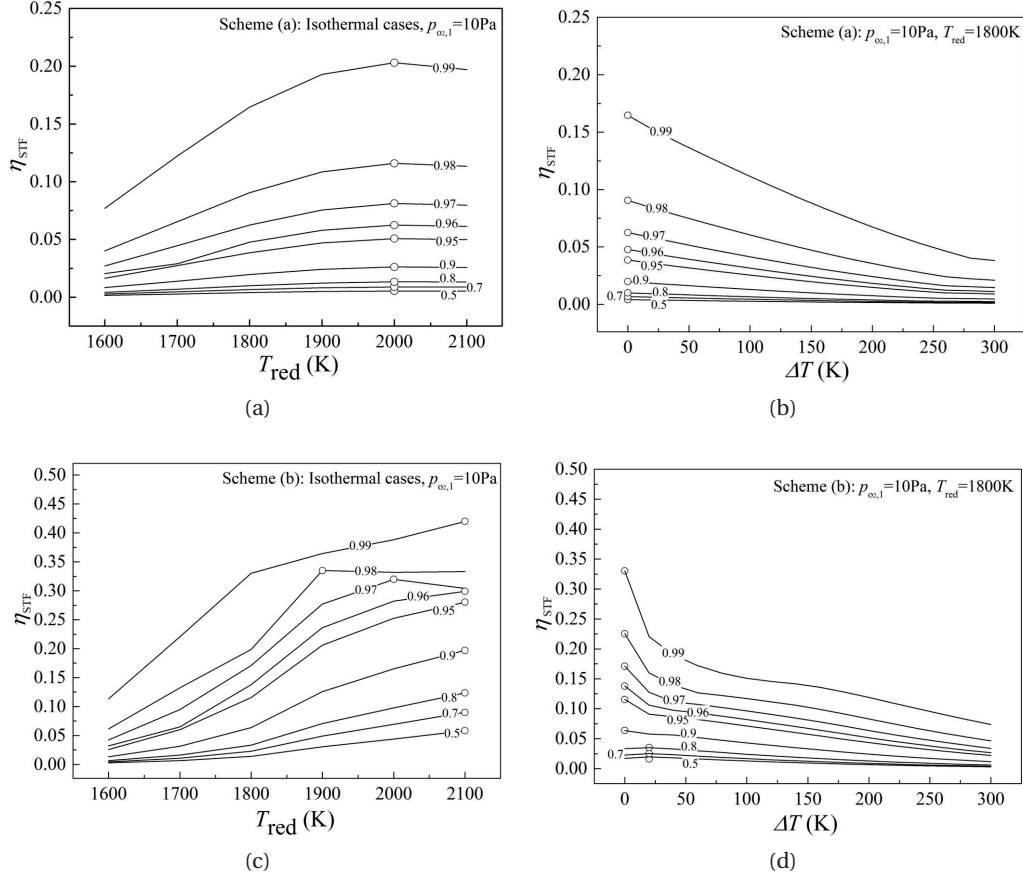


Figure B.5 – Solar-to-fuel efficiency for isothermal conditions at  $p_{O_2,1} = 10$  Pa and varying  $T_{red}$  and  $\epsilon_g$ , for (a) scheme (a), and (c) scheme (b); and non-isothermal conditions at  $p_{O_2,1} = 10$  Pa and  $T_{red} = 1800$  K for varying  $\Delta T$  and  $\epsilon_g$ . The maximal efficiencies for each  $\epsilon_g$  are marked by the dots.

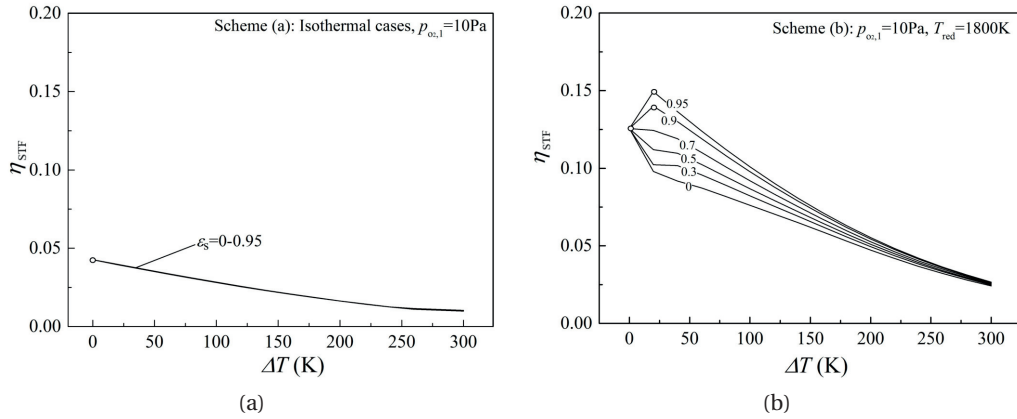


Figure B.6 – Solar-to-fuel efficiency as a function of  $\Delta T$  for various  $\epsilon_s$  at  $p_{O_2,1} = 10$  Pa and  $T_{red} = 1800$  K for (a) scheme (a), and (b) scheme (b). The optimal cases are indicated by the dots.



# C Supplementary data for tubular receiver modeling

## C.1 Effect of flux distribution at aperture

A Gaussian distribution of the incidence solar irradiation (equation 3.2) was assumed at the receiver aperture. The effect of the uniformity of the distribution was investigated by varying its standard deviation ( $\delta$ ).

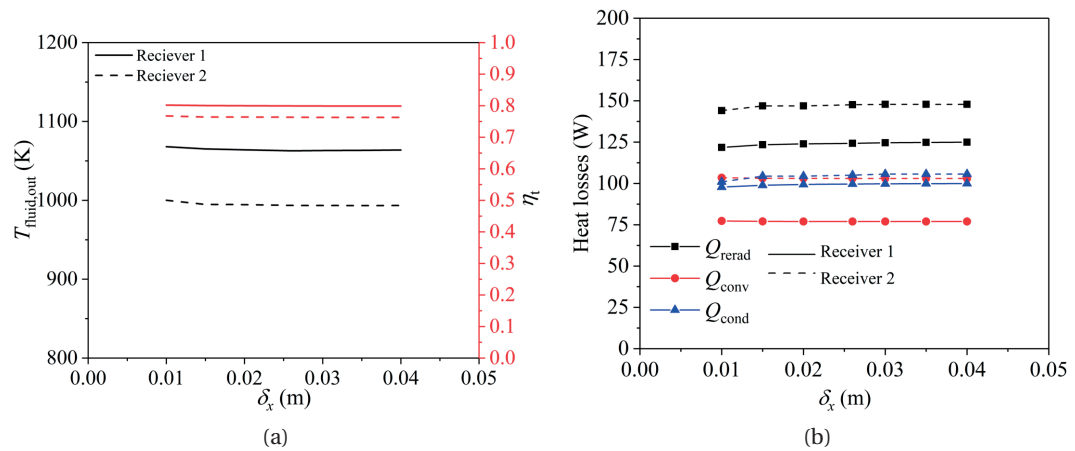


Figure C.1 – (a) Fluid outlet temperature (black lines) and solar-to-thermal efficiency (red lines) as a function of  $\delta_x$ , and (b) composition of heat losses for receiver 1 (solid lines) and receiver 2 (dotted lines).

## C.2 Effect of the thin wall thickness

The thin wall thickness was varied from  $10^{-3}$  to  $10^{-8}$  m with the maximum fluid outlet temperature difference below 1 K. The temperature variation was within 0.1 K when the wall thickness was smaller than  $10^{-5}$  m.

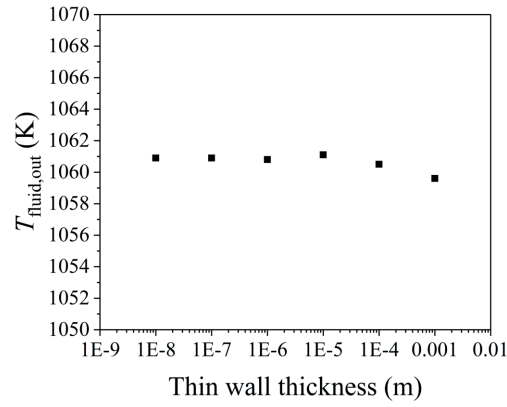


Figure C.2 – (a) Fluid outlet temperature (black lines) and solar-to-thermal efficiency (red lines) as a function of  $\delta_x$ , and (b) composition of heat losses for receiver 1 (solid lines) and receiver 2 (dotted lines).

## **D Supplementary data for the compact solar reactor experimentation**

## D.1 Technical drawing for the reactor frame

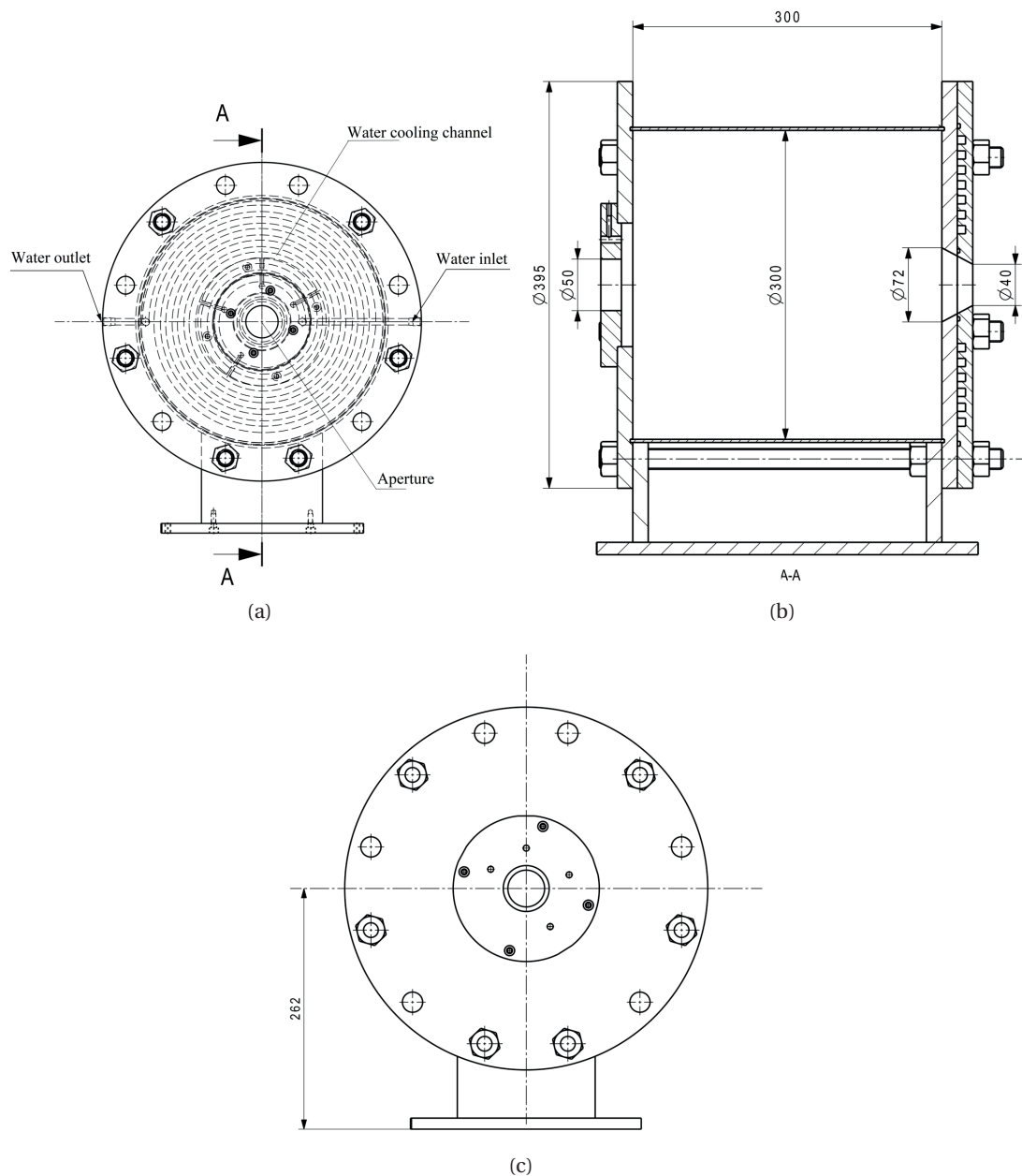


Figure D.1 – Technical drawings for the reactor steel frame: (a) the front view showing the water-cooled front and reactor aperture, (b) side view for A-A, and (c) back view of the reactor.



## D.2 Technical drawing for the bipolar plate

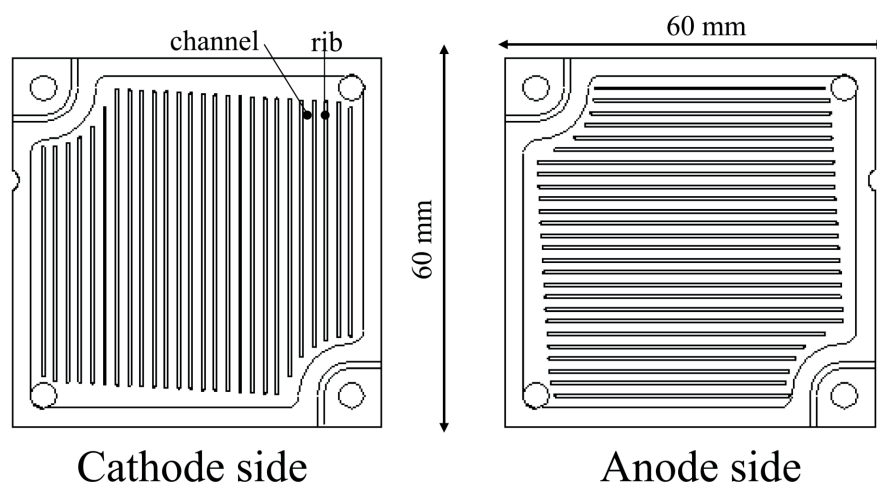


Figure D.2 – Bipolar plate design for both cathode and anode side with the channel width of 1.5 mm and the rib width of 0.5 mm (Almus AG).



# E Supplementary data for a novel integrated solar reactor concept model

## E.1 Thermal conductivities

Note that the thermal conductivities for composite electrodes were assumed to be independent of their solid compositions.  $x_i$  is the molar fraction of fluid species  $i$  and  $k_i$  is the temperature dependent thermal conductivity obtained by a free thermodynamic database, Coolprop [139].

Table E.1 – Thermal conductivities.

Parameters	Values
Conductivity of Ni-YSZ cathode [196]	5.84 W/m/K
Conductivity of LSM-YSZ anode [196]	1.86 W/m/K
Conductivity of YSZ electrolyte [196]	2.16 W/m/K
Conductivity of steel channel [161]	27.5 W/m/K
Conductivity of fluid mixture cathode [161]	$\sum_{i=\text{H}_2, \text{H}_2\text{O}, \text{CO}, \text{CO}_2, \text{CH}_4} x_i k_i$
Conductivity of fluid mixture anode [161]	$\sum_{i=\text{O}_2, \text{N}_2} x_i k_i$

## E.2 Heat capacities

Table E.2 – Heat capacities.

Parameters	Values
Heat capacity of Ni-YSZ cathode [196]	600 J/kg/K
Heat capacity of LSM-YSZ anode [196]	607 J/kg/K
Heat capacity of YSZ electrolyte [196]	400 J/kg/K
Heat capacity of steel channel [161]	200 J/kg/K
Heat capacity of fluid mixture cathode [161]	$\sum_{i=\text{H}_2, \text{H}_2\text{O}, \text{CO}, \text{CO}_2, \text{CH}_4} x_i c_{p,i}$
Heat capacity of fluid mixture anode [161]	$\sum_{i=\text{O}_2, \text{N}_2} x_i c_{p,i}$

## E.3 Fluid and solid densities

Table E.3 – Densities .

Parameters	Values
Density of Ni-YSZ cathode [196]	3030 kg/m <sup>3</sup>
Density of LSM-YSZ anode [196]	3310 kg/m <sup>3</sup>
Density of YSZ electrolyte [196]	5160 kg/m <sup>3</sup>
Density of steel channel [161]	6500 kg/m <sup>3</sup>
Density of fluid mixture cathode [161]	$\sum_{i=\text{H}_2, \text{H}_2\text{O}, \text{CO}, \text{CO}_2, \text{CH}_4} x_i \rho_i$
Density of fluid mixture anode [161]	$\sum_{i=\text{O}_2, \text{N}_2} x_i \rho_i$

## E.4 Intrinsic electrical conductivities

Table E.4 – Intrinsic electrical conductivities.

Parameters	Values
Conductivity of YSZ, $\sigma_{0,\text{YSZ}}$ [59]	$3.34 \cdot 10^4 \exp(-10300/T)$ , S/m
Conductivity of Ni, $\sigma_{0,\text{Ni}}$ [161]	$3.27 \cdot 10^6 - 1065.3T$ , S/m
Conductivity of LSM, $\sigma_{0,\text{LSM}}$ [161]	$(8.855 \cdot 10^7 / T) \exp(1082.5/T)$ , S/m
Conductivity of steel gas channel, $\sigma_{0,\text{ch}}$ [197]	$1.04 \cdot 10^7 - 0.005T$ , S/m

## E.5 Model parameters for the III-V PV cell

The temperature dependent bandgap is given by [198, 199]:

$$E_g = E_g(0K) - \frac{\alpha T^2}{T + \sigma} \quad (E.1)$$

where  $\alpha$  and  $\sigma$  are constants determined by the materials (see table E.5). The alloy semiconductors' band gap is calculated based on the compositions [200]:

$$E_g(A_{1-x}B_x) = (1-x)E_g(A) + xE_g(B) - x(1-x)p \quad (E.2)$$

where A and B are the two alloy compositions,  $x$  is the molar fraction of alloy B in the composition, and  $p$  is an alloy dependent parameter correcting the nonlinear behavior. The detailed parameters that used in the PV cell model are listed in table E.5. Note that the shunt resistances were neglected during the data fitting and the series resistances were considered identical for each sub-cell and hence a total series resistance is accounted,  $R_s = R_{s,1} + R_{s,2} + R_{s,3}$ .

Table E.5 – Parameters for the PV cell model [10]

Parameters	Sub-cell 1		Sub-cell 2		Sub-cell 3
Material	GaP	InP	GaAs	InAs	Ge
$E_g(298\text{ K}, \text{ eV})$	2.857	1.411	1.519	0.42	0.7437
$\alpha, \text{ eV/K}$	$5.771 \cdot 10^{-4}$	$3.63 \cdot 10^{-4}$	$5.405 \cdot 10^{-4}$	$4.19 \cdot 10^{-4}$	$4.774 \cdot 10^{-4}$
$\sigma, \text{ K}$	372	162	204	271	235
Alloy composition	$\text{In}_{0.49}\text{Ga}_{0.51}\text{P}$		$\text{In}_{0.01}\text{Ga}_{0.99}\text{As}$		Ge
$p, \text{ eV}$	1.018		1.192		0
$\kappa_1, \text{ A/m}^2$	$5.51 \cdot 10^{-3}$		$9.73 \cdot 10^{-3}$		$2.61 \cdot 10^{-3}$
$\kappa_2, \text{ A/m}^2$	$8.20 \cdot 10^{-3}$		$20.7 \cdot 10^{-3}$		$2.61 \cdot 10^{-3}$
$R_s, \Omega$	0.0370				
$A_{\text{PV,ref}}, \text{ m}^2$	0.49				

## E.6 SOEC model validations

Note: All other parameters which are not listed here are identical to the reference case conditions in section 5.8.2.

Table E.6 – SOEC model validation for hydrogen production [3, 11].

Parameters	Value
Operation temperatures	1173 K, 1223 K, and 1273 K
Operation pressure	1 bar
Pre-exponential factor for anode exchange,current density	$2.051 \cdot 10^9 \text{ A/m}^2$
Pre-exponential factor for cathode,exchange current density	$1.344 \cdot 10^{10} \text{ A/m}^2$
Activation energy for anode	$1.2 \cdot 10^5 \text{ J/mol}$
Activation energy for cathode	$1.0 \cdot 10^5 \text{ J/mol}$
Electrodes' porosity	0.48
Electrodes' tortuosity	5.4
Average pore radius	$1.07 \text{ } \mu\text{m}$
Average particle radius	$1.07 \text{ } \mu\text{m}$
Electrolyte thickness	$1000 \text{ } \mu\text{m}$
Cathode thickness	$100 \text{ } \mu\text{m}$
Anode thickness	$100 \text{ } \mu\text{m}$
Cathode inlet gas molar composition ( $\text{H}_2\text{O}/\text{H}_2$ )	0.6/0.4
Anode inlet gas molar composition ( $\text{N}_2/\text{O}_2$ )	0.79/0.21

Table E.7 – SOEC model validation for CO production [4].

Parameters	Value
Operation temperatures	1173 K
Operation pressure	1 bar
Exchange current density	3.25 A/cm <sup>2</sup>
Exchange current density	1.3 A/cm <sup>2</sup>
Activation energy for anode	1.2·10 <sup>5</sup> J/mol
Activation energy for cathode	1.0·10 <sup>5</sup> J/mol
Electrodes' porosity	0.35
Electrodes' tortuosity	3.25
Average pore radius	0.5 μm
Average particle radius	0.5 μm
Electrolyte thickness	10 μm
Cathode thickness	315 μm
Anode thickness	20 μm
Cathode inlet gas molar composition (CO <sub>2</sub> /CO)	0.5/0.5, 0.7/0.3
Anode inlet gas molar composition (N <sub>2</sub> /O <sub>2</sub> )	0.79/0.21

Table E.8 – SOEC model validation for syngas production [5].

Parameters	Value
Operation temperatures	1083 K
Operation pressure	1 bar
Pre-exponential factor for anode exchange current density	2.11·10 <sup>11</sup> A/m <sup>2</sup>
Pre-exponential factor for cathode exchange current density	5.275·10 <sup>10</sup> A/m <sup>2</sup>
Activation energy for anode	1.2·10 <sup>5</sup> J/mol
Activation energy for cathode	1.0·10 <sup>5</sup> J/mol
Electrodes' porosity	0.35
Electrodes' tortuosity	3.5
Average pore radius	1.0 μm
Average particle radius	2.5 μm
Electrolyte thickness	90 μm
Cathode thickness	40 μm
Anode thickness	40 μm
Cathode inlet gas molar composition (CO <sub>2</sub> /H <sub>2</sub> O/H <sub>2</sub> )	0.3/0.6/0.1
Anode inlet gas molar composition (N <sub>2</sub> /O <sub>2</sub> )	0.79/0.21

## E.7 2D CFD simulation for an insulated pipe

The pipe with 4 mm outer radius was insulated with alumina of 15 cm thickness. The thermal properties of the alumina was taken from [201]. The pipe inlet conditions were 1.555 g/min flow rate of water vapor at 1200 K. The predicted outlet temperature of the water vapor was 964 K (average over the outlet) and agreed well with our experimental data, which showed a 300 K temperature drop under the identical conditions.

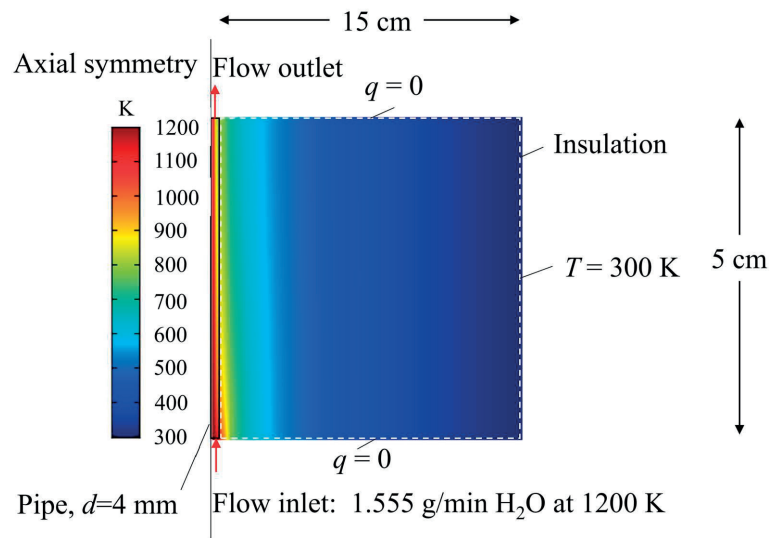


Figure E.1 – Modeling domain and temperature distribution (in K) for an insulated pipe (4 mm in diameter, 5 cm in length).



## E.8 Cell voltage partitioning with different flow arrangements

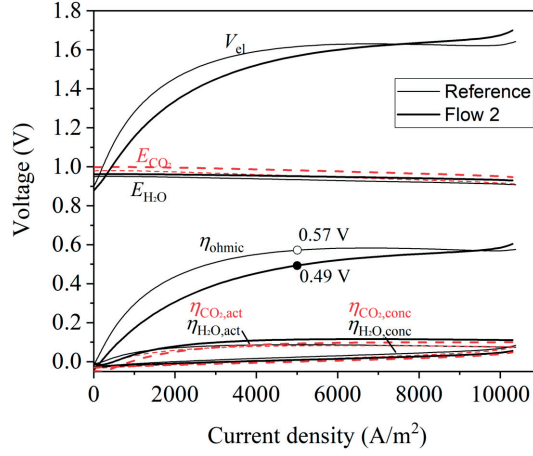


Figure E.2 – The cell voltage breakdown for the reference case and flow 2 with reference case in thin lines and the flow 2 in thick lines.

## E.9 Cathode inlet gas compositions

Operation current density for SOEC with different inlet gas compositions.

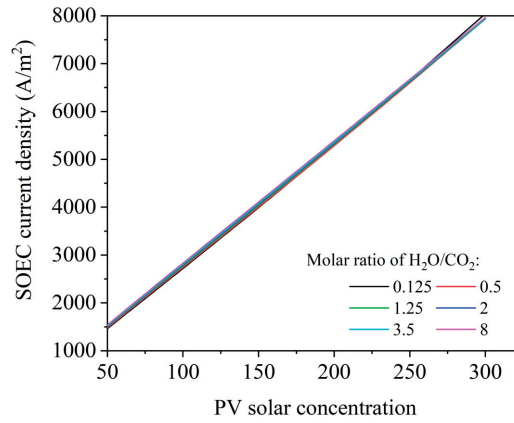


Figure E.3 – Operation current density of the SOEC under various PV solar concentrations and molar ratios of  $\text{H}_2\text{O}/\text{CO}_2$  at the cathode inlet for indirect connection cases.

## E.10 WGSR vs. eletrochemical reactions

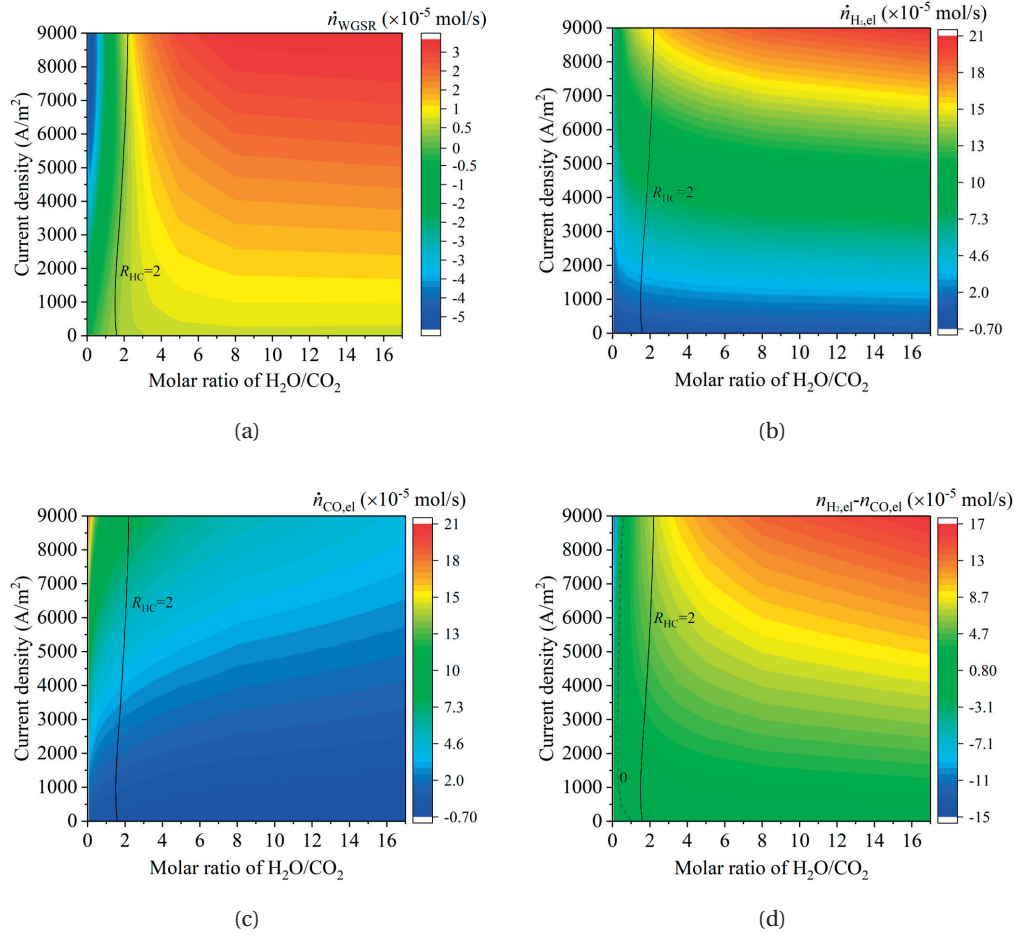


Figure E.4 – Contour plots for (a) the WGSR contributions, (b) electrochemical hydrogen generation, (c) electrochemical CO generation, and (d) the H<sub>2</sub> and CO production difference due to electrochemical reactions under various molar ratios of H<sub>2</sub>O/CO<sub>2</sub> at the cathode inlet and current densities. The  $R_{HC} = 2$  is indicated in solid black line and the dashed line is for the cases when the electrochemical generation of H<sub>2</sub> and CO are equal.

## E.11 SOEC temperature

SOEC average temperature under various cathode inlet ratios of  $\text{H}_2\text{O}/\text{CO}_2$ .

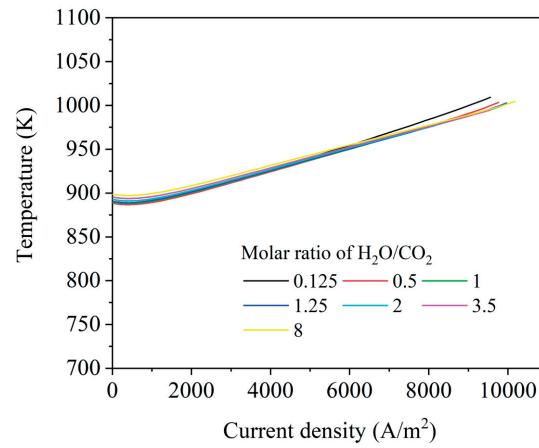


Figure E.5 – SOEC average temperature as a function of current density under various inlet ratios of  $\text{H}_2\text{O}/\text{CO}_2$  (differentiated by colors).



## Bibliography

- [1] Z. Zhan, W. Kobsiriphat, J. R. Wilson, M. Pillai, I. Kim, and S. a. Barnett, "Syngas production by coelectrolysis of CO<sub>2</sub>/H<sub>2</sub>O: the basis for a renewable energy cycle," *Energy & Fuels*, vol. 23, no. 6, pp. 3089–3096, 2009.
- [2] D. H. Lobón, E. Baglietto, L. Valenzuela, and E. Zarza, "Modeling direct steam generation in solar collectors with multiphase CFD," *Applied Energy*, vol. 113, pp. 1338–1348, jan 2014.
- [3] A. MOMMA, T. Kato, Y. KAGA, and S. Nagata, "Polarization behavior of high temperature solid oxide electrolysis cells (SOEC)," *Journal of the Ceramic Society of Japan*, vol. 105, no. 5, pp. 369–373, 1997.
- [4] G. Narasimhaiah and V. M. Janardhanan, "Modeling CO<sub>2</sub> electrolysis in solid oxide electrolysis cell," *Journal of Solid State Electrochemistry*, vol. 17, no. 8, pp. 2361–2370, 2013.
- [5] Q. X. Fu, J. Dailly, A. Brisse, and M. Zahid, "High-temperature CO<sub>2</sub> and H<sub>2</sub>O electrolysis with an electrolyte-supported solid oxide cell," *Solid Oxide Fuel Cells 12 (Sofc Xii)*, vol. 35, no. 1, pp. 2949–2956, 2011.
- [6] K. Nishioka, T. Takamoto, T. Agui, M. Kaneiwa, Y. Uraoka, and T. Fuyuki, "Evaluation of temperature characteristics of high-efficiency InGaP/InGaAs/Ge triple-junction solar cells under concentration," *Solar Energy Materials and Solar Cells*, vol. 85, no. 3, pp. 429–436, 2005.
- [7] P. Gilman and A. Dobos, "System Advisor Model, SAM 2011.12. 2: General Description," tech. rep., 2012.
- [8] J. R. Thome and J. E. Hajal, "Two-phase flow pattern map for evaporation in horizontal tubes: latest version," *Heat Transfer Engineering*, vol. 24, no. 6, pp. 3–10, 2003.
- [9] R. Suwanwarangkul, E. Croiset, E. Entchev, S. Charojrochkul, M. D. Pritzker, M. W. Fowler, P. L. Douglas, S. Chewathanakup, and H. Mahaudom, "Experimental and modeling study

## Bibliography

---

- of solid oxide fuel cell operating with syngas fuel,” *Journal of Power Sources*, vol. 161, no. 1, pp. 308–322, 2006.
- [10] G. Segev, G. Mittelman, and A. Kribus, “Equivalent circuit models for triple-junction concentrator solar cells,” *Solar Energy Materials and Solar Cells*, vol. 98, pp. 57–65, 2012.
- [11] M. Ni, M. K. H. Leung, and D. Y. C. Leung, “Parametric study of solid oxide steam electrolyzer for hydrogen production,” *International Journal of Hydrogen Energy*, vol. 32, pp. 2305–2313, 2007.
- [12] IEA, “Energy and Climate Change,” *World Energy Outlook Special Report*, pp. 1–200, 2015.
- [13] C. Perkins and A. W. Weimer, “Likely near-term solar-thermal water splitting technologies,” *International Journal of Hydrogen Energy*, vol. 29, pp. 1587–1599, dec 2004.
- [14] A. Steinfeld, “Solar thermochemical production of hydrogen—a review,” *Solar Energy*, vol. 78, pp. 603–615, may 2005.
- [15] W. Becker, R. Braun, M. Penev, and M. Melaina, “Production of Fischer–Tropsch liquid fuels from high temperature solid oxide co-electrolysis units,” *Energy*, vol. 47, no. 1, pp. 99–115, 2012.
- [16] M. E. Gálvez, P. G. Loutzenhiser, I. Hischer, and A. Steinfeld, “CO<sub>2</sub> splitting via two-step solar thermochemical cycles with Zn/ZnO and FeO/Fe<sub>3</sub>O<sub>4</sub> redox reactions: thermodynamic analysis,” *Energy & Fuels*, vol. 22, no. 5, pp. 3544–3550, 2008.
- [17] M. D. Allendorf, R. B. Diver, N. P. Siegel, and J. E. Miller, “Two-step water splitting using mixed-metal ferrites: thermodynamic analysis and characterization of synthesized materials,” *Energy & Fuels*, vol. 22, no. 6, pp. 4115–4124, 2008.
- [18] P. Furler, J. Scheffe, M. Gorbar, L. Moes, U. Vogt, and A. Steinfeld, “Solar Thermochemical CO<sub>2</sub> Splitting Utilizing a Reticulated Porous Ceria Redox System,” *Energy & Fuels*, vol. 26, no. 11, p. 121024073702001, 2012.
- [19] M. Roeb and C. Sattler, “Isothermal Water Splitting,” *Science*, vol. 341, no. 6145, pp. 470–471, 2013.
- [20] T. Pregger, D. Graf, W. Krewitt, C. Sattler, M. Roeb, and S. Möller, “Prospects of solar thermal hydrogen production processes,” *International Journal of Hydrogen Energy*, vol. 34, pp. 4256–4267, may 2009.
- [21] N. P. Siegel, J. E. Miller, I. Ermanoski, R. B. Diver, and E. B. Stechel, “Factors affecting the efficiency of solar driven metal oxide thermochemical cycles,” *Industrial & Engineering Chemistry Research*, vol. 52, no. 9, pp. 3276–3286, 2013.

- 
- [22] W. C. Chueh and S. M. Haile, "A thermochemical study of ceria: exploiting an old material for new modes of energy conversion and CO<sub>2</sub> mitigation," *Philosophical Transactions of the Royal Society a-Mathematical Physical and Engineering Sciences*, vol. 368, no. 1923, pp. 3269–3294, 2010.
- [23] J. Lapp, J. H. Davidson, W. Lipinski, and W. Lipiński, "Efficiency of two-step solar thermochemical non-stoichiometric redox cycles with heat recovery," *Energy*, vol. 37, no. 1, pp. 591–600, 2012.
- [24] I. Ermanoski, N. P. Siegel, and E. B. Stechel, "A New Reactor Concept for Efficient Solar-Thermochemical Fuel Production," *Journal of solar energy engineering*, vol. 135, p. 31002, 2013.
- [25] W. C. Chueh, C. Falter, M. Abbott, D. Scipio, P. Furler, S. M. Haile, and A. Steinfeld, "High-flux solar-driven thermochemical dissociation of CO<sub>2</sub> and H<sub>2</sub>O using nonstoichiometric ceria.," *Science (New York, N.Y.)*, vol. 330, pp. 1797–801, dec 2010.
- [26] P. Furler, J. R. Scheffe, and A. Steinfeld, "Syngas production by simultaneous splitting of H<sub>2</sub>O and CO<sub>2</sub> via ceria redox reactions in a high-temperature solar reactor," *Energy & Environmental Science*, vol. 5, no. 3, pp. 6098–6103, 2012.
- [27] B. J. Hathaway, R. Bala Chandran, A. C. Gladen, T. R. Chase, and J. H. Davidson, "Demonstration of a Solar Reactor for Carbon Dioxide Splitting via the Isothermal Ceria Redox Cycle and Practical Implications," *Energy and Fuels*, vol. 30, no. 8, pp. 6654–6661, 2016.
- [28] D. Marxer, P. Furler, M. Takacs, and A. Steinfeld, "Solar thermochemical splitting of CO<sub>2</sub> into separate streams of CO and O<sub>2</sub> with high selectivity, stability, conversion, and efficiency," *Energy Environ. Sci.*, vol. 10, no. 5, pp. 1142–1149, 2017.
- [29] R. Bader, L. J. Venstrom, J. H. Davidson, and W. Lipiński, "Thermodynamic Analysis of Isothermal Redox Cycling of Ceria for Solar Fuel Production," *Energy & Fuels*, vol. 27, pp. 5533–5544, may 2013.
- [30] S. Brendelberger and C. Sattler, "Concept analysis of an indirect particle-based redox process for solar-driven H<sub>2</sub>O/CO<sub>2</sub> splitting," *Solar Energy*, vol. 113, pp. 158–170, mar 2015.
- [31] M. NI, M. LEUNG, and D. LEUNG, "Technological development of hydrogen production by solid oxide electrolyzer cell (SOEC)," *International Journal of Hydrogen Energy*, vol. 33, pp. 2337–2354, may 2008.
- [32] S. Koumi Ngoh, L. Ayina Ohandja, A. Kemajou, and L. Monkam, "Design and simulation of hybrid solar high-temperature hydrogen production system using both solar photo-

## Bibliography

---

- voltaic and thermal energy,” *Sustainable Energy Technologies and Assessments*, vol. 7, pp. 279–293, 2014.
- [33] A. Houaijia, M. Roeb, N. Monnerie, and C. Sattler, “Concentrating Solar Systems as Heat and Electricity Source for a Solid Oxide Electrolyzer,” *International Journal of Energy Research*, 2015.
- [34] C. Graves, S. D. Ebbesen, M. Mogensen, and K. S. Lackner, “Sustainable hydrocarbon fuels by recycling CO<sub>2</sub> and H<sub>2</sub>O with renewable or nuclear energy,” *Renewable and Sustainable Energy Reviews*, vol. 15, no. 1, pp. 1–23, 2011.
- [35] C. K. Ho and B. D. Iverson, “Review of high-temperature central receiver designs for concentrating solar power,” *Renewable and Sustainable Energy Reviews*, vol. 29, pp. 835–846, jan 2014.
- [36] J. Pye, J. Coventry, F. Venn, J. Zapata, E. Abbasi, C. A. Asselineau, G. Burgess, G. Hughes, and W. Logie, “Experimental testing of a high-flux cavity receiver,” *AIP Conference Proceedings*, vol. 1850, 2017.
- [37] J. Martinek, C. Bingham, and A. W. Weimer, “Computational modeling and on-sun model validation for a multiple tube solar reactor with specularly reflective cavity walls. Part 1: Heat transfer model,” *Chemical Engineering Science*, vol. 81, pp. 298–310, oct 2012.
- [38] J. Martinek, C. Bingham, and A. W. Weimer, “Computational modeling of a multiple tube solar reactor with specularly reflective cavity walls. Part 2: Steam gasification of carbon,” *Chemical Engineering Science*, vol. 81, pp. 285–297, oct 2012.
- [39] R. Bala Chandran, R. M. De Smith, J. H. Davidson, R. B. Chandran, R. M. D. Smith, and J. H. Davidson, “Model of an integrated solar thermochemical reactor / reticulated ceramic foam heat exchanger for gas-phase heat recovery,” *International Journal of Heat and Mass Transfer*, vol. 81, pp. 404–414, feb 2015.
- [40] S. Haussener, D. Hirsch, C. Perkins, a. Weimer, a. Lewandowski, and a. Steinfeld, “Modeling of a Multitube High-Temperature Solar Thermochemical Reactor for Hydrogen Production,” *Journal of Solar Energy Engineering*, vol. 131, no. 2, p. 024503, 2009.
- [41] T. Melchior, C. Perkins, A. W. Weimer, and A. Steinfeld, “A cavity-receiver containing a tubular absorber for high-temperature thermochemical processing using concentrated solar energy,” *International Journal of Thermal Sciences*, vol. 47, pp. 1496–1503, nov 2008.



- 
- [42] T. Melchior and A. Steinfeld, "Radiative Transfer Within a Cylindrical Cavity With Diffusely/Specularly Reflecting Inner Walls Containing an Array of Tubular Absorbers," *Journal of Solar Energy Engineering*, vol. 130, no. 2, p. 021013, 2008.
- [43] M. Prakash, S. Kedare, and J. Nayak, "Investigations on heat losses from a solar cavity receiver," *Solar Energy*, vol. 83, pp. 157–170, feb 2009.
- [44] M. Lin and S. Haussener, "Techno-economic modeling and optimization of solar-driven hightemperature electrolysis systems," *Solar Energy*, vol. 155, pp. 1389–1402, 2017.
- [45] M. Lin and S. Haussener, "Solar fuel processing efficiency for ceria redox cycling using alternative oxygen partial pressure reduction methods," *Energy*, vol. 88, pp. 667–679, 2015.
- [46] M. Lin, J. Reinhold, N. Monnerie, and S. Haussener, "Modeling and design guidelines for direct steam generation solar receivers," *Applied Energy*, vol. 216, pp. 761–776, 2018.
- [47] M. Lin and S. Haussener, "An integrated concentrated solar fuel generator concept utilizing a tubular solid oxide electrolysis cell as the solar absorber," *In preparation*, 2018.
- [48] J. Sanz-Bermejo, J. Muñoz-Antón, J. Gonzalez-Aguilar, and M. Romero, "Optimal integration of a solid-oxide electrolyser cell into a direct steam generation solar tower plant for zero-emission hydrogen production," *Applied Energy*, vol. 131, pp. 238–247, oct 2014.
- [49] A. A. AlZahrani and I. Dincer, "Design and analysis of a solar tower based integrated system using high temperature electrolyzer for hydrogen production," *International Journal of Hydrogen Energy*, no. 2016, pp. 1–15, 2016.
- [50] J. Holladay, J. Hu, D. King, and Y. Wang, "An overview of hydrogen production technologies," *Hydrogen Production - Selected papers from the Hydrogen Production Symposium at the American Chemical Society 234th National Meeting & Exposition, August 19-23, 2007, Boston, MA, USA*, vol. 139, no. 4, pp. 244–260, 2009.
- [51] B. E. Săgol, U. Seidel, N. Szabó, K. Schwarzburg, and T. Hannappel, "Basic concepts and interfacial aspects of high-efficiency III-V multijunction solar cells," *CHIMIA International Journal for Chemistry*, vol. 61, no. 12, pp. 775–779, 2007.
- [52] J. Koh, D. Yoon, and C. H. Oh, "Simple Electrolyzer Model Development for High-Temperature Electrolysis System Analysis Using Solid Oxide Electrolysis Cell," *Journal of Nuclear Science and Technology*, vol. 47, no. 7, pp. 599–607, 2010.

## Bibliography

---

- [53] a. Bertei and C. Nicolella, "Common inconsistencies in modeling gas transport in porous electrodes: The dusty-gas model and the Fick law," *Journal of Power Sources*, vol. 279, pp. 133–137, 2015.
- [54] Y. Vural, L. Ma, D. B. Ingham, and M. Pourkashanian, "Comparison of the multicomponent mass transfer models for the prediction of the concentration overpotential for solid oxide fuel cell anodes," *Journal of Power Sources*, vol. 195, no. 15, pp. 4893–4904, 2010.
- [55] M. Ni, "An electrochemical model for syngas production by co-electrolysis of H<sub>2</sub>O and CO<sub>2</sub>," *Journal of Power Sources*, vol. 202, pp. 209–216, 2012.
- [56] D. E. Ridler and M. V. Twigg, *Steam reforming*, vol. 2. Wolfe Publishing Ltd: Cleveland, UK, 1989.
- [57] B. A. Haberman and J. B. Young, "Three-dimensional simulation of chemically reacting gas flows in the porous support structure of an integrated-planar solid oxide fuel cell," *International Journal of Heat and Mass Transfer*, vol. 47, no. 17, pp. 3617–3629, 2004.
- [58] F. J. Salzano, G. Skaperdas, and A. Mezzina, "Water vapor electrolysis at high temperature: systems considerations and benefits," *International journal of hydrogen energy*, vol. 10, no. 12, pp. 801–809, 1985.
- [59] J. R. Ferguson, J. M. Fiard, and R. Herbin, "Three-dimensional numerical simulation for various geometries of solid oxide fuel cells," *Journal of Power Sources*, vol. 58, no. 2, pp. 109–122, 1996.
- [60] V. Menon, Q. Fu, V. M. Janardhanan, and O. Deutschmann, "A model-based understanding of solid-oxide electrolysis cells (SOECs) for syngas production by H<sub>2</sub>O/CO<sub>2</sub> co-electrolysis," *Journal of Power Sources*, vol. 274, pp. 768–781, 2015.
- [61] L. F. Shampine, J. Kierzenka, and M. W. Reichelt, "Solving boundary value problems for ordinary differential equations in MATLAB with bvp4c," *Tutorial notes*, pp. 437–448, 2000.
- [62] B. L. Kistler, "A user's manual for DELSOL3: A computer code for calculating the optical performance and optimal system design for solar thermal central receiver plants," tech. rep., 1986.
- [63] T. Neises and M. J. Wagner, "Simulation of Direct Steam Power Tower Concentrated Solar Plant," *ASME 2012 6th International Conference on Energy Sustainability, Parts A and B*, pp. 499–507, 2012.

- 
- [64] M. J. Wagner, *Simulation and predictive performance modeling of utility-scale central receiver system power plants*. University of Wisconsin–Madison, 2008.
- [65] J. R. Howell, R. Siegel, M. Pinar Mengüç, and M. P. M. John R. Howell, Robert Siegel, *Thermal Radiation Heat Transfer*, vol. 1. 2010.
- [66] J. Sanz-Bermejo, V. Gallardo-Natividad, J. Gonzalez-Aguilar, and M. Romero, “Comparative System Performance Analysis of Direct Steam Generation Central Receiver Solar Thermal Power Plants in Megawatt Range,” *Journal of Solar Energy Engineering*, vol. 136, no. 1, p. 011028, 2014.
- [67] Y. A. Cengel, M. A. Boles, and M. Kanoğlu, *Thermodynamics: an engineering approach*, vol. 5. McGraw-Hill New York, 2002.
- [68] W. De Soto, S. a. Klein, and W. a. Beckman, “Improvement and validation of a model for photovoltaic array performance,” *Solar Energy*, vol. 80, pp. 78–88, 2006.
- [69] J. A. Duffie and W. A. Beckman, *Solar Engineering of Thermal Processes: Fourth Edition*. 2013.
- [70] F. Bizzarri, M. Bongiorno, A. Brambilla, and G. Gruosso, “Model of Photovoltaic Power Plants for Performance Analysis and Production Forecast,” vol. 4, no. 2, pp. 278–285, 2013.
- [71] T. L. Gibson and N. a. Kelly, “Optimization of solar powered hydrogen production using photovoltaic electrolysis devices,” *International Journal of Hydrogen Energy*, vol. 33, no. 21, pp. 5931–5940, 2008.
- [72] J. H. Lienhard, *A heat transfer textbook*, vol. 108. Courier Corporation, 2013.
- [73] G. Xu, F. Liang, Y. Yang, Y. Hu, K. Zhang, and W. Liu, “An improved CO<sub>2</sub> separation and purification system based on cryogenic separation and distillation theory,” *Energies*, vol. 7, no. 5, pp. 3484–3502, 2014.
- [74] M. T. Ho, G. W. Allinson, and D. E. Wiley, “Reducing the Cost of CO<sub>2</sub> Capture from Flue Gases Using Pressure Swing Adsorption,” *Industrial & Engineering Chemistry Research*, vol. 47, no. 14, pp. 4883–4890, 2008.
- [75] M. Jamel, a. Abd Rahman, and a.H. Shamsuddin, “Advances in the integration of solar thermal energy with conventional and non-conventional power plants,” *Renewable and Sustainable Energy Reviews*, vol. 20, pp. 71–81, apr 2013.
- [76] Q. Fu, C. Mabilat, M. Zahid, A. Brisse, and L. Gautier, “Syngas production via high-temperature steam/CO<sub>2</sub> co-electrolysis: an economic assessment,” *Energy & Environmental Science*, vol. 3, no. 10, p. 1382, 2010.

## Bibliography

---

- [77] D. G. Milobar, J. J. Hartvigsen, and S. Elangovan, "A techno-economic model of a solid oxide electrolysis system," *Faraday Discuss.*, vol. 182, pp. 329–339, 2015.
- [78] D. Ferrero, M. Gamba, A. Lanzini, and M. Santarelli, "Power-to-Gas Hydrogen: Techno-economic Assessment of Processes towards a Multi-purpose Energy Carrier," *Energy Procedia*, vol. 101, no. September, pp. 50–57, 2016.
- [79] G. Saur, *Wind-to-hydrogen project: electrolyzer capital cost study*. Citeseer, 2008.
- [80] C. Singer, R. Buck, R. Pitz-Paal, and H. Muller-Steinhagen, "Assessment of Solar Power Tower Driven Ultrasupercritical Steam Cycles Applying Tubular Central Receivers With Varied Heat Transfer Media," *Journal of Solar Energy Engineering*, vol. 132, no. 4, p. 041010, 2010.
- [81] A. Meier, N. Gremaud, and A. Steinfeld, "Economic evaluation of the industrial solar production of lime," *Energy conversion and management*, vol. 46, no. 6, pp. 905–926, 2005.
- [82] D. B. Myers, G. D. Ariff, B. D. James, J. S. Lettow, C. E. Thomas, and R. C. Kuhn, "Cost and performance comparison of stationary hydrogen fueling appliances," *The Hydrogen Program Office*, 2002.
- [83] R. Rivera-Tinoco, C. Mansilla, and C. Bouallou, "Competitiveness of hydrogen production by High Temperature Electrolysis: Impact of the heat source and identification of key parameters to achieve low production costs," *Energy Conversion and Management*, vol. 51, pp. 2623–2634, dec 2010.
- [84] M. A. Laguna-Bercero, "Recent advances in high temperature electrolysis using solid oxide fuel cells: A review," *Journal of Power Sources*, vol. 203, pp. 4–16, apr 2012.
- [85] F. M. Sapountzi, J. M. Gracia, C. K.-J. Weststrate, H. O. Fredriksson, and J. H. Niemantsverdriet, "Electrocatalysts for the generation of hydrogen, oxygen and synthesis gas," *Progress in Energy and Combustion Science*, vol. 58, pp. 1–35, 2017.
- [86] Z. Zhan, W. Kobsiriphat, J. R. Wilson, M. Pillai, I. Kim, and S. A. Barnett, "Syngas production by coelectrolysis of CO<sub>2</sub>/H<sub>2</sub>O: the basis for a renewable energy cycle," *Energy & Fuels*, vol. 23, no. 6, pp. 3089–3096, 2009.
- [87] R. Knibbe, M. L. Traulsen, A. Hauch, S. D. Ebbesen, and M. Mogensen, "Solid oxide electrolysis cells: Degradation at high current densities," *Journal of the Electrochemical Society*, vol. 157, no. 8, pp. B1209–B1217, 2010.
- [88] Q. Fang, L. Blum, and N. H. Menzler, "Performance and Degradation of Solid Oxide Electrolysis Cells in Stack," *Journal of the Electrochemical Society*, vol. 162, no. 8, pp. F907–F912, 2015.

- 
- [89] M. R. Shaner, H. A. Atwater, N. S. Lewis, and E. W. McFarland, "A comparative technoeconomic analysis of renewable hydrogen production using solar energy," *Energy Environ. Sci.*, vol. 9, no. 7, pp. 2354–2371, 2016.
- [90] A. Abanades, C. Rubbia, and D. Salmieri, "Thermal cracking of methane into hydrogen for a CO<sub>2</sub>-free utilization of natural gas," *International Journal of Hydrogen Energy*, vol. 38, no. 20, pp. 8491–8496, 2013.
- [91] J. E. O'Brien, M. G. McKellar, C. M. Stoots, J. S. Herring, and G. L. Hawkes, "Parametric study of large-scale production of syngas via high-temperature co-electrolysis," *International Journal of Hydrogen Energy*, vol. 34, no. 9, pp. 4216–4226, 2009.
- [92] S. Abanades and G. Flamant, "Thermochemical hydrogen production from a two-step solar-driven water-splitting cycle based on cerium oxides," *Solar Energy*, vol. 80, no. 12, pp. 1611–1623, 2006.
- [93] M. Lundberg, "Model calculations on some feasible two-step water splitting processes," *International journal of hydrogen energy*, vol. 18, no. 5, pp. 369–376, 1993.
- [94] R. J. Panlener, R. N. Blumenthal, and J. E. Garnier, "A thermodynamic study of nonstoichiometric cerium dioxide," *Journal of Physics and Chemistry of Solids*, vol. 36, no. 11, pp. 1213–1222, 1975.
- [95] I. Riess and M. Ricken, "On the specific heat of nonstoichiometric ceria," *Journal of Solid State Chemistry*, vol. 57, no. 3, pp. 314–322, 1985.
- [96] W. C. Chueh and S. M. Haile, "Ceria as a thermochemical reaction medium for selectively generating syngas or methane from H<sub>2</sub>O and CO<sub>2</sub>," *ChemSusChem*, vol. 2, no. 8, pp. 735–739, 2009.
- [97] B. C. Pai, G. Ramani, R. M. Pillai, and K. G. Satyanarayana, "Role of magnesium in cast aluminium alloy matrix composites," *Journal of materials science*, vol. 30, no. 8, pp. 1903–1911, 1995.
- [98] T. Dulski, *Trace elemental analysis of metals: methods and techniques*. Routledge, 2017.
- [99] P. Charvin, A. Stéphane, L. Florent, and F. Gilles, "Analysis of solar chemical processes for hydrogen production from water splitting thermochemical cycles," *Energy conversion and management*, vol. 49, pp. 1547–1556, jun 2008.
- [100] F. Cherubini, M. Raugei, and S. Ulgiati, "LCA of magnesium production," *Resources, Conservation and Recycling*, vol. 52, pp. 1093–1100, jul 2008.

## Bibliography

---

- [101] E. S. Gratz, X. Guan, J. D. Milshtein, U. B. Pal, and A. C. Powell, "Mitigating Electronic Current in Molten Flux for the Magnesium SOM Process," *Metallurgical and Materials Transactions B*, vol. 45, pp. 1–12, mar 2014.
- [102] J. B. Rawlings and J. G. Ekerdt, *Chemical reactor analysis and design fundamentals*. Nob Hill Pub, Llc, 2002.
- [103] T. Kodama and N. Gokon, "Thermochemical cycles for high-temperature solar hydrogen production," *Chemical Reviews*, vol. 107, no. 10, pp. 4048–4077, 2007.
- [104] F. G. Kerry, *Industrial gas handbook: gas separation and purification*. CRC Press, 2007.
- [105] M. Rydén and M. Arjmand, "Continuous hydrogen production via the steam-iron reaction by chemical looping in a circulating fluidized-bed reactor," *International Journal of Hydrogen Energy*, vol. 37, no. 6, pp. 4843–4854, 2012.
- [106] J. Martinek, R. Viger, and A. W. Weimer, "Transient simulation of a tubular packed bed solar receiver for hydrogen generation via metal oxide thermochemical cycles," *Solar Energy*, vol. 105, pp. 613–631, 2014.
- [107] C.-K. Yang, Y. Yamazaki, A. Aydin, and S. M. Haile, "Thermodynamic and kinetic assessments of strontium-doped lanthanum manganite perovskites for two-step thermochemical water splitting," *Journal of Materials Chemistry A*, vol. 2, p. 13612, jul 2014.
- [108] L. Nalbandian, A. Evdou, and V. Zaspalis, "La<sub>1-x</sub>Sr<sub>x</sub>MO<sub>3</sub> (M = Mn, Fe) perovskites as materials for thermochemical hydrogen production in conventional and membrane reactors," *International Journal of Hydrogen Energy*, vol. 34, pp. 7162–7172, sep 2009.
- [109] A. Evdou, L. Nalbandian, and V. T. Zaspalis, "Perovskite membrane reactor for continuous and isothermal redox hydrogen production from the dissociation of water," *Journal of Membrane Science*, vol. 325, pp. 704–711, dec 2008.
- [110] V. K. Dhir, "Mechanistic Prediction of Nucleate Boiling Heat Transfer—Achievable or a Hopeless Task?," *Journal of Heat Transfer*, vol. 128, no. 1, p. 1, 2006.
- [111] G. Son, V. K. Dhir, and N. Ramanujapu, "Dynamics and heat transfer associated with a single bubble during nucleate boiling on a horizontal surface," *Journal of Heat Transfer*, vol. 121, no. 3, pp. 623–631, 1999.
- [112] S. Das and H. Puneekar, "On Development of a Semi-Mechanistic Wall Boiling Model," *ASME 2013 International Mechanical Engineering Congress and Exposition*, no. 34, pp. V08BT09A075–V08BT09A075, 2013.

- 
- [113] S. Abishek, A. J. King, and R. Narayanaswamy, "Computational analysis of two-phase flow and heat transfer in parallel and counter flow double-pipe evaporators," *International Journal of Heat and Mass Transfer*, vol. 104, pp. 615–626, 2017.
- [114] E. Krepper, B. Končar, and Y. Egorov, "CFD modelling of subcooled boiling—Concept, validation and application to fuel assembly design," *Nuclear Engineering and Design*, vol. 237, pp. 716–731, apr 2007.
- [115] H. Li, S. A. Vasquez, H. Puneekar, and R. Muralikrishnan, "Prediction of Boiling and Critical Heat Flux Using an Eulerian Multiphase Boiling Model," in *Volume 6: Fluids and Thermal Systems; Advances for Process Industries, Parts A and B*, pp. 463–476, ASME, 2011.
- [116] G. P. Celata, K. Mishima, and G. Zummo, "Critical heat flux prediction for saturated flow boiling of water in vertical tubes," *International Journal of Heat and Mass Transfer*, vol. 44, no. 22, pp. 4323–4331, 2001.
- [117] C. Lifante, T. Frank, and A. Burns, "Wall boiling modeling extension towards critical heat flux," *Nureth-15*, 2013.
- [118] N. Kurul and M. Z. Podowski, "On the Modeling of Multidimensional Effects in Boiling Channels," in *27th National Heat Transfer Conference*, pp. 21–26, 1991.
- [119] J. C. Jo, W. S. Kim, C.-Y. Choi, and Y. K. Lee, "Numerical Simulation of Subcooled Flow Boiling Heat Transfer in Helical Tubes," *Journal of Pressure Vessel Technology*, vol. 131, no. 1, p. 011305, 2009.
- [120] J. R. Thome, "Engineering data book III," *Wolverine Tube Inc*, vol. 2010, 2004.
- [121] Z. Liu and R. Winterton, "A general correlation for saturated and subcooled flow boiling in tubes and annuli, based on a nucleate pool boiling equation," *International Journal of Heat and Mass Transfer*, vol. 34, pp. 2759–2766, nov 1991.
- [122] L. Cheng, G. Ribatski, and J. R. Thome, "Two-phase flow patterns and flow-pattern maps: fundamentals and applications," *Applied Mechanics Reviews*, vol. 61, no. 5, p. 50802, 2008.
- [123] G. A. Roth and F. Aydogan, "Theory and implementation of nuclear safety system codes - Part II: System code closure relations, validation, and limitations," *Progress in Nuclear Energy*, vol. 76, pp. 55–72, 2014.
- [124] F. Escanes, C. D. Pérez-Segarra, and A. Oliva, "Numerical simulation of capillary-tube expansion devices," *International Journal of Refrigeration*, vol. 18, no. 2, pp. 113–122, 1995.



## Bibliography

---

- [125] O. García-Valladares, C. D. Pérez-Segarra, and A. Oliva, "Numerical simulation of capillary tube expansion devices behaviour with pure and mixed refrigerants considering metastable region. Part I: Mathematical formulation and numerical model," *Applied Thermal Engineering*, vol. 22, no. 2, pp. 173–182, 2002.
- [126] D. Colorado, J. A. Hernández, O. García-Valladares, A. Huicochea, and J. Siqueiros, "Numerical simulation and experimental validation of a helical double-pipe vertical condenser," *Applied Energy*, vol. 88, no. 6, pp. 2136–2145, 2011.
- [127] J. R. Thome, D. Favrat, N. Kattan, J. R. Thome, and D. Favrat, "Flow boiling in horizontal tubes: Part 1—Development of a diabatic two-phase flow pattern map," *Journal of Heat Transfer*, vol. 120, no. 1, pp. 140–147, 1998.
- [128] J. Martinek and Z. Ma, "Granular Flow and Heat-Transfer Study in a Near-Blackbody Enclosed Particle Receiver," in *Journal of Solar Energy Engineering*, vol. 137, p. 051008, American Society of Mechanical Engineers, 2015.
- [129] S. Haussener, D. Thomey, M. Roeb, and A. Steinfeld, "Multi-scale modelling of a solar reactor for the high-temperature step of a sulphur-iodine-based water splitting cycle," in *ASME 2012 Heat Transfer Summer Conference collocated with the ASME 2012 Fluids Engineering Division Summer Meeting and the ASME 2012 10th International Conference on Nanochannels, Microchannels, and Minichannels*, pp. 287–296, American Society of Mechanical Engineers, 2012.
- [130] K. Reddy, T. S. Vikram, and G. Veershetty, "Combined heat loss analysis of solar parabolic dish – modified cavity receiver for superheated steam generation," *Solar Energy*, 2015.
- [131] J. Zhu, K. Wang, H. Wu, D. Wang, J. Du, and A. G. Olabi, "Experimental investigation on the energy and exergy performance of a coiled tube solar receiver," *Applied Energy*, vol. 156, pp. 519–527, 2015.
- [132] J. I. Zapata, C.-A. Asselineau, J. Pye, M. Kaufer, and G. Hughes, "An integrated optical and thermal model of cavity receivers for paraboloidal dish concentrators," in *Proc. 2014 Asia-Pacific Solar Research Conference*, 2014.
- [133] A. Faghri and Y. Zhang, *Transport phenomena in multiphase systems*. Academic Press, 2006.
- [134] a. Steinfeld and M. Schubnell, "Optimum aperture size and operating temperature of a solar cavity-receiver," *Solar Energy*, vol. 50, pp. 19–25, jan 1993.
- [135] S. Paitoonsurikarn and K. Lovegrove, "Numerical Investigation of Natural Convection Loss in Cavity-Type Solar Receivers in Solar Dish Applications," *Solar 2002-Australian and New Zealand Solar Energy Society*, vol. 133, no. May 2011, p. 6, 2002.



- 
- [136] U. Leibfried and J. Ortjohann, "Convective Heat Loss from Upward and Downward-Facing Cavity Solar Receivers: Measurements and Calculations," *Journal of Solar Energy Engineering*, vol. 117, no. 2, p. 75, 1995.
- [137] I. Hischier, D. Hess, W. Lipinski, M. Modest, and A. Steinfeld, "Heat Transfer Analysis of a Novel Pressurized Air Receiver for Concentrated Solar Power via Combined Cycles," *Journal of Thermal Science and Engineering Applications*, vol. 1, no. 4, p. 041002, 2009.
- [138] L. Friedel, "Improved friction pressure drop correlations for horizontal and vertical two-phase pipe flow," in *European two-phase flow group meeting, Paper E*, vol. 2, p. 1979, 1979.
- [139] I. H. Bell, J. Wronski, S. Quoilin, and V. Lemort, "Pure and pseudo-pure fluid thermophysical property evaluation and the open-source thermophysical property library CoolProp," *Industrial & engineering chemistry research*, vol. 53, no. 6, pp. 2498–2508, 2014.
- [140] D. Steiner, "Heat Transfer to Boiling Saturated Liquids (VDI-Wärmeatlas)," *VDI Heat Atlas. VDI-Gesellschaft Verfahrenstechnik und Chemieingenieurwesen (GCV), Düsseldorf, Germany (JW Fullarton, translator)*, 1993.
- [141] S. Z. Rouhani and E. Axelsson, "Calculation of void volume fraction in the subcooled and quality boiling regions," *International Journal of Heat and Mass Transfer*, vol. 13, no. 2, pp. 383–393, 1970.
- [142] M. a. Woldesemayat and A. J. Ghajar, "Comparison of void fraction correlations for different flow patterns in horizontal and upward inclined pipes," *International Journal of Multiphase Flow*, vol. 33, no. 4, pp. 347–370, 2007.
- [143] Y. Taitel, A. E. Dukler, D. Harrison, and F. Particles, "A model for predicting flow regime transitions in horizontal and near horizontal gas-liquid flow," *AIChE Journal*, vol. 22, no. 1, pp. 47–55, 1976.
- [144] A. M. Elsafi, "On thermo-hydraulic modeling of direct steam generation," *Solar Energy*, vol. 120, pp. 636–650, 2015.
- [145] M. Cooper, "Heat flow rates in saturated nucleate pool boiling – a wide- ranging examination using reduced properties," *Advances in Heat Transfer*, vol. 16, pp. 157–239, 1984.
- [146] D. C. Groeneveld, "Post-dryout heat transfer at reactor operating conditions," tech. rep., 1973.

## Bibliography

---

- [147] D. Biberg, "Explicit approximation for the wetted angle in two-phase stratified pipe flow," *Canadian Journal Of Chemical Engineering*, vol. 77, no. 3, pp. 1221–1224, 1999.
- [148] F. W. Dittus and L. M. K. Boelter, "Heat transfer in automobile radiators of the tubular type," *International Communications in Heat and Mass Transfer*, vol. 12, no. 1, pp. 3–22, 1985.
- [149] N. Kattan, J. R. Thome, and D. Favrat, "Flow Boiling in Horizontal Tubes : Part 3 — Development of a New Heat Transfer Model Based on Flow Pattern," *Journal of Heat Transfer*, vol. 120, no. 1, pp. 156–165, 1998.
- [150] VDI-Gesellschaft, *VDI Heat Atlas*, vol. 1. 2015.
- [151] K. Gungor and R. Winterton, "A general correlation for flow boiling in tubes and annuli," *International Journal of Heat and Mass Transfer*, vol. 29, pp. 351–358, mar 1986.
- [152] R. Gupta, R. K. Wanchoo, and T. R. Jafar Ali, "Laminar flow in helical coils: A parametric study," in *Industrial and Engineering Chemistry Research*, vol. 50, pp. 1150–1157, 2011.
- [153] S. Kakaç, R. K. Shah, and W. Aung, *Handbook of single-phase convective heat transfer*. Wiley New York et al., 1987.
- [154] A. Fluent, "Ansys fluent," *Academic Research. Release*, vol. 17.2, 2016.
- [155] P. Aguiar, C. S. Adjiman, and N. P. Brandon, "Anode-supported intermediate temperature direct internal reforming solid oxide fuel cell. I: Model-based steady-state performance," *Journal of Power Sources*, vol. 138, no. 1-2, pp. 120–136, 2004.
- [156] R. Bader, S. Haussener, and W. Lipiński, "Optical Design of Multisource High-Flux Solar Simulators," *Journal of Solar Energy Engineering*, vol. 137, no. 2, p. 21012, 2015.
- [157] J. E. O'Brien, "Thermodynamics and Transport Phenomena in High Temperature Steam Electrolysis Cells," *Journal of Heat Transfer*, vol. 134, no. 3, p. 031017, 2012.
- [158] G. Levêque, R. Bader, W. Lipiński, and S. Haussener, "Experimental and numerical characterization of a new 45 kWel multisource high-flux solar simulator," *Optics Express*, vol. 24, no. 22, pp. 1360–1373, 2016.
- [159] E. Guillot, I. Alxneit, J. Ballestrin, J. L. Sans, and C. Willsh, "Comparison of 3 heat flux gauges and a water calorimeter for concentrated solar irradiance measurement," in *Energy Procedia*, vol. 49, pp. 2090–2099, 2013.
- [160] M. T. Balta, O. Kizilkan, and F. Yilmaz, "Energy and exergy analyses of integrated hydrogen production system using high temperature steam electrolysis," *International Journal of Hydrogen Energy*, pp. 1–10, 2016.

- 
- [161] Y. Luo, Y. Shi, W. Li, and N. Cai, "Comprehensive modeling of tubular solid oxide electrolysis cell for co-electrolysis of steam and carbon dioxide," *Energy*, vol. 70, pp. 420–434, 2014.
- [162] J. Deseure, J.-M. Klein, Y. Bultel, and L. Dessemond, "3-D Simulations of Charge and Mass Distribution in Tubular SOEC," *ECS Transactions*, vol. 7, no. 1, pp. 2031–2039, 2007.
- [163] Y. Luo, Y. Shi, W. Li, and N. Cai, "Dynamic electro-thermal modeling of co-electrolysis of steam and carbon dioxide in a tubular solid oxide electrolysis cell," *Energy*, vol. 89, pp. 637–647, 2015.
- [164] M. Ni, "2D thermal-fluid modeling and parametric analysis of a planar solid oxide fuel cell," *Energy Conversion and Management*, vol. 51, no. 4, pp. 714–721, 2010.
- [165] V. Menon, "A Model-based Understanding of Reversible Oxide-ion-conducting and Proton-conducting Solid Oxide Fuel Cells (SOFCs)," *KIT Scientific Publishing/Dissertation (Doctoral thesis)*, p. 170, 2015.
- [166] Comsol, *COMSOL Multiphysics Reference Manual, version 5.3*, COMSOL, Inc. 2017.
- [167] M. F. Modest, *Radiative Heat Transfer*. 2013.
- [168] M. Kvesić, U. Reimer, D. Froning, L. Lüke, W. Lehnert, and D. Stolten, "3D modeling of a 200 cm<sup>2</sup> HT-PEFC short stack," *International Journal of Hydrogen Energy*, vol. 37, no. 3, pp. 2430–2439, 2012.
- [169] D. A. Nield and A. Bejan, *Convection in porous media*, vol. 24. Springer, 2013.
- [170] R. B. Bird, "Transport phenomena," *Applied Mechanics Reviews*, vol. 55, no. 1, pp. R1–R4, 2002.
- [171] R. J. Kee, M. E. Coltrin, and P. Glarborg, "Reacting Flow Chemically Theory and Practice," in *Reacting Flow Chemically Theory and Practice*, 2003.
- [172] A. J. Bard, L. R. Faulkner, N. York, C. @bullet, W. Brisbane, and S. E. Toronto, *ELECTRO-CHEMICAL METHODS Fundamentals and Applications*. 1944.
- [173] A. Roine, "Outokumpu HSC chemistry for windows: chemical reaction and equilibrium software with extensive thermochemical database," *User's guide, version*, vol. 5, 2002.
- [174] M. Zeng, J. Yuan, J. Zhang, B. Sundén, and Q. Wang, "Investigation of thermal radiation effects on solid oxide fuel cell performance by a comprehensive model," *Journal of Power Sources*, vol. 206, pp. 185–196, 2012.
- [175] G. J. Saunders, J. Preece, and K. Kendall, "Formulating liquid hydrocarbon fuels for SOFCs," *Journal of Power Sources*, vol. 131, no. 1-2, pp. 23–26, 2004.

## Bibliography

---

- [176] G. J. Saunders and K. Kendall, "Reactions of hydrocarbons in small tubular SOFCs," in *Journal of Power Sources*, vol. 106, pp. 258–263, 2002.
- [177] S. H. Jensen, X. Sun, S. D. Ebbesen, R. Knibbe, and M. Mogensen, "Hydrogen and synthetic fuel production using high temperature solid oxide electrolysis cells (SOECs)," *International Journal of Hydrogen Energy*, vol. 35, no. 18, pp. 9544–9549, 2010.
- [178] G. H. J. Broers and B. W. Treijtel, "Carbon deposition boundaries and other constant parameter curves, in the triangular representation of C- H- O equilibria, with applications to fuel cells," *Advanced Energy Conversion*, vol. 5, no. 4, pp. 365–382, 1965.
- [179] J. H. Nam and D. H. Jeon, "A comprehensive micro-scale model for transport and reaction in intermediate temperature solid oxide fuel cells," *Electrochimica Acta*, vol. 51, no. 17, pp. 3446–3460, 2006.
- [180] H. Zhu and R. J. Kee, "Modeling Distributed Charge-Transfer Processes in SOFC Membrane Electrode Assemblies," *Journal of The Electrochemical Society*, vol. 155, no. 7, p. B715, 2008.
- [181] M. Suzuki and T. Oshima, "Estimation of the Co-ordination number in a Multi-Component Mixture of Spheres," *Powder Technology*, vol. 35, no. 2, pp. 159–166, 1983.
- [182] P. Costamagna, "Modeling of Solid Oxide Heat Exchanger Integrated Stacks and Simulation at High Fuel Utilization," *Journal of The Electrochemical Society*, vol. 145, no. 11, p. 3995, 1998.
- [183] K. Nishioka, T. Takamoto, T. Agui, M. Kaneiwa, Y. Uraoka, and T. Fuyuki, "Annual output estimation of concentrator photovoltaic systems using high-efficiency InGaP/InGaAs/Ge triple-junction solar cells based on experimental solar cell's characteristics and field-test meteorological data," *Solar Energy Materials and Solar Cells*, vol. 90, no. 1, pp. 57–67, 2006.
- [184] K. Nishioka, T. Takamoto, T. Agui, M. Kaneiwa, Y. Uraoka, and T. Fuyuki, "Evaluation of InGaP/InGaAs/Ge triple-junction solar cell and optimization of solar cell's structure focusing on series resistance for high-efficiency concentrator photovoltaic systems," *Solar Energy Materials and Solar Cells*, vol. 90, no. 9, pp. 1308–1321, 2006.
- [185] W. J. Chang, K. H. Lee, H. Ha, K. Jin, G. Kim, S. T. Hwang, H. M. Lee, S. W. Ahn, W. Yoon, H. Seo, J. S. Hong, Y. K. Go, J. I. Ha, and K. T. Nam, "Design Principle and Loss Engineering for Photovoltaic-Electrolysis Cell System," *ACS Omega*, vol. 2, no. 3, pp. 1009–1018, 2017.
- [186] A. Nakajo, C. Stiller, G. Härkegård, and O. Bolland, "Modeling of thermal stresses and probability of survival of tubular SOFC," *Journal of Power Sources*, vol. 158, no. 1, pp. 287–294, 2006.

- 
- [187] J. Li, W. Kong, and Z. Lin, "Theoretical studies on the electrochemical and mechanical properties and microstructure optimization of micro-tubular solid oxide fuel cells," *Journal of Power Sources*, vol. 232, pp. 106–122, 2013.
- [188] E. Lay-Grindler, J. Laurencin, G. Delette, J. Aicart, M. Petitjean, and L. Dessemond, "Micro modelling of solid oxide electrolysis cell: From performance to durability," *International Journal of Hydrogen Energy*, vol. 38, no. 17, pp. 6917–6929, 2013.
- [189] M. E. Lynch, D. Ding, W. M. Harris, J. J. Lombardo, G. J. Nelson, W. K. S. Chiu, and M. Liu, "Flexible multiphysics simulation of porous electrodes: Conformal to 3D reconstructed microstructures," *Nano Energy*, vol. 2, no. 1, pp. 105–115, 2013.
- [190] J. D. Hyman and C. L. Winter, "Stochastic generation of explicit pore structures by thresholding Gaussian random fields," *Journal of Computational Physics*, vol. 277, pp. 16–31, 2014.
- [191] D. Yuan and F. A. Kröger, "Stabilized zirconia as an oxygen pump," *Journal of The Electrochemical Society*, vol. 116, no. 5, pp. 594–600, 1969.
- [192] X. D. Zhang, J. J. Li, and X. Guo, "Oxygen pump based on stabilized zirconia," *Review of Scientific Instruments*, vol. 86, no. 11, 2015.
- [193] A. Spirin, A. Lipilin, V. Ivanov, S. Pararin, A. Nikonov, V. Khrustov, D. Portnov, N. Gavrilov, and A. Mamaev, "Solid Oxide Electrolyte Based Oxygen Pump," *Advances in Science and Technology*, vol. 65, no. December 2014, pp. 257–262, 2010.
- [194] A. V. Spirin, A. V. Nikonov, A. S. Lipilin, S. N. Pararin, V. V. Ivanov, V. R. Khrustov, A. V. Valentsev, and V. I. Krutikov, "Electrochemical cell with solid oxide electrolyte and oxygen pump thereof," *Russian Journal of Electrochemistry*, vol. 47, no. 5, pp. 569–578, 2011.
- [195] C. Zhou, J. E. O'Brien, G. Rajan, S. Marsillac, and X. Zhang, "Water Splitting Using High Temperature Solid Oxide Photoelectrochemical Cell and Visible Sunlight: Searching for the Appropriate Semiconductor Materials," *Journal of The Electrochemical Society*, vol. 164, no. 7, pp. H497–H502, 2017.
- [196] K. J. Daun, S. B. Beale, F. Liu, and G. J. Smallwood, "Radiation heat transfer in planar SOFC electrolytes," *Journal of Power Sources*, vol. 157, no. 1, pp. 302–310, 2006.
- [197] R. A. Serway, "Principles of Physics," tech. rep., 1998.
- [198] A. Luque and S. Hegedus, *Handbook of Photovoltaic Science and Engineering*. 2011.
- [199] Y. Varshni, "Temperature dependence of the energy gap in semiconductors," *Physica*, vol. 34, no. 1, pp. 149–154, 1967.

## Bibliography

---

- [200] I. Vurgaftman, J. R. Meyer, and L. R. Ram-Mohan, “Band parameters for III-V compound semiconductors and their alloys,” *Journal of Applied Physics*, vol. 89, no. 11 I, pp. 5815–5875, 2001.
- [201] C. L. Yaws, *Yaws’ Handbook of Properties of the Chemical Elements*. 2011.

# CURRICULUM VITAE

---

## PERSONAL INFORMATION

Name: Meng Lin  
Nationality: China  
Date of birth: March 16<sup>th</sup>, 1988

## EDUCATION AND ACADEMIC EXPERIENCE

2013.9-2018.3      **École polytechnique fédérale de Lausanne (EPFL)**, Mechanical Engineering, PhD student  
2013.3-2013.7      **Shanghai Jiao Tong University (SJTU)**, Mechanical Engineering Research assistant  
2011.12-2012.6      **North Dakota State University (NDSU)**, Mechanical Engineering Visiting scholar  
2010.9- 2013.3      **Shanghai Jiao Tong University (SJTU)**, Mechanical Engineering Master of Science  
2006.9-2010.7      **University of Shanghai for Science and Technology (USST)**, Energy and Power Engineering. Bachelor of Science

## PUBLICATIONS IN PEER-REVIEWED SCIENTIFIC JOURNALS

1. **Meng Lin**, and Sophia Haussener. "Techno-economic modeling and optimization of solar-driven high temperature electrolysis systems." *Solar Energy* 155 (2017): 1389–1402.
2. Lihao Han, **Meng Lin**, and Sophia Haussener. "Reliable Performance Characterization of Mediated Photocatalytic Water-Splitting Half Reactions." *ChemSusChem* 10 (2017): 2158–2166.
3. **Meng Lin**, and Sophia Haussener. "Solar fuel processing efficiency for ceria redox cycling using alternative oxygen partial pressure reduction methods." *Energy* 88 (2015): 667-679.
4. **Meng Lin**, Sophia Haussener. "Modeling and design guidelines for direct steam generation solar receivers." *Applied Energy* 216 (2018): 761-776.
5. **Meng Lin**, Sophia Haussener. "An integrated concentrated solar fuel generator concept utilizing a tubular solid oxide electrolysis cell as the solar absorber". (In preparation)

## **PATENTS AND LICENSES**

1. Saurabh Tembhurne, **Meng Lin**, Sophia Haussener. Integrated Photo-Electrochemical Device for Concentrated Irradiation. International Patent Application n° PCT/IB2017/055019, 2017.08.

## **ORAL AND POSTER CONTRIBUTIONS TO CONFERENCES**

1. **Meng Lin**, **Sophia Haussener**. Thermodynamic analysis of ceria redox cycling for solar fuel processing using different methods for  $p_{O_2}$  reduction. ASME 2014 8th International Conference on Energy Sustainability, Boston (2014.7). (Oral Presentation)
2. **Meng Lin**, **Sophia Haussener**. Modeling and optimization of a multi-tubular solar receiver for solar-driven high temperature electrolysis. ASME 9th International Conference on Energy Sustainability, San Diego (2015.8). (Oral Presentation)
3. **Meng Lin**, Sophia Haussener. Modeling and optimization of a multi-tubular solar receiver for solar-driven high temperature electrolysis. First Thermal and Fluids Engineering Summer Conference, New York (2015.7). (Oral Presentation)
4. **Meng Lin**, Sophia Haussener. Techno-economic analysis of a solar driven hybrid PV-CST high temperature electrolysis system for syngas production. 13<sup>th</sup> symposium on modeling & experimental validation of fuel cells, batteries & electrolysis, Lausanne (2016.3). (Oral Presentation)
5. Mathias Niffeler, **Meng Lin**, Arata Nakajo, Marco Cantoni, Sophia Haussener, Jan Van Herle . Evolution of the Properties of LSM-YSZ Solid Oxide Fuel/Electrolysis Cell Electrodes During Exposure Tests. 13<sup>th</sup> symposium on modeling & experimental validation of fuel cells, batteries & electrolysis, Lausanne (2016.3). (Poster)
6. **Meng Lin**, **Sophia Haussener**. Numerical simulation of a helical-tube solar receiver for solar-driven high temperature electrolysis. ASME 10th International Conference on Energy Sustainability, Charlotte (2016.7). (Oral Presentation)
7. **Meng Lin**, Sophia Haussener. Numerical and experimental study of an integrated solar reactor for solar-driven high temperature electrolysis. ASME 11th International Conference on Energy Sustainability, Charlotte (2017.6). (Oral Presentation)
8. **Meng Lin**, **Sophia Haussener**. Numerical and experimental investigation of a novel double-helical receiver for solar-driven high temperature electrolysis. ASME Summer Heat Transfer Conference, Bellevue (2017.7). (Oral Presentation)

Note: The underlined authors are presenting authors.



